COMMAND GENERATION FOR FLEXIBLE SYSTEMS

BY

WILLIAM EARL SINGHOSE

S.B.M.E., MASSACHUSETTS INSTITUTE OF TECHNOLOGY, 1990
M.S.M.E., STANFORD UNIVERSITY, 1992

SUBMITTED TO THE DEPARTMENT OF MECHANICAL ENGINEERING
IN PARTIAL FULFILLMENT OF THE REQUIREMENTS FOR THE DEGREE OF

DOCTOR OF PHILOSOPHY

AT THE

MASSACHUSETTS INSTITUTE OF TECHNOLOGY
MAY 1997

SIGNATURE OF AUTHOR _____
WILLIAM E. SINGHOSE
DEPARTMENT OF MECHANICAL ENGINEERING, MAY 9, 1997

CERTIFIED BY _____
PROFESSOR WARREN P. SEERING
COMMITTEE CHAIRMAN

ACCEPTED BY _____
AIN A. SONIN
CHAIRMAN, DEPARTMENTAL GRADUATE COMMITTEE

COMMAND GENERATION FOR FLEXIBLE SYSTEMS

BY
WILLIAM EARL SINGHOSE

SUBMITTED TO THE DEPARTMENT OF MECHANICAL ENGINEERING ON MAY 9, 1997
IN PARTIAL FULFILLMENT OF THE REQUIREMENTS FOR THE DEGREE OF
DOCTOR OF PHILOSOPHY.

ABSTRACT

For many types of mechanical systems flexibility presents the biggest challenge to the control system. If the mechanical components undergo deflection during the course of operation, it may prove difficult to track a desired trajectory or avoid obstacles. Furthermore, once the system has reached a setpoint, the residual vibration will degrade positioning accuracy and may cause a delay in task completion. Even if the mechanical components are very stiff, a closed-loop controller may introduce flexibility of its own that is detrimental to system performance.

The desired motion of a system is fed into a command generator that transforms the desired motion into a reference command. The reference command is then used to either drive an open-loop system, or form an error signal for a closed-loop system. Not every control system has a closed-loop controller; however, every control system does have some form of command generator. In many systems the command generator may not be immediately obvious and it may not be programmed into a computer. For example, the command generator for a construction crane is the human operator who attempts to produce an appropriate reference command in real time.

This thesis presents methods for designing command generators for flexible systems. Specifically, it is concerned with what shape the reference commands should have. If the commands have an appropriate shape, then they will produce the desired motion, while reducing the detrimental effects of flexibility. In this thesis, the reference command is treated as a design variable (within some bounds) rather than a given parameter.

THESIS COMMITTEE: PROF. WARREN P. SEERING, CHAIRMAN
PROF. STEPHEN H. CRANDALL
PROF. JEAN-JACQUES E. SLOTINE
PROF. GEORGE C. VERGHESE
DR. NEIL C. SINGER

ACKOWLEDGEMENTS

I would like to generously thank the many people and organizations that assisted and supported my work. This thesis, perhaps more than most Ph.D. dissertations, is the product of collaboration with numerous people. My advisor, Warren Seering, was continually encouraging, insightful, and optimistic. A special thanks also goes to Neil Singer for his groundbreaking work in the field of command generation and his help with gaining access to numerous industrial machines.

My coauthors provided invaluable help and allowed me to engage in far more endeavors than I could have by working in isolation. These people include: Arun Banerjee, Kristen Bohlke, Ethan Crain, Thomas Chuang, Steve Derezinski, Hans Jacob Feder, Bart Mills, Lucy Pao, Lisa Porter, Tarun Singh, Timothy Tuttle, and Isela Villanueva. Also aiding directly in my research where the UROP and bachelor's students that I worked with: Joel Ford, Becky Masterson, and Ravi Sastry. Professors Stephen Crandall, Jean-Jacques Slotine, and George Verghese have my thanks for acting as committee members and forcing me to consider my work from several different points of view. My discussions over the years with Professor Thomas Kane provided valuable insights on both dynamics and life.

In addition to those involved directly with my research, my family and friends gave me valuable support during my time at MIT. My office mates, especially Dan Frey and Raj Suri, provided interesting discussions and insights that helped me achieve a larger perspective on my work. The MIT track team provided a helpful diversion by allowing me to work out with them and to coach them. Special thanks goes to the MIT Pole Vaulters and Lisa Porter for continually motivating the quest for hugeness.

Financial support for this work was provided by Convolve, Inc., the Office of Naval Research Fellowship Program, the Massachusetts Space Grant Fellowship program, and MIT's Lincoln Laboratory through grant BX-6473.

PATENT NOTICE

The methods described in this dissertation are patented (#4,916,635; April 10, 1990 and #5,638,267; June 10, 1997). Commercial use of these methods requires written permission from the Massachusetts Institute of Technology and Convolve, Inc.

TABLE OF CONTENTS

TABLE OF FIGURES

1 INTRODUCTION TO COMMAND GENERATION

1.1 Introduction

The performance of mechanical systems depends on numerous variables such as the mechanical design, the operating environment, and the control system. The most important influence on performance varies from system to system and may change over time, or with the task being performed. However, the control system is almost always an important factor in system performance. Given the increasing use of computers to control mechanical systems and the trend toward faster, lighter, and more flexible structures, control system design and implementation will continue to gain in importance.

The control system must perform functions such as positioning, trajectory tracking, suppression of residual vibration, obstacle avoidance, and disturbance rejection. Figure 1.1 shows a block diagram of a generic control system. The desired motion, D(t), is fed into a command generator. The command generator transforms the desired motion into a reference command, r(t), which is compared to the measured state of the system, $\hat{y}(t)$. This comparison yields an error signal, e(t), that the closed-loop controller uses to generate the control signal, u(t). The control signal is then used to drive the actuators of the physical plant.

The reference command, r(t), is a representation of the desired motion in the "language" of the system being controlled. For example, suppose an XY stage must perform an "L" shaped motion. The system components only understand voltages, encoder counts, and the like. The command generator must translate the desired motion into a signal that can be used by the system. One such command that could represent an "L" shaped motion is shown in Figure 1.2. The solid and dashed lines describe the desired X and Y locations as a function of time. Initially, the Y command decreases at a constant rate in the negative direction. This represents travel down the vertical leg of the "L". Once the knee of the "L" is reached, the Y command stops changing. The X command then increases at a constant rate to achieve motion along the foot of the "L". Figure 1.2 shows that the commands form an "L" when plotted in the XY space.

The commands shown in Figure 1.2 are only one possible way to perform the desired motion. Figure 1.3 shows an alternate set of commands that also produce an "L" shaped motion. In this

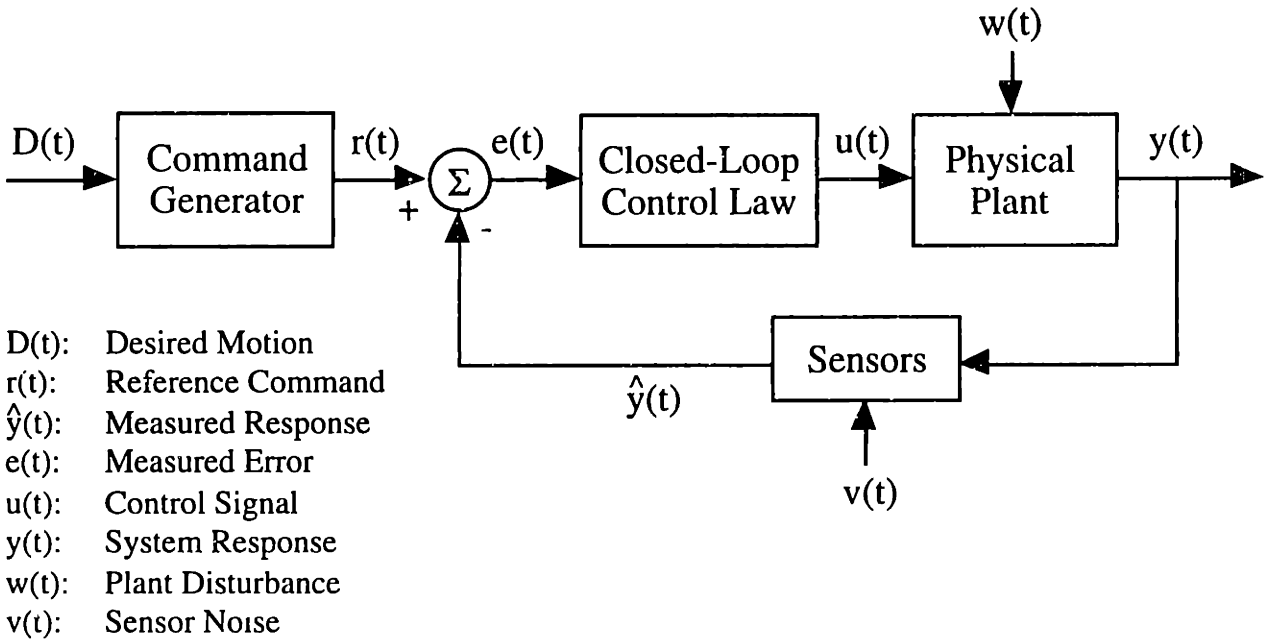

Figure 1.1: Block Diagram of a Generic Control System.

case, the system travels half way down the vertical leg and then stops for a small length of time before continuing. Similarly, the travel along the foot is temporarily delayed at the midpoint. The important point to note is that the commands used to perform a desired motion can have a variety of shapes. As we will see, the shape of the commands can greatly affect system performance.

Not every control system has a closed-loop controller; however, every control system does have some form of command generator. In many systems the command generator may not be immediately obvious and it may not be programmed into a computer. In the above example, the command generator is the programmer who specifies the reference commands given that the desired motion is an "L". With other types of systems, such as construction cranes, a human operator acts as the command generator to produce a reference command in real-time that attempts to produce a desired motion. The success of the control system depends largely on the experience and skill of the operator. That is, the performance is highly dependent on the command generator.

For many types of systems, flexibility presents the biggest challenge to the control system. If the mechanical components undergo deflection during the course of operation, it may prove difficult to track a desired trajectory or to avoid obstacles. Furthermore, once the system has reached a setpoint, the residual vibration will degrade positioning accuracy and may cause a delay in task completion. Even if the mechanical components are very stiff, a closed-loop controller may introduce flexibility of its own that is detrimental to system performance.

Given the importance of system flexibility, it is not surprising that an enormous amount of research and development has gone into dealing with this problem. Solutions to the problem of

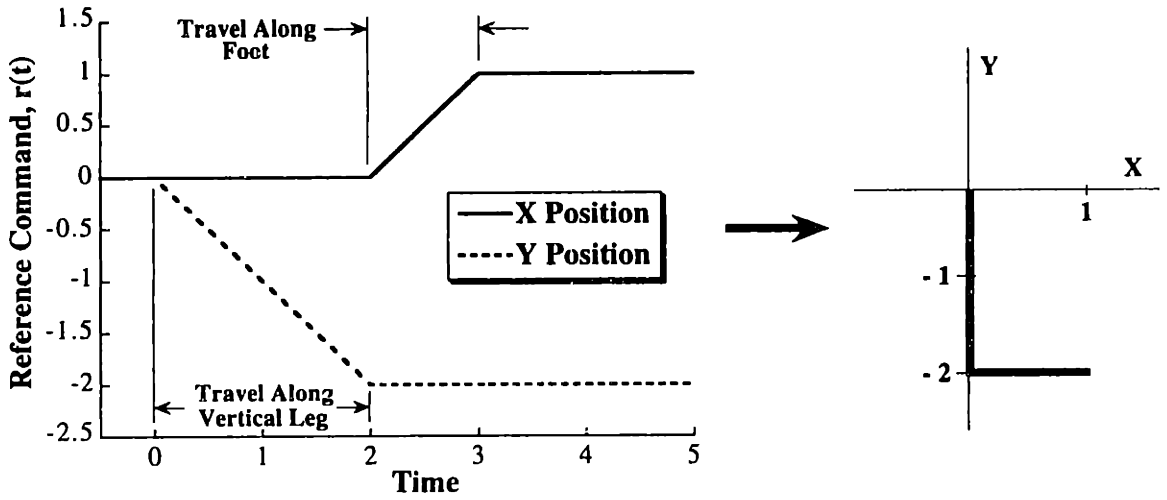

Figure 1.2: Reference Commands to Perform an "L" Shaped Motion.

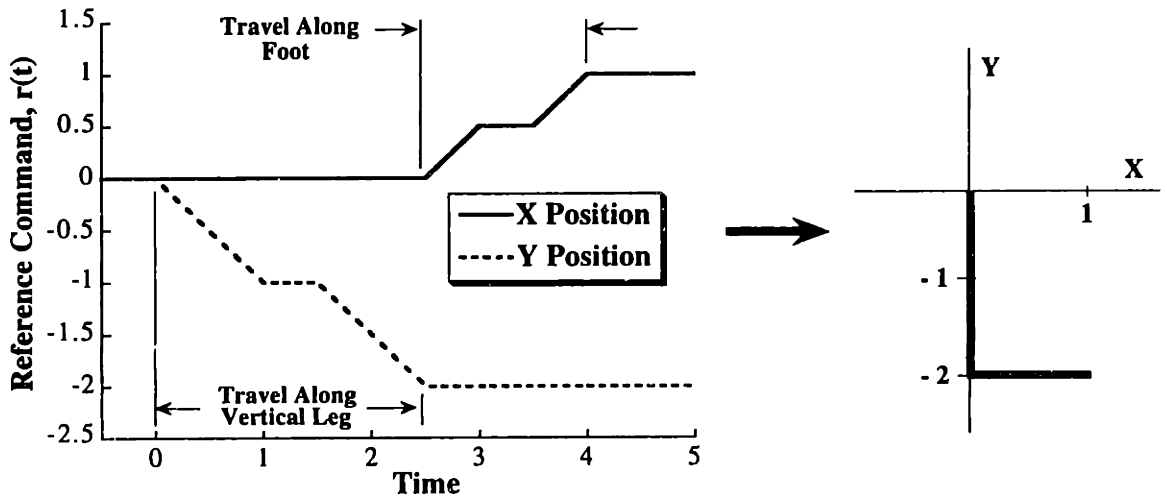

Figure 1.3: Alternate Reference Commands to Perform an "L" Shaped Motion.

flexibility include stiffening the mechanical structure, adding damping to the system, using additional sensors or actuators, designing a sophisticated closed-loop controller, and using specially shaped reference commands.

This thesis presents methods for designing command generators for flexible systems. Specifically, it is concerned with what shape the reference commands should have. If the commands have an appropriate shape, then they will produce the desired motion, while reducing the detrimental effects of flexibility. In this thesis, the reference command is treated as a design variable (within some bounds) rather than a given parameter.

This first chapter illustrates the impact that the reference command can have on system performance. It also gives some background on previously proposed command shaping schemes and presents the design philosophy that will be used throughout the thesis. At the end of this

chapter, the principle contributions of this thesis will be outlined. Chapter 2 describes analysis tools that can be used to generate and evaluate shaped commands. Chapter 3 presents methods for generating shaped reference commands in real-time.

Chapter 4 describes commands that are multi-switch bang-bang functions. That is, the actuators are always producing full positive or full negative effort. These types of commands produce very rapid motion. Chapter 5 addresses the issue of command generation for a somewhat larger class of commands called on-off control. In this case, the generated commands are either a constant positive value, zero, or a constant negative value. The need for such control arises when the system has on-off actuators such as reaction jets, or the control system is attempting to achieve some type of optimal trajectory. Chapter 6 proposes methods for facilitating the implementation of on-off control schemes. Chapter 7 compares various command generation schemes, while Chapter 8 discusses their effects on high-level performance specifications. Finally, Chapter 9 summarizes the results and suggests areas for further work.

1.2 Significance of the Reference Command

Recently, interest in the command generator component of the control system has increased substantially. This interest has be motivated by recent success in command generator design and the realization that the reference command can have a significant impact on system performance. This section attempts to demonstrate the importance of the reference command.

1.2.1 Undamped Second-Order Systems

The importance of the reference command can be illustrated by investigating the dynamic response of an undamped second-order harmonic oscillator. Let us assume that the desired motion is a rapid change in position from 0 to 1. Given this desired motion, the most obvious command generator produces a step function. Figure 1.4 shows the step response of an undamped oscillator with a frequency of 1 Hz.

In an attempt to reduce vibration, a command generator that produces a ramp function in response to the desired motion could be used. Figure 1.5 shows the response to a ramp command that lasts for 0.5 sec. The vibration is reduced to 63% of the step-induced vibration. The cost of this reduced vibration is an increase in rise time. With a step input the system first reaches 99% of the desired distance at 0.25 sec., while the ramp input produces a rise time of 0.5 sec.

If the frequency of vibration is taken into account, a command generator can be implemented that produces a special staircase command. Figure 1.6 shows that this staircase command causes the system to make the desired motion without any residual vibration. The price for this improved performance is increased rise time as compared to the step input. The rise time is 0.5 sec., the same as with the ramp input. All three reference commands produce the desired motion, a rapid change in position, but the commands produce vastly different amounts of residual vibration.

Details on how to create a command generator like the one used to produce the staircase command will be given in Section 1.3. The output of these command generators is not always a staircase, rather the shape of the command depends on the desired motion fed into the command generator. The distinguishing characteristic of the shaped reference commands is that they move the system without residual vibration.

1.2.2 Damped Second-Order Systems

The results of the previous section may be considered somewhat exaggerated because systems equipped with "good" closed-loop controllers do not respond like undamped oscillators. If the system is equipped with sensors that can measure the vibration, or a model can be constructed to predict the vibration, then a closed-loop controller can often produce a well-damped response.

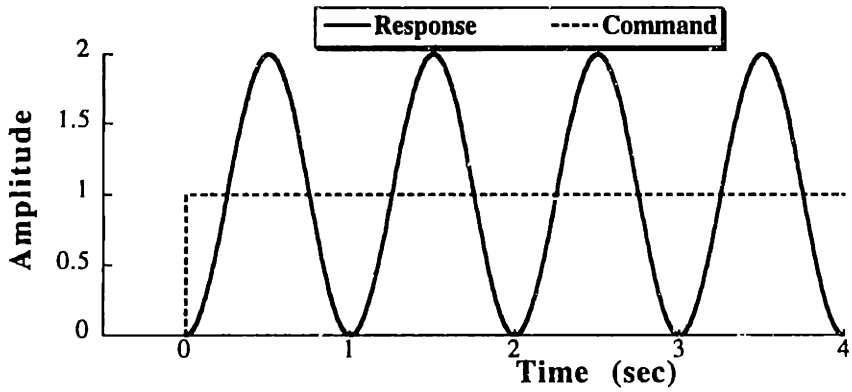

Figure 1.4: Step Response of an Undamped Second-Order System.

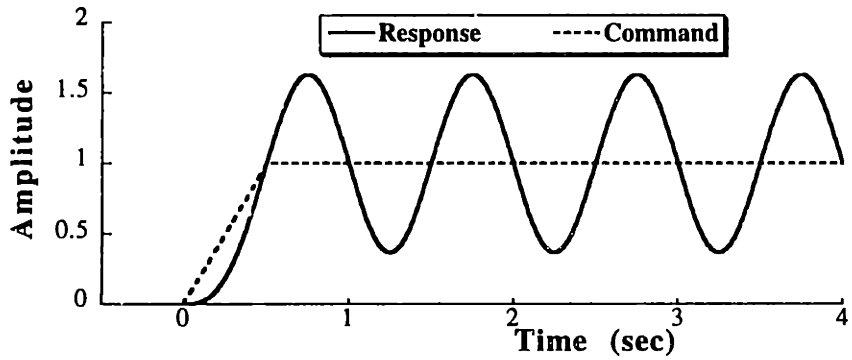

Figure 1.5: Ramp Response of an Undamped Second-Order System.

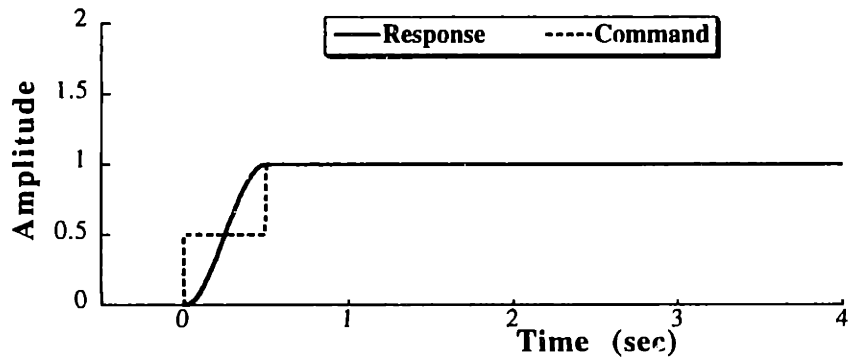

Figure 1.6: Staircase Response of an Undamped Second-Order System.

To investigate the case when the system has a good closed-loop controller, we can examine the response of a well-damped harmonic oscillator. Figure 1.7 shows step, ramp, and staircase responses of a system with a damping ratio of 0.707. For this case, the effect of the reference command is less pronounced, but it is still quite significant. The ramp command reduces the overshoot slightly, while increasing the rise time substantially. The step command settles the system to within 1% at 1.05 sec. On the other hand, the staircase command yields a settling time of only 0.62 sec. and, as can be seen from the figure, the price of this improved settling time is only a slightly longer rise time.

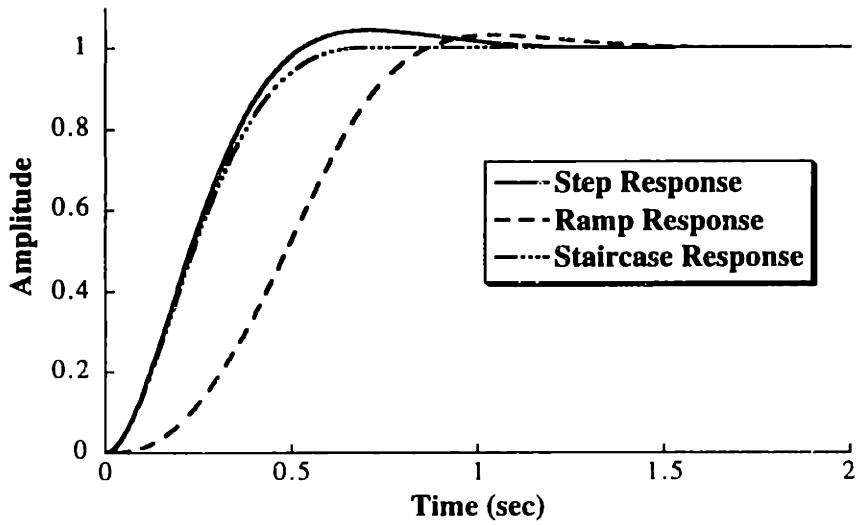

Figure 1.7: Response of Well-Damped (ζ=0.707) Second-Order System to Step, Ramp, and Staircase Commands.

1.2.3 Multi-Mode Systems

The importance of the reference command shape is not limited to second-order systems. The performance of multi-mode and nonlinear systems can also strongly depend on the reference command. Figure 1.8 shows the response of a two-mode system to both step and staircase commands. The system has a 1 Hz mode with a damping ratio of 0.2 and a 2.5 Hz mode with a damping ratio of 0.05. In this case, the staircase command has more steps than for a single-mode system, but the result is still zero residual vibration at the cost of a small increase in rise time.

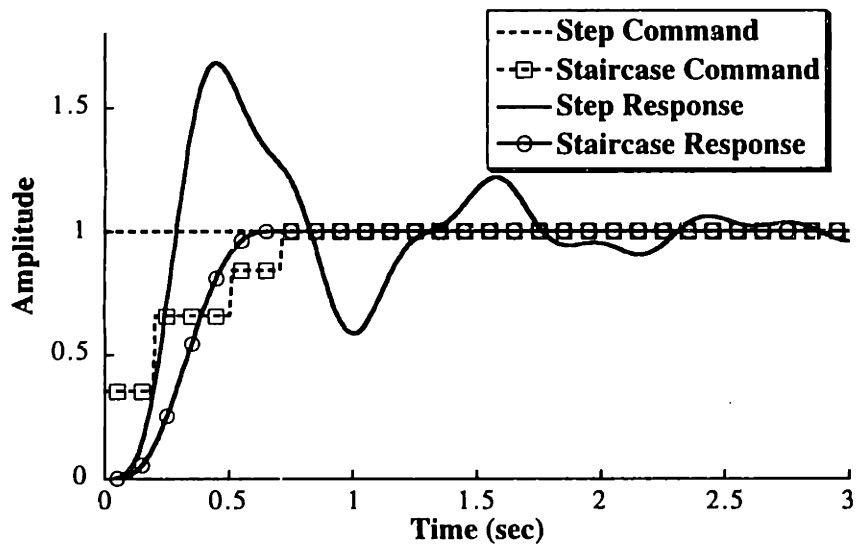

Figure 1.8: Fourth-Order System Response to Step and Staircase Commands.

1.3 Classes of Shaped Commands

The preceding section demonstrated the important role of the reference command. The commands that were specially shaped for the system under consideration yielded substantial performance improvements (residual vibration reduction) with very little cost (increase in rise time). This section describes two broad classes of reference commands, those that are pre-computed and those that are generated in real-time. Within each class, there are many subclasses of commands that will be described throughout the remainder of this thesis.

1.3.1 Pre-Computed Command Profiles

The shaped command profiles shown in Section 1.2 could have been pre-computed at the start of the motion. That is, the command generator could simply output a properly scaled staircase command when it receives a desired motion that is a rapid change in position. The shape of the entire command would be set at the instant that the desired motion was received by the command generator. It would not depend on events that occur between the beginning of the motion and the end of the motion.

Pre-computed commands come in a variety of forms including those with sharp transitions such as staircase commands and those with smoothly changing values. Some types of pre-computed commands have smooth shapes so as not to excite high frequencies, while other types of commands are generated by superimposing smooth functions and their harmonics so as to decrease vibration at a specific frequency [3, 29, 47, 63-65, 142, 147, 167-169]. Meckl and Seering constructed input functions from ramped sinusoids and versine functions [63, 65, 66]. By using higher order harmonics, the command profile was made to approach the shape of a bang-bang function. A similar approach developed by Aspinwall used harmonics of a sine series [3]. Swigert used damped trigonometric series to construct command profiles [142]. A similar concept was used by Wiederrich and Roth to synthesize cam profiles [168, 169].

Commands producing time-optimal motion are another category of pre-computed command profiles. The time-optimal command for flexible linear systems with only pole dynamics and subject to actuator limits is a multi-switch bang-bang function such as that shown in Figure 1.9 [4, 11, 21, 52, 78, 80, 85, 93, 111, 117, 149, 165]. The times at which the bang-bang command switches between positive and negative values depend on the system parameters and the desired move distance. A time-optimal command generator receives the desired motion command and then generates the command profile that switches at the appropriate times.

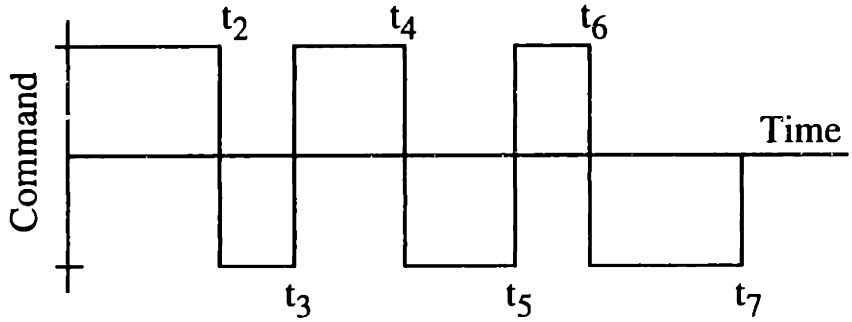

Figure 1.9: Typical Time-Optimal Command Profile.

One potential problem with pre-computed command profiles is their inherent open-loop nature. If a new motion is desired before a motion in progress is completed, then either the new motion must be delayed until after completion of the current motion, or the current motion must be interrupted. If a pre-computed command is interrupted there is no guarantee that its vibration reducing properties will be preserved.

1.3.2 Real-Time Command Shaping

Rather than pre-computing complete command profiles, a shaped command can be generated in real-time by filtering the reference command. In this case, the command generator can be thought of as having two distinct components as shown in Figure 1.10. The first component transforms the desired motion into a reference command, c(t), using a standard approach and disregarding the system flexibility. For example, a desired motion that is a rapid change in position is converted into a step change in the reference command. The second component of the command generator takes into account the system flexibility and filters the reference command to produce a shaped reference command, r(t). If the filtering process does not require an excessive amount of computation, then this process can be implemented in real time.

For linear systems, the filters can be described as having a finite impulse response (FIR) or an infinite impulse response (IIR). A substantial amount of research has been devoted to the design of both FIR and IIR filters [74, 83, 145, 173]. Recently, a new variation of FIR filtering, called input shaping, has been proposed to specifically target vibration of mechanical systems [101, 102]. Input shaping is implemented by convolving the reference command with a sequence of impulses (filter coefficients), also known as the input shaper. This process is illustrated in Figure 1.11 using a step command and an input shaper containing two impulses. The result is a staircase command like those discussed in the previous section. The design objective is to choose the impulse amplitudes and time locations so that the shaped (filtered) command reduces the detrimental effects of system flexibility.

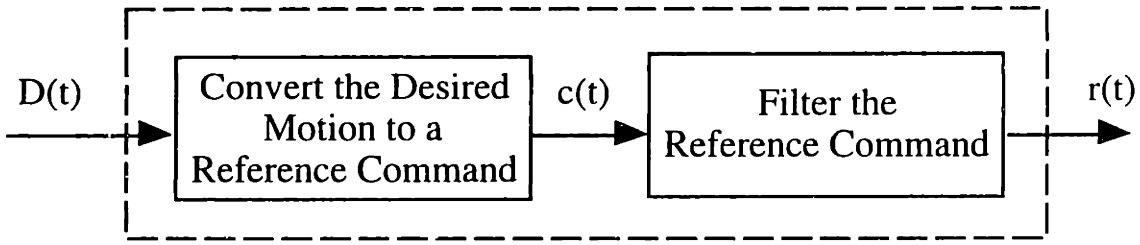

D(t): Desired Motion
c(t): Initial Reference Command
r(t): Filtered Reference Command

Figure 1.10: Command Generator for Real-Time Command Shaping.

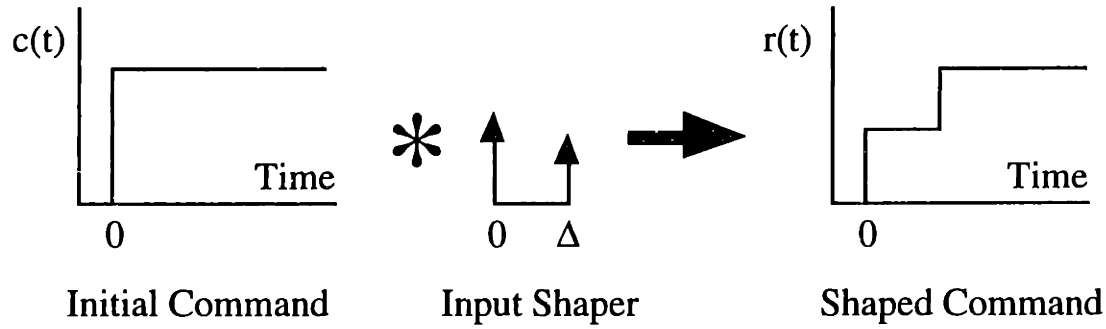

Figure 1.11: Input Shaping a Step to Produce a Staircase Command.

The design procedure with input shaping differs from traditional digital FIR filtering in at least one significant way; no pass-band is specified. Traditional FIR filters can be considered as one of five basic types:[1]

1) Lowpass filter: Pass low frequency vibrations, attenuate high frequencies.
2) Highpass filter: Pass high frequency vibrations, attenuate low frequencies.
3) Bandpass filter: Pass a range of frequencies, attenuate frequencies above and below this range.
4) Bandstop filter: Attenuate a range of frequencies, pass frequencies above and below this range.
5) All-pass filter: Pass all frequencies, introduce predictable phase shifts at certain frequencies.

The frequency domain performance specifications for the five types of FIR filters are compared to the performance specifications for an input shaper in Figure 1.12. The gray areas are desired regions for the filter transfer function. Each type of filter has some desired passband, but the input shaper does not. Although the all-pass filter does not have a stop band it has specifications for introducing predictable phase shifts for different frequency ranges.

The type of traditional FIR filter most closely related to input shaping is the bandstop filter, where a range of frequencies are suppressed. However, these filters are designed so that

[1] *Handbook of Filter Synthesis*, pg. 1 [173].

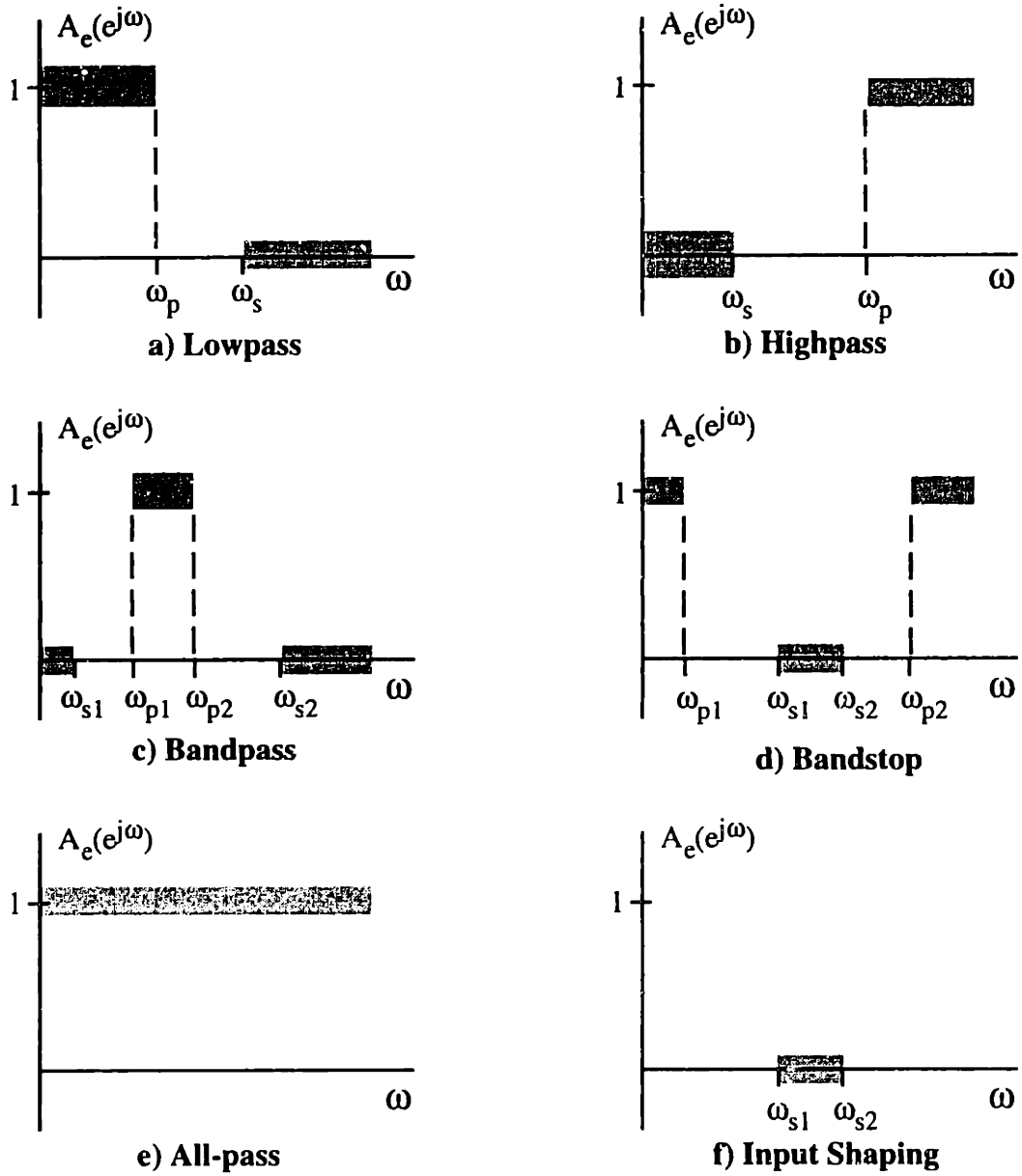

Figure 1.12: Frequency Domain Performance Specifications.

frequencies outside of the stop band are passed with only minor attenuation. Input shaping has no such performance requirement. In mechanical systems, the primary objective is to suppress the vibration modes of the structure. Therefore, only stop bands are specified in the design of input shapers.

Without the requirement of a pass band, the set of performance specifications for input shaping is less extensive than for stopband filtering. In fact, many input shapers do not have a range of stop frequencies, ω_{s1} - ω_{s2}, as shown in Figure 1.12f. Instead, limits on the transfer function amplitude are applied at only a single frequency, or a set of individual frequencies. As a result of

the simplicity of the performance specifications, many types of input shapers have been determined in closed-form.

In addition to the fundamental difference of pass band specifications, input shaping has certain characteristics that differ from the general characteristics of traditional FIR filtering. The frequencies being suppressed by input shaping are assumed to have damping, while traditional filtering methods are often based on frequency domain techniques that assume undamped dynamics. The number of filter coefficients is generally chosen with filtering, but not with input shaping. Finally, the length of an input shaper is almost always minimized, on the other hand, filters are usually designed by minimizing the stop-band amplitude or the pass-band ripple.

Input shaping is advantageous when compared to traditional FIR filtering because it has a low number of impulses (filter coefficients), short duration (filter length), and large robustness to modeling errors (width of stop band) [99, 126]. Several tools for designing input shapers will be discussed in Chapter 2. These methods are then used in Chapter 3 to design shapers that meet a variety of performance specifications.

1.4 Design Philosophy

The design of command generators in this thesis is based on the following principles:

1) The generator should have robustness to modeling errors.

2) The performance specifications should be achievable in an actual implementation.

3) The neighborhood around "optimal" solutions should be examined for "near-optimal" solutions that provide significant performance improvements in auxiliary performance measures.

4) The performance specifications should be considered somewhat flexible.

1.4.1 Robustness to Modeling Uncertainty

If a command generator is to produce a command with an appropriate shape, it must have some information about the system for which it is generating commands. For example, if a crane operator is to move a payload forward 1 meter by pressing a button and then releasing it after some amount of time, the operator needs to have some idea of how far the crane will move for every second the button is pressed. If a command generator is to produce a command that results in zero residual vibration, then the generator must know the frequencies and damping ratios of the system. Stated succinctly, a command generator must have a model of the system being controlled.

Given that no model is perfectly accurate, the shaped command will cause a motion that is different than the intended response. If the shaped command is attempting to move the system with zero residual vibration, then the actual response will have some finite amount of vibration. If a command generator is to work successfully on a real system, then it must have robustness to errors in the system model.

Most of the command generators developed in this thesis will be made robust to modeling errors. Without robustness, command generators have limited utility for most real systems. Early forms of command generators such as posicast control [24, 25, 140, 141, 144], suffered from poor robustness properties. The recently proposed robust command generators have proven very beneficial for real systems [28, 34, 58, 87, 97, 129, 134, 152]. One of the central ideas that permeates this work is that command generators can and should be made robust to all types of applicable modeling errors.

1.4.2 Use of Achievable Performance Specifications

Command generators are designed based on a set of desired performance specifications. These specifications include constraints on quantities such as residual vibration amplitude, rise time, settling time, etc. Another concept that appears frequently in this thesis is the idea that the performance specifications should be achievable in practice. For example, real systems always

exhibit some level of residual vibration. Therefore, when a constraint is placed on the residual vibration amplitude, it is better to limit the vibration to some low level rather than require the vibration to be identically zero. To achieve the theoretical possibility of zero residual vibration, some other performance criteria must be sacrificed.

To demonstrate this concept we analyze the performance of three types of input shapers. A zero vibration (ZV) shaper is designed by requiring that it produce commands that cause zero residual vibration when the model is perfect [24, 25, 101, 140, 141, 144]. For a single-mode system, this constraint leads to a shaper containing two impulses, like the one shown previously in Figure 1.11. A ZV shaper is very sensitive to modeling errors. To illustrate this, we can generate a *sensitivity curve*, which is a plot of the percentage residual vibration (vibration with shaping divided by vibration without shaping) versus the normalized frequency (the actual frequency, ω_a, divided by the modeling frequency, ω_m). To compare robustness quantitatively, the *insensitivity* is defined as the width of the curve that lies below a specified level, normalized by the modeling frequency. If the width is measured at the 5% level, then the ZV shaper has a 5% insensitivity of 0.06 as shown in Figure 1.13

For the shaping process to be effective on real systems, the shaper must have robustness to modeling errors. One type of robust shaper can be obtained by requiring the derivative with respect to the frequency of the residual vibration be equal to zero. That is, the sensitivity curve must have zero slope at the modeling frequency. The sensitivity curve for a zero vibration and derivative (ZVD) shaper is also shown in Figure 1.13. If we measure the width of the ZVD curve at 5% we find that it is 0.286, nearly 5 times more robust than the ZV shaper.

The price of the increased robustness is an increase in rise time. A ZV shaper has a duration equal to one half period of the vibration being targeted for elimination. This means that the shaped reference command will take one half period longer to reach a desired setpoint than the corresponding unshaped command. (This is the value of Δ shown in Figure 1.11.) On the other hand, a ZVD shaper has a duration of one vibration period.

Another type of input shaper is the extra-insensitive (EI) shaper. Unlike the ZV and ZVD shapers, the EI shaper does not attempt to force the vibration to zero at the modeling frequency. Rather, the vibration is limited to some low, but acceptable level of residual vibration. The sensitivity curve for an EI shaper designed to limit vibration below 5% is also shown in Figure 1.13. The EI shaper provides a substantial increase in robustness over the ZVD shaper, while having the same duration. The increased robustness was obtained by simply replacing the unrealistic criterion of exactly zero residual vibration with an achievable performance specification.

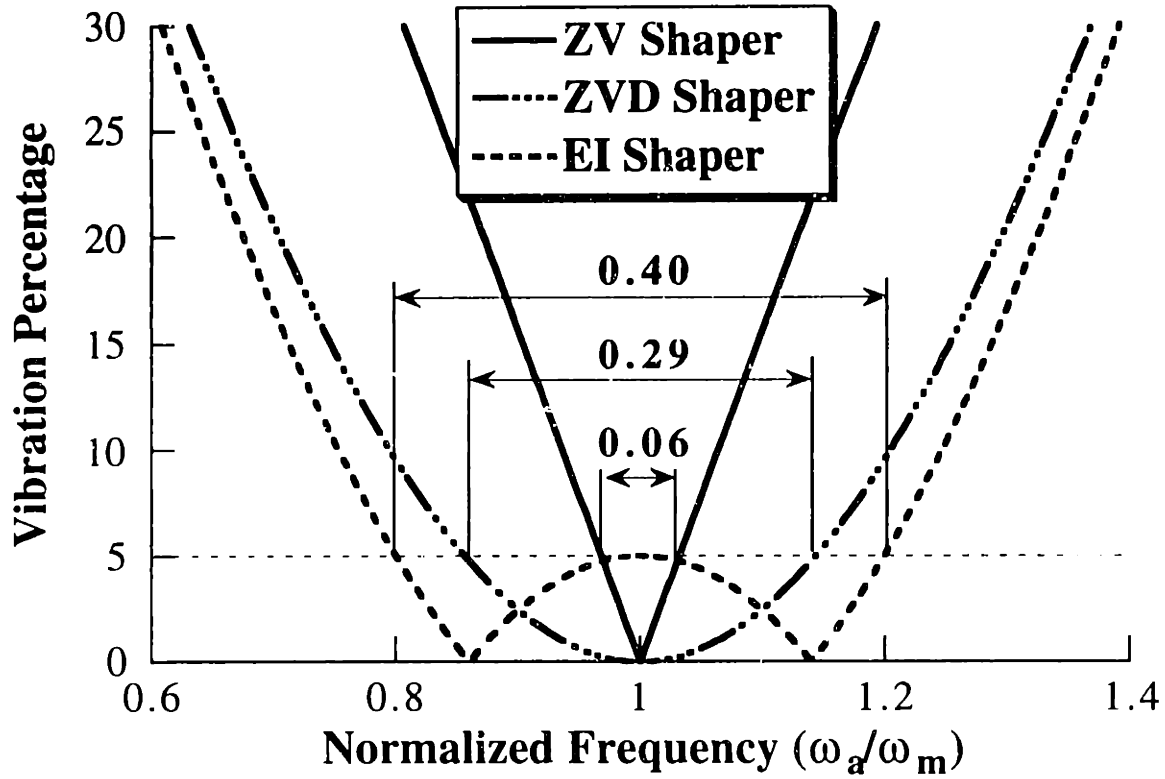

Figure 1.13: Sensitivity Curves for ZV, ZVD, and EI Shapers.

1.4.3 Exploitation of Flatness Near Optimal Solutions

In the engineering pursuit we are continually faced with tradeoffs. One such tradeoff in the design of command generators that should be obvious from this first chapter is the relationship between rise time and residual vibration amplitude. In most cases low levels of residual vibration cannot be obtained with a command that produces the fastest rise time. To achieve low levels of residual vibration, the rise time must be increased. Another example is the increase in rise time that is required to improve robustness. In general, improving one performance measure requires sacrificing some other performance measure. That is, we cannot get something for nothing.

Throughout this thesis, we *attempt* to get something for nothing, or at least for very little. An example of this is the EI input shaper. The EI shaper gives up the theoretical possibility of exactly zero residual vibration in exchange for a substantial increase in robustness. Given that zero residual vibration cannot be obtained on real systems, the EI shaper has given up essentially nothing to obtain its improved robustness. Wherever possible, we attempt to give up unimportant quantities to improve important performance measures.

Justification for this course of action can be made if we consider command generation as an optimization problem where the goal is to minimize an objective function such as rise time. In addition to the parameter being minimized, there are other important measures that we try to control

such as residual vibration amplitude and robustness to modeling errors. The solution to many types of optimization problems must be at a "stationary" point [21]. That is, the partial derivative of the cost function with respect to the minimized parameter must be zero at the minimum point. Stated differently, the cost function is flat at the global minimum.

Figure 1.14 shows an objective surface that has its global minimum when the parameter values are (1, 0.1). The derivative with respect to both parameters of the objective function, J, is zero at the global minimum. Because the function is flat, there is a possibility that we can move away from the minimum point a substantial amount without significantly increasing the cost. If we move away in the right direction, then we might be able to improve the performance in one of the auxiliary parameters (vibration, robustness, etc.) with little increase in cost. For example, if objective values of up to 0.05 are acceptable, then the parameters may be chosen anywhere in the blue or green areas of Figure 1.14. Many of the proposed command generation schemes in this thesis take advantage of this effect when it exists.

1.4.4 Modification of Performance Specifications

To exploit the possible flatness of the solution space, we often need to modify the performance specifications. The ZVD problem statement requires the residual vibration to be exactly zero when the model is perfect. The EI problem statement allows there to be some small level of residual vibration when the model is perfect. The EI performance specifications are only a slight variation of the ZVD performance specifications. This can be seen by reducing the acceptable vibration in the EI formulation to zero. The EI performance specifications then converge to the ZVD specifications and the solutions are the same. This concept is demonstrated in Figure 1.15. As the acceptable limit on residual vibration is lowered, the sensitivity curve for the EI shaper approaches the sensitivity curve for the ZVD shaper.

The idea that the performance specifications should have some flexibility is used throughout this thesis. As we will see, problem statements that are slight deviations from well established problem statements frequently lead to much better overall solutions by some expanded performance criteria.

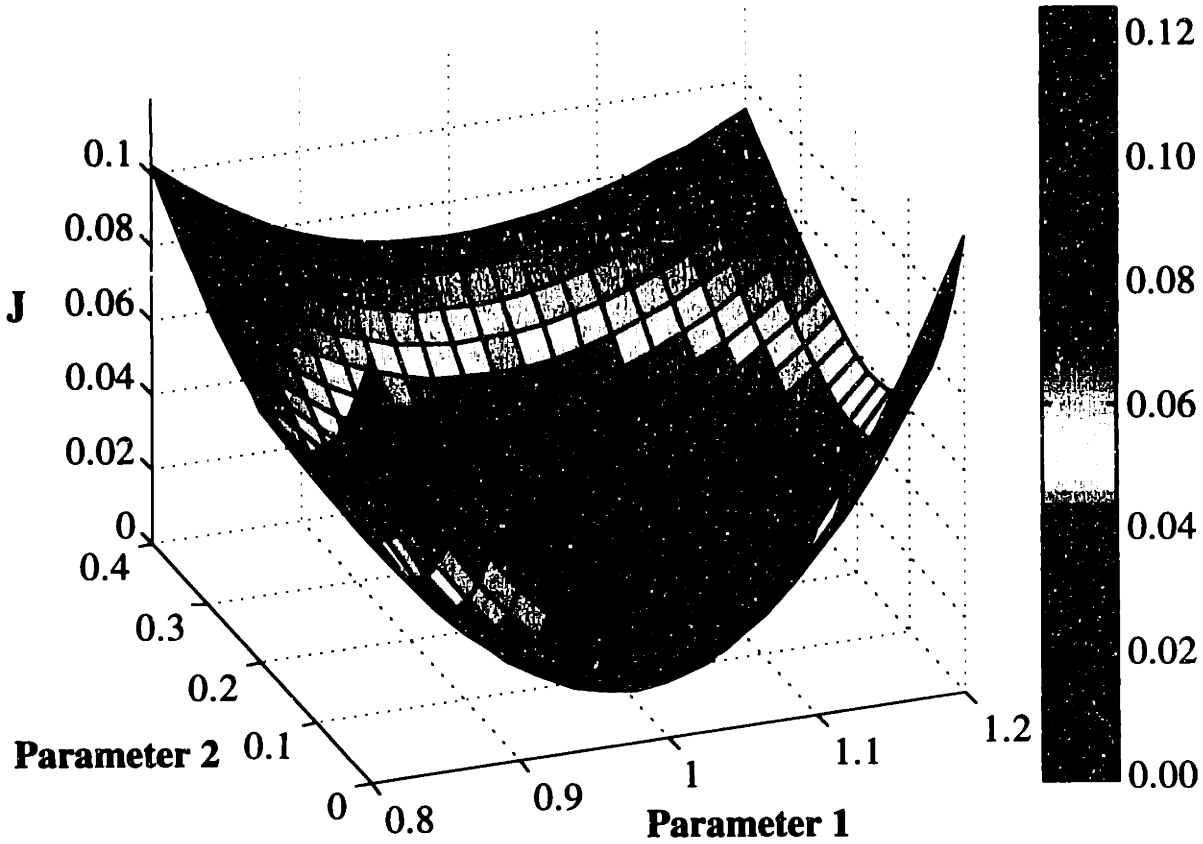

Figure 1.14: Typical Objective Surface Near the Global Minimum.

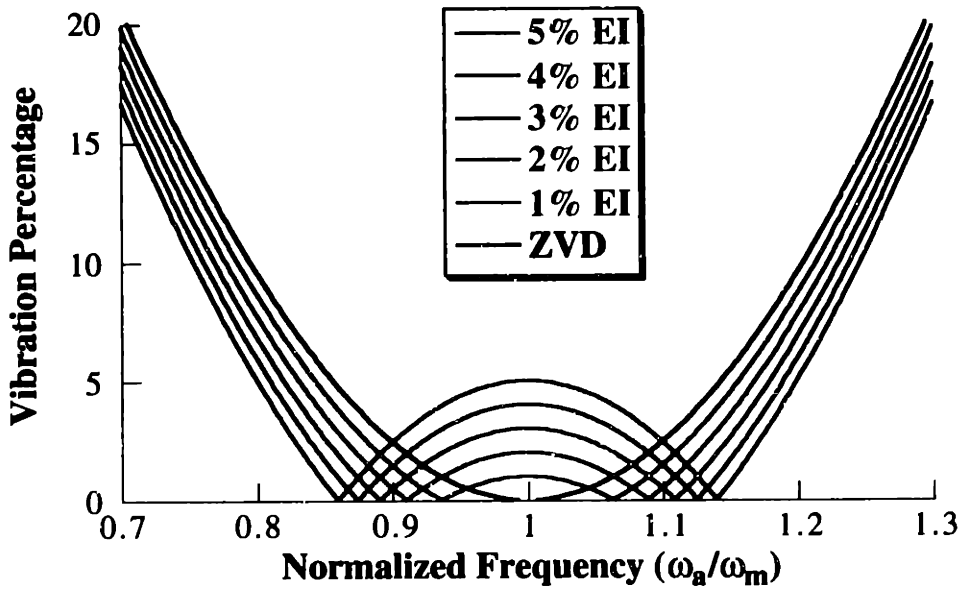

Figure 1.15: EI Sensitivity Curve as a Function of the Vibration Limit.

1.5 Problem Statement and Primary Thesis Contributions

In most cases, the reference command to a flexible system is not uniquely determined by the desired motion. This nonuniqueness arises because desired motions are often specified in very general terms such as, "a rapid motion from point A to point B." Converting the specification of "rapid motion" into a reference command is an underdetermined problem. Therefore, there are numerous (and possibly infinite) reference commands that can produce a given desired motion.

Even when the desired motion is known fairly explicitly, such as, "a constant velocity circular trajectory", the system flexibility makes it impossible to produce the desired motion exactly. The problem then becomes that of performing the "best" or, in most cases, a "satisfactory" approximation to the desired motion. The criteria for judging performance then becomes a variable and again the mapping from desired motion to reference command becomes nonunique.

This thesis makes several contributions to the field of command generation for flexible systems. That is, it provides methods for sorting through the range of possible reference commands to select one that meets some desired set of performance specifications. In addition to providing design methods, certain types of performance specifications will be presented and shown to be advantageous. The primary contributions are briefly described here.

Because shaped commands are based on a system model that will be imperfect, there is a need to generate commands that are robust to modeling errors. Chapter 3 presents methods that produce input shapers that have better robustness properties than previously reported input shapers. Furthermore, algorithms are presented that allow an input shaper to have any desired level of robustness to both frequency and damping errors. These same concepts are used in Chapter 4, where multi-switch bang-bang commands are explored. New forms of multi-switch bang-bang commands are developed and shown to have a higher robustness-to-move-duration ratio than previously reported robust time-optimal commands.

In certain types of systems, such as spacecraft, there is a need to limit the use of actuator fuel. This thesis proposes an alternative to time-optimal commands that uses considerably less fuel, while being very nearly time-optimal. The method is then expanded to allow the use of any desired amount of actuator fuel. An analysis of the fuel usage and move duration tradeoff reveals the existence of very favorable operating points.

The significant amount of literature on command generation for flexible systems has concentrated on eliminating *residual* vibration. In many types of systems, the *transient* deflection is also of vital importance. This thesis presents a systematic method for generating commands that limit transient deflection to a desired level, while still satisfying constraints on residual vibration, robustness to modeling errors, actuator limits, and fuel usage.

2 TOOLS FOR GENERATING AND ANALYZING SHAPED COMMANDS

2.1 Introduction to Generation and Analysis of Shaped Commands

In order to design a command generator, such as the input shaping process described in Chapter 1, the specific mathematical operations of the command generator must be determined. These values are determined by solving a set of constraint equations that attempt to represent a set of performance specifications. When command generators are designed for flexible systems, they are usually required to meet constraints on one or more of the following performance measures: 1) Residual vibration amplitude, 2) Rise time, 3) Settling time, 4) Robustness to modeling errors, 5) Excitation of unmodeled modes, 6) Peak actuator effort ,7) Transient deflection amplitude (internal forces), 8) Fuel usage, 9) Ease of implementation, and 10) Compatibility with a human operator. The above list is incomplete and can be expanded to include any number of additional performance requirements such as actuator cycling, required expertise of designer, etc. Note that disturbance rejection is not an appropriate performance measure for shaped command signals. Disturbance rejection is a function of the closed-loop controller.

After a designer has chosen performance specifications, shaped command signals satisfying those specifications must be generated. Furthermore, it is often desirable to evaluate the command performance relative to perfo.mance measures not used in the design process. For example, commands generated to suppress residual vibration might be evaluated for their robustness even though robustness was not a design specification. Several tools have been developed to accomplish command generation and evaluation. This chapter discusses such tools and gives examples of their use.

2.2 Impulse Response

If the impulse response, or the step response, of a linear system is known, then the response to a shaped command signal can be obtained by treating the command as a superposition of these elementary inputs. For example, a pulse input can be treated as a superposition of two step inputs, one of which is negatively valued and delayed in time. This is demonstrated in Figure 2.1. The response to the pulse is the superposition of the responses to the two individual step inputs.

A pulse input can also be considered a step input convolved with a positive and a negative impulse delayed in time. This case is shown in Figure 2.2. For example, assume that an input command is a 2 second pulse function. The corresponding impulse sequence is then given by:

$$\begin{bmatrix} A_i \\ t_i \end{bmatrix} = \begin{bmatrix} 1 & -1 \\ 0 & 2 \end{bmatrix} \tag{2.1}$$

The decomposition demonstrated in Figure 2.2 is not restricted to step functions convolved with impulse sequences. For example, a trapezoidal velocity profile can be considered to be a ramp input convolved with a sequence of impulses as shown in Figure 2.3. Note that if a finite-length command is to be decomposed into a semi-infinite length function (step, ramp, etc.) convolved with a sequence of impulses, then the impulse amplitudes must sum to zero. If, on the other hand, a command is formed by convolving a sequence of impulses with a finite length command, then the impulse amplitudes should sum to one so that the shaped command reaches the same final setpoint as the unshaped command.

Decomposing a command into some function convolved with an impulse sequence is of particular value when the residual vibration is of interest. A nondimensional measure of the residual vibration can be obtained by forming an expression for the amplitude of residual vibration caused by the impulse sequence and then dividing by the amplitude of residual vibration from a single unity-magnitude impulse. If the system is a second-order harmonic oscillator with natural frequency ω and damping ratio ζ, then this percentage residual vibration is [98]:

$$V = e^{-\zeta\omega t_n}\sqrt{[C(\omega)]^2 + [S(\omega)]^2} \tag{2.2}$$

where, $C(\omega) = \sum_{i=1}^{n} A_i e^{\zeta\omega t_i} \cos(\omega\sqrt{1-\zeta^2}\, t_i)$, $\quad S(\omega) = \sum_{i=1}^{n} A_i e^{\zeta\omega t_i} \sin(\omega\sqrt{1-\zeta^2}\, t_i)$ (2.2a, 2.2b)

A_i and t_i are the amplitudes and time locations of the impulses and n is the number of impulses.

If we consider the function used in the convolution as an unshaped command and the result of the convolution as a shaped command, then (2.2) provides a measure of how well the input shaping process will work, regardless of the unshaped command. That is, the value given by (2.2) is the amplitude of residual vibration caused by the shaped command divided by the amplitude of residual caused by the unshaped command. The increase in rise time associated with

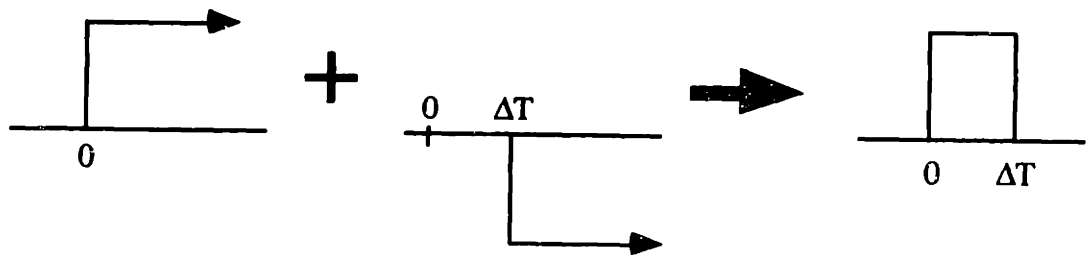

Figure 2.1: Forming a Pulse by Superimposing Two Step Functions.

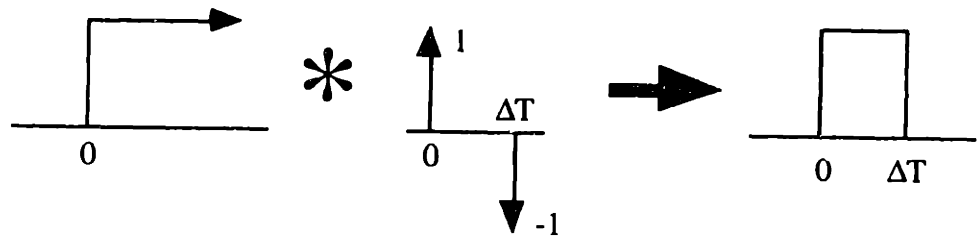

Figure 2.2: Forming a Pulse by Convolving a Step with Two Impulses.

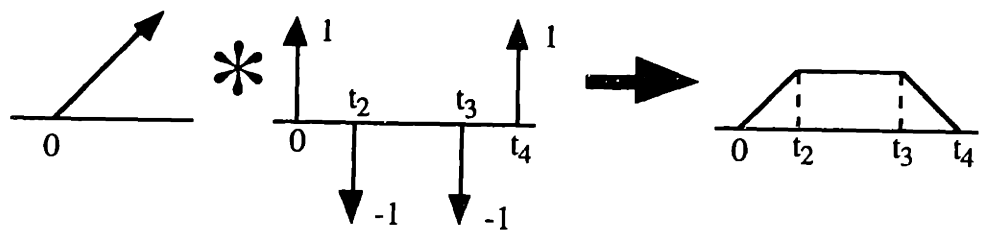

Figure 2.3: Forming a Trapezoid by Convolving a Ramp with Impulses.

the shaping process is simply the time duration of the input shaper. Furthermore, the settling time is also equal to the duration of the shaper, assuming that the shaping performs as expected.

2.2.1 Input Shaper Design Using the Impulse Response

Equation (2.2) provides an easy method for evaluating the residual vibration from a command profile. It also provides a means for designing input shapers. To demonstrate this, an example from the literature is repeated here [98, 140]. The goal of this exercise is to generate an input shaper that yields zero residual vibration. This requires that (2.2) be set equal to zero at the frequency and damping of the system under consideration. In this case, both the cosine summation (2.2a) and the sine summation (2.2b) must be zero independently:

$$0 = \sum_{i=1}^{n} A_i e^{\zeta \omega t_i} \cos(\omega \sqrt{1-\zeta^2}\, t_i) \tag{2.3}$$

$$0 = \sum_{i=1}^{n} A_i e^{\zeta \omega t_i} \sin(\omega \sqrt{1-\zeta^2}\, t_i) \tag{2.4}$$

To minimize the time delay, the first impulse must be placed at time zero:

$$t_1 = 0 \tag{2.5}$$

Furthermore, the impulse amplitudes must sum to one:

$$\sum_{i=1}^{n} A_i = 1 \tag{2.6}$$

The solution to (2.3)-(2.6) that minimizes the shaper duration is undefined because the impulse amplitudes go to positive and negative infinity as the shaper duration decreases. To avoid this difficulty, the impulse amplitudes can be restricted to positive values. The ramifications of this restriction will be addressed in Chapter 3.

Given that there are four equations to be satisfied, an input shaper that contains two impulses is sought because two impulses give four unknowns (two amplitudes and two time locations). In this case i = 2 and substituting (2.5) into (2.3), (2.4), and (2.6) yields:

$$0 = A_1 + A_2 e^{\zeta\omega t_2} \cos(\omega\sqrt{1-\zeta^2}\, t_2) \tag{2.7}$$

$$0 = A_2 e^{\zeta\omega t_2} \sin(\omega\sqrt{1-\zeta^2}\, t_2) \tag{2.8}$$

$$1 = A_1 + A_2 \tag{2.9}$$

To satisfy (2.8) and keep the impulse sequence as short as possible, the argument of the sine term must equal π. From this realization, we get:

$$t_2 = \frac{\pi}{\omega\sqrt{1-\zeta^2}} \tag{2.10}$$

That is, the second impulse must occur at one half period of the damped natural frequency. Substituting (2.10) into (2.7) and utilizing (2.9), we get:

$$0 = A_1 + (1 - A_1)\exp\left(\frac{\zeta\omega}{\sqrt{1-\zeta^2}}\right) \tag{2.11}$$

Solving for A_1 we get:

$$A_1 = \frac{1}{1 - \exp\left(\frac{-\zeta\omega}{\sqrt{1-\zeta^2}}\right)} \tag{2.12}$$

A_2 is then obtained from (2.12) and (2.9) as:

$$A_2 = 1 - \frac{1}{1 - \exp\left(\frac{-\zeta\omega}{\sqrt{1-\zeta^2}}\right)} \tag{2.13}$$

The two-impulse sequence given by (2.5), (2.10), (2.12), and (2.13) is called a zero vibration (ZV) shaper because it satisfies the constraint that the residual vibration must be zero when the model is perfect. The above derivation is the simplest example of how the impulse response can be

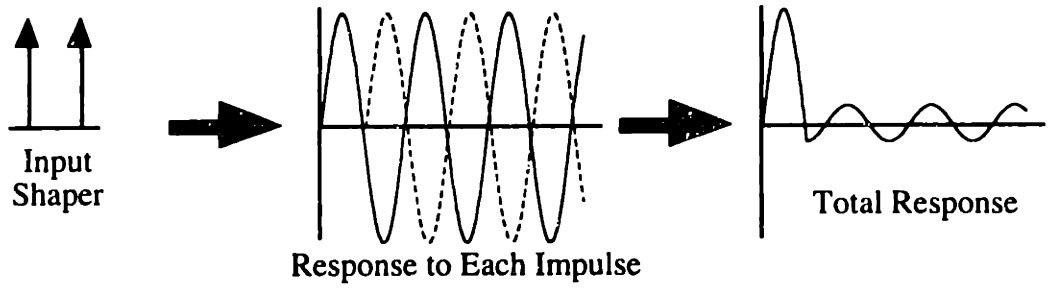

Figure 2.4: Response to ZV Shaper with a 5% Frequency Error.

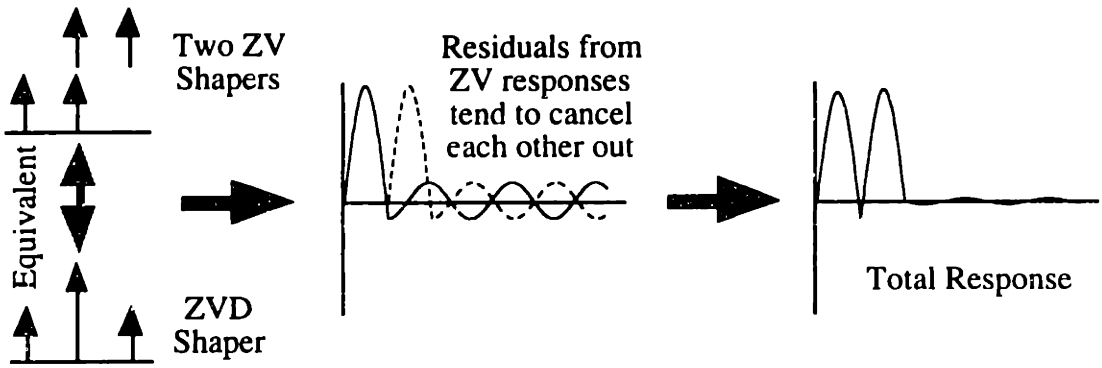

Figure 2.5: Response to a ZVD Shaper with a 5% Frequency Error.

used to design an input shaper. Other types of shapers are derived by combining (2.2) with additional constraint equations, such as robustness constraints. In many cases, these input shapers cannot be obtained in closed form, rather a numerical optimization is performed to obtain the impulse amplitudes and time locations. Several types of input shapers are described in Chapter 3.

2.2.2 Robustness Using the Impulse Response

The robustness of certain types of input shapers can be illustrated using the impulse response. To demonstrate this point, we use an example similar to one appearing in Singer's thesis [98]. Figure 2.4 shows the response of a harmonic oscillator to a ZV shaper when the there is a 5% error in model of the frequency. The vibration is canceled to a first order, but there is a considerable amount of residual vibration because the second impulse is not at the correct time location.

Figure 2.5 shows a similar analysis for a ZVD shaper. If we consider the ZVD shaper to be composed of two ZV shapers, one shifted in time by one half cycle of the vibration, then we see that the shaper will be robust because the vibration resulting from the second ZV shaper tends to cancel the vibration from the first ZV shaper. That is, each ZV shaper cancels the vibration to a first order and then the two ZV shapers work together to cancel the vibration to a second order level. Although, the robustness of the ZVD shaper can be demonstrated in this manner, the robustness of other types of shapers is not as easily seen using the impulse response.

2.3 Sensitivity Curves

The information shown in Figures 2.4 and 2.5 tells us what the residual vibration will be when there is a 5% error in the estimation of the frequency. It also indicates that the ZVD shaper can tolerate modeling errors better than the ZV shaper; however, the robustness of a shaped command is best demonstrated with sensitivity curves. These curves display the amount of residual vibration as a function of the modeling parameters. The modeling parameters are usually the modal frequencies and/or damping ratios. If the information is shown as just a function of the system frequency, then the sensitivity curve is equivalent to the frequency Bode plot. If the sensitivity to two parameters is shown simultaneously, the resulting figure is a sensitivity surface. Sensitivity surfaces will be used in Chapter 3.

Sensitivity curves allow for quantitative measures of robustness. For example, we can measure the width of a sensitivity curve as some acceptable level of residual vibration, thereby obtaining a numerical measure of the robustness. Recall that sensitivity curves were used to describe the robustness properties of the three types of shapers discussed in Chapter 1. The shape of a sensitivity curve depends on the constraints used to design its corresponding input shaper. For example, Figure 2.6 shows the sensitivity curve for a shaper designed to suppress vibration over the frequency range of 0.6 Hz < f < 1.4 Hz.

Sensitivity curves can also be used to predict the effect of unmodeled modes. If the sensitivity curve is plotted over a wide range of frequencies, then the curve will reveal the level of vibration to be expected if an unmodeled mode exists. For example, Figure 2.7 shows the sensitivity curves for two different input shapers. In both cases, the residual vibration is zero at the modeling frequency and there is some robustness to errors in the estimation of this frequency. However, at high frequencies, the two shapers have vastly different properties. Shaper 1 never yields more than 100% residual vibration. That is, any unmodeled modes will not be excited more than without shaping. Shaper 2, on the other hand, can cause vibration in unmodeled high modes that exceeds the level when input shaping is not used. For example, if an unmodeled mode exists at 7 times the modeling frequency (ω_a/ω_m=7), then it will be excited to five times the level of excitation that occurs without input shaping. In practice, unmodeled high modes are excited less than that predicted by the sensitivity curve [86].

While being an excellent tool for displaying robustness and excitation of unmodeled modes, sensitivity curves reveal little about the other performance criteria. For example, the shaper corresponding to Figure 2.6 is 1.7 periods in duration. This may be unacceptably long, but the sensitivity curve does not reveal this penalty. Furthermore, Shaper 1 in Figure 2.7 was shown to have benefits in terms of high mode excitation, but it is approximately 30% longer than Shaper 2.

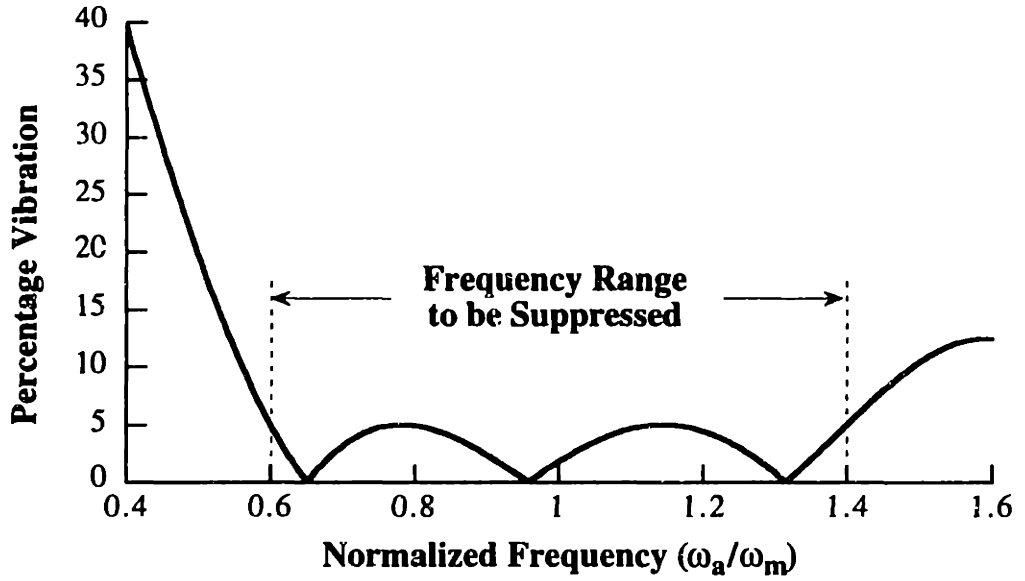

Figure 2.6: Sensitivity Curve of an Input Shaper Designed to Suppress a Range of Frequencies.

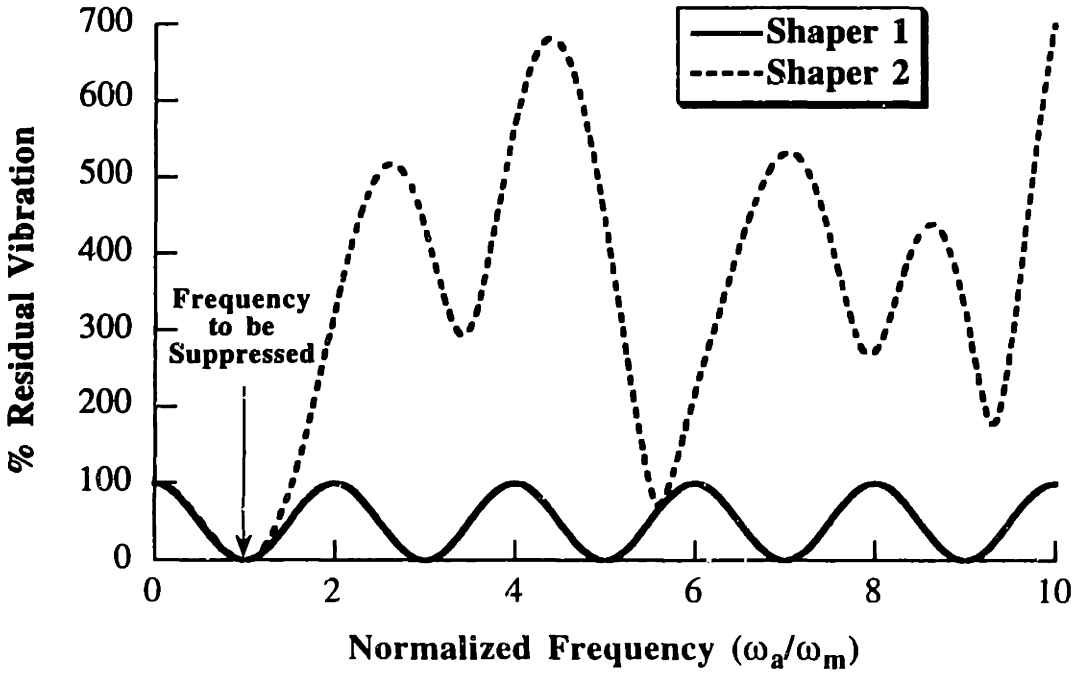

Figure 2.7: Sensitivity Curve Showing Potential Excitation of High Modes.

2.4 Pole-Zero Analysis

Another useful method for generating and explaining the effectiveness of shaped command signals is to use s-plane or z-plane analysis to determine the location of the zeros and/or poles of the command shaping process. If a shaped command contains zeros near the poles of the system being controlled, then the vibration from those poles is attenuated by the zeros of the command. Furthermore, poles introduced by the command can be used to cancel the unwanted dynamics of zeros.[2] The extreme of this idea is to generate a command which is the inverse of the plant dynamics. The combined system would then, in theory, have a unity transfer function. That is, the system would respond perfectly to a commanded trajectory. Several well known problems exist with plant inversion techniques. Examples of such problems include poor robustness and the generation of unrealizable commands.

The process of input shaping does not attempt to cancel all system dynamics, just the flexible poles. Figure 2.8 shows the zero locations for some typical input shapers designed for undamped systems. Figure 2.8a shows that a ZV shaper places a single zero over each of the flexible poles. If the poles deviate from their modeled locations, the attenuating effect of the zeros decreases. ZVD shapers places two zeros over each pole (Figure 2.8b). When a pole deviates from its modeled location, the two zeros have a greater attenuating effect than the single zero provided by a ZV shaper. EI shapers do not place zeros directly at the pole locations, rather at nearby locations (Figure 2.8c). The plots shown in Figure 2.8 are only for regions of the s-plane near the plant poles. Each of the shapers have an infinite number of zeros. These additional zeros lie near odd multiples of the modeling frequency along the $j\omega$ axis.

Command shaping methods which introduce poles as well as zeros can be evaluated in this manner. For example, the IIR filtering method proposed in [34] can interpreted as placing zeros at the flexible poles of the physical system, while placing poles at locations which are far away from the $j\omega$ axis. The poles are introduced to control the level of actuator effort.

2.4.1 Investigating Robustness Using Pole-Zero Analysis

Qualitative information concerning the robustness of a shaping scheme is immediately available from the pole-zero plot. The pole and zero locations from the shaping process are fixed, but modeling errors make the locations of the plant poles and zeros uncertain. The pole-zero plot gives some indication of the area in the s-plane in which the plant dynamics can exist and still be attenuated by the shaping scheme.

---

[2] Canceling non minimum phase zeros with poles is a practical impossibility because any finite modeling error will cause instability.

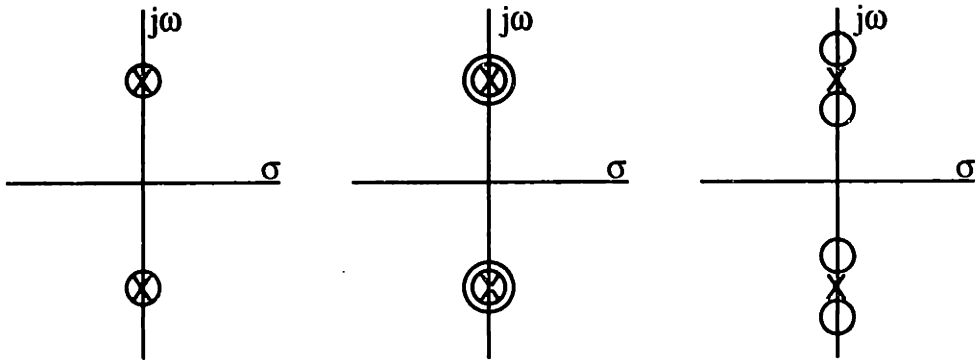

a) ZV b) ZVD c) EI

Figure 2.8: Zero Locations of Typical Input Shapers.

By reexamining Figure 2.8 we can see why the EI shaper gives greater robustness than the ZVD shaper. The two zeros from the EI shaper are at distinct locations; therefore, the flexible plant poles can be exactly canceled at two distinct values, rather than just the single value provided by the ZVD shaper. Additionally, the zero separation extends the attenuating effect of the zeros to a larger area than that provided by the two repeated zeros of the ZVD shaper.

One can imagine a robust shaping scheme that clusters several zeros in some region of the s-plane where the flexible plant poles are expected to exist. The drawback with additional zeros is that the rise time is increased. This effect is not directly evident from the pole-zero representation.

2.4.2 Shaper Design Using Pole-Zero Analysis

Pole-zero representation can be used to design input shapers [13, 46, 59, 94, 111, 153]. The z-plane version of this approach is especially useful when there is a course digital time step that must be taken into account. These methods formulate the problem by expressing the shaper transfer function as an algebraic expression involving the desired zero locations. The shaper transfer function can be expressed as:

$$H(z)=\frac{C}{z^{2n}}\left(z-p_1\right)\left(z-p_1^*\right)\ \cdots\ \left(z-p_n\right)\left(z-p_n^*\right) \tag{2.14}$$

where p_i and p_i^* represent a pair of complex poles and n is the number of flexible modes being targeted for elimination. The transfer function must have as many poles at z = 0 as zeros in the numerator so that the shaped command will be causal. After the pole locations are entered into (2.14), the transfer function is manipulated so that is takes the form of:

$$H(z)=C\frac{z^{2n}+a_1z^{2n-1}+\ \cdots\ +a_{2n}}{z^{2n}} \tag{2.15}$$

A transfer function described by (2.15) can easily be converted back into the time domain using the inverse Laplace transform. The result of the transformation is the desired impulse sequence.

One drawback of this approach is that there is no guarantee that the resulting impulse sequence will be physically realizable. That is, it can contain large positive and negative valued impulses that, when used to shape the command, produce a command signal that saturates the actuators. This difficulty can be avoided by using an artificially coarse sampling rate. This approach can be thought of as inserting zero-amplitude impulses at the true digital time step between finite-amplitude impulses at some multiple of the sampling period. Methods for selecting this surrogate sampling period are usually based on the constraint that all the impulses must have positive values. To demonstrate such a method, an example using the six-step procedure proposed by Tuttle [153] is reproduced here.

Consider a system with modes at 1 Hz and 4 Hz and damping ratios at each mode of 0.1.

Step 1: Identify the unwanted system poles and cover them with zeros in the z-plane. The location of the two pairs of complex poles in the s-plane can be written as:

$$\begin{aligned} s_1, s_1^* &= -\zeta_1\omega_1 \pm j\omega_1\sqrt{1-\zeta_1^2} \\ s_2, s_2^* &= -\zeta_2\omega_2 \pm j\omega_2\sqrt{1-\zeta_2^2} \end{aligned} \tag{2.16}$$

Using the relationship:

$$z = e^{sT} \tag{2.17}$$

and the given values for the natural frequencies and damping ratios, the z-plane poles can be calculated as:

$$\begin{aligned} p_1, p_1^* &= \exp(-0.2\pi T \pm j1.99\pi T) \\ p_2, p_2^* &= \exp(-0.8\pi T \pm j7.96\pi T) \end{aligned} \tag{2.18}$$

To eliminate residual vibration, a shaper zero must be placed at the location of each of these poles.

Step 2: Add additional zeros for robustness. For systems with uncertain modes, additional zeros can be placed at or near the nominal pole locations to improve the shaper robustness. For simplicity, it will be assumed that a single zero at each pole is adequate for this example.

Step 3: Construct the shaper transfer function. As shown by (2.15), the shaper transfer function contains the zeros from steps 1 and 2 as well as four poles at the z-plane origin:

$$H(z) = \frac{C}{z^4}\left(z-p_1\right)\left(z-p_1^*\right)\left(z-p_2\right)\left(z-p_2^*\right) \tag{2.19}$$

where C is a constant.

Step 4: Calculate the resulting impulse sequence. By substituting the expressions from (2.18) into (2.19) and multiplying the numerator terms together, the shaper transfer function takes the form:

$$H(z) = C\frac{z^4 + a_1z^3 + a_2z^2 + a_3z + a_4}{z^4} \tag{2.20}$$

where, with help from the trigonometric identity:

$$2\cos\theta = e^{j\theta} + e^{-j\theta} \tag{2.21}$$

a_1 through a_4 can be found readily to be:

$$\begin{aligned} a_1 &= -2(R_1\cos\theta_1 + R_2\cos\theta_2), \\ a_2 &= R_1^2 + 4R_1R_2\cos\theta_1\cos\theta_2 + R_2^2, \\ a_3 &= -2\left(R_1R_2^2\cos\theta_1 + R_1^2R_2\cos\theta_2\right), \\ a_4 &= R_1^2R_2^2 \end{aligned} \tag{2.22}$$

where,

$$\begin{aligned} R_1 &= e^{-0.2\pi T}, \quad R_2 = e^{-0.8\pi T}, \\ \theta_1 &= 1.99\pi T, \quad \theta_2 = 7.96\pi T \end{aligned} \tag{2.23}$$

The transfer function in (2.20) can be transformed from the z-plane to the s-plane by mapping the poles and zeros according to (2.17). Performing this mapping and taking the inverse Laplace transform yields:

$$h(t) = C[\delta(t) + a_1\delta(t-T) + a_2\delta(t-2T) + a_3\delta(t-3T) + a_4\delta(t-4T)] \tag{2.24}$$

Equation 2.24 describes the input shaper as a function of the sampling period, T. If T is small compared to the vibration periods being targeted for elimination, then the impulse amplitudes can take on large positive and negative values. As a result, the shaped command can take on unrealistically large values. This can lead to actuator saturation and degradation of the shaping process. This necessitates the use of an additional constraint that limits the impulse amplitudes. The next step is one possible method for implementing such a constraint.

Step 5: Plot the impulse amplitudes as a function of T and select a sequence that meets actuator constraints. In Figure 2.9, each of the impulse amplitudes, as calculated from (2.22) is plotted as a function of T. Assuming that the unshaped command utilizes the complete dynamic range of the actuator, a shaper with all positive impulses will ensure that the shaped command does not saturate the actuator. From the plot in Figure 2.9, it can be seen that smallest value of T at which all impulse amplitudes are non-negative occurs at T=0.147 seconds. Note that the sampling period of the system does not have to be set equal to 0.147 sec. Rather, the impulses that compose the shaper will lie at multiples of 0.147 sec.

Step 6: Normalize amplitudes and implement. From the value of T found in step 5, the impulse amplitudes can be fully determined. Typically, in order that the shaper has unity gain, the constant, C, is used to scale the amplitudes to sum to unity. Completing this final task yields the desired input shaper:

$$h(t) = 0.516\delta(t) + 0.042\delta(t-0.147) + 0.237\delta(t-0.441) + 0.205\delta(t-0.588) \tag{2.25}$$

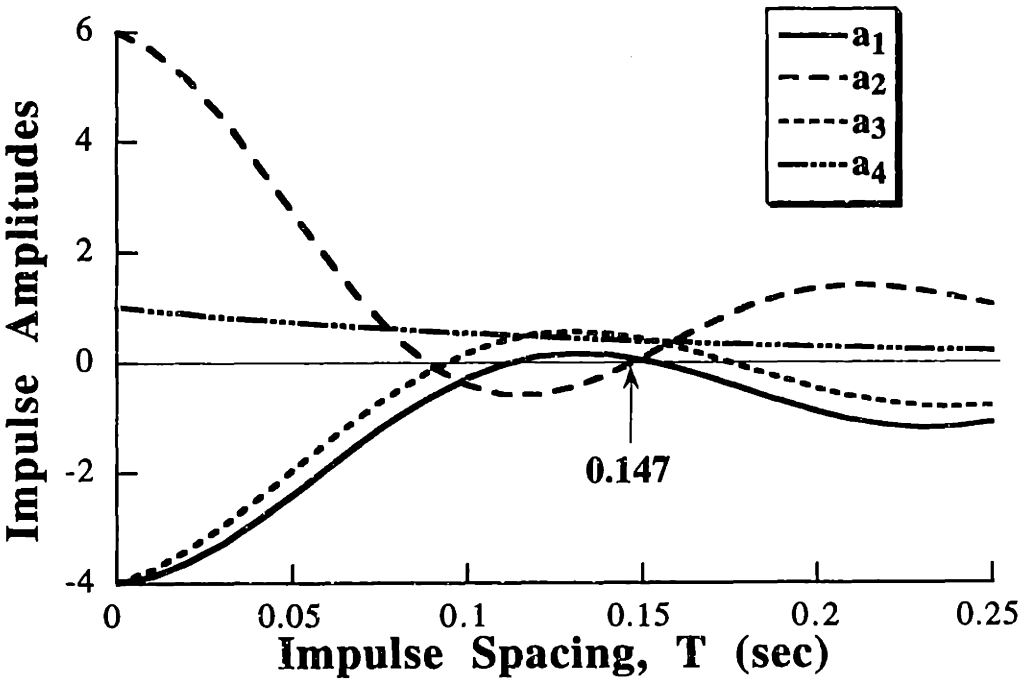

Figure 2.9: Impulse Amplitudes vs. Sampling Period (Impulse Spacing).

2.5 Optimal Control

An enormous amount of work has been performed in the area of optimal control. The techniques in this field can be used to generate both open and closed-loop control systems. Here we are concerned with the subset of techniques which generate command profiles rather than feedback control systems. Due to its complexity for flexible systems, only a general overview of this approach will be given here. Specific details can be found in a number of general purpose references [4, 21, 85] and papers devoted to optimal control of flexible systems [23, 52, 76, 80, 104, 111, 117, 132, 146, 165, 166]

The optimal control approach involves minimizing or maximizing a cost function subject to a set of constraints. The procedure outlines conditions, such as zero partial derivatives of the cost function, which lead to "stationary" values of the cost function. These necessary conditions can ensure that a candidate solution is a local minimum. Additional "sufficient" conditions can then be utilized to verify that a perspective solution is the global optimal.

Although the optimal control approach is systematic and produces necessary and sufficient conditions for optimal commands, the method does not contain a method for actually generating the commands. A number of methods have been proposed for generating commands based on this approach, but only recently have practical methods been developed for generating commands for flexible systems. These methods can be cumbersome to work with and are unproven for some types of optimal command profiles for flexible systems. More detail on this approach will be given in Chapter 4.

The optimal control formulation does not provide a means for evaluating the finished product. That is, once a command profile is obtained and verified, there is no direct procedure for assessing its overall usefulness. The other tools discussed in this chapter must be used to analyze the effectiveness of the resulting command profile.

Note that optimal open-loop command generation is compatible with closed loop control. The command profile can be used as a reference signal for the closed-loop controller to track. Or, if the command profile is known for every point in the state space, then the closed-loop control action is based on the known command. For this approach to be feasible, the command must be known as an analytic function of the state space, or must be easily calculated from the state variables. In the vast majority of cases, the command cannot be obtained in an analytic form. As mentioned above, numerically calculating the command based on the state is difficult and cannot be done in real time. In these cases, the commands could be pre-generated for a wide array of possibie states and then stored for retrieval on demand. Obviously, this becomes intractable for a large number of possible states or commands that are complex functions of the state.

2.6 Vector Diagrams

A vector diagram is a graphical representation of an impulse sequence in polar coordinates (r-θ space). A vector diagram is created by setting r equal to the amplitude of an impulse and by setting $\theta = \omega t$, where ω (rad/sec) is a chosen frequency and t is the time location of the impulse. Figure 2.10 shows a typical impulse sequence and its corresponding vector diagram. The angle of the first vector is zero because the first impulse occurs at time zero. The angle of the second vector is $\theta_2 = \omega T_2$ because the second impulse time location is T_2.

Vector diagrams become useful tools for representing input shapers when ω is set equal to the modeling frequency and the first impulse is placed at time zero. When a vector diagram is created in this manner, the amplitude of the vector resultant, A_R, is proportional to the amplitude of residual vibration of a system driven by the shaped command [6]. The angle of the resultant is the phase of the vibration relative to the system response to an impulse at time zero. This result enables us to determine residual vibration by summing the vectors on the vector diagram. Figure 2.11 compares a vector diagram representation of vibration with a time domain representation of vibration for a second-order undamped system given the impulse sequence of Figure 2.10. On a vector diagram, vibration appears as a vector, whereas, in the time domain, vibration appears as a sinusoid. Note that the vector resultant has a larger magnitude than either of the individual vectors. Correspondingly, the residual vibration from the sequence of impulses is larger than the vibration from either of the two impulses.

2.6.1 Effects of Damping on the Vector Diagram

When the system has viscous damping, the vector diagram representation of vibration must be modified in two ways. First, we must use the damped natural frequency for plotting the vector diagram. This corresponds to using:

$$\theta = \sqrt{1-\zeta^2}\,\omega t \qquad (2.14)$$

where t is the time location of the impulse. Second, the amplitudes of the vectors must be scaled to account for damping. As time progresses the amplitude of response decays as $e^{-\zeta\omega t}$. Therefore, when the resultant is calculated the amplitude of each vector must be scaled by a factor of $e^{-\zeta\omega t}$ before the vector sum is computed. When these two steps are performed, the resultant is again proportional to the residual vibration.

2.6.2 Designing Input Shapers Using the Vector Diagram

We can use the vector diagram in a straightforward manner to generate input shapers that yield zero residual vibration. To do this, we place n arbitrary vectors on a vector diagram and then

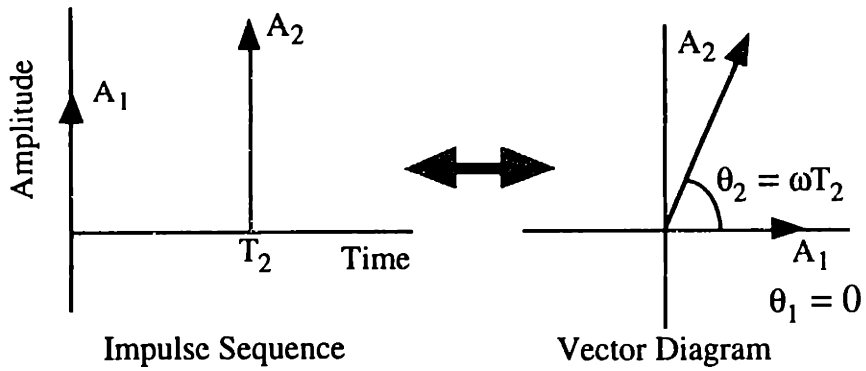

Figure 2.10: An Impulse Sequence and its Corresponding Vector Diagram.

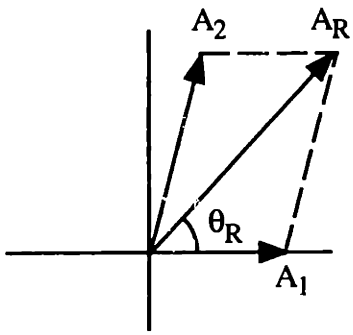

A_R = The amplitude of the vibration after impulses A_1 and A_2 have been applied to the system.

θ_R = The phase of the residual vibration.

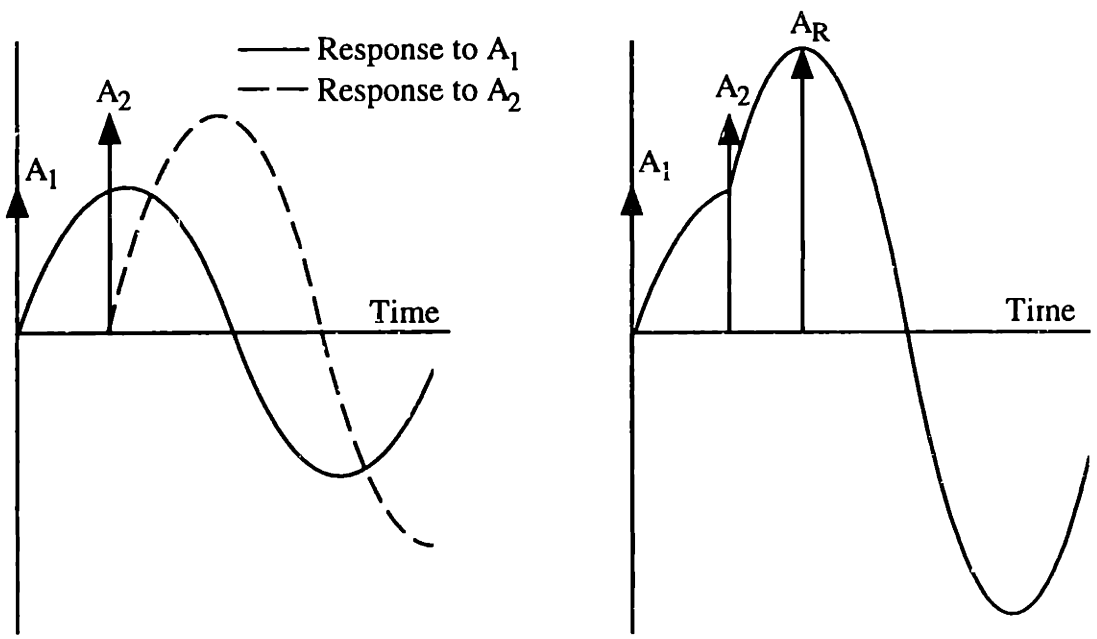

Figure 2.11: Vector Diagram and Time Domain Representations of Vibration.

cancel the resultant of the first n vectors with a single vector. When the n+1 vectors are converted into an input shaper, and the sequence is convolved with a desired system input, the resulting shaped input will cause no residual vibration. Additionally, if the sum of impulse amplitudes is normalized to one, the system will stop at the commanded setpoint.

The magnitude and angle of the canceling vector, A_{n+1}, are given by [122]:[3]

$$|A_{n+1}| = \sqrt{|R_x|^2 + |R_y|^2} \tag{2.15}$$

$$\theta_{n+1} = \pi + \tan^{-1}\left(\frac{R_y}{R_x}\right) \tag{2.16}$$

where R_x and R_y are the horizontal and vertical components of the resultant. These components are given by:

$$R_x = \sum_{i=1}^{n} A_i \cos\theta_i \tag{2.17}$$

$$R_y = \sum_{i=1}^{n} A_i \sin\theta_i \tag{2.18}$$

When an input shaper is designed in this way, the resulting impulse amplitudes must be scaled so that they sum to one. This ensures that the shaper transfer function will have a unity gain. Stated differently, this ensures that the shaped command will have the same final setpoint as the unshaped command.

Note that this procedure does not guarantee the shortest shaper that will yield zero residual vibration. However, with some additional constraints, the vector diagram can be very useful in designing robust input shapers [113, 120-122, 134, 138]. This will be demonstrated in Chapter 3.

2.6.3 Effects of Modeling Errors on the Vector Diagram

Sensitivity curves can be obtained directly from a vector diagram if we analyze how a modeling error changes the diagram. When the natural frequency of a system differs from the assumed natural frequency, the error can be represented on a vector diagram by shifting each vector through an angle ϕ [6]. If ω_a is the actual natural frequency of the system and ω_m is the modeling frequency, then the error in frequency is $\omega_m - \omega_a$. The angle through which a vector is shifted, ϕ, is related to the frequency error by the equation:

$$\phi = (\omega_m - \omega_a)t \tag{2.19}$$

The error in modeling usually leads to a non-zero resultant. The resultant that is formed represents the vibration that is induced by the error in frequency. Therefore, a sensitivity curve can be generated by plotting the residual amplitude vs. frequency error.

2.6.3 Investigating Robustness Using the Vector Diagram

Although sensitivity curves can be obtained directly from a vector diagram and they reveal quantitative measures of robustness, they do not indicate *why* a shaper is robust. The mechanism

[3] The $\tan^{-1}$ function used in the expression for θ_{n+1} must retain the quadrant value of R_x and R_y. In other words, θ_{n+1} is just π plus the angle of the resultant from the first n vectors.

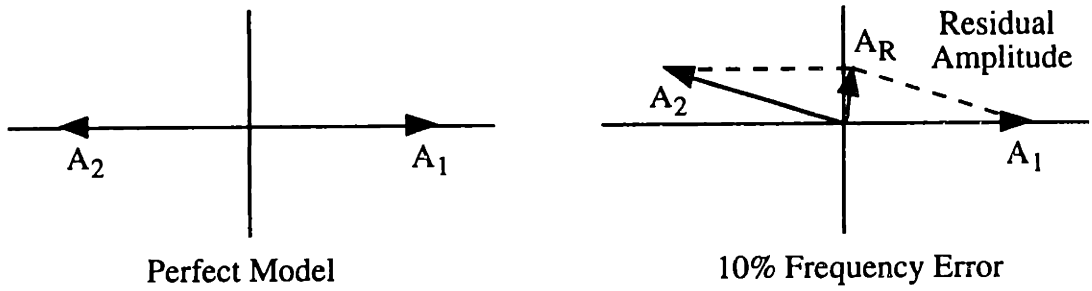

Figure 2.12: Vector Diagram Representation of a ZV Shaper.

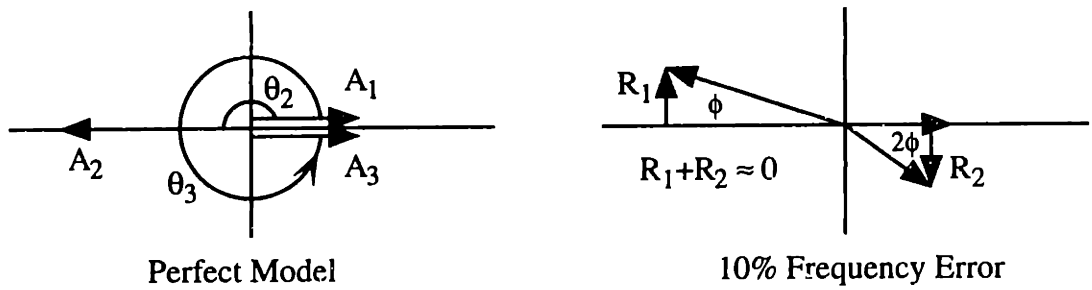

Figure 2.13: Vector Diagram Representation of a ZVD Shaper.

which produces robustness can be seen with the use of a vector diagram. To demonstrate this mechanism we follow an example from Singer's thesis [98].

Figure 2.12 shows the vector diagram representation of a ZV shaper when the model is perfect and when the frequency is 10% longer than expected. Using 2.19, we find that the second vector is rotated 18° off the negative horizontal axis. When a modeling error exists, the second vector doe not cancel the first vector. The vector sum, A_R, represents the residual vibration.

Figure 2.13 shows the ZVD shaper under identical circumstances. The modeling error causes both the second and third vectors to be in the wrong locations. The second vector is rotated ϕ (18°) off the negative horizontal axis and the third vector is rotated 2ϕ (36°) off the positive horizontal axis. The error in the second impulse causes a resultant, R_1, which is approximately ϕA_2 directed in the positive vertical direction. The error in the third vector causes a resultant, R_2, which is approximately $2\phi A_3$ directed in the negative vertical direction. Because $A_2 = 2A_3$, the resultants R_1 and R_2 approximately cancel out giving a near-zero total resultant due to the modeling error.

2.7 Phase Plane Analysis

The phase plane (velocity vs. position) can be used to both design and analyze input shapers. The effect of an impulse is an instantaneous change in velocity. If we consider an undamped second-order system and use the input shaper shown in Figures 2.10 and 2.11, then the phase plane description is shown in Figure 2.14. The first impulse gives the system an initial velocity. The system vibrates through less than one quarter of a cycle[4] and then the second impulse adds additional velocity. The distance, A_R, from the origin to the circle which describes the velocity vs. position after the second impulse is applied represents the amplitude of residual vibration. This radius is equal to the amplitude of the resultant vector shown on the vector diagram in Figure 2.11.

2.7.1 Designing Input Shapers Using the Phase Plane

From the above example, it should be clear that an impulse sequence that drives the phase plane plot to the origin after the final impulse will result in zero residual vibration. The simplest such impulse sequence is the ZV shaper. The first impulse of the ZV shaper gives the system an initial velocity. The phase plane plot then travels on a circular arc to the negative velocity axis. At this point the second impulse occurs and drives the phase plane plot to the origin.

Knowing that any impulse sequence that drives the system to the origin will result in zero residual vibration, allows us to design input shapers directly on the phase plane. For example, if we start with the shaper shown in Figure 2.14, we must add an impulse that drives the plot to the origin. This can be accomplished with an impulse of amplitude A_R, located on the negative velocity axis, as shown in Figure 2.15. After a shaper is constructed in this manner, the impulse amplitudes must be scaled so that they sum to one.

When the impulses are converted back into the time domain, the third impulse (with amplitude A_R) does not lie one half cycle (π rad) after the first impulse. The time duration between the impulses is obtained by dividing the value of the angular arc between each impulse by ω. Note that the phase plane plot travels farther than π rad by the time the third impulse is applied. This means that the third impulse occurs later in time than one half period of the vibration.

2.7.2 Investigating Robustness Using the Phase Plane

The quality of robustness can be demonstrated on the phase plane by constructing the plot assuming a modeling error [98]. Figure 2.16 shows the plot corresponding to a ZV shaper when the frequency is 10% higher than the modeling frequency. The first impulse drives the system to point 1. If the frequency was correct, the system would travel on a circular arc for 180° until the

[4] One circular revolution (360°) on the phase plane is equivalent to one cycle of vibration.

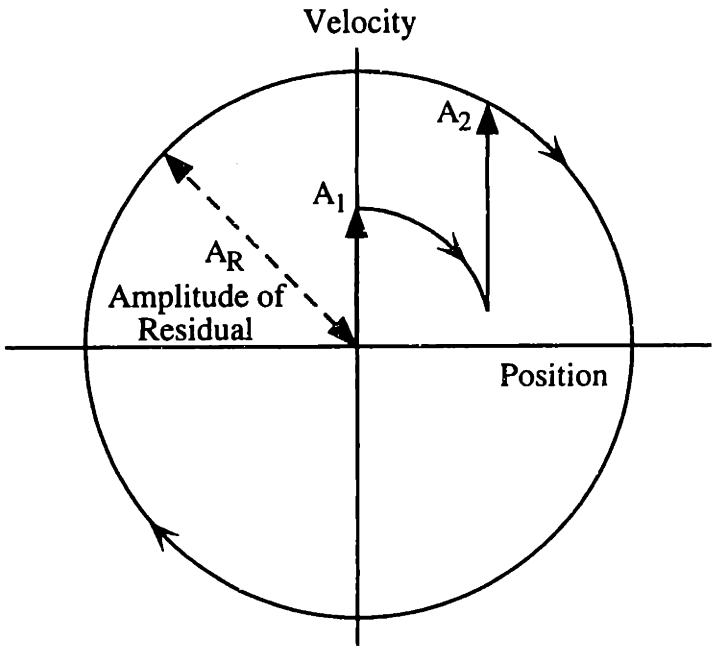

Figure 2.14: Phase Plane Representation of an Impulse Sequence.

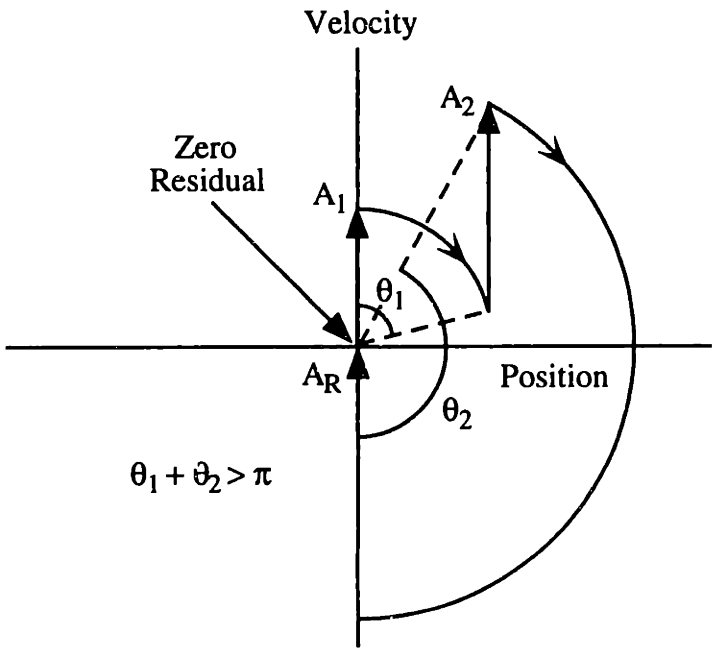

Figure 2.15: Phase Plane Representation of a Zero Vibration Impulse Sequence.

negative velocity axis was encountered and the second impulse would be applied. The modeling error causes the system to travel past the negative velocity axis by 18° to point 2 before the second impulse is applied. The second impulse then drives the system to point 3, rather than to the origin.

Figure 2.17 shows the phase plane plot for a ZVD shaper when there is a 10% modeling error. The first impulse drives the system to point 1. The system travels on a circular arc past the negative velocity axis (where the second impulse should be applied) to point 2. The second

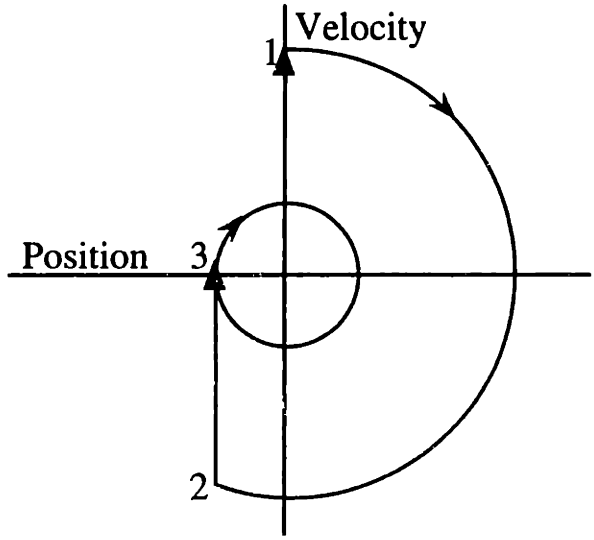

Figure 2.16: Phase Plane for ZV Shaper with a 10% Frequency Error.

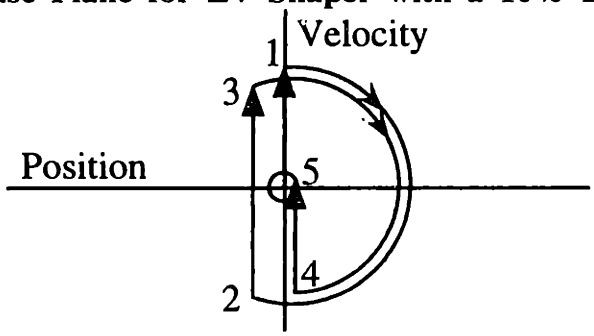

Figure 2.17: Phase Plane for ZVD Shaper with a 10% Frequency Error.

impulse drives the system to point 3. The system then travels again on a circular arc for 198° (110% of the distance it is designed to travel). This brings the system near the negative velocity axis (point 4) at which point the final impulse drives the system back close to the origin at point 5. Figures 2.16 and 2.17 are drawn on the same scale so that it is evident that the ZVD shaper yields much lower residual vibration than the ZV shaper. The ZVD shaper has robustness because the error in travel angle between the first and second impulses is counteracted by the angle error between the second and third impulses.

The robustness of the ZVD and EI shapers can be compared by constructing phase plane plots using a range of modeling errors. Figure 2.18 shows the phase plane plots when the frequency error is varied from 5% to 20% of the modeling frequency in steps of 2.5%. The yellow line corresponds to a frequency error of 5% and the color darkens as the frequency error increases to 20% which is shown in red. Note that the plots for all cases lie on the same initial circular arc (shown in red). that results from the application of the first impulse. The residual vibration using the ZVD shaper increases steadily with modeling error. On the other hand, the residual using the EI shaper actually decreases over a certain range of increasing modeling error.

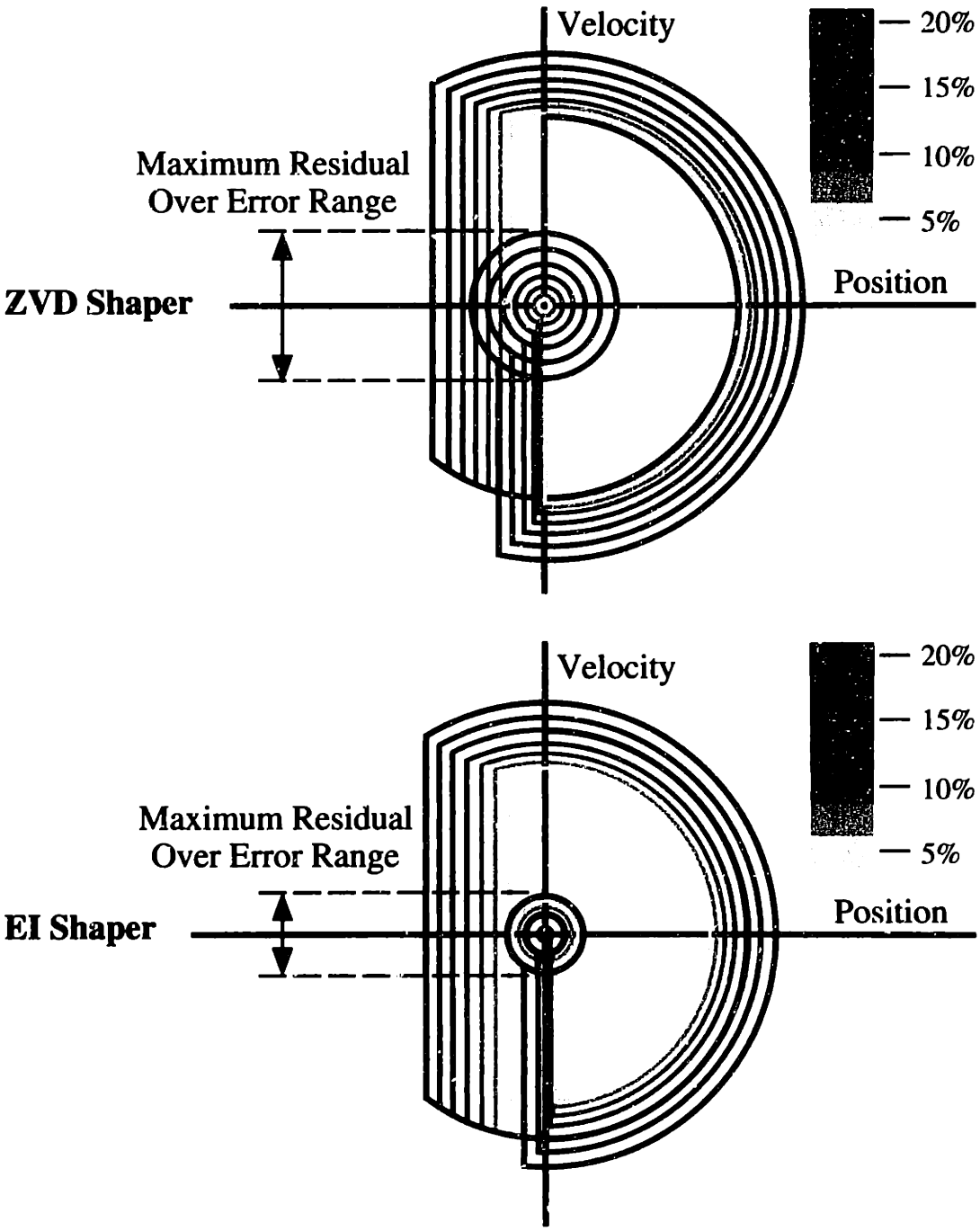

Figure 2.18: Phase Plane Plots for the ZVD and EI Shapers with Frequency Errors Ranging From 5% to 20%.

2.8 Deflection Plots

Certain types of command profiles are generated to limit the transient deflection in the elastic modes, as well as, eliminate the residual vibration. By limiting the deflection, the endpoint can be made to closely follow a desired trajectory. Furthermore, the internal loading is proportional to the elastic deflection, so limiting deflection can reduce the possibility of damage to the system or to a sensitive payload it may be manipulating.

The most obvious method for analyzing the effectiveness of these types of commands is to perform a numerical simulation of the system under consideration and examine the resulting transient deflection. If the system has a small number of modes, then this process can be done quickly and easily. However, if the system has many uncertain modes, then the deflection of the real system may be vastly different than the value predicted by the simulation. The difference arises because the deflection depends on the amplitude and phasing of the vibration in each mode. If the modeling frequencies differ from the actual frequencies, then the relative phase will be incorrect and the deflection can exceed the predicted level.

Figure 2.19 shows the deflection for a two-mass and spring system when subjected to two different command profiles. Both commands move the system the same distance and yield zero residual vibration; however, Command 2 causes 20% less deflection. The price for this reduced deflection is a slightly increased move duration as can be noted by the time that the two deflection curves go to zero. Generation of deflection-limiting commands will be discussed in Chapter 4.

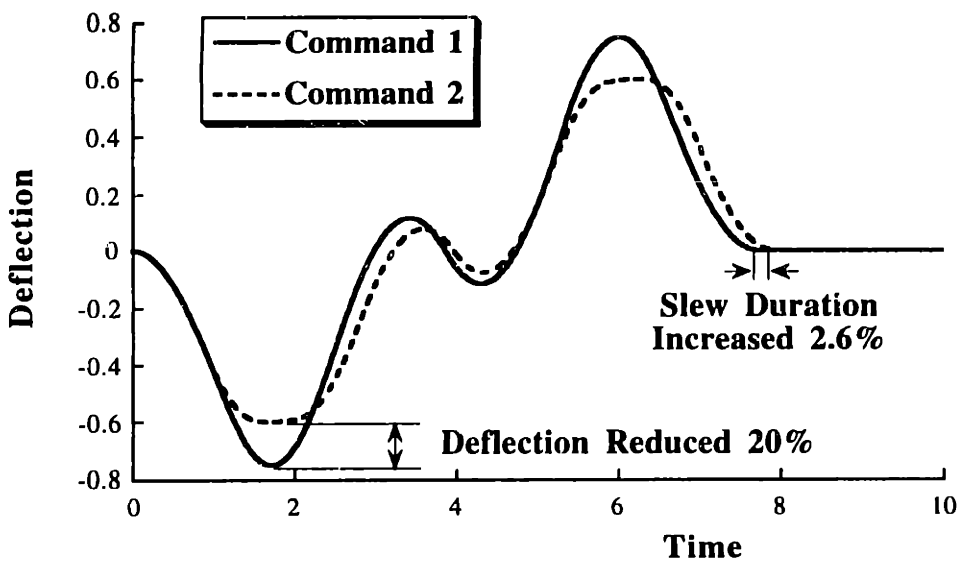

Figure 2.19: Deflection Caused by Two Different Commands.

2.9 Fuel Usage Plots

Command profiles designed for spacecraft should take into account fuel usage due to the expense of space-based fuel and the limited quantity that can be carried up with the spacecraft. The amount of fuel used during a given command sequence is a function of the system parameters, the desired move distance, and the type of command used. Commands that produce the same maneuver in roughly the same time can use vastly different amounts of fuel.

To compare different types of command profiles, the fuel usage can be plotted as a function of some variable of interest. For example, Figure 2.20 shows the fuel usage (defined as the duration of time that the actuators are turned on) for the time-optimal control of a two-mass and spring system as a function of the move distance. Also shown in Figure 2.20 is the fuel usage of an alternative type of command which uses considerably less fuel yet moves the system nearly as quickly as the time-optimal command. Commands designed to satisfy fuel usage constraints are discussed in Chapter 5.

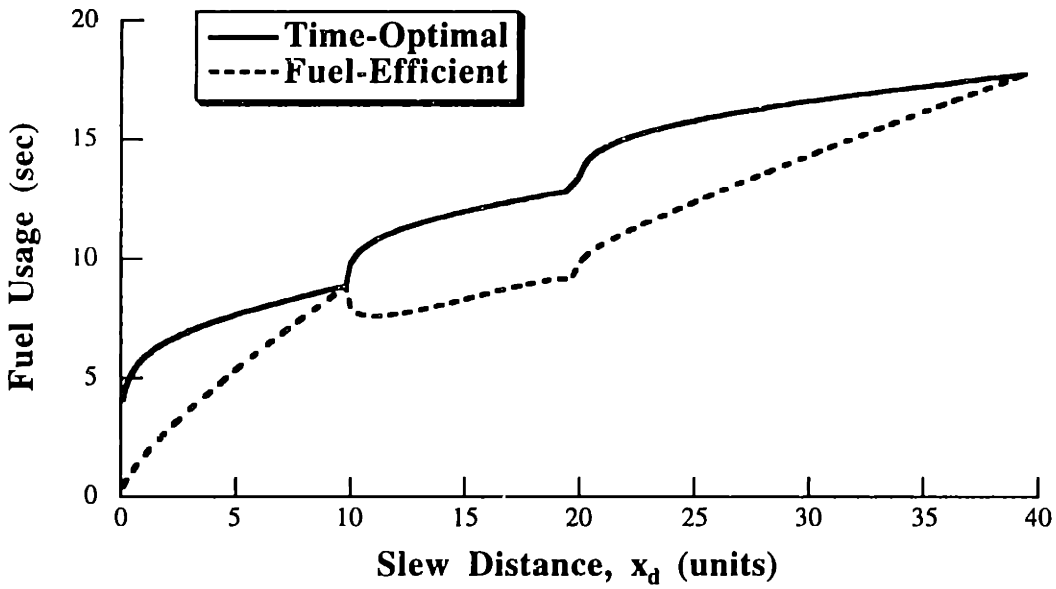

Figure 2.20: Fuel Usage of Time-Optimal and Fuel-Efficient Commands.

2.10 Computational Count

The difficulty of using a command shaping method should always be considered. Of course, the difficulty of use depends on the expertise of the engineer implementing the scheme and the available hardware. Putting those issues aside, the relative difficulty of two possible methods can be examined by determining the number of computations required to implement the method.

There are two distinct types of computations that should be examined: off-line computation and real-time computation. Off-line computation consists of any calculations which must, or can be, performed before the system goes into operation. An expanded definition of off-line computation could include the time needed for the engineer to master the proposed method. Real-time computation can be very important, as it may limit the servo rate of the closed-loop controller. An effective measure of this burden is simply the number of multiplies and adds that must be performed at each time step of the controller. An expanded definition of real-time computation could include that amount of memory space that a shaping method needs. This memory space is unavailable for other possible uses and could limit the sophistication of the closed-loop controller.

2.11 Hardware Experiments and Numerical Simulation

By far the most accurate means of assessing many of the performance criteria is to conduct experiments on real hardware. Throughout the remainder of this thesis, measurements taken from real machines will be used to verify and evaluate many of the proposed command shaping schemes. The experimental results include data from coordinate measuring machines, gantry cranes, XY stages, and hard disk drive test stands.

Carefully constructed numerical simulations can also provide excellent information without the expense of hardware experiments. Results from computer simulations will be used where hardware experiments would have proved too expensive or difficult to perform. These instances occur when a large number of experiments are needed to demonstrate a result, or the technology is intended for expensive hardware such as spacecraft. The simulations used here range from simple linear models of harmonic oscillators to nonlinear models of gantry cranes to a very sophisticated simulations of the space shuttle with payloads attached to its robotic manipulator arm.

2.12 Summary of Analysis Tools

The discussion in this chapter has been condensed in Table 1. Each of the tools is tabulated and their usefulness for evaluating the performance measures and designing commands is listed. The evaluation of each tool has been broken down very coarsely into "Useful" represented by the solid circles and "Somewhat Useful", represented by the half-filled circles. When neither symbol is present, the category does not apply or the tool is of little use.

An important point to note is that no single tool (with the possible exception of hardware experiments) provides good information about all of the possible performance criteria. A full evaluation of any command shaping scheme requires the use of several different tools. As a corollary, any shaping scheme designed and evaluated with a single tool is possibly deficient in some performance criteria.

Table 2.1: Summary of Tool Usage.

● - Useful
◒ - Somewhat Useful

	Residual Vibration	Rise Time	Settling Time	Robustness	Unmodelled Modes	Actuator Effort	Deflection	Fuel Usage	Implementation	Human Compatibility	Design of Commands
Impulse Response	●	●	●	◒		◒		◒	◒	◒	●
Sensitivity Curves				●	●	◒					●
Pole-Zero	●			◒	◒						●
Optimal Control	●					●					◒
Vector Diagrams	●	●	●	◒		◒				◒	●
Phase Plane	●	●	●	◒		◒				◒	●
Deflection Plots	●						●				
Fuel Usage Plots								●			
Computational Count									●		
Experiments	●	●	●	●	●	●	●	●	●	●	

3 DESIGN OF ROBUST INPUT SHAPERS

3.1 Introduction to Robust Input Shapers

In Chapter 1, command generators were classified into two categories. One type of generator pre-computes the entire command profile for a given desired motion. The second type generates commands in real-time so that the control system can respond, in real-time, to any variation of the desired motion. This chapter addresses the design of real-time command generators. The topic is further narrowed by considering only those real-time command generators that can be treated as finite impulse response (FIR) filters. FIR filters that are designed to generate commands for mechanical systems are usually called input shapers, so that nomenclature will be used here.

Three types of input shapers were introduced in Chapter 1: zero vibration (ZV), zero vibration and derivative (ZVD), and extra-insensitive (EI). Chapter 2 then introduced tools that can be used to design and analyze the performance of input shapers (as well as pre-computed commands). In this chapter several new types of input shapers are developed and compared to those previously proposed. The next section of this chapter extends the EI shaping concept to obtain input shapers that are even more robust to modeling errors, but have longer durations.[5] Section 3.3 generalizes the EI concept to produce input shapers that can have any desired level of robustness. The trade-off between robustness and shaper length is examined. Section 3.4 utilizes the results from the earlier sections to design and analyze robust shapers for suppressing multi-mode vibration. Section 3.5 introduces input shapers that contain negative impulses. The tradeoffs associated with using negative impulses are discussed and methods for dealing with some of the undesirable side effects are presented. Finally, Section 3.6 presents a method for designing input shapers using a fixed time duration. Each of the following sections include simulation and/or experimental results to demonstrate the key ideas.

The amplitudes and time locations of the impulses in an input shaper are determined by solving a set of constraint equations. The constraint equations can be formulated to meet a variety of

[5] Recall that system rise time increases with the duration of the input shaper.

performance specifications. The constraint equations considered in the next several sections can be categorized as follows:

1) Residual vibration constraints.

2) Robustness constraints.

3) Requirement of time optimality.

4) Constraints on the impulse amplitudes.

The constraint on residual vibration amplitude can be expressed as the ratio, V, of the residual vibration amplitude with shaping to that without shaping [101]:

$$V(\omega,\zeta) = e^{-\zeta\omega t_n}\sqrt{\left(C(\omega,\zeta)\right)^2 + \left(S(\omega,\zeta)\right)^2} \tag{3.1}$$

where,

$$C(\omega,\zeta) = \sum_{i=1}^{n} A_i e^{\zeta\omega t_i}\cos\left(\omega\sqrt{1-\zeta^2}\,t_i\right) \tag{3.1a}$$

$$S(\omega,\zeta) = \sum_{i=1}^{n} A_i e^{\zeta\omega t_i}\sin\left(\omega\sqrt{1-\zeta^2}\,t_i\right) \tag{3.1b}$$

A_i and t_i are the amplitudes and time locations of the impulses, ω is the vibration frequency, ζ is the damping ratio, and n is the number of impulses in the input shaper. The zero vibration (ZV) shaper is obtained by setting (3.1) equal to zero and solving for the impulse amplitudes and time locations. Note that when V is set equal to zero, (3.1) produces two equations because both the cosine summation, (3.1a), and the sine summation, (3.1b), are squared, so they must be zero independently if the entire expression is to equal zero.

The earliest appearance of the ZV shaper was in work done by O.J.M. Smith in the late 1950's [140, 141]. Smith called his approach posicast (positive-cast) control because [141]:

> The final value is reached just when the velocity goes to zero. This is what happens when a fisherman drops his fly in the water at the maximum-position and zero-velocity instant.

When implementing posicast control using analog equipment and transmission delay lines, Tallman and Smith [144] noted that the performance was very sensitive to parameter variations. Tallman and Smith also proposed that systems with multiple modes could be treated by assembling a compensator (input shaper) for each mode and then cascading them together. Cook demonstrated this idea using a multi-mode simulation [25].

Sensitivity to parameter variations was not the only difficulty with posicast control when it was first introduced. The convolution required to implement the method in real time was difficult to perform without digital computers. Although Smith's theoretical framework allowed for shaping any reference command, posicast control was usually presented as a method for modifying only

step functions. This reduced the implementation problem to one of introducing time delayed versions of the original step input and is described in the work by Tallman and Smith using transmission delay lines [144]. Because the transmission delay lines used by Tallman and Smith could not create long enough delays for systems with low frequency dynamics, other researchers proposed alternate methods for producing the necessary time delays . Shields and Cook [95] used the truncated Fourier series method developed by Wierwille [170] to produce approximate time delays. They specifically noted that the procedure could be applied to any continuous signal, not just step functions. The Wierwille method produces somewhat distorted delays, so the overall process was very sensitive to parameter variations. Mee proposed another approach to implementing posicast control that used sampling circuits to produce the required delays [67]. Several other researchers made additional contributions by implementing and expanding Smith's idea for using posicast control on higher-order systems [24, 25, 61, 143].

Successful implementation of ZV shaping requires stationary plant dynamics and an accurate system model such as that used recently by Bederson et. al., for a spherical pointing motor [10]. Because ZV shaping is sensitive to modeling errors, it has limited utility for real systems and consequently it did not come into widespread use. However, interest in input shaping was increased by Singer and Seering's development of a robust input shaper [96, 98, 101]. Their form of robust input shaping was achieved by requiring that the derivative with respect to the frequency of the residual vibration be equal to zero at the modeling frequency. That is:

$$0 = \frac{d}{d\omega}\left[e^{-\zeta\omega t_n} \sqrt{\left(C(\omega,\zeta)\right)^2 + \left(S(\omega,\zeta)\right)^2} \right] \tag{3.2}$$

The price that is paid for the improved robustness of the ZVD shaper is an increase in the shaper duration and, therefore, a decrease in the system rise time.

Due to the transcendental nature of the constraint equations used to design input shapers, there are multiple possible solutions. To make the rise time as fast as possible, the shaper must be made as short as possible. Therefore, the time optimality requirement is:

$$\min(t_n) \tag{3.3}$$

where t_n is the time of the final impulse.

If the shaping process is to have unity gain, then the impulse amplitudes must sum to one:

$$\sum_{i=1}^{n} A_i = 1 \tag{3.4}$$

If the amplitudes sum to a value other than one, then the shaped command will not reach the same final setpoint as the unshaped command.

If the amplitudes of each individual impulse are not constrained, then their values are driven to positive and negative infinity by the time optimality constraint [98]. There are two possible

solutions to this problem: limit the magnitude of the impulses to a specific value or require all the impulse amplitudes to have positive values. Requiring positive impulse amplitudes and enforcing the summation constraint of (3.4) leads to all impulse amplitudes being in the range $0 \leq A_i \leq 1$. The requirement of positive amplitudes will be used in this section, as well as in Sections 3.3 and 3.4. In Section 3.5 the impulses are allowed to take on negative values, but constraints on the impulse amplitudes are introduced to keep the amplitudes from approaching infinity.

As will be demonstrated in the remainder of this introduction, Singer's work prompted considerable research activity. Hyde utilized Singer's optimization code to produce optimized input shapers for multi-mode systems [40, 42, 43]. He showed that satisfying the constraint equations for all modes simultaneously led to shorter input shapers than convolving shapers designed separately for each mode. Furthermore, the "simultaneous" shapers tended to have fewer impulses. These effects will be explored in some detail in Section 3.4. Hyde later used input shaping to improve contact transition control [39, 41].

In his thesis, Singer explained the effectiveness of his input shaping scheme using several analysis tools such as vector diagrams, phase planes, and transfer functions. Singhose used the vector diagram representation to create the EI shaper [121, 122, 138], while Singh and Heppler used the vector diagram to generate multi-mode shapers with very few impulses [106, 107]. Other researchers concentrated on the transfer function analysis. Bhat and Miu used Laplace transform analysis to show that ZV shaping places one zero on top of each of the flexible pole and that ZVD shaping places two zeros over each flexible pole [12-17]. Many authors have taken this result a step further and used the idea to design input shapers in the s-plane and z-plane [45, 46, 51, 58, 59, 71, 88, 94, 109, 112, 153]. Recall that Tuttle's procedure for designing input shapers in the z-plane was demonstrated in Chapter 2 [153].

Input shaping has been implemented on a great variety of systems ranging from high-precision machinery to industrial gantry cranes. Rappole and Singer used an input shaper targeted at the two lowest modes to greatly reduce the vibrations of a silicon handling robot [87]. It was shown by several authors that the performance of coordinate measuring machines can be improved with shaped commands [45, 46, 94, 128, 139]. The throughput of a hard disk drive head testing machine was improved using input shaping [129]. Input shaping was a major component of an experiment in flexible satellite control that flew on the Space Shuttle in March, 1995 [134, 151, 152].

In addition to high-precision machinery, input shaping has proven valuable for systems with long periods of vibration. Banerjee used input shaping to reduce deflections and residual vibration during the simulation of a large space-based antenna [6, 9]. Vibrations of long reach manipulators were decreased with input shaping [44, 50, 58, 59]. Input shaping has also proven effective for

controlling oscillations of systems, such as gantry cranes, that have suspended payloads [49, 72, 73, 97, 133, 157].

Another command shaping scheme, that has also shown benefit for suspended payloads, is a variation of input shaping developed at Sandia National Laboratories. This method adds well-damped poles to the shaping filter [34]. The result is an Infinite Impulse Response (IIR) filter that places zeros near the system flexible poles and poles somewhere else in the z-plane so that the transfer function of the filter does not greatly exceed unity. This process has also been applied to the control of open liquid containers to obtain slosh-free motion [30-33] and to the slewing of a flexible beam with a hydraulic robot [82]. A survey paper on the work done by Sandia in this area is listed in the references [89]. Lin used a simulation of a welding robot to demonstrate the utility of this approach [51]. Furthermore, Bodson has implemented an adaptive version of this method on a flexible-beam testbed [18].

In addition to eliminating residual vibration, input shaping has shown benefits for reducing the detrimental effects of transient deflection [75, 79, 118]. More specifically, input shaping was shown to be beneficial for trajectory following with a five-bar-linkage manipulator [27, 28, 171] and with an xy positioning system [116, 124, 125]. Reduction of transient deflection with input shaping also aids in obstacle avoidance [35], as will be demonstrated in Chapter 8.

Input shaping has been combined with a variety of adaptive and closed-loop control schemes. Magee and Book developed a shaping scheme that continuously changes the input shaper in response to changes in the physical plant [19, 55-60]. Tzes and Yurkovich proposed an alternate form of adaptive input shaping [154, 156]. Zou and Wang placed the input shaper inside the closed-loop control path and also utilized a rigid-body inverse dynamics term [172]. Tzes, et. al. used an acceleration feedback loop to compliment the effects of input shaping [155]. Hillsley and Yurkovich combined input shaping with a post-maneuver damping controller to improve large angle slewing [37, 38]. Khorrami, et. al. combined input shaping with an adaptive nonlinear controller [48]. Singh and Vadali proposed using input shaping with a Lyapunov controller to perform three-dimensional maneuvers of flexible spacecraft [108]. Pao proposed a shaping method that exploits the use of multiple actuators [77].

Input shaping has been the subject of several studies that compare various techniques for controlling flexible structures. Love, et. al. compared input shaping to other techniques for pick and place tasks [54]. Watkins and Yurkovich investigated large angle slewing of a flexible planar truss [161, 162]. Other studies have compared input shaping to traditional notch and pass-band filters [99, 126], and to time-optimal control [75, 79, 118, 160, 164].

Although Singer's work can be regarded as the catalyst for most of the above research, his main contribution of robustness to modeling errors was not modified or improved upon by most

follow-on research. The adaptive input shaping schemes represent one approach for attempting to improve robustness. These require a somewhat more complicated implementation and the use of sensor measurements to continually redesign the input shapers proposed by Singer. A more direct approach for increasing the robustness is simply to design an input shaper with better robustness constraints. This concept is represented by the work of Singhose [113, 121, 122, 138], who demonstrated that additional robustness could be obtained by relaxing the requirement of zero residual vibration when the model is exact. A significant portion of this chapter will be devoted to further improving the robustness of the input shaping process.

3.2 Multi-Hump Extra-Insensitive Input Shapers

As we have seen, an EI shaper has more robustness than a ZVD shaper and both have the same duration. Singer showed that his process could be used to generate a more robust shaper by forming the second derivative of (3.1) with respect to ω and setting it equal to zero. The shaper that results from satisfying this additional constraint is called a ZVDD shaper. This additional constraint increases the robustness, but also increases the shaper duration by one half period of the vibration. Singer showed that the algorithm can be extended indefinitely with repeated differentiation of (3.1) [98]. For each differentiation, an additional impulse is added to the shaper and the shaper is lengthened by one-half period of the frequency. Closed-form solutions of the ZVDD shapers for damped systems exist [101]. This section describes methods for extending the EI design algorithm to produce more robust shapers. These new shapers have more than one hump in their sensitivity curves, so they are called multi-hump extra-insensitive shapers. They have significantly more robustness, for the same duration, than the shapers obtained with Singer's extended algorithm.

3.2.1 Undamped Multi-Hump Extra-Insensitive Input Shapers

The EI shaper first presented in Chapter 1 consists of three-impulses, has a length equal to one period of vibration, and has a corresponding sensitivity curve that contains one hump. A natural extension would be to design a shaper with two humps in its sensitivity curve, like the one shown in Figure 3.1. We hypothesize that there exists a shaper containing four evenly spaced impulses with a duration of one and a half periods that will form the sensitivity curve of Figure 3.1. Justification for this hypothesis comes from the ZVDD shaper which consists of four evenly spaced impulses lasting 1.5 periods of vibration.

To simplify the equations in the following derivation, the problem of determining the time and amplitude parameters for the two-hump EI input shaper will be formulated using a vector diagram. Recalling the information from Chapter 2, we know a modeling error appears on the vector diagram as a rotation of each vector through an angle $\phi_i=\Delta\omega t_i$, where $\Delta\omega$ is the frequency error. Once the vectors have been rotated away from their starting positions, their resultant sum represents the residual vibration that will occur in the presence of the modeling error represented by $\Delta\omega$. A vector diagram of the proposed two-hump EI shaper is shown in Figure 3.12. To clarify the distinction between impulses and the vectors used to represent them, vectors will be denoted as, $\hat{A}_i$, while impulses and vectors lengths will be denoted as A_i. For more details on the vector diagram representation of input shapers refer again to Chapter 2 or see one of the references [98, 121, 122, 138].

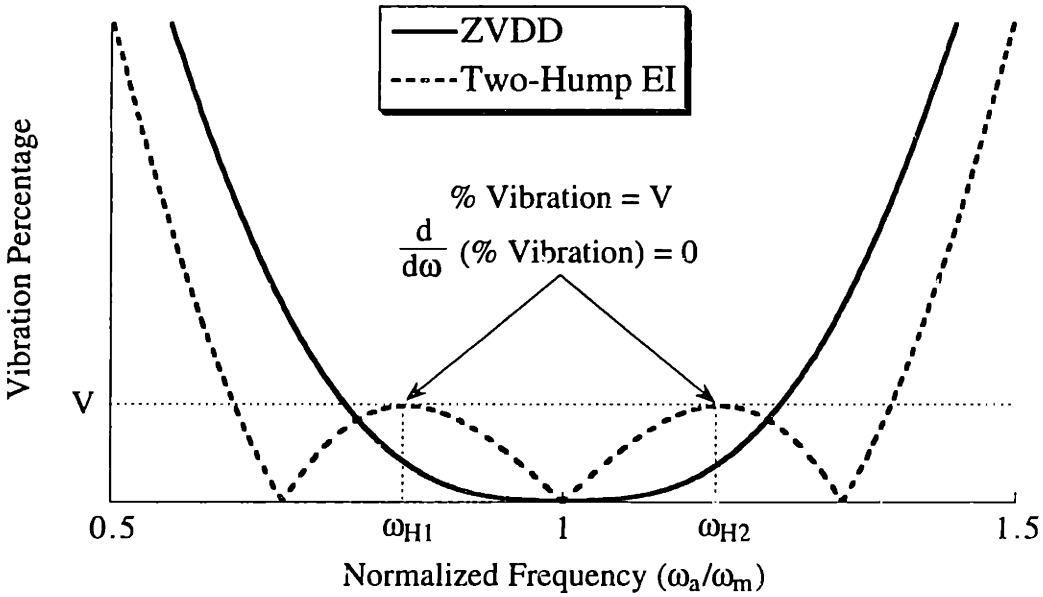

Figure 3.1: Sensitivity Curves of the ZVDD and Two-Hump EI Shapers.

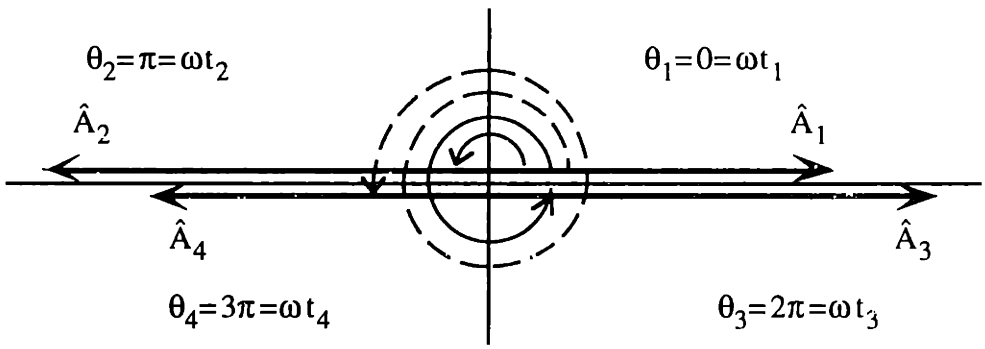

Figure 3.2: Vector Diagram Representation of the Two-Hump EI Input Shaper.

By examining Figure 3.1, we can construct the set of constraint equations that must be satisfied by the shaper in Figure 3.2. The first requirement suggested by Figure 3.1 is that the vibration must be zero when the actual frequency is exactly equal to the modeling frequency. This requires that the resultant of the vectors shown in Figure 3.2 must sum to zero when $\Delta\omega=\phi_i=0$:

$$A_1 - A_2 + A_3 - A_4 = 0 \tag{3.5}$$

A_2 and A_4 have negative values associated with them because they point in the opposite direction of A_1 and A_3. Given that the desired sensitivity curve is symmetrical and the impulse time spacings are uniform, then the shaper impulse amplitudes must be symmetrical. This yields:

$$A_1 = A_4 \quad \text{and} \tag{3.6}$$

$$A_2 = A_3 \tag{3.7}$$

Equations (3.5)-(3.7) are not independent; (3.5) and (3.6) yield (3.7). Therefore, (3.7) is not used

in the following derivation.

Figure 3.1 also indicates that at ω_{H1}, a frequency lower than the modeling frequency, the vibration must equal V and the derivative must equal zero. Using the vector diagram notation these constraints are:

$$V = \sqrt{\left(\sum_{i=1}^{4}(-1)^{i-1}A_i\cos((i-1)\phi)\right)^2 + \left(\sum_{i=1}^{4}(-1)^{i-1}A_i\sin((i-1)\phi)\right)^2} \tag{3.8}$$

and:

$$0 = \frac{d}{d\phi}\sqrt{\left(\sum_{i=1}^{4}(-1)^{i-1}A_i\cos((i-1)\phi)\right)^2 + \left(\sum_{i=1}^{4}(-1)^{i-1}A_i\sin((i-1)\phi)\right)^2} \tag{3.9}$$

where, $\phi=\Delta\omega t_2$, and $\Delta\omega$ is the difference between ω and ω_{H1}. Note that ϕ represents the frequency shift from the modeling frequency to the frequency which corresponds to the peek of the left hump in the sensitivity curve. The variable ϕ is a function of V and will not appear in the final formulas that describe the shaper. Equations 3.8 and 3.9 contain trigonometric terms with arguments of (i-1)ϕ. This occurs because the first vector, $\hat{A}_1$, does not rotate in response to a modeling error; it still occurs at time zero ($\theta_1 = 0$). However, $\hat{A}_2$ rotates ϕ, $\hat{A}_3$ rotates 2ϕ, and $\hat{A}_4$ rotates 3ϕ; each vector $\hat{A}_i$ rotates (i-1)ϕ.

Finally, the impulse amplitudes must sum to one:

$$\sum_{i=1}^{4}A_i = 1 \tag{3.10}$$

The five equations for the two-hump EI shaper (Eqs. 3.5, 3.6, 3.8-3.10) contain five unknowns (A_1, A_2, A_3, A_4, ϕ) and one design parameter, V. We can solve for the input shaper amplitudes as a function of V. Combining (3.5), (3.6), and (3.10) yields:

$$A_1 = (1-2A_2)/2 \tag{3.11}$$

By expanding (3.8) and (3.9), combining terms, and using (3.10), we obtain:[6]

$$\left[3\sin(3\phi)+4\sin(2\phi)-\sin(\phi)\right]A_1^2 - 2\sin(2\phi)A_1 + \frac{\sin(\phi)}{4} = 0 \tag{3.12}$$

$$\left[4+2\cos(\phi)-4\cos(2\phi)-2\cos(3\phi)\right]A_1^2 + 2\left[\cos(2\phi)-1\right]A_1 + (1-\cos(\phi))/2 - V^2 = 0 \tag{3.13}$$

Equation 3.12 can be solved for cos(ϕ):

$$\cos(\phi) = \frac{1}{3}\left(1+\frac{1}{4A_1}\right) \tag{3.14}$$

Plugging this into (3.13) yields:

$$A_1 \equiv A_{12H}(V) = \frac{3X^2+2X+3V^2}{16X} \tag{3.15}$$

where, $X = \sqrt[3]{V^2\left(\sqrt{1-V^2}+1\right)}$ (3.16)

[6] The following algebraic solution was obtained by Dr. Lisa J. Porter [120, 134].

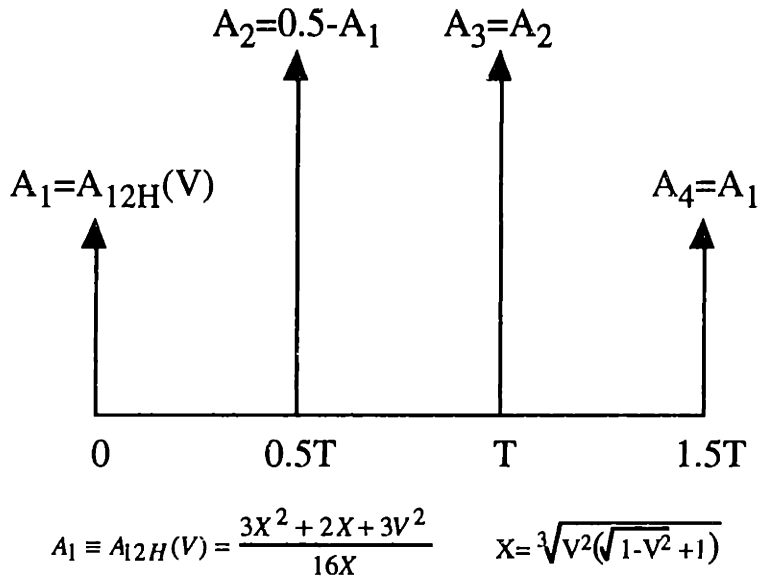

Figure 3.3: The Undamped Two-Hump EI Shaper.

Therefore, the two-hump EI shaper for undamped systems shown in Figure 3.3 is given by:

$$\begin{array}{llll} A_1 = A_{12H}(V) & A_2 = \frac{1}{2} - A_1 & A_3 = A_2 & A_4 = A_1 \\ t_1 = 0 & t_2 = 0.5T & t_3 = T & t_4 = 1.5T \end{array} \tag{3.17}$$

where T is the period of vibration being targeted for elimination.

Figure 3.1 compares the two-hump EI shaper to a traditionally designed shaper (a ZVDD shaper) that also has a length of one and one-half periods of vibration. When V = 5%, the insensitivity to modeling errors (the width of the sensitivity curve) is increased 51% without increasing the shaper length.

If even more robustness is required, a three-hump EI shaper can be designed. The desired sensitivity curve is shown in Figure 3.4. The equations describing the three-hump EI shaper will only be briefly presented because they are very similar to those for the two-hump EI shaper. The amplitude sum constraint is:

$$\sum_{i=1}^{5} A_i = 1 \tag{3.18}$$

Like the one-hump EI shaper, the vibration must equal V when the model is exact, therefore:

$$A_1 - A_2 + A_3 - A_4 + A_5 = V \tag{3.19}$$

By symmetry of the sensitivity curve, we get:

$$A_1 = A_5 \quad \text{and} \tag{3.20}$$

$$A_2 = A_4 \tag{3.21}$$

At the left hump of the sensitivity curve, the vibration must be V and the derivative of the vibration expression with respect to ϕ must equal zero. These two constraints are:

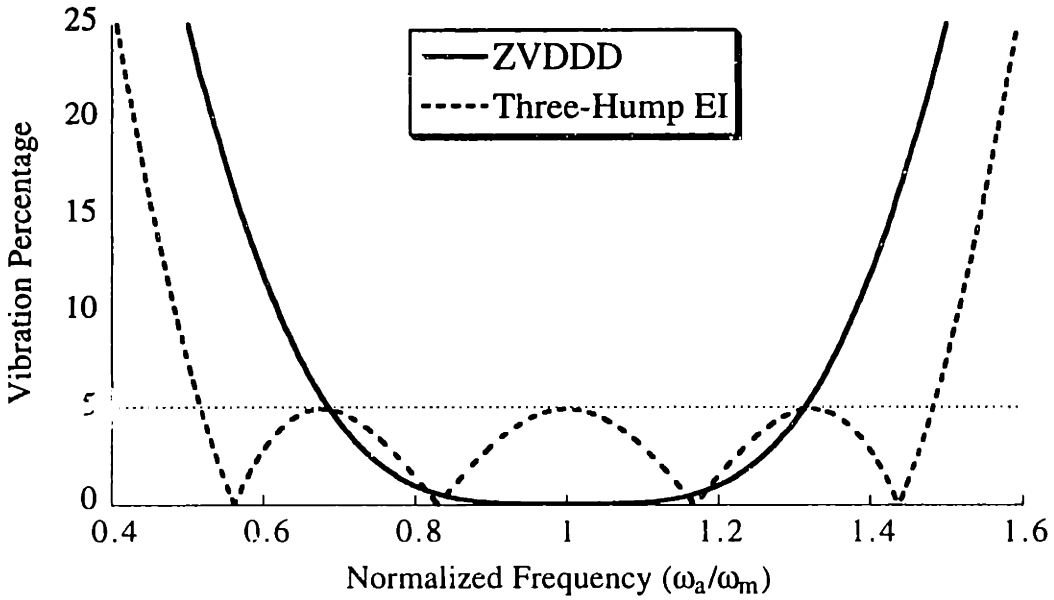

Figure 3.4: Sensitivity Curves of the ZVDDD and Three-Hump EI Shapers.

$$V = \sqrt{\left(\sum_{i=1}^{5}(-1)^{i-1}A_i\cos((i-1)\phi)\right)^2 + \left(\sum_{i=1}^{5}(-1)^{i-1}A_i\sin((i-1)\phi)\right)^2} \tag{3.22}$$

$$0 = \frac{d}{d\phi}\sqrt{\left(\sum_{i=1}^{5}(-1)^{i-1}A_i\cos((i-1)\phi)\right)^2 + \left(\sum_{i=1}^{5}(-1)^{i-1}A_i\sin((i-1)\phi)\right)^2} \tag{3.23}$$

where, once again, ϕ is used to represent the frequency shift (angular rotation on a vector diagram) from the modeling frequency to the frequency corresponding to the left hump in the sensitivity curve.

Combining (3.18)-(3.21) we find:

$$A_2 = (1-V)/4 \tag{3.24}$$

$$A_3 = 1 - 2A_1 - (1-V)/2 \tag{3.25}$$

Plugging (3.24) and (3.25) into (3.22) and (3.23) reduces the problem to two equations with two unknowns (A_1 and ϕ).[7] The use of several trigonometric identities and algebraic manipulations reduces the equations to functions of A_1 and $\cos\phi$ only. These equations are:

$$16\left[1-\cos^2(\phi)\right]\cos(\phi)A_1^2 + \left[\left(3\cos^2(\phi)-1\right)(1-V) - 2\cos(\phi)(1+V)\right]A_1 + \left[\frac{1-V^2}{8} - \frac{(1-V)^2}{8}\cos(\phi)\right] = 0 \tag{3.26}$$

$$4\left(1-\cos^2(\phi)\right)^2 A_1^2 + 2\left(\cos^2(\phi)-1\right)\left[1 - \frac{1-V}{2}(1+\cos(\phi))\right]A_1 + \frac{1-V}{4}\left[\frac{1-V}{4}\left(\cos^2(\phi)+2\cos(\phi)-3\right) + (1-\cos(\phi))\right] = 0 \tag{3.27}$$

[7] Again, the solution from this point on was developed by Dr. Lisa J. Porter [120, 134].

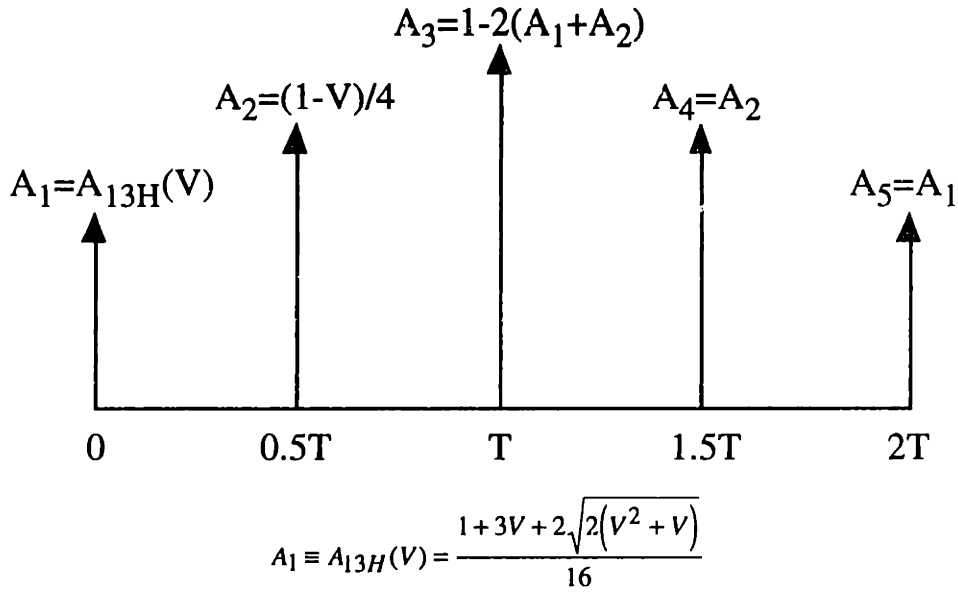

Figure 3.5: The Undamped Three-Hump EI Shaper.

Equation 3.26 is a cubic in cosϕ and the only real solution is:

$$\cos\phi = (1-V)/(16A_1) \tag{3.28}$$

Substituting (3.28) into (3.27) yields a quartic equation in A_1. Mathematica was used to obtain the four roots. The solution we are seeking is the one that maximizes ϕ (this maximizes the Δω, and therefore, the insensitivity). From (3.28) we know that we should pick the root that gives the largest value for A_1. This root is:

$$A_1 \equiv A_{13H}(V) = \frac{1+3V+2\sqrt{2\left(V^2+V\right)}}{16} \tag{3.29}$$

Therefore, the undamped three-hump EI shaper shown in Figure 3.5 is given by:

$$\begin{array}{ccccccc} A_1 \equiv A_{13H}(V) & & A_2 = (1-V)/4 & & A_3 = 1-2(A_1+A_2) & A_4 = A_2 & A_5 = A_1 \\ t_1 = 0 & & t_2 = 0.5T & & t_3 = T & t_4 = 1.5T & t_5 = 2T \end{array} \tag{3.30}$$

Figure 3.4 compares the robustness of the three-hump EI shaper to the robustness of a traditionally designed shaper (a ZVDDD shaper) that also has a length of two cycles of vibration. When V = 5%, the three-hump EI shaper increases the insensitivity 54% without increasing the shaper length. Figures 3.1 and 3.4 demonstrate that the extended EI design algorithm produces input shapers that have more insensitivity for a given shaper length than traditionally designed shapers.

The multi-hump EI design procedure can easily be used for damped systems. Three modifications to the above analysis must be performed. First, the damped vibration equation (3.1) and the derivative of the damped vibration equation (3.2) must be used in the set of constraints. In the above derivations the undamped versions (Eqs. 3.8, 3.9, 3.22, and 3.23) were used. Second,

Table 3.1: Damped Multi-Hump EI Shapers.

Shaper	$t_i = (M_0 + M_1\zeta + M_2\zeta^2 + M_3\zeta^3)T,\ T = 2\pi/\omega$				
	$A_i = M_0 + M_1\zeta + M_2\zeta^2 + M_3\zeta^3$				
		M_0	M_1	M_2	M_3
Two-Hump EI	t_2	0.49890	0.16270	-0.54262	6.16180
	t_3	0.99748	0.18382	-1.58270	8.17120
	t_4	1.49920	-0.09297	-0.28338	1.85710
	A_1	0.16054	0.76699	2.26560	-1.22750
	A_2	0.33911	0.45081	-2.58080	1.73650
	A_3	0.34089	-0.61533	-0.68765	0.42261
	A_4	0.15997	-0.60246	1.00280	-0.93145
Three-Hump EI	t_2	0.49974	0.23834	0.44559	12.4720
	t_3	0.99849	0.29808	-2.36460	23.3990
	t_4	1.49870	0.10306	-2.01390	17.0320
	t_5	1.99960	-0.28231	0.61536	5.40450
	A_1	0.11275	0.76632	3.29160	-1.44380
	A_2	0.23698	0.61164	-2.57850	4.85220
	A_3	0.30008	-0.19062	-2.14560	0.13744
	A_4	0.23775	-0.73297	0.46885	-2.08650
	A_5	0.11244	-0.45439	0.96382	-1.46000

the assumption of a symmetrical input shaper must be discarded. The discarded symmetry equations (Eqs. 3.6, 3.7, 3.20, and 3.21) are replaced by constraints describing the sensitivity curve on the right side of the modeling frequency. The above undamped procedure only constrained the left side of the sensitivity curve, because the symmetry of the input shaper ensured symmetry of the sensitivity curve. Third, the set of constraint equations must be solved numerically.

The damped equations for the two- and three-hump EI shapers were solved numerically for a range of damping ratios. To capture the resulting data in usable form, curves were fit to the impulse amplitudes and time locations using the damping ratio as an independent variable. The amplitudes and time locations of the two-hump EI V = 5% shaper and the three-hump EI V = 5% shaper are given in Table 3.1. The curve fits for the two-hump EI shaper have maximum errors in the impulse times and amplitudes of less than 0.5% over the range $0 \le \zeta \le 0.3$. The curve fits for the three-hump EI shaper are accurate to within 0.4% over the range $0 \le \zeta \le 0.2$.

3.2.2 EI Shapers in the S-Plane

The time domain and the vector diagram were used throughout the development of the multi-hump EI shapers. However, a better understanding of the multi-hump EI shapers can be obtained if we examine them in the s-plane. The zero locations for the multi-hump EI shapers in the s-plane are shown in Figure 3.6. The two-hump shaper places three zeros near the flexible system pole. Note that the shaper does not contribute any poles to the system dynamics. One of the shaper zeros lies directly on top of the pole and the others are on either side of the pole along a line of

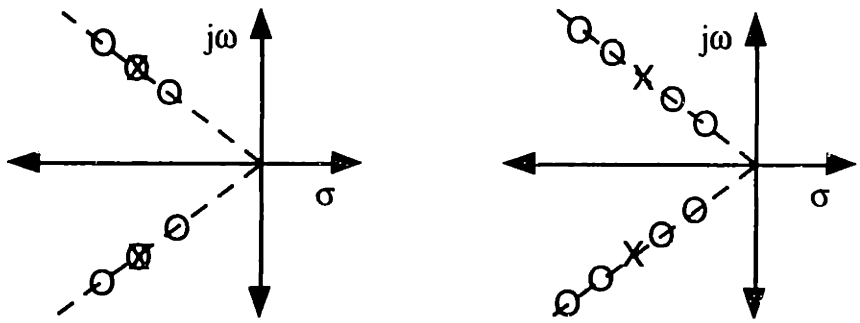

a) Two-Hump EI **b) Three-Hump EI**

Figure 3.6: Zero Locations of the Two- and Three-Hump EI Input Shapers in the S-Plane.

constant damping. The shaper zeros lie on a line of constant damping because the constraints force the vibration to zero at different frequencies, but the same damping ratio. Although not shown in the figure, for each of these three zeros, an additional infinite series of zeros exists spaced periodically along a line parallel to the imaginary axis.

If the system model is exact, the center zero completely cancels the pole dynamics, leading to zero residual vibration. If the pole moves away from its modeled location due to a modeling error or configuration change, the residual vibration will increase in value until the pole is about half way between the two zeros. As the pole continues to move away from the modeled location, attenuation of the vibration is dominated by the zero the pole is approaching. If the pole proceeds all the way to one of the outer zeros, then the vibration will again go to zero. This corresponds to the frequencies where the vibration goes to zero on the sensitivity curve shown in Figure 3.1 If the pole travels beyond the outer zeros, the vibration will increase steadily.

The three-hump EI shaper places four zeros near the modeling frequency, two on either side along a line of constant damping. This configuration leads to a small amount of residual vibration when the system model is exact. However, it allows the vibration to go to zero at four frequencies near the modeling frequency.

Examining the EI shapers in the s-plane suggests other possible design strategies. Instead of placing the zeros along a line of constant damping, the zeros could be placed at nearby damping values to achieve added insensitivity to errors in the damping ratio. Alternatively, more zeros could be placed on one side of the pole than on the other, or the zeros could be unevenly spaced. These techniques would result in shapers with skewed insensitivity [122].

3.2.3 Simulation and Experimental Results with EI Shapers

Computer simulations using the multi-hump EI shapers were performed using a two-mass and

spring system. The system parameters, m_1, m_2, and k, were all set equal to one. Two-hump and three-hump EI input shapers, with V = 5%, were designed for the resulting frequency of $1/(2\pi)$ Hz. The ZVDD and ZVDDD shapers were also designed for the nominal frequency. The system was given step inputs shaped with one of the four input shapers and the position of the second mass as a function of time was recorded.

To test the performance of the input shapers in the presence of modeling errors, k was varied from its nominal value of one. Figure 3.7a shows the response of the system with the ZVDD shaped input as k is varied from 1 to 1.8 in steps of 0.1. The envelope containing the residual vibration over this parameter variation has a width of 0.267. Figure 3.7b shows that the envelope with the two-hump EI shaper (V = 0.05) over the same parameter variation is approximately 2.7 times smaller (envelope of 0.10). Even though the two-hump EI and the ZVDD shaper have the same time duration, the two-hump EI bounds the residual vibration to a much lower level. Note that the envelope on residual vibration is predicted exactly by the sensitivity curve of Figure 3.1.

Figure 3.8a shows the response of the system with the ZVDDD shaped input as k is varied from 1 to 2.1 in steps of 0.1. A larger parameter variation is shown because the ZVDDD shaper is designed to be more insensitive to modeling errors than the ZVDD shaper. Figure 3.8b shows that the envelope of the residual vibration is 3.5 times smaller for the same parameter variation when the three-hump EI shaper is used. When k = 1, the system model is perfect and the residual vibration equals 5% (the envelope is 0.10).

The performance of the multi-hump EI shapers was tested on real hardware using the Middeck Active Control Experiment (MACE), which flew on board the Space Shuttle Endeavor in March 1995 [152]. As shown in Figure 3.9, the MACE hardware is designed to represent a typical satellite with multiple pointing mechanisms. A goal of the experimental program is to develop control algorithms that allow both gimbals to operate accurately in the presence of disturbances.

In one set of experiments, a white noise disturbance was fed into the actuator of one of the gimbals and the response of the other gimbal was recorded. Figure 3.10 shows the frequency response of the MACE structure without shaping and when a two-hump EI shaper is used to shape the disturbance signal. The two-hump notch in the frequency response is readily apparent at the system frequency near 2 Hz. Other experiments recorded the step response of the structure. Figure 3.11 shows the shaped and unshaped response of one gimbal when it is stepped approximately 3 degrees. The shaper eliminated virtually all of the residual vibration. The very low frequency drift in the position was caused by the umbilical which connected the free-floating hardware to the electronics box.

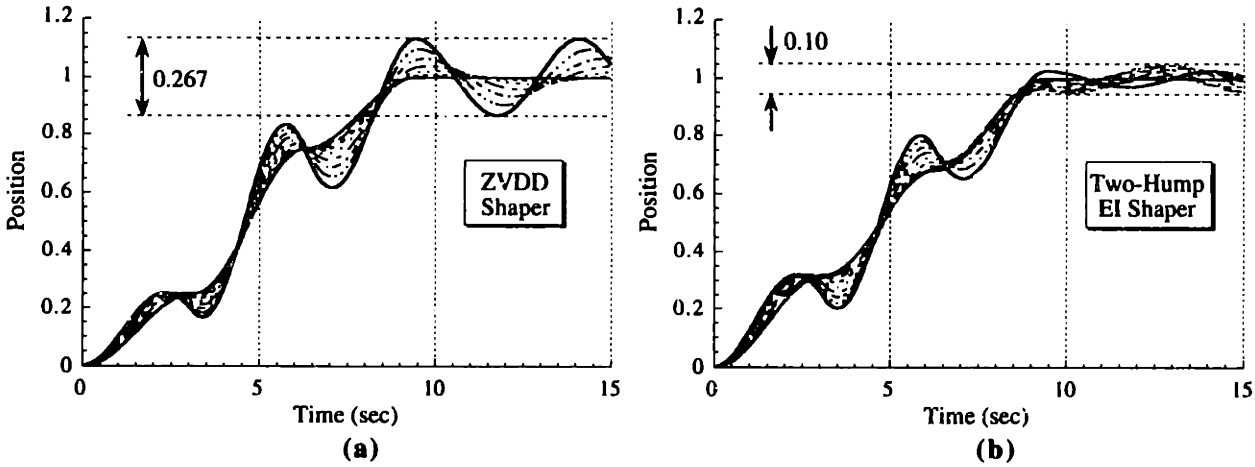

Figure 3.7: Responses with the ZVDD & 2-Hump EI Shapers ($1 \leq k \leq 1.8$).

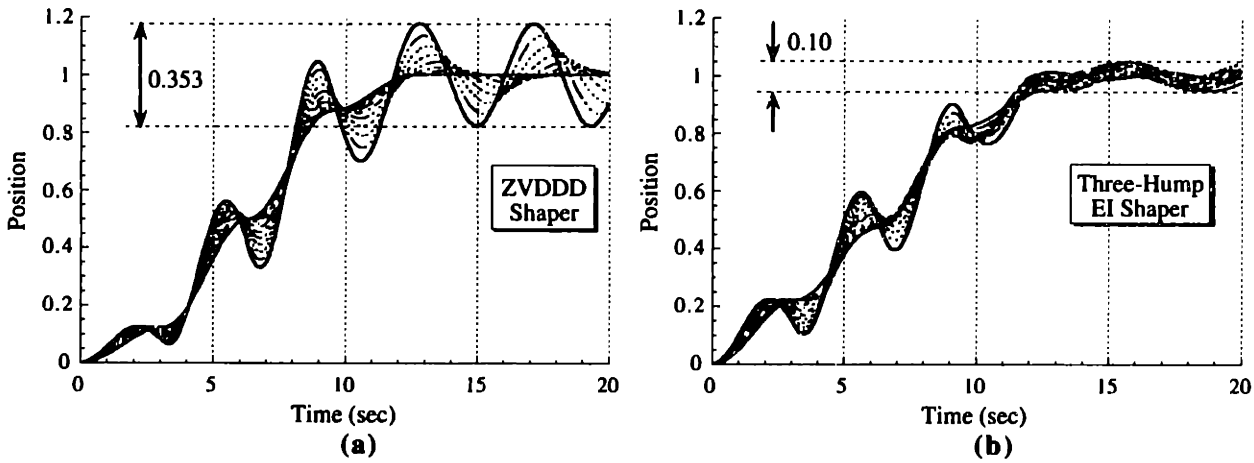

Figure 3.8: Responses with the ZVDDD & 3-Hump EI Shapers ($1 \leq k \leq 2.1$).

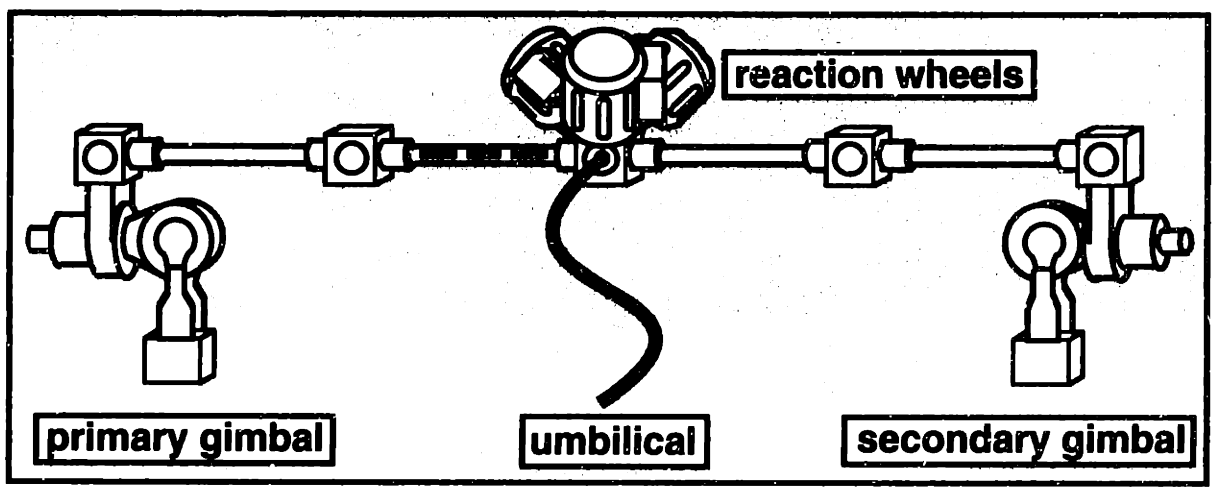

Figure 3.9: Experimental Hardware Used in the MACE Experiment.[8]

[8] Figure is courtesy of Dr. Timothy Tuttle [151, 152].

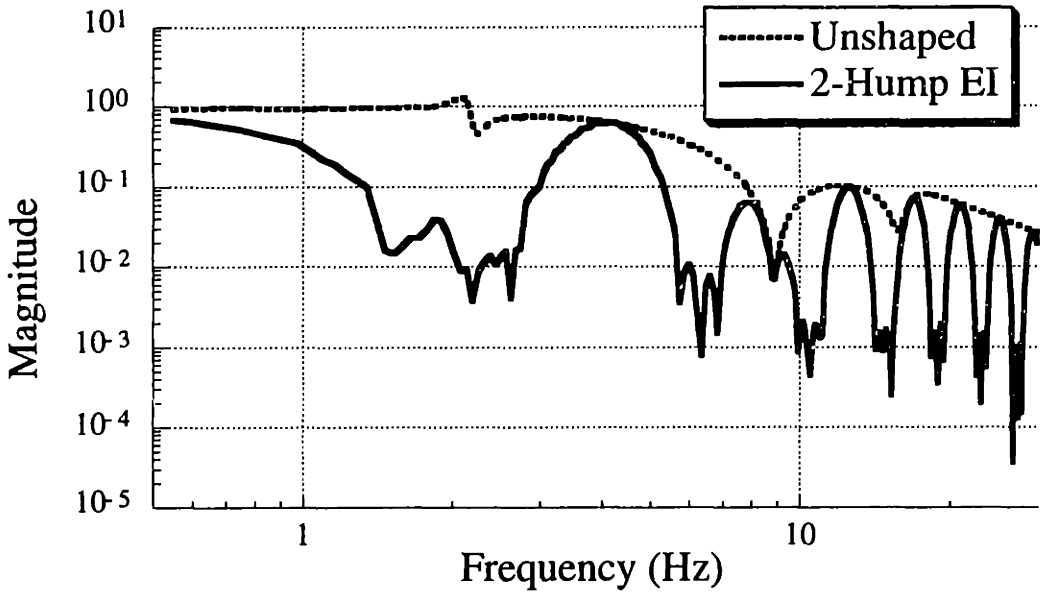

Figure 3.10: Experimental Frequency Response of the MACE Structure.

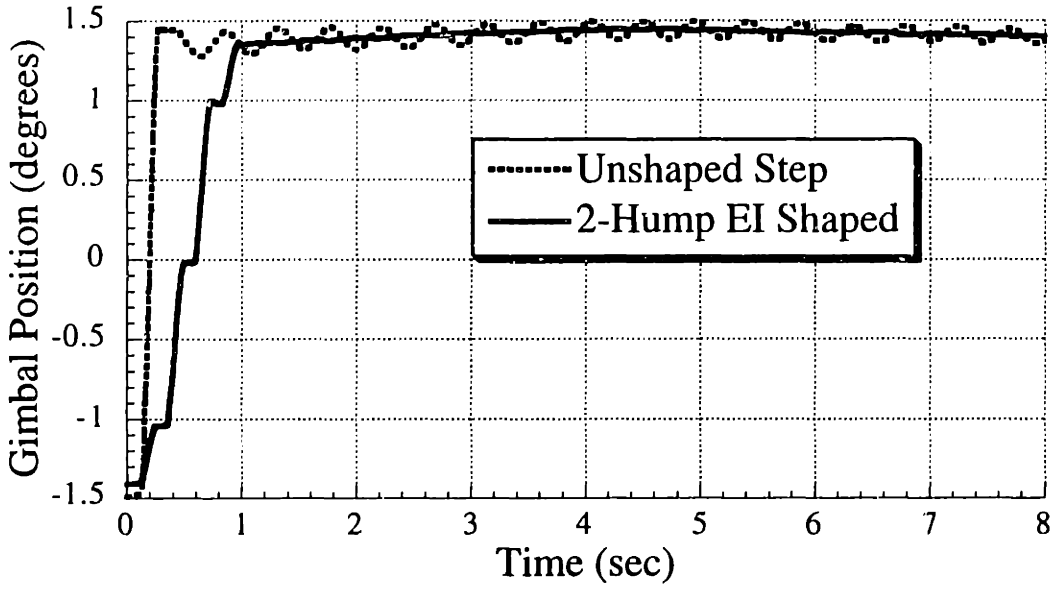

Figure 3.11: Experimental Step Responses of the MACE Structure.

3.2.4 Discussion of Multi-Hump EI Shapers

A design method has been developed that generates input shapers that are significantly more insensitive to modeling errors than traditionally designed shapers of comparable duration. Computer simulations of a single-mode system demonstrated the advantages of the new shapers. Results from the MACE experiment performed aboard the Space Shuttle Endeavor demonstrated the vibration-reducing ability of the new shapers.

3.3 Specified-Insensitivity Input Shapers

The previous section extended the EI shaper design method so that shapers with additional robustness could be obtained. The increases in robustness came in discrete steps with each added hump in the sensitivity curve. This section presents methods for designing shapers to have any desired level of robustness.

If we consider both the derivative (Singer) method and the EI method for obtaining robustness, we realize that both methods formulate "reasonable" robustness constraints and then solve for the shaper that satisfies the constraints. Given the great variety of systems that can benefit from input shaping, it seems desirable to develop a shaping method that allows the robustness to be tailored to a given system. Some systems may require robustness which is significantly different than that available with the standard input shapers. For Specified Insensitivity (SI) shapers, the constraint equations that must be satisfied do not remain fixed; rather, they vary with the desired level of robustness. Two procedures for obtaining SI shapers will be presented. The first procedure is a brute force method that yields approximate solutions. The degree of approximation can be easily controlled and the solutions obtained are usually very close to the exact solutions. The second procedure is more sophisticated and difficult to formulate, but it yields exact solutions.

3.3.1 Using Parameter Sampling to Obtain Approximate SI Shapers

The most straightforward method for generating a shaper with specified robustness is to use the technique of frequency sampling [100]. This method requires repeated use of the expression for residual vibration, (3.1). In each case, the residual vibration is set less than or equal to a tolerable level of vibration, V_{tol}:

$$V_{tol} \geq e^{-\zeta\omega t_n}\sqrt{\left(C(\omega,\zeta)\right)^2+\left(S(\omega,\zeta)\right)^2} \tag{3.31}$$

where the C and S functions are given in (3.1a) and (3.1b).

For example, if a 5% insensitivity[9] of I = 0.4 is desired (±20% frequency errors), then the constraint equations limit the vibration to below V_{tol} at specific frequencies between $0.8\omega_m$ and $1.2\omega_m$. In effect, the amplitude of residual vibration is constrained at a regular sampling period over the frequency interval of interest. The set of equations that must be satisfied consists of (3.3), (3.4), and M versions of (3.31), where M is the number of frequency sampling points. Each of the M equations is enforced at a different value of ω. This procedure is illustrated in Figure 3.12 for V_{tol} = 5% and I = 0.4.

In most cases, the shapers designed with this procedure will have sensitivity curves that

[9] Remember from Chapter 1 that the 5% insensitivity is the width of the sensitivity curve that lies below 0.05.

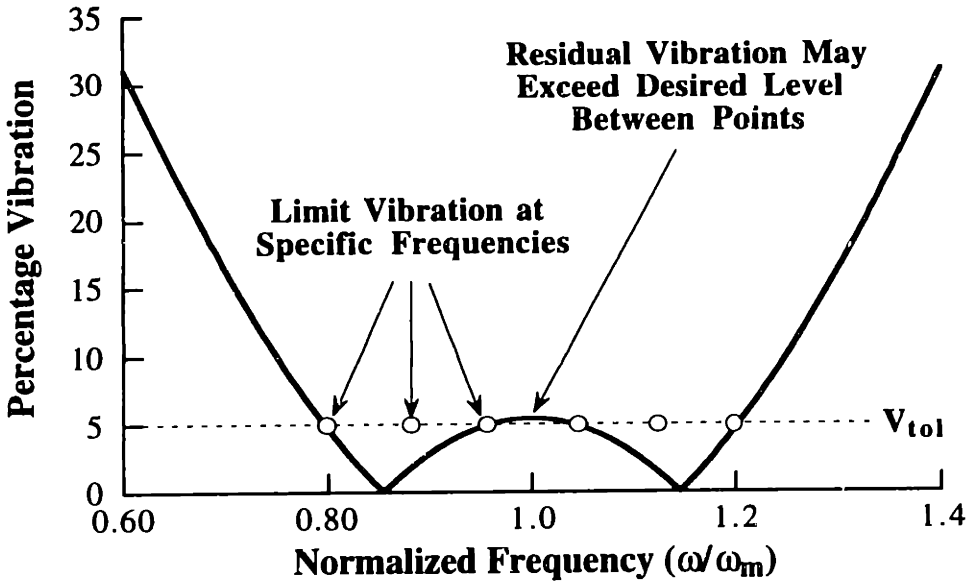

Figure 3.12: Frequency Sampling Leads to Approximate Solutions.

slightly exceed V_{tol} during some portion of the frequency range being suppressed. For a given frequency range, the number of constraint equations increases with M, but the result approaches the exact solution. That is, the maximum value of the sensitivity curve within the frequency range of interest approaches V_{tol}.

As I increases, the shape of the sensitivity curve evolves in a predictable way. For $\zeta = 0$, $V_{tol} = 5\%$, and $I < 0.22$ the curve touches zero at one point within the frequency range and is increasing on either side. For $0.22 \leq I < 0.59$, the sensitivity curve contains one hump within the range. For $0.59 \leq I < 0.87$, the sensitivity curve contains two humps. This process of adding humps to increase insensitivity continues as I increases. The evolution of the sensitivity curve is shown in Figure 3.13 for the undamped, single-mode SI shaper. Figure 3.13a shows I increasing from 0.06 to 0.2, while Figure 3.13b continues the progression by displaying I = 0.3 to 0.9. Throughout this section we will be concerned with symmetrical SI shapers. That is, the required insensitivity is centered about the modeling frequency. For example, I = 0.6 means that the frequency range being limited is $0.7\omega_m$ to $1.3\omega_m$. Even though the required insensitivity range is symmetrical, the resulting sensitivity curve may not be symmetrical. See again Figure 3.13.

The technique of frequency sampling can be used to design asymmetrical SI shapers. In this case, asymmetrical refers to the constrained frequency range, not the sensitivity curve. If the designer thinks that it is more likely that the system frequency will decrease over time, then the frequency range being suppressed could be specified as $0.7\omega_m$ to $1.2\omega_m$. The asymmetrical I = 0.5 SI shaper would result in a faster rise time than the symmetrical I = 0.6 SI shaper, but would be less effective at limiting residual vibration if the frequency increased.

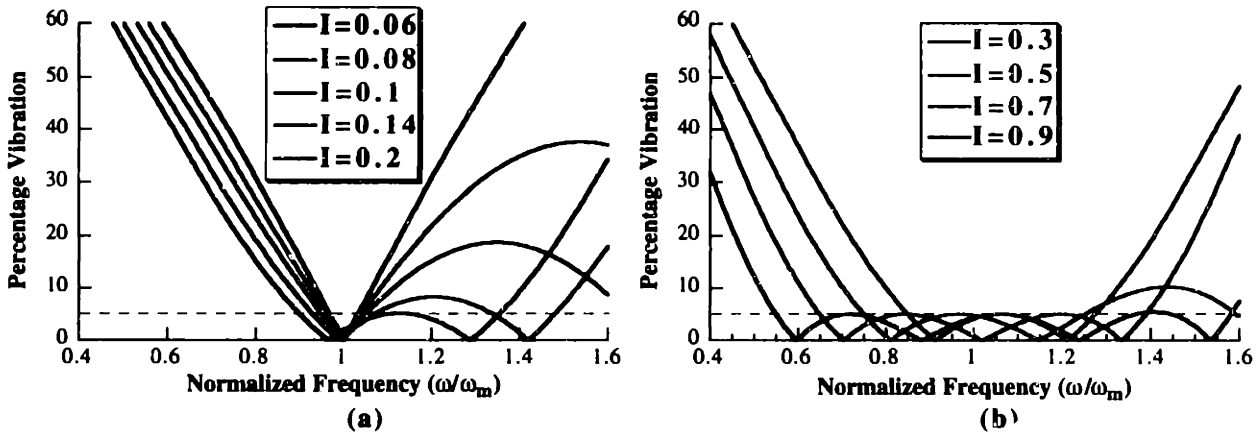

Figure 3.13: Evolution of the Sensitivity Curve (V_{tol} = 5% and ζ = 0).

A process similar to frequency sampling can be used to specify robustness to errors in the estimated damping ratio. This process, damping sampling, proceeds in the same fashion as frequency sampling, except the vibration constraints are enforced at N distinct damping ratios over a specified range. Frequency and damping sampling can be combined to suppress vibration over any frequency and damping range. This combined parameter sampling process is as straightforward to implement as frequency sampling; the residual vibration constraints are simply enforced over a two-dimensional parameter space consisting of MxN points.

Figure 3.14 shows a three-dimensional sensitivity curve for an SI shaper designed with parameter sampling. The shaper was required to suppress vibration over the range $0 \le \zeta \le 0.2$ and have a frequency insensitivity of 0.6. Note that the damping axis on the curve is not normalized. Using a normalized damping ratio (ζ/ζ_m) complicates the issue because small changes in damping appear as large changes in normalized damping when ζ_m is near zero, as it often is. In the limiting case, when ζ_m equals zero, the normalized damping ratio is undefined.

3.3.2 Exact SI Shapers

Parameter sampling is a useful technique for generating SI shapers that limit vibration amplitude to V_{tol} over most of the parameter space of interest. However, limiting vibration to less than V_{tol} over the entire range would, in theory, require satisfying an infinite number of equations. In this section we will present a method for obtaining exact solutions with very few constraint equations. Instead of enforcing only limitations on the amplitude of residual vibration, the method places constraints on the slope of the sensitivity curve by incorporating (3.2). The process will be demonstrated for obtaining frequency robustness only. The method consists of five steps:

1) Determine the minimum required number of sensitivity curve humps, H.

2) Limit the residual vibration amplitude to below V_{tol} at the edges of the frequency range to be suppressed [$(1-I/2)\omega_m$ and $(1+I/2)\omega_m$].

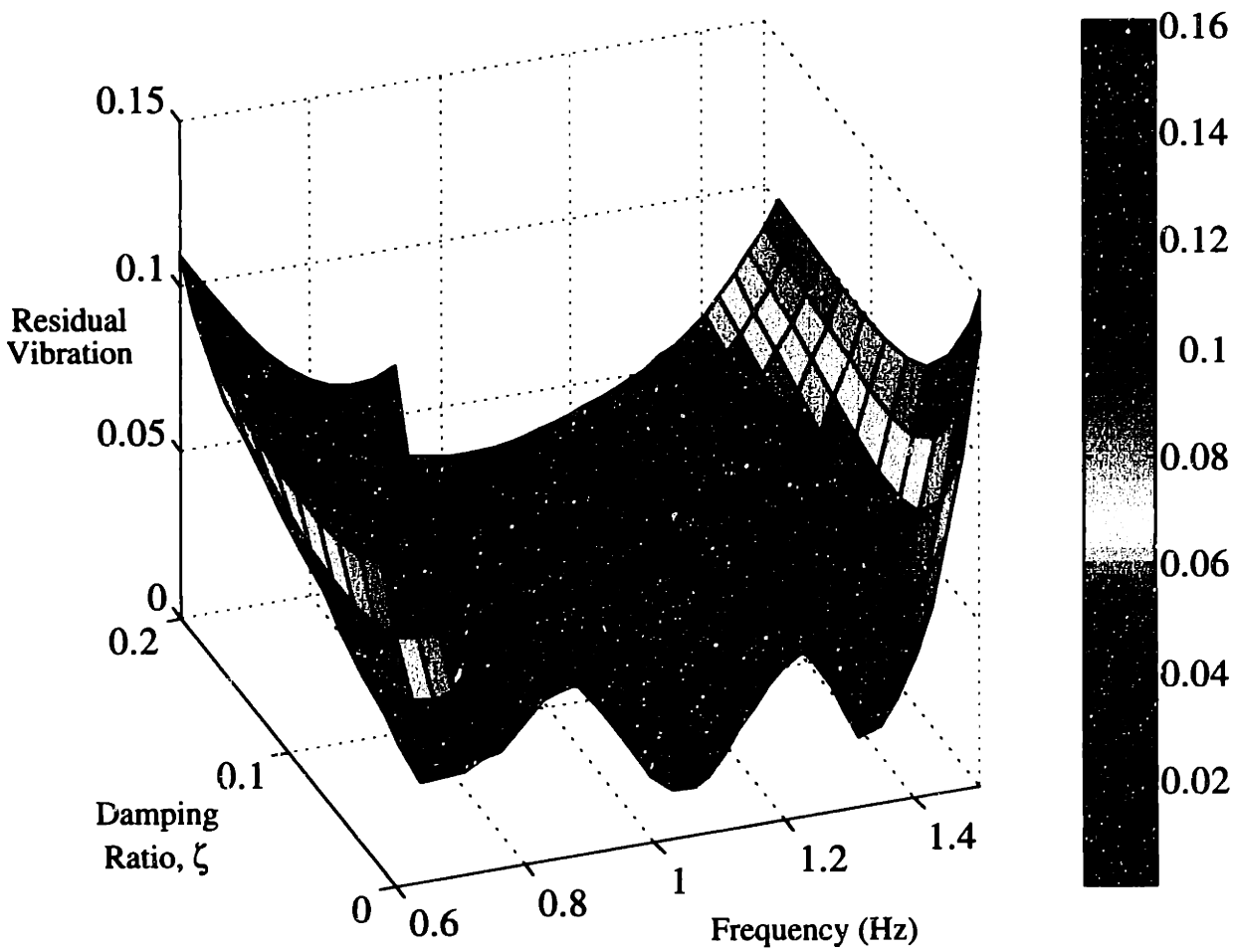

Figure 3.14: Three-Dimensional Sensitivity Curve of SI Shaper Designed with V_{tol} = 5%, I=0.6, and Suppressed Damping Range of $0 \leq \zeta \leq 0.2$.

3) Set the residual vibration to V_{tol} and the slope of the sensitivity curve to zero at the H unknown hump frequencies where the sensitivity curve reaches a local maximum.

4) Limit the residual vibration to zero at H+1 unknown frequencies. These frequencies must alternate between the edge and hump frequencies where the vibration is set to V_{tol}.

5) Solve the constraint equations generated by steps 1-4 combined with (3.3) and (3.4).

Steps 2-4 for generating constraint equations for the exact SI shaper with H = 2 and V_{tol} = 5% are shown graphically in Figure 3.15.

The first step in formulating the set of constraint equations is to determine the number of humps in the sensitivity curve. For a specific set of parameter values, V_{tol}, I and ζ, the number of humps can be determined by employing the following algorithm. Assume that H = 0 and solve the

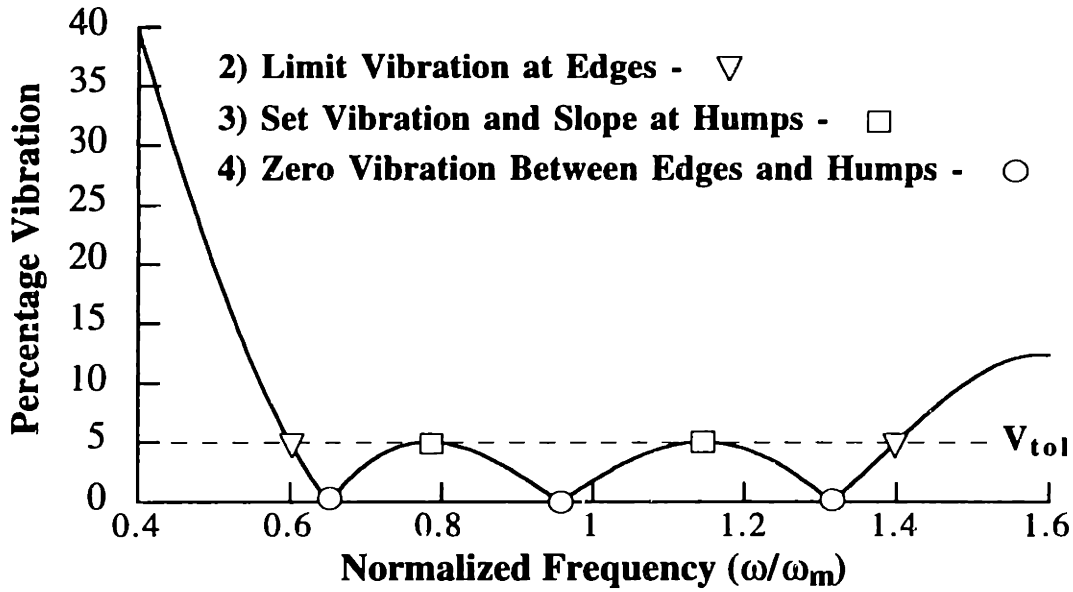

Figure 3.15: Constraint Generation for Exact SI Shaper When H=2 and V_{tol}=5%.

Table 3.2: H as a Function of I and ζ for V = 5%.

Value of Insensitivity, I	I<a	a≤I<b	b≤I<c	c≤I
Number of Humps, H	0	1	2	3
where,	$a=0.2218+0.3143\zeta+0.1819\zeta^2+0.4934\zeta^3$			
	$b=0.5916+0.7647\zeta+0.6000\zeta^2+0.3708\zeta^3$			
	$c=0.8737+1.0616\zeta-0.2847\zeta^2+3.2416\zeta^3$			

equations generated by steps 2-4. If the sensitivity curve remains below V_{tol} throughout the range specified by I, then H = 0. If the sensitivity curve exceeds V_{tol}, then resolve the equations using H = 1. The process is repeated until the minimum value of H that effectively limits the residual is obtained.

The value of H has been determined for a large set of V_{tol}, I, and ζ. The results can be condensed into a decision tree as shown in Table 3.2 for V_{tol} = 5%. To use Table 3.2, calculate a, b, and c using the system damping ratio. Then, select H from the column in which I satisfies the inequality relations. Table 3.2 can be used for insensitivities well into the three-hump region; however, the extremely large insensitivity of three-hump SI shapers is rarely needed on real mechanical systems.

Once the number of sensitivity curve humps has been determined, the constraint equations can be stated explicitly. For the second step, the two equations which limit the vibration at the edges of the sensitivity range are:

$$V_{tol} \geq e^{-\zeta\omega_e t_n}\sqrt{\left(C(\omega_e,\zeta)\right)^2+\left(S(\omega_e,\zeta)\right)^2} \qquad \omega_e=(1+I/2)\omega_m \tag{3.32}$$

where the C and S functions are given in (3.1a) and (3.1b).

The vibration is now set equal to V_{tol} and the slope of the sensitivity curve is set equal to zero at the peeks of each of the H humps of the sensitivity curve. These 2H equations are:

$$V_{tol} = e^{-\zeta\omega h_j t_n}\sqrt{\left(C(\omega h_j,\zeta)\right)^2 + \left(S(\omega h_j,\zeta)\right)^2} \qquad j = 1,\ldots,H \tag{3.33}$$

$$0 = \frac{d}{d\omega h_j}\left[e^{-\zeta\omega h_j t_n}\sqrt{\left(C(\omega h_j,\zeta)\right)^2 + \left(S(\omega h_j,\zeta)\right)^2}\right] \qquad j = 1,\ldots,H \tag{3.34}$$

where ωh_j are the unknown frequencies at which the peeks of the sensitivity curve humps occur.

Fourth, the sensitivity curve must be forced to zero between each hump of the sensitivity curve. This gives rise to H+1 equations given by:

$$0 = e^{-\zeta\omega z_k t_n}\sqrt{\left(C(\omega z_k,\zeta)\right)^2 + \left(S(\omega z_k,\zeta)\right)^2} \qquad k = 1,\ldots,H+1 \tag{3.35}$$

where ωz_k are unknown frequencies that interlace the edge and hump frequencies. That is, $(1-I/2)\omega < \omega z_1 < \omega h_1 < \omega z_2 < \cdots$.

Finally, the above constraints, (3.32)-(3.35), are numerically solved along with (3.3) and (3.4). When the optimization is performed, the unknown frequencies, as well as the impulse amplitudes and time locations are obtained.

The above procedure will generate an exact solution over a large range of damping ratios and insensitivities. However, a problem arises when both I and ζ have large values. Generating a shaper with a large I requires forcing the sensitivity curve to alternate several times between 0 and V_{tol}. See again Figure 3.13. While this is not a problem for low values of ζ, it is impossible for large values of ζ. The function describing the ζ, I space which permits a solution is complicated and is not given here. If the problem is posed with an untenable set of parameters, then the optimization simply fails to find a solution. In these cases, the technique of parameter sampling can still be used to generate an approximate solution. This is done by generating MxN constraint equations from (3.31). Each equation is applied at a different set of parameter values (ω_m, ζ_n). As a general rule, if $\zeta < 0.2$, then a solution is possible with the exact procedure for almost any realistic value of I.

3.3.3 Characteristics of the SI Shaper

There are several interesting properties of the SI shaper. Figure 3.16 shows the duration of the undamped SI shaper as a function of the frequency insensitivity, I. The length of the shaper and, therefore, the rise time increase with I. The length does not steadily increase, rather there are locations where the slope changes rapidly. It turns out that these points correspond to shapers previously presented in the literature and in this thesis. The first node, at approximately I = 0.06,

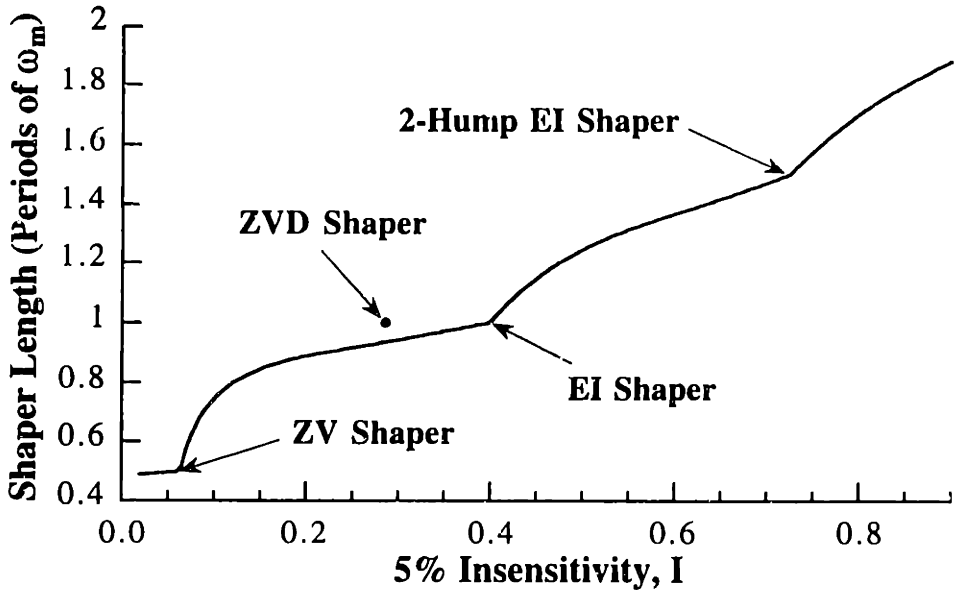

Figure 3.16: Length of Undamped SI Shaper as a Function of Insensitivity.

corresponds to the ZV shaper; the second node at approximately I = 0.4 corresponds to the EI shaper, and the third node at approximately I = 0.72 corresponds to the two-hump EI shaper developed in the previous section. The ZVD shaper does not correspond to any SI shaper; it does not maximize insensitivity for its length.

Figure 3.17 shows the amplitude of the first shaper impulse as a function of I and ζ for V_{tol} = 5%. Solutions are shown for $0 \le \zeta \le 0.3$. Each dot represents a solution obtained with the above procedure. The figure is divided into 0, 1, and 2-hump regions by thick lines. Thin lines further divide the data into regions where A_1 remains constant or changes as I varies. If I is held constant and ζ is increased, then A_1 increases. On the other hand, if ζ is held constant and I is varied, A_1 changes in a complicated manner. For low values of I, A_1 is equal to the first impulse of a ZV shaper. As I is increased, A_1 decreases in amplitude until it reaches the value of the first impulse of a single-hump EI shaper. A_1 remains constant at this value over a large range of I. With further increases, A_1 transforms into the value corresponding to a two-hump EI shaper. Similar trends occur in the values of the other SI shaper impulses.

When given the task of designing an input shaper, a controls engineer will be faced with the trade-off of robustness versus rise time (shaper length). Figure 3.16 provides important information because the time cost of obtaining a desired level of robustness is immediately available. However, it is unlikely that an extremely specific value of robustness will be required, rather an acceptable range, say $0.4 \le I \le 0.5$, would be under consideration. The question then arises as to which value of I should be chosen for the design of the shaper. If I = 0.4 is chosen, the shaper will have a length of T, where T is the period of vibration being targeted. If I = 0.5 is

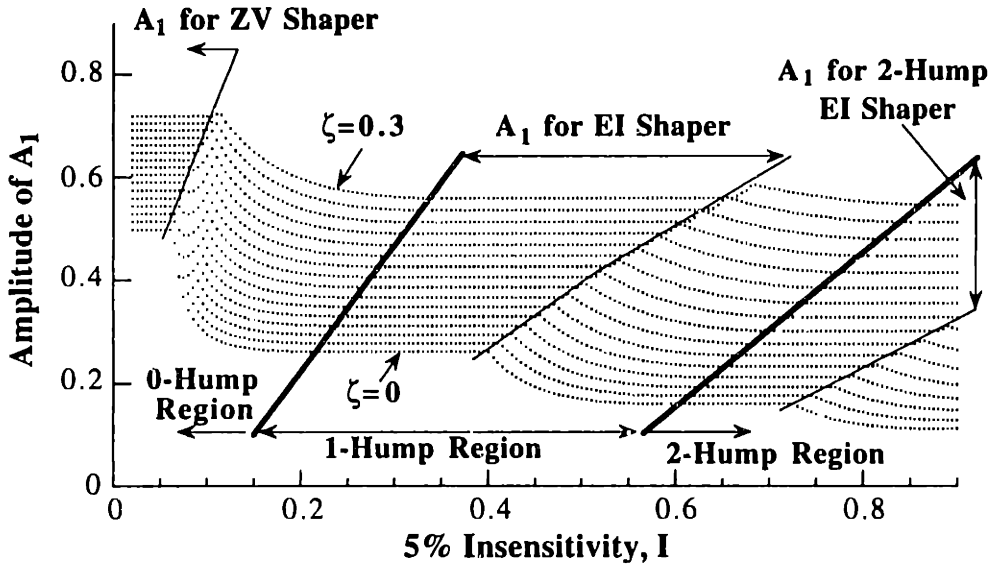

Figure 3.17: Amplitude of A_1 for the SI Shaper as a Function of I and ζ.

chosen, the insensitivity increases 25%, but the length of the shaper increases to about 1.25T.

The optimal value of I will depend on several factors including the relative importance of rise time and robustness. To aid in this decision, we can calculate the ratio of insensitivity to shaper length. Figure 3.18 shows the ratio of (5% insensitivity)/(shaper length) as a function of I. The points at which the SI shaper equal the ZV, EI, and two-hump EI shapers are local maximum points. This result indicates that if the desired insensitivity range includes one of these points, then those shapers are good choices.

3.3.5 Application to a Linear System with Uncertain Parameters

To demonstrate the utility of the SI shapers, simulations of the benchmark two-mass, spring system were performed. When the system parameters are all equal to one ($m_1 = m_2 = k = 1$), the system has a natural frequency of 0.2251 Hz ($\sqrt{2}$ rad). A bang-bang command will move the mass center in a time-optimal manner, but large residual oscillations will usually occur. By shaping the bang-bang command, rapid motion can be attained without residual vibration. Suppose that there is a large uncertainty in the spring constant, say k is between 0.5 and 1.7. This range of k corresponds to a frequency range of approximately ±30% from the nominal value. To accommodate this range of possible spring constants, the insensitivity of the input shaper must be 0.6. The SI shaper with I = 0.6 and V_{tol} = 5% centered about 0.2251 Hz is:

$$\begin{bmatrix} A_i \\ t_i \end{bmatrix} = \begin{bmatrix} 0.1598 & 0.3402 & 0.3402 & 0.1598 \\ 0 & 2.0238 & 4.0476 & 6.0715 \end{bmatrix} \tag{3.36}$$

Figure 3.19 shows the response of the system to a unity-magnitude bang-bang input when k varies from 0.5 to 1. These responses are labeled with the prefix BB and marked with open

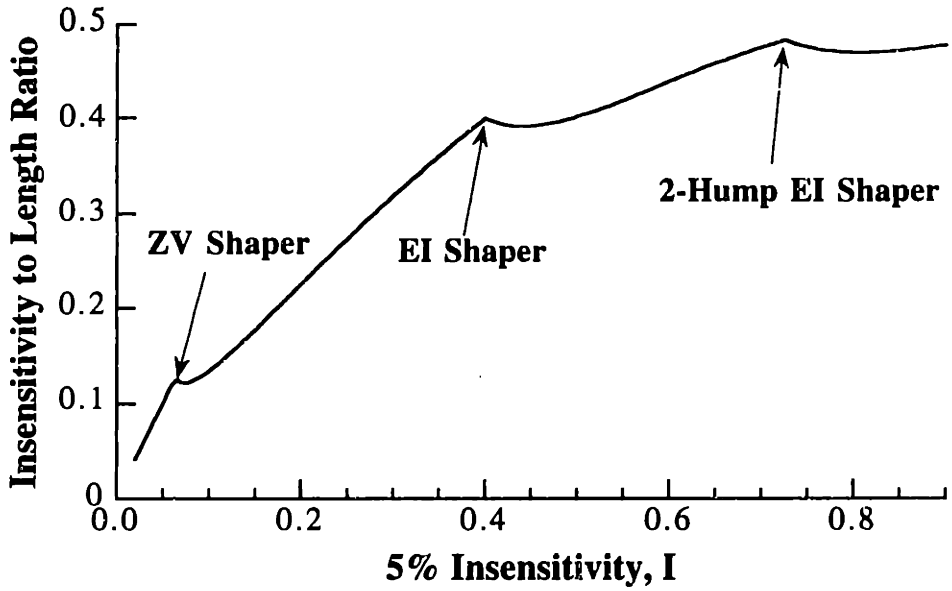

Figure 3.18: Insensitivity to Shaper Length Ratio [I/(Periods of ω_m)].

circles. Significant residual vibration exists for all cases. Also shown in Figure 3.19 are the responses when the bang-bang input is shaped with the SI shaper. Note that over this large range of parameter values, the shaped residual vibration always remains small. If the shaped vibration amplitude is divided by the unshaped vibration, then the resulting percentage vibration is less than 5% for each of the cases shown. The responses for values of k from 1 to 1.7 show similar results.

3.3.6 Application to a Nonlinear System

Certain types of nonlinear systems change dynamic characteristics when they change configuration. An example of such a system is a two-link flexible robotic arm like the one sketched in Figure 3.20. A spring and damper at both the shoulder and elbow model PD controllers at those joints. By varying the system parameters, the range of frequencies that the system exhibits can be set. Note that this system is nonlinear and the input shaping procedure described above does not strictly apply. That is, an SI shaper designed to limit vibration over the frequency range of the system may not keep the vibration to below V_{tol} for every type of motion. However, given the robustness of the shaping algorithm to modeling errors, it seems reasonable to implement shaping on this system in much the same manner that it is implemented on a linear system with uncertain parameters.

Here a case is considered when the system has a first natural frequency of 3 Hz with the arm fully extended ($\theta_2 = 0°$), and a first natural frequency of 4.5 Hz with the arm fully bent back on itself ($\theta_2 = 180°$). The system varies ±20% from the average frequency of 3.75 Hz. To simplify the example, the contribution of the second mode is severely limited by setting the spring and

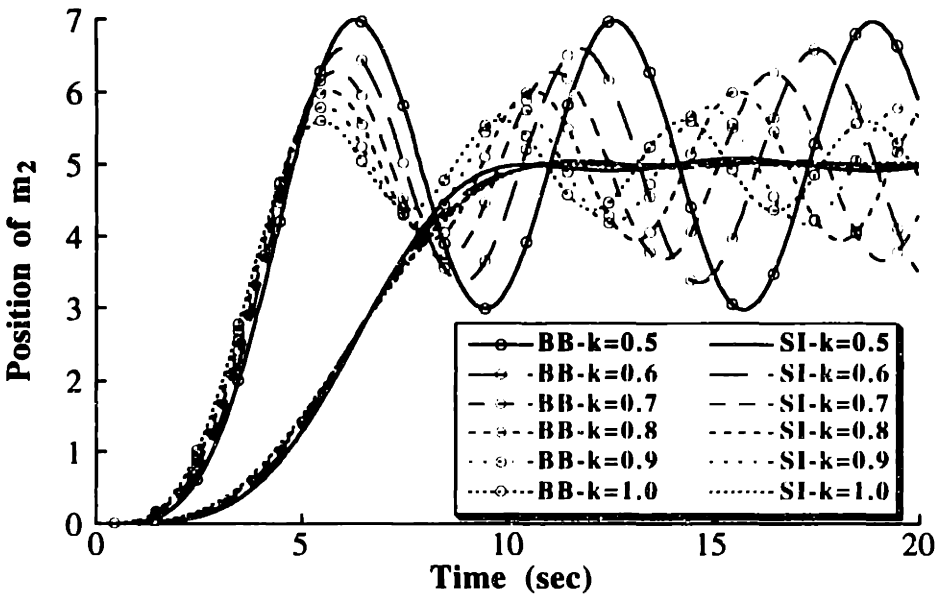

Figure 3.19: Response to Unshaped and SI Shaped Bang-Bang Inputs.

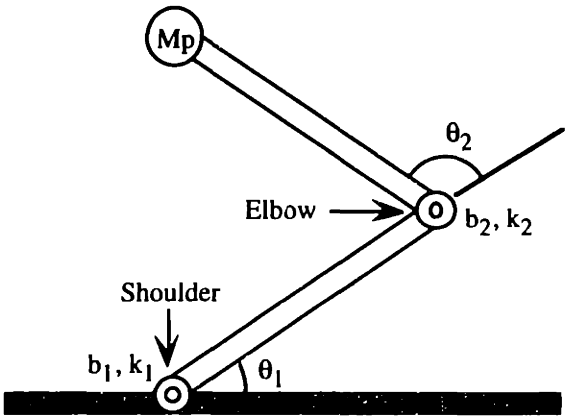

Figure 3.20: Nonlinear Two-Link Arm.

damper at the elbow to high values so that the shoulder dynamics dominate the response. The shaper used for this system is an SI shaper with I = 0.4 and V_{tol} = 5% designed for 3.75 Hz:

$$\begin{bmatrix} A_i \\ t_i \end{bmatrix} = \begin{bmatrix} 0.2625 & 0.475 & 0.2625 \\ 0 & 0.1333 & 0.2667 \end{bmatrix} \tag{3.37}$$

There are a great variety of possible motions that the system can perform. A representative set of results will be presented here. Figure 3.21 shows the shaped and unshaped responses of the shoulder joint (θ_1) when the arm is moved from an initial state of $\theta_2 = 90°$ to a final state of $\theta_2 = 180°$. Even though the system rapidly changes frequency by 20% during the motion, the input shaping reduces the vibration to only 7.8% of the unshaped vibration amplitude for the same motion. Although this exceeds the 5% level for which the shaper was designed, the shaping is still

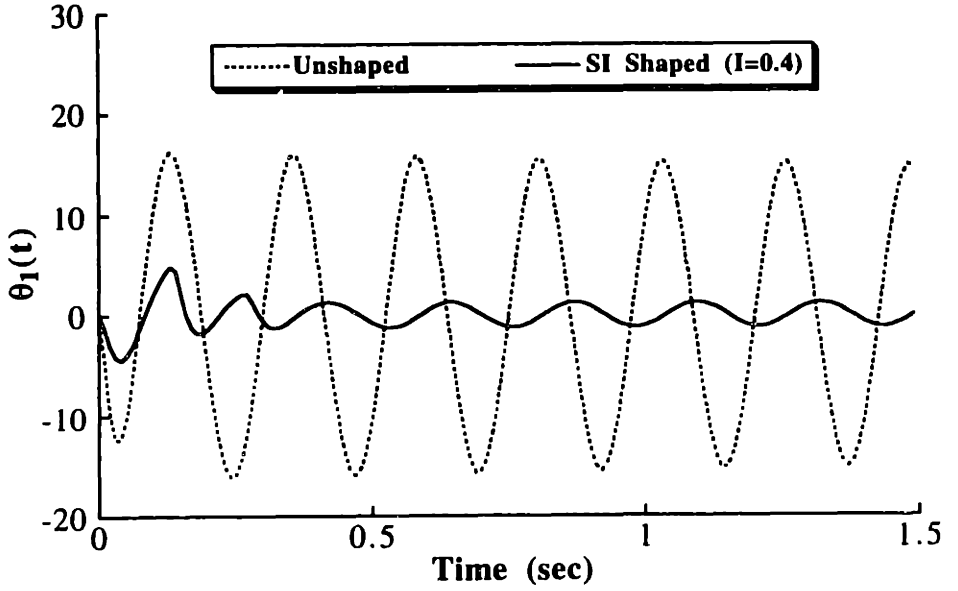

Figure 3.21: Response of Two-Link Arm When θ_2 is Changed from 90° to 180°.

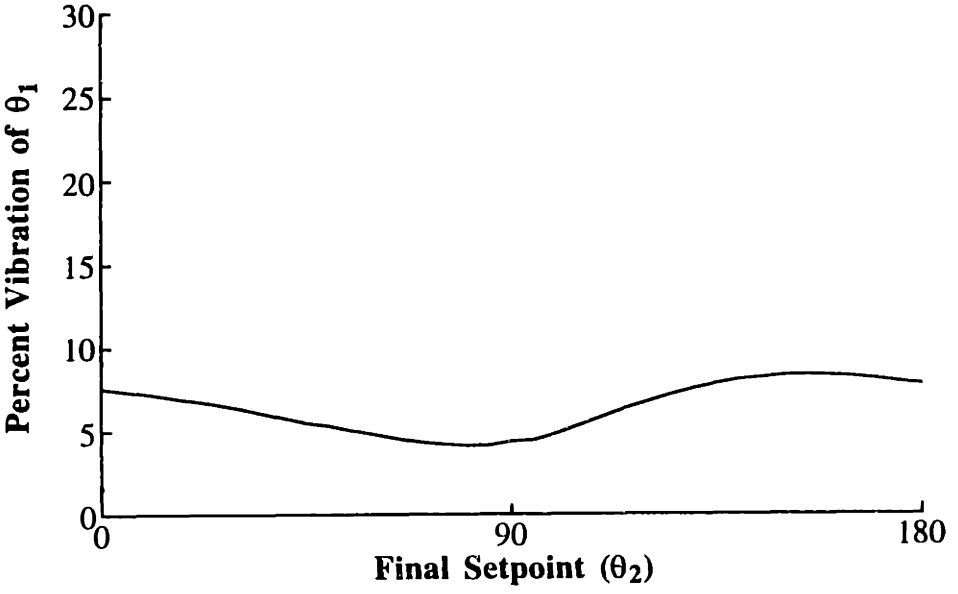

Figure 3.22: Residual Vibration When System Starts at θ_2=90° and Moves to Various Final Setpoints.

very effective. Figure 3.22 shows the percentage vibration for motions starting at $\theta_2 = 90°$ and ending at a range of final angles. The residual vibration is lowest for motions which terminate near 90° because the system does not change frequency significantly during the motion. However, the vibration is very low even for motions which terminate at the edges of the workspace.

3.3.7 Discussion of SI Shapers

In this section procedures were presented that produce input shapers with a specified level of

robustness to modeling errors. One procedure is easy to formulate, but can lead to a large number of constraint equations which must be satisfied numerically. Furthermore, only approximate solutions can be obtained. The other procedure yields exact solutions with very few constraint equations, but it is somewhat more difficult to formulate and does not yield a solution for all parameter values. Characteristics of the shaping method demonstrate a nonlinear relation between robustness and rise time. For certain degrees of robustness, the procedure produces previously reported input shapers. Simulations of a linear system with uncertain parameters and a nonlinear two-link arm demonstrated the effectiveness of the proposed shaping algorithm.

3.4 Multi-Mode Input Shapers

The methods described in the previous sections can be applied to multi-mode systems. The design of input shapers for multi-mode systems can proceed in two ways. Shapers for each mode can be calculated separately and then convolved together,[10] or the constraint equations for each mode can be solved simultaneously [42, 87, 110]. The next subsection of this thesis will briefly review the technique of convolving single-mode input shapers together to obtain two-mode shapers. Then, two-mode shapers will be designed by solving the constraint equations simultaneously for both modes. New techniques are presented that allow the calculation of simultaneous, or direct, input shapers over a large range of frequency ratios. The properties of the convolved and direct shapers are compared and simulation results are used to illustrate the trade-offs between convolved and direct shapers.

3.4.1 Convolved Two-Mode Shapers

The simplest way to obtain a two-mode shaper is to convolve two single-mode shapers together. The single-mode shapers are obtained using the methods of the previous sections, or the formulas available in the references. For example, suppose a system has undamped modes at 1 Hz and 2.5 Hz, then ZVD shapers for each mode can be obtained as [101]:

$$\begin{bmatrix} A_i \\ t_i \end{bmatrix} = \begin{bmatrix} 0.25 & 0.5 & 0.25 \\ 0 & 0.5 & 1.0 \end{bmatrix} \text{ (1 Hz Shaper)} \tag{3.38}$$

$$\begin{bmatrix} A_i \\ t_i \end{bmatrix} = \begin{bmatrix} 0.25 & 0.5 & 0.25 \\ 0 & 0.2 & 0.4 \end{bmatrix} \text{ (2.5 Hz Shaper)} \tag{3.39}$$

When describing a two-mode shaper, the constraints used to eliminate each mode will be stated explicitly. For example, if ZVD constraints are used for the first mode and ZV constraints are used for the second mode, then the result is called a ZVD-ZV shaper.

Convolving the shapers given in (3.38) and (3.39), generates a ZVD-ZVD shaper described by:

$$\begin{bmatrix} A_i \\ t_i \end{bmatrix} = \begin{bmatrix} 0.0625 & 0.125 & 0.0625 & 0.125 & 0.25 & 0.125 & 0.0625 & 0.125 & 0.0625 \\ 0 & 0.2 & 0.4 & 0.5 & 0.7 & 0.9 & 1.0 & 1.2 & 1.4 \end{bmatrix} \tag{3.40}$$

The sensitivity curves for the single-mode shapers and the convolved two-mode shaper are shown in Figure 3.23. The convolved shaper is very robust to modeling errors of the 2.5 Hz mode. The second mode can range between 2.0 Hz and 3.5 Hz and the residual vibration will remain small. Note that the vibration suppression of the convolved two-mode shaper near 3 Hz is due to the contribution from the 1 Hz shaper. Single-mode shapers suppress vibration at odd multiples of their design frequency. When an input shaper is convolved with a second shaper, the vibration suppression properties at these higher frequencies is passed on to the resulting two-mode shaper.

[10] This procedure dates back to the work of O.J.M. Smith [141].

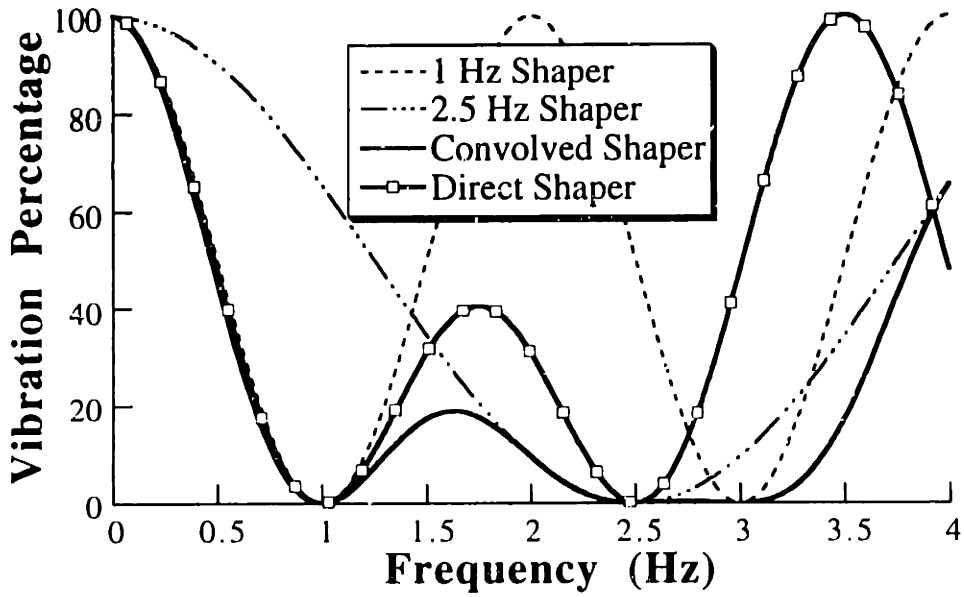

Figure 3.23: Convolved and Direct Two-Mode ZVD-ZVD Shapers for 1 Hz and 2.5 Hz.

3.4.2 Simultaneous Two-Mode Shapers

Unlike the convolved shapers, where constraints on each mode are solved separately, the direct solution is obtained by simultaneously solving the constraint equations for both modes. The vibration and robustness constraints that must be solved for a direct ZVD-ZVD shaper are [42]:

$$\begin{aligned} &\Sigma_{i=1}^{n} A_i e^{-\zeta_j \omega_j t_i} \sin(t_i \omega_j \sqrt{1-\zeta_j^2}) = 0 \qquad j = 1,2 \\ &\Sigma_{i=1}^{n} A_i e^{-\zeta_j \omega_j t_i} \cos(t_i \omega_j \sqrt{1-\zeta_j^2}) = 0 \qquad j = 1,2 \end{aligned} \tag{3.41}$$

$$\begin{aligned} &\Sigma_{i=1}^{n} A_i t_i e^{-\zeta_j \omega_j t_i} \sin(t_i \omega_j \sqrt{1-\zeta_j^2}) = 0 \qquad j = 1,2 \\ &\Sigma_{i=1}^{n} A_i t_i e^{-\zeta_j \omega_j t_i} \cos(t_i \omega_j \sqrt{1-\zeta_j^2}) = 0 \qquad j = 1,2 \end{aligned} \tag{3.42}$$

In this section, the impulses will again be required to have positive amplitudes.

Rappole obtained a closed-form description of the ZV-ZV and ZVD-ZVD direct shapers for undamped modes by assuming the shapers contain three and five impulses, respectively [87]. Unfortunately, these assumptions on the number of impulses only yield time-optimal shapers for mode ratios, $R = (\omega_2/\omega_1)$, up to three. For larger mode ratios the time-optimal direct solution contains more than the assumed number of impulses.

An obvious drawback to the direct approach of solving the constraint equations simultaneously is that it is not as easy as convolving two single-mode shapers. In general, the shapers must be obtained using an optimization program. The shapers presented here were obtained using the General Algebraic Modeling System (GAMS), a comprehensive optimization program [20]. In

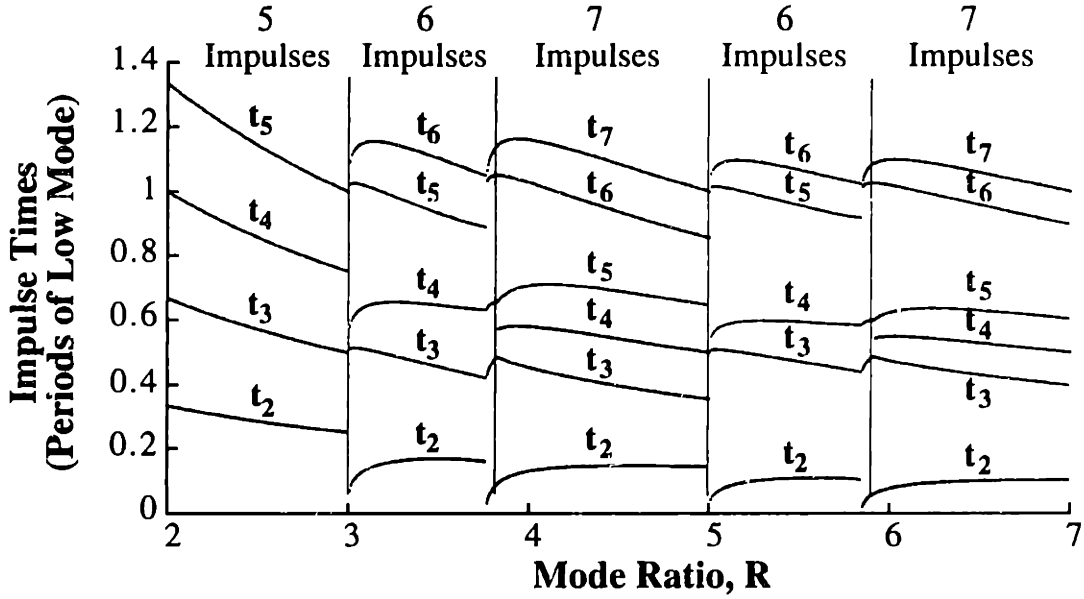

Figure 3.24: Direct ZVD-ZVD Shaper Impulse Times.

spite of this drawback, there are several advantages to the direct solution that will be demonstrated in the next section.

Returning to the example system with two undamped modes at 1 Hz and 2.5 Hz, the direct ZVD-ZVD shaper is:

$$\begin{bmatrix} A_i \\ t_i \end{bmatrix} = \begin{bmatrix} 0.1673 & 0.1489 & 0.3677 & 0.1489 & 0.1673 \\ 0 & 0.2857 & 0.5714 & 0.8571 & 1.1429 \end{bmatrix} \tag{3.43}$$

A comparison of the sensitivity curve for the direct solution of (3.43) with the sensitivity curve for the convolved solution of (3.40) is shown in Figure 3.23. Although the robustness to errors in the low mode (1 Hz) are approximately the same, the convolved shaper is much more robust to modeling errors in the second mode (2.5 Hz). A comparison of the impulse times shows that the direct solution has four fewer impulses and is 18.4% shorter in duration.

To fully appreciate the direct shapers, they must be examined as a function of the mode ratio. Figure 3.24 shows the times for each of the impulses in the direct two-mode ZVD-ZVD shaper as a function of the mode ratio. For mode ratios from 1 to 3, the results match the closed-form two-mode shapers presented previously [87]. But, for mode ratios above 3, the curves become more complex. The direct shaper contains 5 impulses for mode ratios up to 3, but then it alternates between 6 and 7 impulses in a fairly regular pattern.

The solution for the two-mode EI-EI shaper presents a challenge because of conflicting constraint equations. To illustrate the problem, consider a shaper designed for modes at 1 Hz and 2.9 Hz. The EI constraints for the low mode require a value of V and a slope of zero at 1 Hz. Furthermore, the sensitivity curve is forced to zero at frequencies on either side of 1 Hz. This

pattern repeats at all odd multiples of the low mode. That is, the vibration is equal to V at 3 Hz, 5 Hz, etc. and the curve goes to zero on either side of 3 Hz, 5 Hz, etc. Now assume that the zero vibration frequencies near the 3 Hz mode that arise from the constraints on the 1 Hz mode occur at 2.9 Hz and 3.1 Hz. The EI constraints associated with the second mode at 2.9 Hz require that the residual vibration be equal to V at 2.9 Hz. The optimization is now posed with two conflicting constraints, set the value of the residual vibration equal to both zero and V at 2.9 Hz.

In order to derive a consistent and well defined solution for a direct two-mode shaper that is analogous to the single-mode EI shaper, the process must be modified to eliminate conflicting constraints. A solution that produces consistently good results is a shaper with EI constraints for the low mode and specified insensitivity (SI) constraints for the high mode [26, 137]. The shaper designed by using EI constraints for the low mode and SI constraints for the high mode is referred to as an EI-SI shaper.

Unlike either the direct ZV-ZV or ZVD-ZVD shapers, the EI-SI shaper has a specified robustness at the high mode which can be set arbitrarily wide. The trade-off is that increased robustness at the second mode increases the shaper duration. So, in contrast to the other simultaneous shapers whose robustness at the second mode and duration are a function of the mode ratio, the robustness at the high mode of the EI-SI shaper is always greater than or equal to the desired amount and the shaper duration is dependent on both the mode ratio and the specified insensitivity.

3.4.3 Comparison of Two-Mode Input Shaper Properties

3.4.3a Shaper Length

The shaper duration is important because it limits the system rise-time; an increase in shaper length degrades rise-time. For the single-mode case, the ZVD and EI shapers have equal length and are twice as long as the ZV shaper. For the two-mode convolved case the total time delay is equal to the sum of the two shaper lengths. A convolved two-mode ZVD or EI shaper will have a length of:

$$T_n = T_{\omega_1} + T_{\omega_2} \tag{3.44}$$

where T_{ω_i} is the period of the i^{th} mode. A convolved shaper is a poor choice for low mode ratio systems because $T_n \approx 2T_{\omega_1}$. Direct shapers do not follow the relation in (3.44); t_n is always less than $T_{\omega_1} + T_{\omega_2}$.

Figure 3.25 compares the time duration of the convolved and direct two-mode ZVD-ZVD shapers as a function of mode ratio. Also shown is the duration of the V = 5% direct EI-SI shaper with vibration suppression enforced ±10% about the second mode. The direct ZVD-ZVD has a maximum time savings of 25% over the convolved ZVD-ZVD shaper, and the average savings is

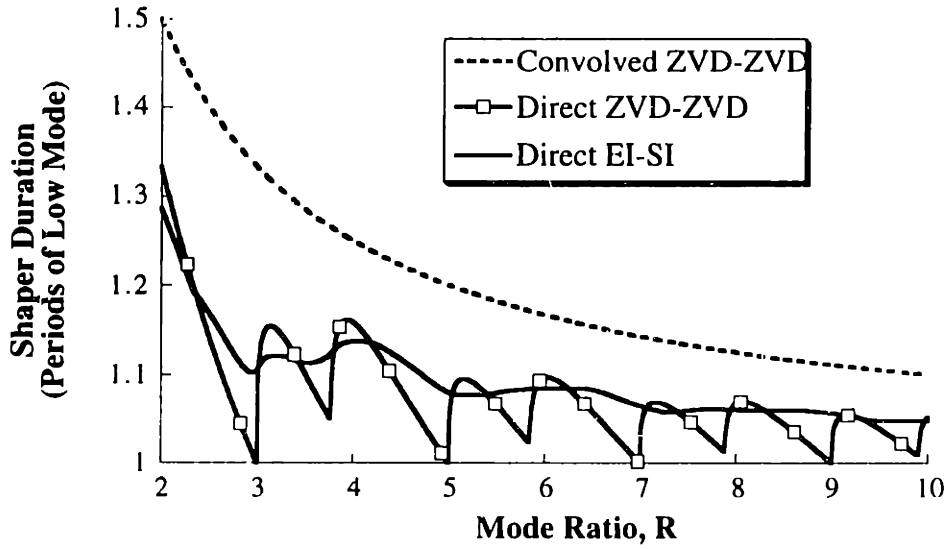

Figure 3.25: Duration of Convolved and Direct Shapers.

10% for the range shown in the figure. The maximum time savings with the EI-SI shaper is about 20% and average is about 10%. As the mode ratio increases, the major gain of implementing the direct shapers, the shorter time duration, becomes less significant and the convolved shapers become a more attractive alternative.

3.4.3b Robustness to Modeling Errors

The sensitivity curves of the two-mode shapers near the low mode are nearly identical for all values of R. That is, the robustness to low mode errors is not greatly effected by the mode ratio. On the other hand, Figure 3.26 shows that the second-mode insensitivity of the convolved ZV-ZV, ZVD-ZVD, and EI-EI shapers vary considerably with R. The convolved EI-EI shaper is more robust than the ZVD-ZVD shaper for all mode ratios. Furthermore, the EI-EI shaper averages 4.4 times the insensitivity of the ZV-ZV shaper.

Figure 3.27 shows the second-mode insensitivity of the direct shapers. The EI-SI shaper was designed using a suppressed frequency range of ±10% of the high mode (specified insensitivity = 0.2). Note that although the constraints require the second-mode insensitivity to be at least 0.2, it can be much larger. The reason for this is that the constraints which suppress the low mode also cause vibration to be suppressed at odd multiples of the low frequency, regardless of additional constraints placed on higher modes.

To demonstrate this effect, the sensitivity curve for the EI-SI shaper designed for 1Hz and 10 Hz is shown in Figure 3.28. The constraints suppressing 1 Hz lead to suppression of 9 Hz and 11 Hz. The 9 and 11 Hz suppression merges with the SI constraints which limit 10 Hz. This combination leads to an insensitivity about 10 Hz that exceeds the minimum required value of 0.2.

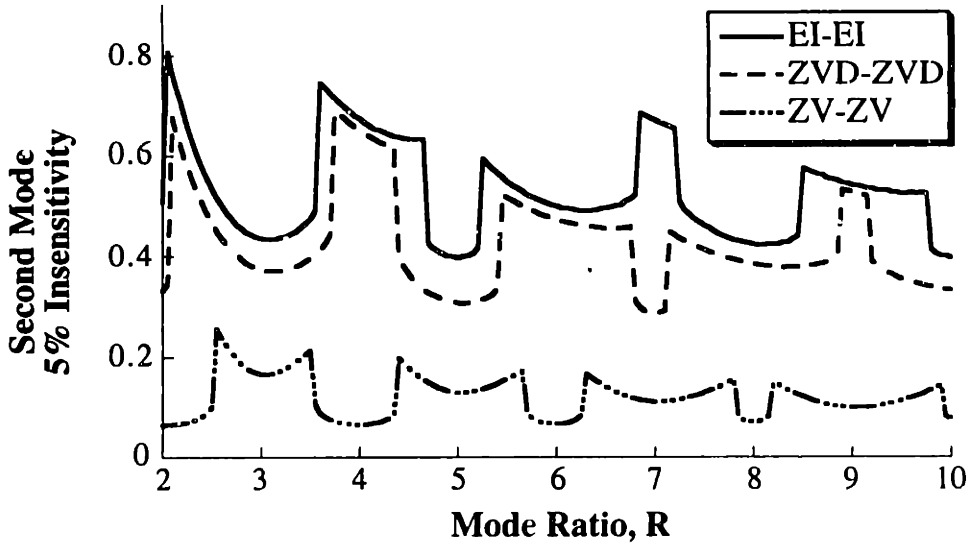

Figure 3.26: Insensitivity of Convolved Shapers.

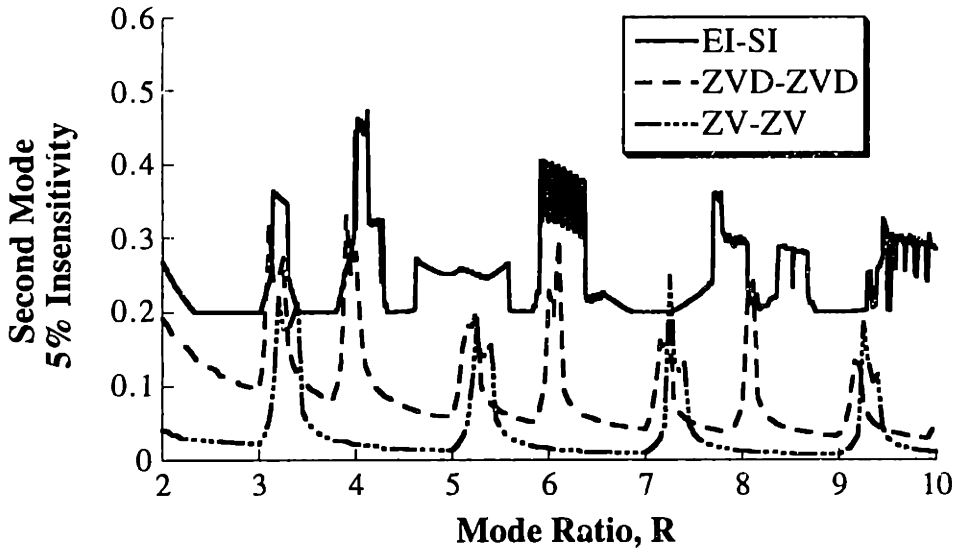

Figure 3.27: Insensitivity of Direct Shapers.

The second-mode robustness obtained with the direct EI-SI shaper greatly exceeds the robustness of the ZVD-ZVD shaper which, in turn, is far superior to the performance of the ZV-ZV shaper. Comparing Figures 3.26 and 3.27 we see that the convolved shapers are more robust than the direct shapers for almost all mode ratios.

Traditionally, insensitivity has been defined as the total width of the sensitivity curve that lies below a specified vibration level. However, this description fails to capture important information in the two-mode case because the sensitivity curves can be highly skewed. (See again Figure 3.23.) To more accurately describe the robustness of the shapers, the total insensitivity can be redefined as the sum of its high and low components, which are the insensitivity to modeling

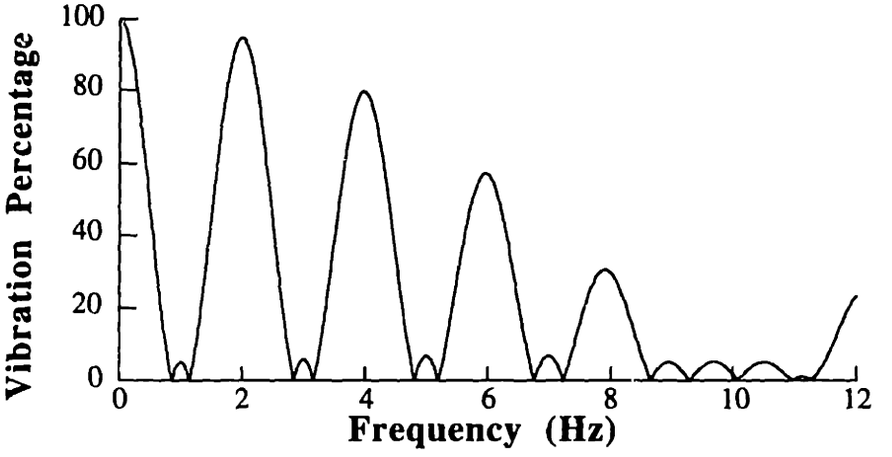

Figure 3.28: Sensitivity Curve for the Direct EI-SI Designed for 1 Hz and 10 Hz.

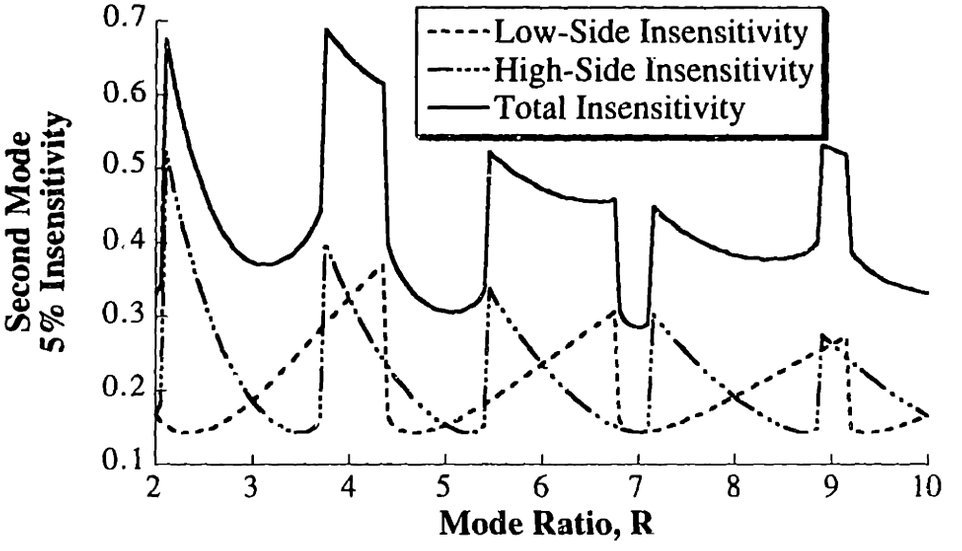

Figure 3.29: Two-Mode Convolved ZVD-ZVD Second-Mode Insensitivity.

errors above and below the modeling frequency [26]. The individual components and total insensitivity of the convolved ZVD-ZVD shaper are shown in Figure 3.29. Although the total insensitivity is large at all mode ratios, the insensitivity is skewed (the high and low insensitivities are vastly different). On the contrary, the high and low insensitivities of the direct shapers are nearly symmetric about the modeling frequency. (See Figures 3.23 and 3.28.)

3.4.3c Computational Intensity During Implementation

The convolution method yields shapers that contain more impulses than those derived using the direct method. Convolved ZVD-ZVD and EI-EI shapers have 9 impulses, while the corresponding direct shapers have between 5 and 7 impulses. This result makes the direct method somewhat more attractive in terms of computational burden during the implementation of the shaping process.

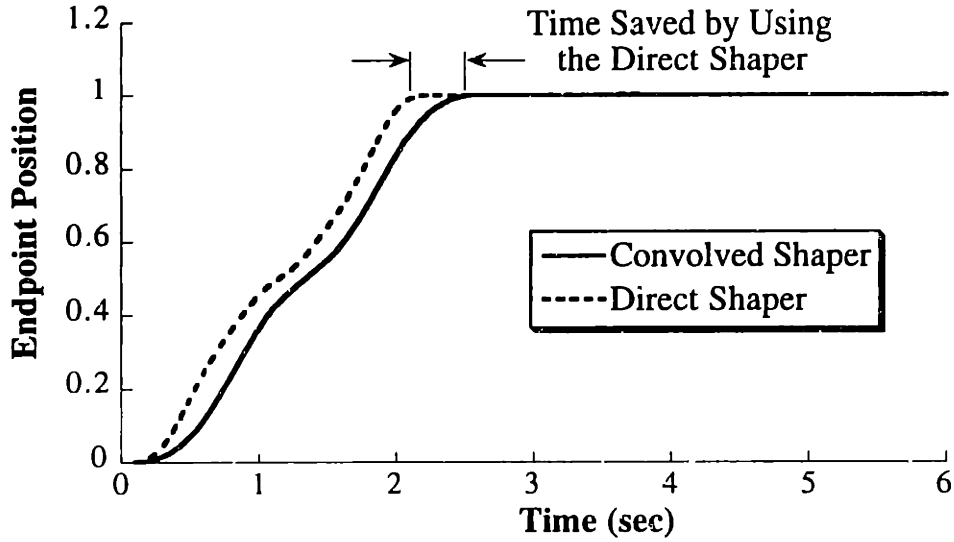

Figure 3.30: Shaped Responses When Model is Exact.

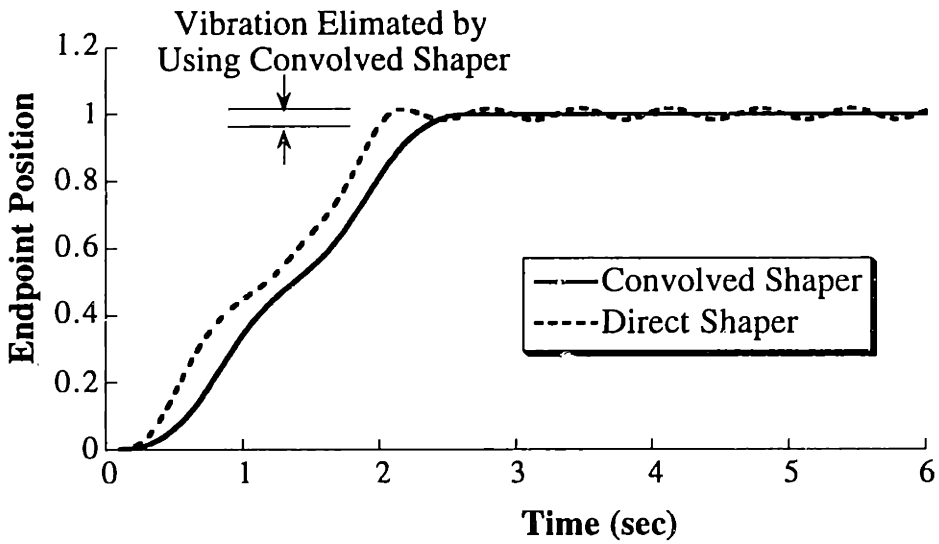

Figure 3.31: Responses with a 10% Frequency Error.

3.4.4 Simulation Results

To demonstrate the key trade-off between convolved and direct shapers, simulations of an undamped two-mode mass-spring system were performed. The system frequencies where set to 1 Hz and 2.5 Hz, giving a mode ratio of 2.5. The system was driven by a step input shaped by either a convolved or a direct ZVD-ZVD shaper. Both shapers completely eliminate the vibration when the system model is exact, but the direct shaper has a faster rise time as shown in Figure 3.30. Figure 3.31 shows the responses with a 10% error in the second mode frequency. The convolved shaper eliminates more of the vibration when there is a modeling error. This is a demonstration of the difference in robustness that was displayed in Figures 3.26 and 3.27.

3.4.5 Summary of Multi-Mode Shapers

This comparison of two-mode input shapers reveals that convolved shapers have greater robustness to second-mode modeling errors, while the direct shapers have a shorter time duration and fewer impulses. To fully measure the robustness of two-mode shapers, high and low side insensitivities should be calculated. Direct shapers have insensitivity that is nearly symmetrical about the modeling frequency. The time advantage obtained with the direct shapers decreases as the mode ratio increases. Finally, second-mode robustness of the direct ZV-ZV and ZVD-ZVD shapers varies greatly with the mode ratio and can be very poor. This problem can be eliminated by using an EI-SI shaper which specifies a minimum level of second-mode robustness.

3.5 Negative Input Shapers

In the previous sections the constraint equations used to determine the input shapers required positive values for the impulse amplitudes. However, move time can be significantly reduced by allowing the shaper to contain negative impulses. This idea first appears in the work by O.J.M. Smith [140, 141, 144]. He suggested a method that broke a step input into three separate steps., the second of which was negative. He then increased the magnitude of the first two steps until the actuator limit was reached. (The amplitude of the final step was determined by the desired setpoint location.) Certain types of negative shapers have been shown to yield the time-optimal commands for linear flexible systems [80]. However, these types of negative shapers cannot be used with arbitrary commands; they must be used with step inputs. Furthermore, the shaper's impulse amplitudes and time locations depend on the desired motion. These types of shapers will be addressed in Chapter 4.

Unlike shapers containing only positive impulses, negative shapers can lead to shaped command profiles whose magnitude exceeds that of the unshaped command for small periods of time. These periods of overcurrenting are not a problem for most applications because amplifiers and motors have peak current capabilities much larger than allowable steady state levels. Another potential drawback with negative input shapers is that they can excite unmodeled high modes [75, 86, 129].

Several researchers have formulated input shaping as a zero-placement algorithm that can give rise to negative shapers [46, 58, 94, 153]. Because negative shapers pose the two difficulties mentioned above, the papers describing zero-placement algorithms have usually included a procedure for eliminating the negative impulses. Recall that the method proposed by Tuttle [153] for eliminating negative impulses was demonstrated in Chapter 2. The negative shapers obtained with zero-placement are not usually time-optimal. That is, there exists negative input shapers with shorter durations that satisfy the same performance specifications. The first paper dedicated to the subject of time-optimal negative input shapers required the numerical solution of a set of simultaneous transcendental equations [86].

This section presents a look-up method that generates time-optimal negative input shapers without solving a set of complicated equations. Additionally, solutions are presented that deal with the problems of actuator overcurrenting and high-mode excitation that can occur with negative shapers. Experimental results demonstrate both the versatility and utility of negative shapers.

3.5.1 Unity-Magnitude (UM) Constraint

If the requirement of positive impulse amplitudes is eliminated, then an alternate constraint must be used to keep the impulse amplitudes from going to positive and negative infinity. Two such

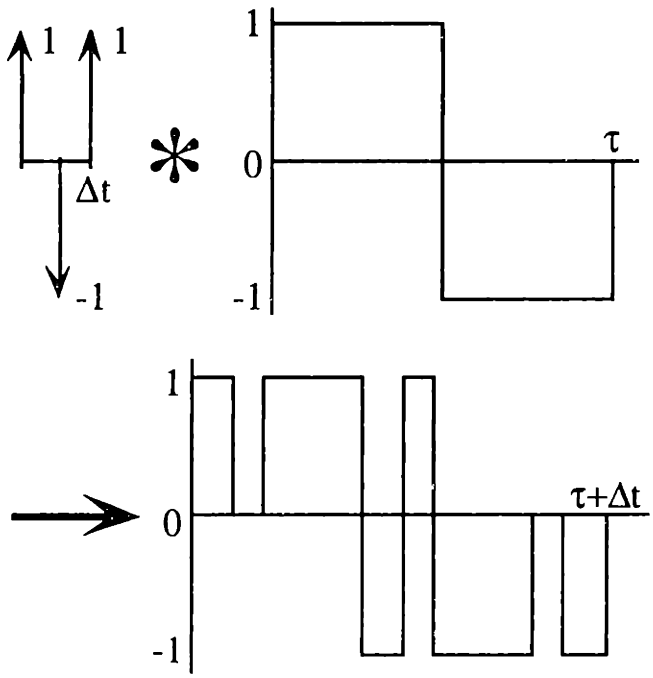

Figure 3.32: Shaping a Bang-Bang Input with a Negative UM-ZV Shaper.

types of constraints will be discussed in this section. The first constraint which limits the impulse magnitudes requires that the impulses have unity magnitude, that is, the amplitudes must switch between 1 and -1:

$$A_i = (-1)^{i+1} \qquad i = 1,\ldots,n \tag{3.45}$$

This constraint yields useful shapers because they can be used with a wide variety of inputs without leading to overcurrenting. For example, if a unity magnitude (UM) negative shaper is used to shape a bang-bang input, then the magnitude of the shaped command will not exceed the magnitude of the unshaped command provided the length of the bang-bang signal is longer than two shaper lengths.[11] Almost all command profiles will meet this requirement. We shall see that the most useful UM negative shapers have lengths of approximately 75% of the system's period of vibration. Figure 3.32 shows a bang-bang input shaped with a negative UM shaper.

3.5.2 Partial-Sum (PS) Constraint

The second magnitude constraint, which leads to faster rise times than the UM constraints, is one which limits the partial sum of the impulse sequence to a magnitude of P. That is, as the impulse amplitudes are summed sequentially, the magnitude of the running sum equals P:

$$\left|\sum_{j=1}^{k} A_j\right| = P \qquad k = 1,\ldots,n-1 \tag{3.46}$$

[11] Also assuming that the bang-bang function switches values at its center.

This constraint is similar to the constraint proposed by O.J.M. Smith [140, 141] and identical to the constraint proposed by Singer and Rappole [86, 98]. For a three-impulse shaper, the partial-sum constraint leads to:

$$A_1 = P, \qquad A_2 = -2P, \qquad A_3 = P + 1 \tag{3.47}$$

When a partial sum (PS) negative shaper is used, almost the entire shaped command will be within ±P*Max, where Max is the maximum unshaped command level. There will, however, be brief periods when the shaped input exceeds P*Max. Figure 3.33 shows a PS negative shaper convolved with an acceleration signal associated with a trapezoidal velocity profile. A PS negative shaper will always cause overcurrenting with any unshaped command that contains a pulse, for example, a bang-bang profile. Periods of overcurrenting appear in Figure 3.33 as the times when the shaped input exceeds unity magnitude.

The amount of time the shaped command requires overcurrenting is a function of the acceleration limit, velocity limit, move distance, system frequency, and input shaper. To investigate this effect, numerous shaped commands were generated while varying the parameters for a trapezoidal velocity profile. For all reasonable moves with P = 1, only 1-3% of the shaped input required overcurrenting. For larger values of P, both the level and duration of the overcurrenting increases.

3.5.3 Types of Robustness Constraints

This section describes negative input shapers which satisfy the following three types of robustness constraints:

- Zero Vibration (ZV) [101, 140, 144].
- Zero Vibration and Derivative (ZVD) [101].
- Extra-Insensitive (EI) [122].

For most of the shapers presented in this section, a closed-form solution cannot be derived. However, numerical solutions can be obtained with optimization programs such as the MATLAB Optimization Toolbox [1] and GAMS [20]. We will present a table that allows the reader to design time-optimal negative input shapers without resorting to an optimization package.

3.5.4 Negative Zero Vibration (ZV) Shapers

Although ZV shapers do not work well on most real systems, we present them here because they are the shortest and, therefore, the highest performance shapers when the system frequencies are known very accurately. If the ZV constraints [(3.1), (3.3), (3.4)] are combined with the unity magnitude amplitude constraint, (3.45), then the impulse time locations of the resulting shaper are rather complex functions of the damping ratio, ζ.

When $\zeta = 0$, the problem simplifies, and we can derive an analytic solution for the UM-ZV

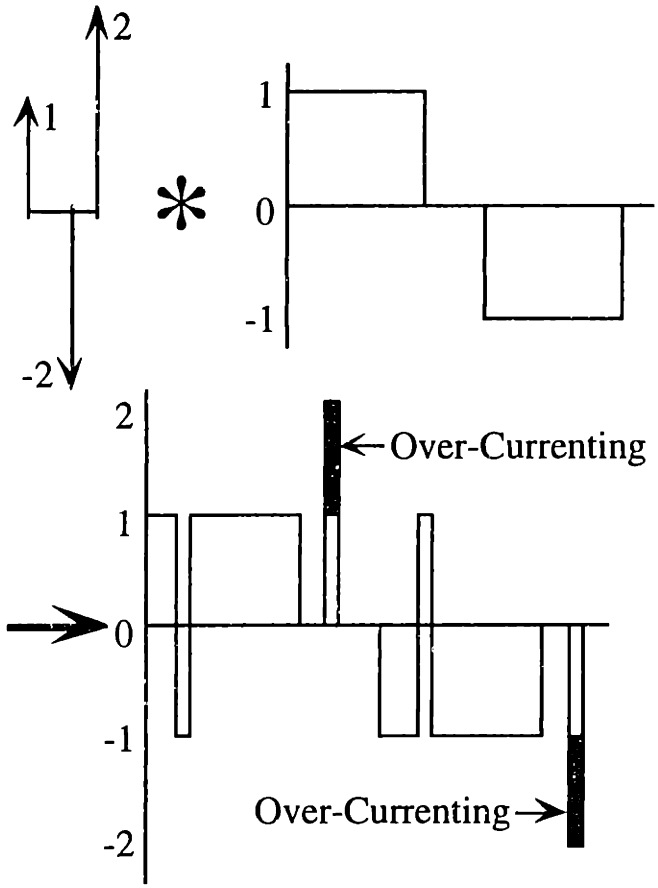

Figure 3.33: Shaping the Acceleration Profile Corresponding to a Trapezoidal Velocity Profile with a Negative PS-ZV Shaper.

shaper. The minimum number of impulses required to satisfy the UM amplitude and ZV vibration constraints is three, so the impulse amplitudes are:

$$A_1 = 1 \qquad A_2 = -1 \qquad A_3 = 1 \tag{3.48}$$

By setting Eq. (3.1) equal to zero, we get two constraint equations because both the sine and cosine terms are squared and must, therefore, be zero independently. The two equations can be obtained by setting (3.1a) and (3.1b) equal to zero:

$$-\sin(\omega t_2) + \sin(\omega t_3) = 0 \tag{3.49}$$

$$1 - \cos(\omega t_2) + \cos(\omega t_3) = 0 \tag{3.50}$$

Rearranging (3.49) and squaring both sides yields:

$$\sin^2(\omega t_2) = \sin^2(\omega t_3) \tag{3.51}$$

Using $\sin^2\alpha = 1 - \cos^2\alpha$, (3.51) can be written as:

$$\cos^2(\omega t_2) = \cos^2(\omega t_3) \tag{3.52}$$

Because $t_2 \neq t_3$, we know from (3.52) that:

$$\cos(\omega t_3) = -\cos(\omega t_2) \tag{3.53}$$

Using (3.53) and (3.50) eliminates t_3:

$$1 - 2\cos(\omega t_2) = 0 \tag{3.54}$$

Solving for t_2 yields:

$$t_2 = \cos^{-1}(0.5)/\omega \tag{3.55}$$

Similarly, using (3.53) and (3.50) to eliminate t_2 gives:

$$t_3 = \cos^{-1}(-0.5)/\omega \tag{3.56}$$

When the partial-sum amplitude constraints are used, a closed-form solution can also be found for the undamped case. The amplitudes of the impulses in the PS-ZV shaper are:

$$A_1 = P \qquad A_2 = -2P \qquad A_3 = P + 1 \tag{3.57}$$

The PS-ZV residual vibration equations are:

$$-2P\sin(\omega t_2) + (P+1)\sin(\omega t_3) = 0 \tag{3.58}$$

$$P - 2P\cos(\omega t_2) + (P+1)\cos(\omega t_3) = 0 \tag{3.59}$$

Equations 3.58 and 3.59 can be solved for both t_2 and t_3 in a manner similar to that used for the UM shaper. The solutions are:

$$t_2 = \frac{1}{\omega}\cos^{-1}\left\{\frac{4P^2 - 2P - 1}{4P^2}\right\} \tag{3.60}$$

$$t_3 = \frac{1}{\omega}\cos^{-1}\left\{\frac{2P^2 - 2P - 1}{2P(P+1)}\right\} \tag{3.61}$$

When P = 1, the length of the PS-ZV shaper is 0.29T, where T is the period of vibration. The UM-ZV shaper has a length of 0.333T, while the positive ZV shaper has a length of 0.5T. Eq. (3.61) reveals that there is a decreasing return in time savings as P increases.

A negative shaper will have slightly poorer performance than a positive shaper in the presence of modeling errors, even though they satisfy the same robustness constraints. For example, the sensitivity curves for the positive ZV shaper and the PS-ZV (P = 1) shaper are shown in Figure 3.34. The positive ZV shaper has a 5% insensitivity of 0.065; that is, the percentage vibration is less than 5% from 0.9675ω to 1.0325ω, (1.0325 - 0.9675 = 0.065). The PS-ZV shaper has a 5% insensitivity of 0.054.

The time savings gained by using negative shapers comes with the risk of high-mode excitation. To assess this risk, we plot the shaper's sensitivity curve over a range of high frequencies. At frequencies where the sensitivity curve is above 100%, high-mode excitation can occur if the system has a second resonance. Figure 3.35 compares the high-mode sensitivity curves for the positive ZV shaper and the PS-ZV shapers for P = 1 and P = 3. Residual vibration for the positive shaper never exceeds 100%, but the negative shapers exceed this value over a large range of high frequencies.

For damped systems an analytic solution of the impulse times for negative ZV shapers has not

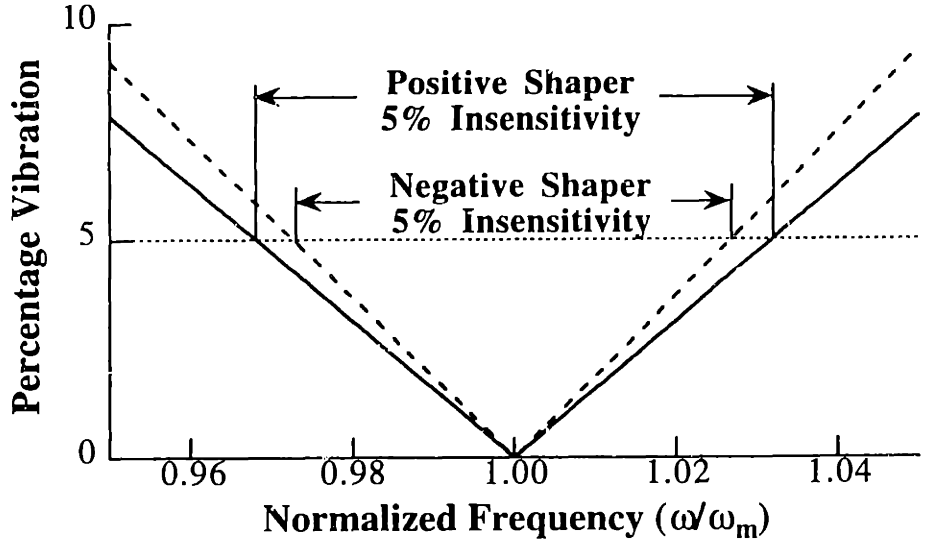

Figure 3.34: Sensitivity Curves for Positive and Negative PS-ZV (P=1) Shapers.

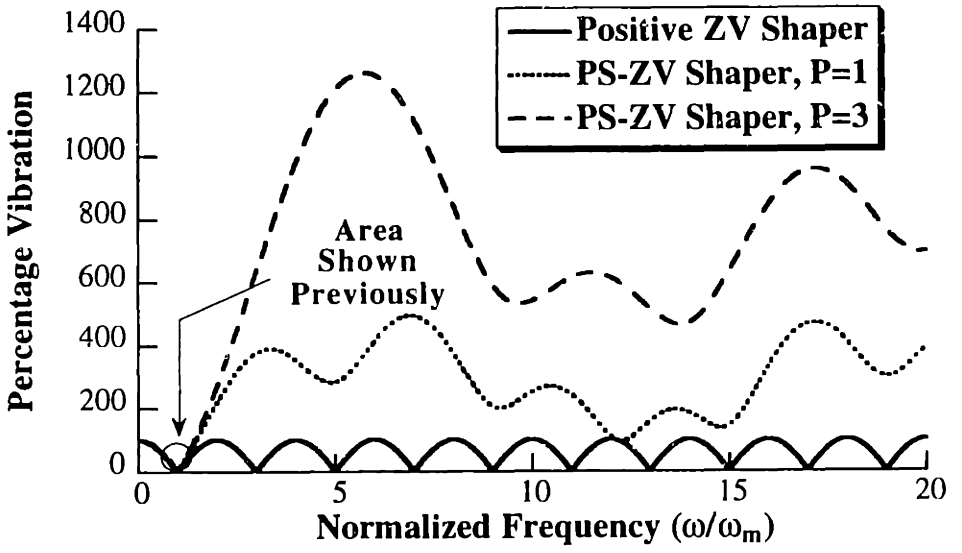

Figure 3.35: High-Mode Sensitivity Curves.

been found. However, curve fits to solutions obtained with GAMS were generated. The curve fits to t_2 and t_3 are shown in Table 3.3. Also included in Table 3.3 are solutions for the other types of shapers which will be described in the following subsections. The curve fits provided give time locations within 0.5% of their actual values over the range $0 \le \zeta \le 0.3$.

3.5.5 Negative Zero Vibration and Derivative (ZVD) Shapers

To satisfy the ZVD constraints, a negative shaper must contain five impulses. For the UM-ZVD shaper the amplitudes are:

$$A_1 = 1 \qquad A_2 = -1 \qquad A_3 = 1 \qquad A_4 = -1 \qquad A_5 = 1 \tag{3.62}$$

Table 3.3: Numerically Determined Negative Input Shapers.

		$t_i = (M_0 + M_1\zeta + M_2\zeta^2 + M_3\zeta^3)T, \quad T = 2\pi/\omega$				
Shaper	A_i	t_i	M_0	M_1	M_2	M_3
UM-ZV	1	t_1	0	0	0	0
	-1	t_2	0.16658	0.29277	0.07544	0.21335
	1	t_3	0.33323	0.00533	0.17914	0.20125
PS-ZV P=1	1	t_1	0	0	0	0
	-2	t_2	0.20970	0.22441	0.08028	0.23124
	2	t_3	0.29013	0.09557	0.10346	0.24624
UM-ZVD	1	t_1	0	0	0	0
	-1	t_2	0.08945	0.28411	0.23013	0.16401
	1	t_3	0.36613	-0.08833	0.24048	0.17001
	-1	t_4	0.64277	0.29103	0.23262	0.43784
	1	t_5	0.73228	0.00992	0.49385	0.38633
PS-ZVD P=1	1	t_1	0	0	0	0
	-2	t_2	0.15234	0.23397	0.15168	0.21310
	2	t_3	0.27731	0.11147	0.04614	0.28786
	-2	t_4	0.63114	0.34930	0.11840	0.52558
	2	t_5	0.67878	0.19411	0.27432	0.48505
UM-EI V=5%	1	t_1	0	0	0	0
	-1	t_2	0.09374	0.31903	0.13582	0.65274
	1	t_3	0.36798	-0.05894	0.13641	0.63266
	-1	t_4	0.64256	0.28595	0.26334	0.24999
	1	t_5	0.73664	0.00162	0.52749	0.19208
PS-EI P=1 V=5%	1	t_1	0	0	0	0
	-2	t_2	0.15631	0.26356	0.05324	0.69457
	2	t_3	0.28080	0.13931	-0.05627	0.75423
	-2	t_4	0.63427	0.34142	0.15371	0.32904
	2	t_5	0.68410	0.18498	0.31059	0.28565
2 Hump UM-EI V=5%	1	t_1	0	0	0	0
	-1	t_2	0.05970	0.31360	0.31759	1.5872
	1	t_3	0.40067	-0.08570	0.14685	1.6059
	-1	t_4	0.59292	0.38625	0.34296	1.2889
	1	t_5	0.78516	-0.08828	0.54174	1.3883
	-1	t_6	1.12640	0.20919	0.44217	0.30771
	1	t_7	1.18640	-0.02993	0.79859	0.12478
2 Hump PS-EI P=1 V=5%	1	t_1	0	0	0	0
	-2	t_2	0.12952	0.29981	0.08010	1.7913
	2	t_3	0.27452	0.22452	-0.20059	1.8933
	-2	t_4	0.58235	0.51403	-0.00620	1.6106
	2	t_5	0.68355	0.26308	0.08029	1.7095
	-2	t_6	1.08870	0.39342	0.14197	0.48868
	2	t_7	1.12080	0.25926	0.35816	0.35035

The time location of each impulse is a complex function of ζ. Solutions where obtained over a wide range of ζ for both the UM and PS amplitude constraints. Curve fits to t_2, t_3, t_4, and t_5 for the UM and PS-ZVD shapers are shown in Table 3.3. The length of the UM-ZVD shaper is 73% of the positive ZVD, while the length of the PS-ZVD shaper is only 68% of the positive ZVD input shaper when P = 1.

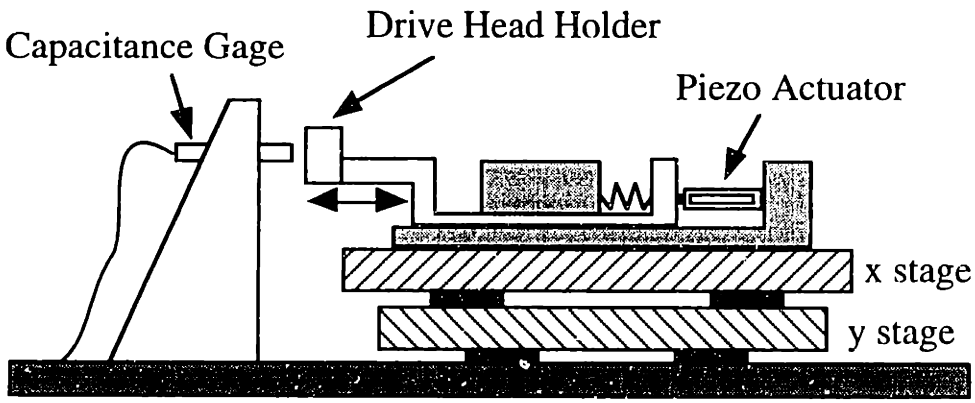

Figure 3.36: Sketch of Drive Head Tester.

3.5.6 Negative Extra-Insensitive (EI) Shapers

Using GAMS, the UM-EI and PS-EI shapers were obtained over a suitable range of V, ζ, and P. Table 3.3 includes curve fits to the time locations of the negative EI shapers when V = 5%. By examining Table 3.3, we find that the EI shapers are essentially the same length as the ZVD shapers regardless of the values for ζ.

The increase in robustness comes only from relaxing the zero vibration constraint at the modeling frequency. There are no additional costs associated with the EI shapers; high-mode sensitivity curves reveal that there is little difference between the two shapers at high frequencies. Solutions to the two-hump EI formulation are also included in Table 3.3.

3.5.7 Negative Input Shaper Experimental Results

Hardware experiments were conducted to accomplish the following goals:

1) Demonstrate the vibration reduction of input shaping.

2) Investigate the time savings of negative shapers.

3) Demonstrate that negative shapers are compatible with many types of actuators.

4) Verify the robustness to modeling errors.

To accomplish the first two tasks, experiments were performed on a machine that tests the reading heads of hard disk drives. A schematic of the machine is shown in Figure 3.36. Reading heads are placed in the machine and the xy stage component of the machine performs a gross motion to position the head near a calibrated hard disk. The xy stages are mounted on air bearings to minimize friction. Once the head has been positioned near the calibration disk, the head is tested by reading the information on the disk. The small moves from track-to-track are accomplished by a spring-loaded piezo actuator. When the piezo moves the reading head to a new track, the force backdrives the air bearing stages and oscillations occur. The machine must wait for the oscillations to dissipate before information can be read from the disk. A capacitance gage measures the position of the head holder.

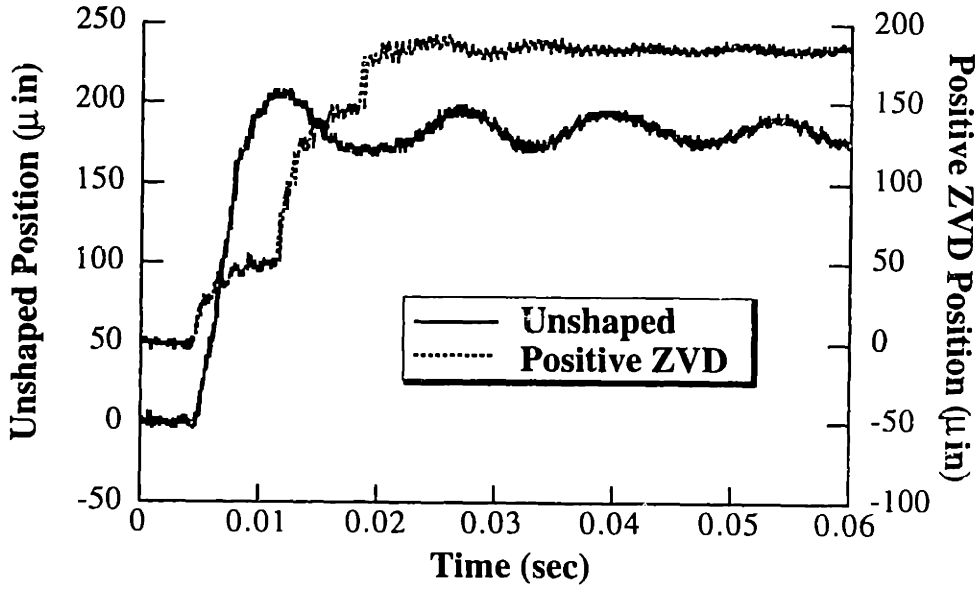

Figure 3.37: Comparison of Shaped and Unshaped Experimental Responses.

Using the standard controller, lightly damped oscillations at 75 and 1700 Hz result from typical moves. Because the low mode dominates the dynamic response, a single-mode shaper was used to shape the command signal. Figure 3.37 compares the shaped and unshaped responses for a 190 μin move. The vertical scale for the shaped response has been shifted upwards so that the residual vibration in each case is clearly visible. The shaper used to generate Figure 3.37 is a positive ZVD shaper. It is quite effective at reducing the level of residual vibration. Even though the shaped response has a longer rise time, the operational speed of the machine is increased because much less time is spent waiting for vibration to dissipate.

The throughput can be increased even further by using negative shapers. Figure 3.38 compares the response for a 110 μin move when positive ZVD and negative UM-EI shapers are used. The level of residual vibration is approximately the same, however, the negative shaper reaches the desired location approximately 15% faster.

The piezo actuator is well suited to negative shapers because it has a negligible time constant. It can respond to the demanding commands that result with a negative shaper. Negative shapers work well on other types of systems as well. To demonstrate their effectiveness on systems with DC motors and to test the robustness to modeling errors, tests were conducted on a rotary table. The Inland Torque Motor used to rotate the table was equipped with an HP HEDS-6110 encoder with 44,000 counts per revolution. The motor was powered by an Aerotech DS16020 amplifier and the control signal was generated by a Macintosh Quadra 700 running a PD controller at 500 Hz. The controller generated trapezoidal velocity profiles based on maximum velocity and acceleration limits. To ensure a vibratory response, a steel beam was mounted to the table surface,

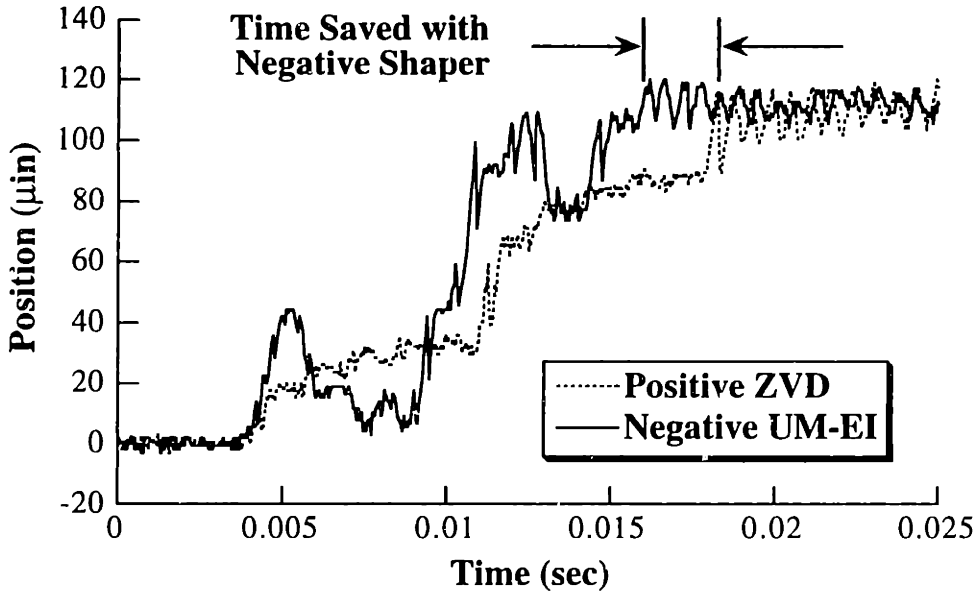

Figure 3.38: Positive and Negative Shaped Experimental Responses.

with 19 inches of the beam free to bend when the table was rotated. A 2 lb. mass was attached to the end of the beam to simulate a payload.

A one radian move was commanded and an FFT on the residual vibration revealed a mode near 2 Hz with a damping ratio of about 0.08. Negative ZV, ZVD, and EI shapers were then calculated from Table 3.3. The table response with each of the shapers was recorded. Additionally, the table response with a positive ZVD shaper was measured, so that the time savings from the negative shapers could be evaluated.

Figure 3.39 compares the unshaped response of the table to the responses with the negative partial sum-ZV, ZVD, and EI shapers. The PS-ZV and PS-EI shapers reduced the vibration to approximately 5% of the unshaped level, while the PS-ZVD reduced the vibration to 0.8%. The ZV shaper left 5% of the vibration because it is very sensitive to modeling errors and the frequency identification had limited accuracy. The EI shaper left 5% of the vibration because it is designed to leave 5% vibration near the modeling frequency.

If we examine the 2% settling time, we find the response with the negative ZV shaper settled in 0.69 sec. and both the negative ZVD and EI responses settled in approximately 0.85 sec. The response with the positive ZVD shaper settled in 0.93 sec., while the unshaped response took 2.78 sec. to settle within 2% of the desired position.

If an evaluation was based only on the above results, we might choose the negative ZV shaper because it gives the fastest settling time. Or, we might choose the negative ZVD shaper because it gives the least amount of residual vibration. However, in most real systems, the actual frequency will deviate from the modeling frequency when the system geometry changes or a payload is

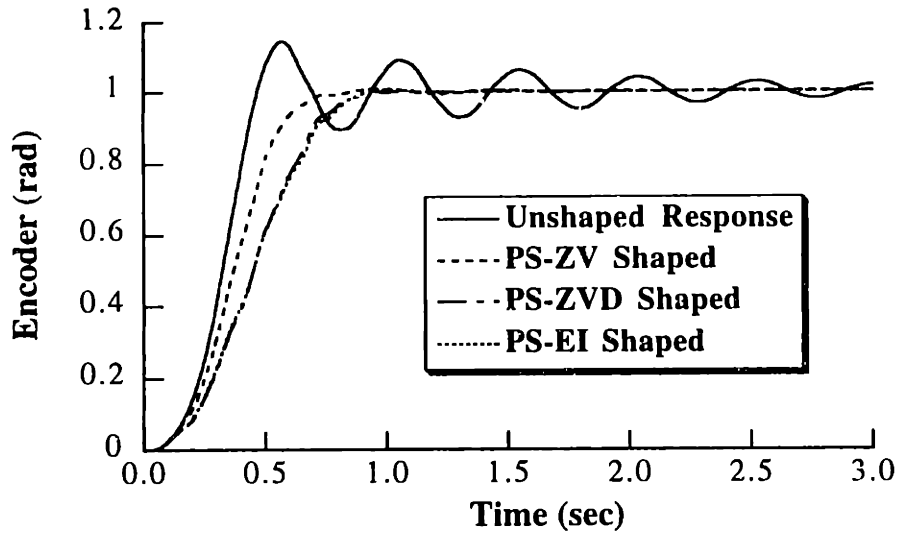

Figure 3.39: Plots of Unshaped and Shaped Rotary Table Responses.

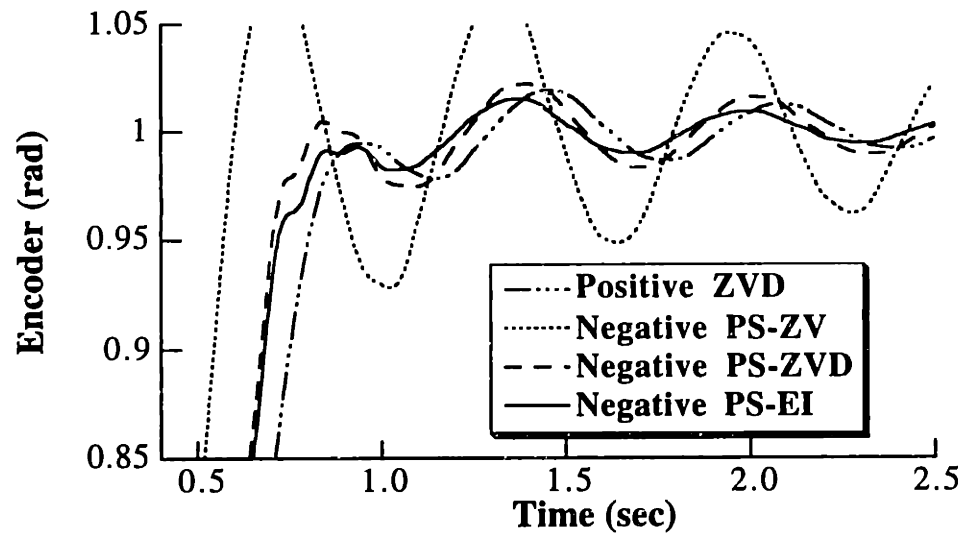

Figure 3.40: Table Vibration When Frequency is 25% Lower than Modeled.

picked up. To evaluate the shapers in the presence of modeling errors, additional mass was added to the steel beam and the experiments were repeated. The extra mass lowered the frequency approximately 25%.

Figure 3.40 compares the responses of the extra-mass system with the negative ZV, ZVD, and EI shapers designed for the original system. Also shown is the response to the positive ZVD shaper. In this case, the negative EI shaper is superior in both vibration suppression and settling time. Note that Figure 3.40 is a close up of the residual vibration. The unshaped vibration would be way off the scale if it were also plotted on Figure 3.40. The experimental results are summarized in Table 3.4.

Table 3.4: Summary of Rotary Table Experimental Data.

Shaper	Original System		Extra-Mass System (25% Lower Frequency)	
	Vibration (% of Unshaped)	2% Settling Time	Vibration (% of Unshaped)	2% Settling Time
None	100	2.78 sec.	122	> 4 sec.
Positive ZVD	0.6	0.93 sec.	21	1.18 sec.
PS-ZV	5.8	0.69 sec.	57	3.27 sec.
PS-ZVD	0.8	0.84 sec.	24	1.44 sec.
PS-EI (V=5%)	5.5	0.85 sec.	17	0.81 sec.

3.5.8 Controlling High-Mode Excitation

Although excitation of unmodeled high modes was not a problem in our experimental results, for certain systems it can limit performance. Figure 3.35 showed that negative shapers can increase vibration at unmodeled modes higher than the frequency for which they were designed. For high-mode excitation to occur, there must be a resonance at a frequency where the sensitivity curve exceeds 100%. Even if high-mode excitation occurs, input shaping will probably decrease the total amount of system vibration. This decrease results from the elimination of the low mode, which usually contributes the majority of vibration amplitude.

In cases where high-mode excitation is performance-limiting, we have several options to choose from:

1) Give up the time savings gained by using a negative shaper and use a positive shaper.

2) Add restrictions on high-mode vibration and solve the augmented set of constraints.

3) Add a digital low-pass filter.

4) Use an input with no high-frequency content.

The first option is the easiest and most appropriate when increasing the speed of the system is not the highest priority. Option 2 is the highest performance solution because we can customize an input shaper to a specific system with a minimal time penalty. Unfortunately, the look-up method provided by Table 3.3 must be abandoned. Options 3 and 4 can still utilize Table 3.3, however, there can be large increases in the computational requirements during run-time.

Option 2, the process of restricting only a few problematic high frequencies is best demonstrated with an example. Suppose we select a PS-EI shaper to eliminate a 1 Hz mode from our system. However, when we use the shaper, we discover that a previously unimportant mode at 7 Hz is excited more than in the unshaped case. We can eliminate this vibration by adding an equation to our set of constraints that limits the vibration at 7 Hz.

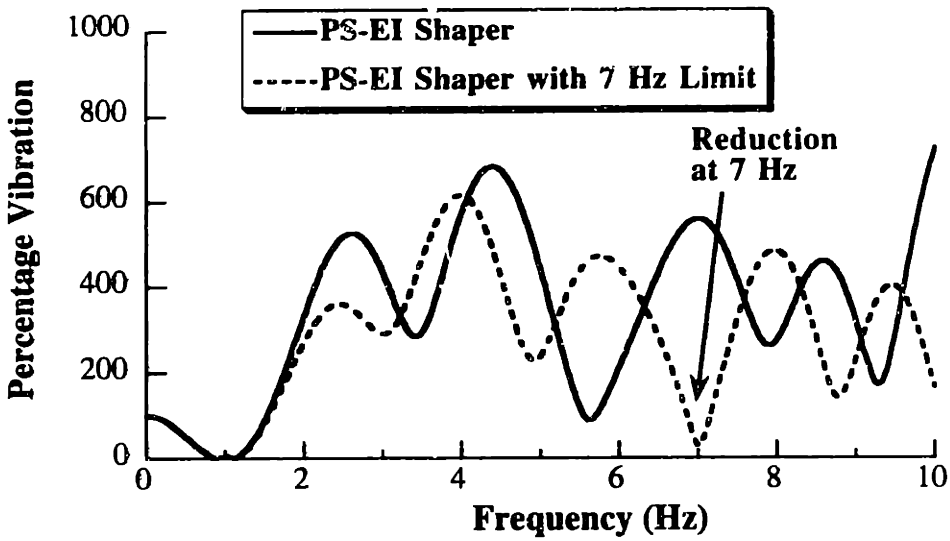

Figure 3.41: Effect of 7 Hz Vibration Limiting.

A five-impulse shaper eliminating the 1 Hz mode and limiting the 7 Hz mode to 50% was calculated with GAMS. The shaper is only 6% longer than a PS-EI shaper designed only for the 1 Hz mode. Sensitivity curves for the EI shaper and the EI shaper with the 7 Hz vibration limitation are shown in Figure 3.41.

If more than one high mode is problematic, we simply add a constraint equation for each mode of vibration and solve the augmented set of constraints. For each mode that is constrained, a small amount of time will be added to the shaper length. However, a negative shaper with high-mode constraints will continue to be shorter than a positive shaper for the low mode until constraints have been placed on a large number of high modes.

The technique of restricting the vibration at a few high modes is advantageous because:

- The shaper is customized to a specific system and, therefore, it does not over-constrain the system.
- The computational requirements during run-time are only slightly increased. (In our example, the run-time computation was completely unaffected because the number of impulses did not increase.)

The drawback of this approach is that it requires the one-time solution of a set of simultaneous, transcendental constraint equations; Table 3.3 cannot be used.

Instead of restricting a few high modes, we can eliminate all high frequencies by adding a low-pass filter. The low-pass filter is used in conjunction with a negative shaper of the designer's choice from Table 3.3 to give a modified input shaper that will not excite modes in the filter's stop band. A time delay is added when we use a low-pass filter because the length of the modified

shaper is equal to the length of the original shaper plus the length of the low-pass filter. The computational requirements can increase significantly because implementation of the modified shaper requires N more multiplies and adds than the original shaper, where N is the low-pass filter length number. To implement the modified shaper, place the low-pass filter in series with the input shaper instead of convolving the shaper and filter together. This procedure reduces the computational load during run-time.

The main benefits of augmenting a negative input shaper with a low-pass filter are:

- It requires no specific information about the high frequencies, just a pass band and a stop band.
- It eliminates a large range of high frequencies.
- It uses well established filter design tools in combination with the solutions from Table 3.3.

This approach has two major drawbacks:

- There is a longer time delay associated with this input shaping process than when we restrict just a few high modes.
- The run-time computation can be prohibitive.

We will not give an example of the fourth option for dealing with high-mode excitation, using an input function that does not contain energy at high frequencies. It often requires more computation than a low-pass filter and performance will vary with the move distance.

3.5.9 Negative Input Shaper Discussion

A simple look-up procedure was developed that allows a controls engineer to design time-optimal negative input shapers without the usual requirement of numerically solving a set of simultaneous transcendental equations. This simple method has been provided for several different types of shapers. If high-mode excitation occurs, several methods can be used to eliminate this problem, while still maintaining much of the time savings gained by using a negative input shaper. Experiments showed the negative shapers give faster rise times than positive input shapers. Additionally, the negative shapers were shown to be compatible with both DC motors and piezo actuators.

3.6 Specified-Duration Input Shapers

Section 3.3 discussed input shapers that had a specified robustness to modeling errors. For some applications, it is desirable to generate shapers that have a specified duration. By specifying the duration, we specify the rise time (and deceleration time) of the system. If input shaping is used to filter commands being generated in real time by a human operator, then it may be desirable to set the lag time to a length with which the operator is comfortable. An example of this situation is the control of gantry cranes like the one sketched in Figure 3.42. These systems often have built in "soft starts" that ramp up and down the motor torque and have the effect of adding a time lag. When these "soft starts" are replaced with an input shaper, it may prove beneficial to set the duration of the shaper equal to the duration of the ramp up. When this is done, the lag that the operator experiences is unchanged.

For this type of problem, the input shaping design process must be modified. For the previous input shapers the length of the shaper was minimized subject to a set of constraint equations that limited residual vibration, established robustness to modeling errors, etc. In this case, the shaper duration is specified, so some other quantity must be optimized. In this section we chose to maximize the robustness for a given shaper length.

As was shown in Section 3.3, M versions of (3.31) can be used to suppress residual vibration over a range of frequencies using frequency sampling. Each version of (3.31) was applied at a unique (and known) frequency within the frequency range being suppressed. Rather than the specify the range of frequencies to be suppressed, here we fix the shaper duration and treat the suppressed frequencies, (ω_1, ..., ω_m), as equally spaced variables. To give the frequencies equal spacing requires:

$$\omega_i = \omega_1 + (i-1)\frac{(\omega_m - \omega_1)}{(m-1)} \qquad i = 1,\ldots,m \tag{3.63}$$

The constraint equations that must be satisfied include the M vibration constraint equations, an impulse amplitude constraint, and a constraint that sets the shaper duration:

$$t_n = \Delta_t. \tag{3.64}$$

where Δ_t is the desired duration of the input shaper. A numerical optimization is performed to satisfy the constraint equations while maximizing the range of the unknown frequencies. That is, (ω_m - ω_1) is maximized. The result of the optimization is a Specified-Duration (SD) shaper whose insensitivity has been maximized.

To demonstrate the SD shaper design process, suppose that we are designing input shapers for a gantry crane that varies its cable length from 20 ft. down to 4 ft. To maximize actuator effort the unity-magnitude (UM) amplitude constraints of (3.45) are used. The additional constraint

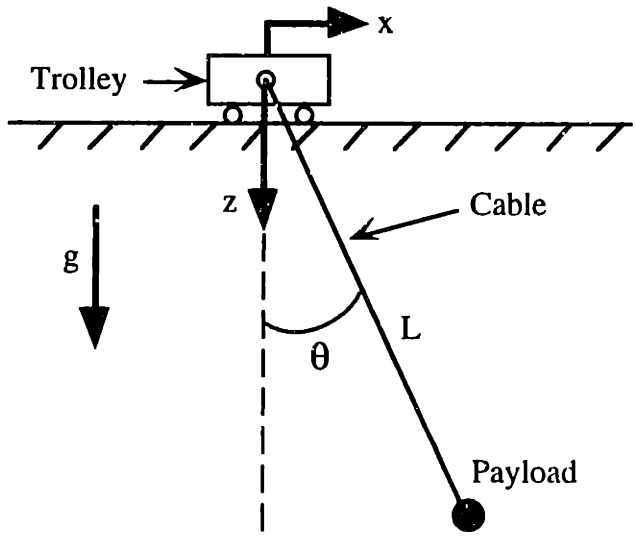

Figure 3.42: Model of a Planar Gantry Crane.

equations consist of (3.63), (3.64) and M versions of (3.31). One version of (3.31) is applied at the frequency, ω_l, that corresponds to 20 ft. (This is 0.2 Hz assuming $\omega = \sqrt{g/L}$.) An additional version of (3.31) is applied at an unknown frequency, ω_m, that is higher in value than ω_l. The frequencies between ω_m and ω_l are then suppressed by the M-2 additional versions of (3.31) and the frequencies used in these equations are obtained from (3.63). An optimization is then performed to obtain the UM SD shaper that maximizes ω_m.

Suppose that for the desired shaper duration ω_m corresponds to a cable length of 8 ft. That is, a single shaper cannot suppress vibration over the entire range of cable lengths. In this case, the optimization is performed again, but this time ω_m plays the role of ω_l. If the new maximized frequency value, ω_{m2}, resulting from the second optimization is above the frequency corresponding to 4 ft., then the shaper design process is complete. The shaper resulting from the first optimization is used to move the crane when the cable is between 20 ft. and 8 ft., while the second shaper is used when the cable is less than 8 ft. in length.

3.6.1 Specified-Duration Shaper Design Algorithm

The specified-duration shaper design algorithm can be summarized as follows:

1) Select a shaper duration (deceleration period), Δ_t.

2) Select a desired limit on the percentage residual vibration amplitude, V_{tol}.

3) Require the vibration to be below V_{tol} at the lowest possible frequency of the system, ω_l, (For cranes this corresponds to the longest cable length).

4) Perform an optimization that maximizes the frequency range over which the residual amplitude can be kept below V_{tol}. The outputs of the optimization and the impulse amplitudes and time

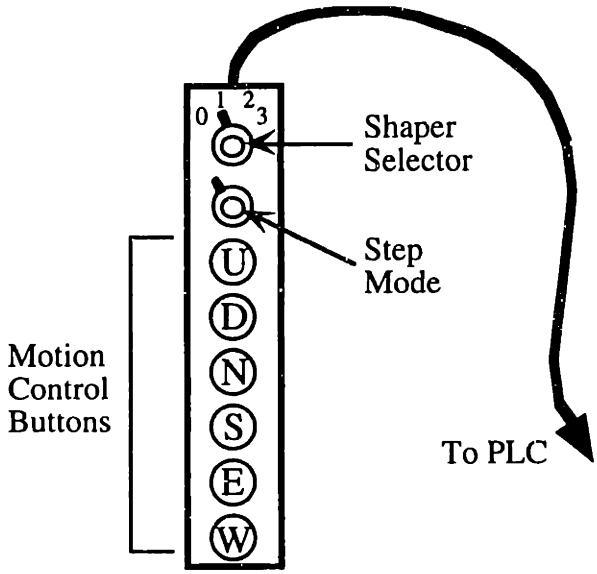

Figure 3.43: Operator Pendant.

locations, and the maximum suppressed frequency, ω_m.

5) If the suppressed frequency range covers the entire desired range, then terminate the algorithm. Otherwise, start at step 3 and replace ω_l with ω_m.

The product of the algorithm is one or more SD shapers which can be used to suppress vibration throughout the desired range.

3.6.2 Experimental Results with Specified-Duration Shapers

The specified-duration input shapers developed in this section were implemented and tested on a 15 ton gantry crane at the Savannah River Technology Center (SRTC). The crane bridge travel is 85 ft., the trolley travel is 43 ft., and the hook travel is 29 ft. Input shaping was implemented with a Convolve, Inc. Input Shaping Crane Controller. This controller is a hardware module that is based on an Allen-Bradley SLC-500 modular PLC Rack. The SLC-500 modular system allows selection of input and output modules so that the controls can be easily customized to any crane configuration without hardware redesign. The controller uses these industrially-hardened PLC and I/O modules for handling all of the crane input and output signals. A proprietary Convolve module was added to the rack to enable the input shaping process. The shaped commands are processed internally and output as analog velocity commands by the SLC-500 analog output module.

The operator presses six on-off buttons on a pendant, sketched in Figure 3.43, to move the crane throughout its workspace (Up/Down, North/South, and East/West). Two additional, four-position switches were added to the crane pendant. The first switch selects the input shaper to be used and the second switch selects a feature called Step Mode (described in [97]) that allows very small motions to be accomplished. The shaping control knob allows the operator to select one of

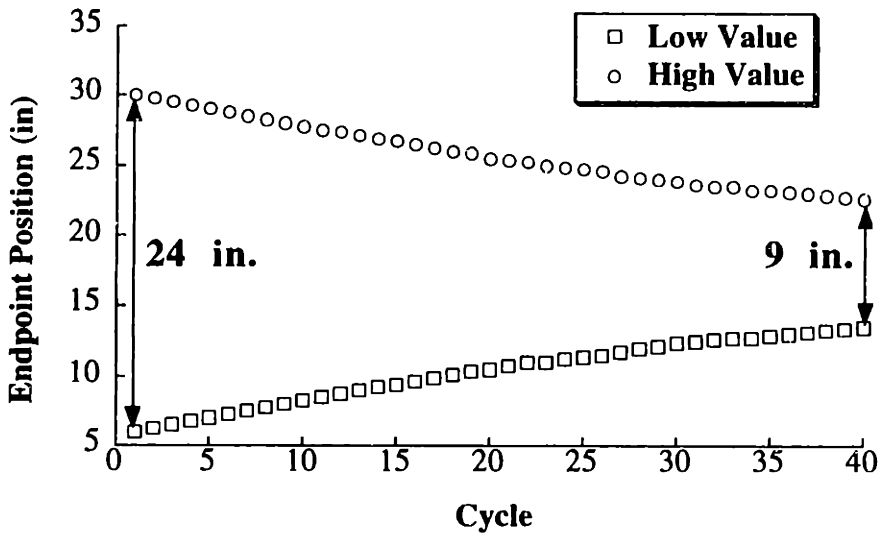

Figure 3.44: Peak-to-Peak Oscillation of Crane with a Cable Length of 28 ft.

four possible states: no shaping, shaper #1, shaper #2, or shaper #3. Using the approach described in the previous subsection, three SD input shapers were designed to eliminate vibration throughout the entire workspace of the crane.

To measure the residual oscillation of the crane, a yard stick was attached to the crane hook and the response was recorded on videotape. By placing a straightedge on the surface of the video monitor, the peak-to-peak residual oscillation was measured. For long cable lengths (endpoint near ground), the setup gave a resolution of 1/8 in. As the cable was shortened and the endpoint moved away from the camera, the resolution deteriorated. At short cable lengths (<15 ft), the resolution was approximately 1/4 - 3/8 in.

The damping ratio of the SRTC crane was determined by moving the crane and recording the peak-to-peak oscillation amplitude over 40 cycles of vibration. Figure 3.44 shows the values of the experimental measurements with a cable length of 28 ft. Even after 40 cycles (nearly 4 minutes), the peak-to-peak oscillation is still 9 in. An exponential curve fit to the data revealed that the damping ratio was approximately 0.004. If the cable length is very short (5 ft. or less), then the damping ratio goes up considerably, to approximately 0.1. Because the damping was so small throughout almost the entire workspace, the damping ratio was modeled as exactly zero.

Using the approximate deceleration period under the standard control system, Δ_t was set equal to 3.0 seconds and the above procedure was used to design three UM SD shapers to span the range of cable lengths from 29 ft. to 9 ft. (The crane rarely operates with cable lengths less than 9 ft. and cannot operate at less than 5 ft.) Figure 3.45 shows the measured percentage residual vibration for each of the UM SD shapers. The percentage residual is obtained by dividing the shaped residual vibration amplitude by the unshaped residual amplitude for the same motion. If the operator

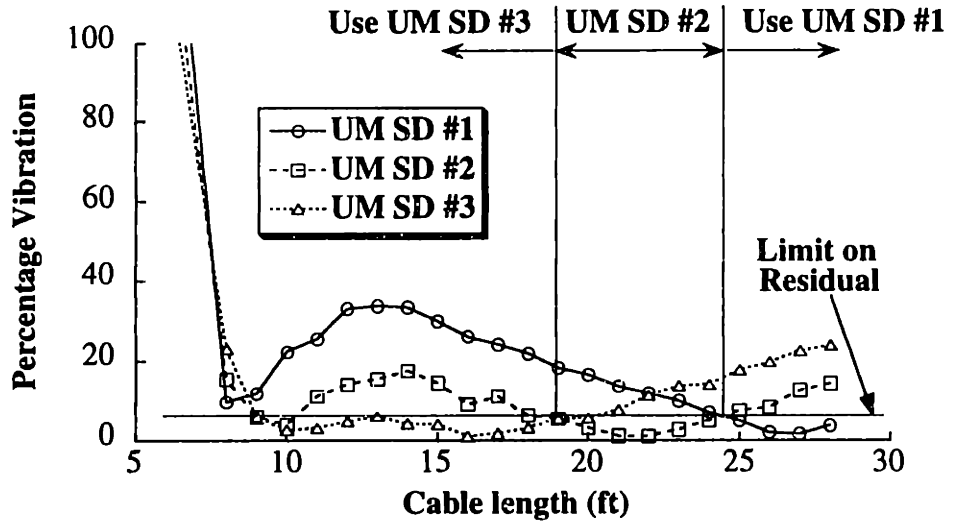

Figure 3.45: Measured Residual Amplitude Using UM SD Shapers.

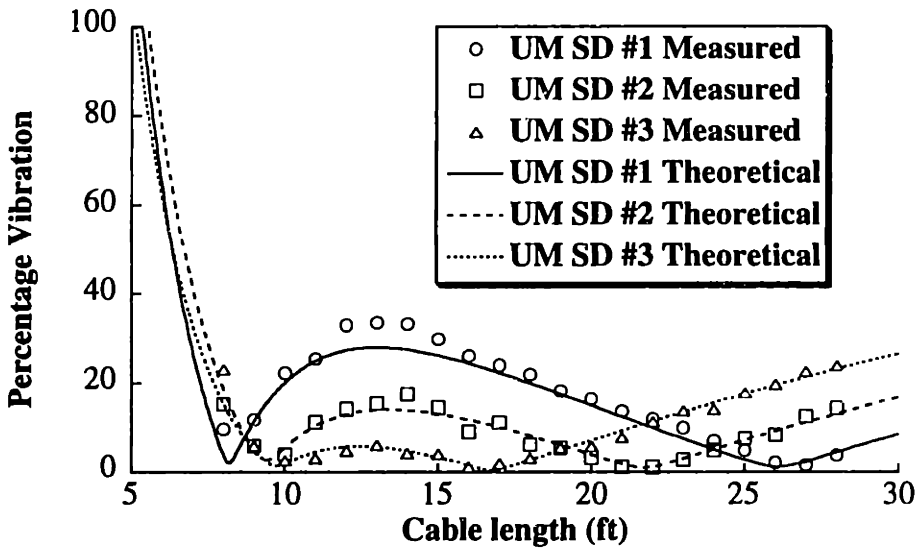

Figure 3.46: Theoretical and Measured UM SD Residual Amplitude.

switches between the three shapers at 24 ft. and 19 ft., then the residual vibration can be kept to below 5% of the unshaped level (for cable lengths down to 9 ft.).

Figure 3.46 compares the measured residual vibration with the UM SD shapers to the theoretical residual amplitudes. Given the uncertainty in the measurement system, there is very good agreement between theoretical and measured values. Notice that the largest deviation between theory and measured values occurs at short cable lengths. This makes sense, as the measurement system has progressively worse resolution as cable length is decreased and the actual damping ratio deviates more from the modeling value of zero.

To compare the new shaping process with previously proposed methods, three UM ZV

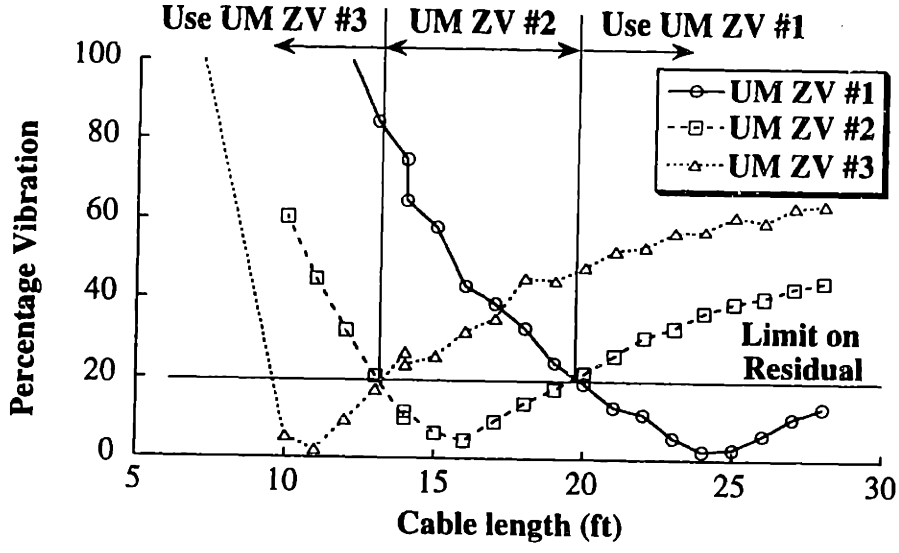

Figure 3.47: Measured Residual Amplitude Using UM ZV Shapers.

shapers were designed to cover the workspace. The shapers were designed to have zero residual vibration at cable lengths of approximately 24 ft, 16 ft, and 11 ft. Figure 3.47 shows the measured percentage residual vibration as a function of cable length. If the operator switches between the three shapers at 20 ft and 13 ft, then the residual vibration can be kept to below 20% of the unshaped level (for cable lengths down to 9 ft.).

Comparing Figures 3.45 and 3.47, we see that the UM SD shapers provide better sway reduction than the UM ZV shapers throughout the workspace. Unlike the UM SD shapers, the deceleration lag is different with each UM ZV shaper. The operator must become accustomed to the different deceleration periods. An advantage of the UM ZV shapers is that the deceleration period is shorter; the maximum shaper length is 1.8 seconds.

3.6.3 Summary of Specified-Duration Shapers

A procedure for designing input shapers that have a specified-duration has been described. Given the fixed shaper duration, the robustness of the shapers is maximized. The new shaping method was implemented on a gantry crane at the Savannah River Technology Center. Experimental results show that the method greatly reduces residual oscillations and closely matches the theoretically predicted performance.

4 ROBUST MULTI-SWITCH BANG-BANG COMMANDS FOR LINEAR FLEXIBLE SYSTEMS

4.1 Introduction to Multi-Switch Bang-Bang Commands

The previous chapter discussed methods for real-time shaping of command signals. The resulting command profiles were not, in general, the minimum-time commands. Command profiles may exist that will move a system faster, subject to the same performance criteria, than those generated by the methods of the previous chapter. This should not be surprising as we have already seen that the negative input shapers described in Section 3.5 move systems faster than shapers containing only positive impulses. The minimum-time commands will, in general, move systems even faster than those formed by using negative input shapers. Recall from Chapter 1 that command generators were classified as either real-time command shapers or generators of pre-computed command profiles. Implementation of minimum-time commands requires a type of command generator that produces pre-computed command profiles.

In order to achieve the fastest possible motion, the actuator limit of the system must be known.[12] Furthermore, the minimum-time command can only be calculated if the initial state and the desired terminal state are known in advance. As a consequence of these requirements, the minimum-time command must, in all but the simplest cases, be pre-computed using a nonlinear optimization.

The time-optimal control of linear flexible systems has been well studied. The intensive work on optimal control during the 1960's resulted in necessary conditions that the time-optimal command must satisfy [21, 85]. Furthermore, sufficient conditions can be generated that verify whether or not a candidate solution is truly the time-optimal command [81, 85, 148, 150].

The chief difficulty with the optimal control methods is that they did not provide a reasonable method for finding the time-optimal commands for flexible systems. One prominent optimal control text states of these problems, "...this boundary value problem is, in general, not very easy

[12] Strictly speaking, the maximum acceleration must be known.

to solve."[13] Several methods have recently been proposed for solving problems of this type. These methods include the Switching Time Optimization algorithm [53, 68] and formulating the state boundary conditions as explicit functions of a parameterized command profile [52, 111, 148, 150]. Tuttle has produced a set of MATLAB functions that reliably generate the time-optimal commands for a wide variety of flexible systems [150].

For many types of linear systems the time-optimal command is a multi-switch bang-bang function [11, 52, 78, 80, 85, 111, 148, 150]. Knowledge of this result simplifies the search for the time-optimal command because only the switch times in the command profile must be determined. This chapter is concerned with the generation of multi-switch bang-bang (MSBB) commands. In some cases, the MSBB commands will be the time-optimal commands and in other cases they may not be. However, in all cases discussed in this chapter, the MSBB commands will be the minimum-time commands that satisfy the requirement of being a MSBB function. We investigate MSBB commands because they provide very fast state transitions, regardless of whether or not they are can be proven to be the time-optimal commands.

In the next section, the MSBB command generation problem is formulated as an input shaping problem similar to that of Chapter 3. In Section 4.3, the extra-insensitive robustness constraints discussed previously are used to generate a new form of robust MSBB commands. Section 4.4 examines in detail both the robustness of time-optimal commands for linear multi-mode systems with pole dynamics and the complexity of the command profiles.[14] Section 4.5 describes a numerical method for checking the validity of numerically obtained time-optimal command profiles. The numerical checking procedure aids in the generation of the command profiles because it provides a means for eliminating candidate solutions that are not truly time-optimal.

[13] Applied Optimal Control, Bryson and Ho, pp. 89.

[14] The time-optimal commands for these types of systems are MSBB functions.

4.2 Input Shaping Generation of Multi-Switch Bang-Bang Commands

As mentioned in the introduction to this chapter, recent work has produced reasonable methods for obtaining the time-optimal commands for linear flexible systems. In addition to obtaining the command profiles, characteristics of the profiles have been studied [76, 78, 131, 132]. In an attempt to overcome the sensitivity to modeling errors, Liu and Wie combined Singer's zero derivative robustness constraint with the traditional constraints used for time-optimal flexible-body control [52]. Singh and Vadali achieved the same result by posing the problem as one of pole-zero cancellation [111]. As it turns out, the resulting command profiles are not very robust in many cases. As we will see in Section 4.3, the robustness of time-optimal commands based on the derivative robustness condition is highly dependent on the desired motion. Furthermore, Section 4.4 will demonstrate that, in multi-mode systems, the robustness of time-optimal commands based on the zero derivative constraint is highly dependent on the mode ratios.

Consider a class of systems that can be represented by:

$$\dot{\mathbf{x}}(t) = \mathbf{F}\mathbf{x}(t) + \mathbf{g}u(t) \tag{4.1}$$

$$y(t) = \mathbf{h}\mathbf{x}(t) \tag{4.2}$$

where, $\mathbf{F}$ is a block diagonal of $[\mathbf{F}_0, \mathbf{F}_1, ..., \mathbf{F}_m]$, $\mathbf{g}=[\mathbf{g}_0\ 0\ g_1\ ...\ g_m]^T$, and $\mathbf{h}=[\mathbf{h}_0\ h_1\ 0\ ...\ h_m\ 0]$. $\mathbf{F}_0$, $\mathbf{g}_0$, and $\mathbf{h}_0$ represent the rigid-body dynamics and are given by:

$$\mathbf{F}_0 = \begin{bmatrix} 0 & 1 \\ 0 & 0 \end{bmatrix}, \quad \mathbf{g}_0 = [0 \quad 1], \quad \mathbf{h}_0 = [1 \quad 0] \tag{4.3}$$

$\mathbf{F}_1, ..., \mathbf{F}_m$ represent the m flexible modes and are given by:

$$\mathbf{F}_j = \begin{bmatrix} 0 & 1 \\ -\omega_j^2 & -2\zeta_j\omega_j \end{bmatrix} \qquad j = 1,\ 2, ...,\ m \tag{4.4}$$

The control signal, u(t), is assumed to be bounded within the range $-u_{max} \le u(t) \le u_{max}$.

The goal of this section is to develop an input shaping formulation that produces the time-optimal commands for systems that can be represented by (4.1) - (4.4). Furthermore, the input shaping process developed here can be used to generate multi-switch bang-bang commands (that may not be time-optimal) for a larger class of problems than those represented by (4.1) - (4.4). To illustrate the proposed process, we consider one specific case of the systems described by (4.1) - (4.4). The model shown in Figure 4.1 represents a system with a single flexible mode and a rigid-body mode. A force input acts on mass m_1, and is restricted to the range $-1 \le u(t) \le 1$. The benchmark model will have parameter values of $m_1 = m_2 = k = 1$ and $b = 0$. These parameters give an undamped frequency of 0.2251 Hz. This simple model is used because:

1) It effectively represents a large class of physical systems.

2) The methods used on this system apply to more complex systems, as we will see in Section 4.4.

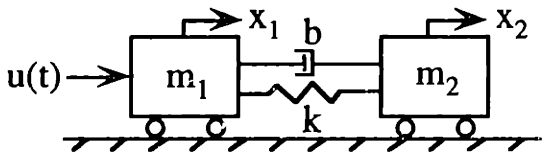

Figure 4.1: Benchmark System Model.

3) Robust commands generated with this model have proven effective when used on more complicated systems [8, 9, 90, 114, 117, 136].

4) This model has been used as a benchmark system for numerous control techniques [8, 11, 52, 76, 78, 79, 90, 103-105, 111, 114, 115, 123, 135, 136, 159, 163, 165, 166].

Several methods have been proposed for determining time-optimal and robust time-optimal commands for this benchmark system. In this section we pose the problem in the form of an input shaping problem similar to those of the previous chapter. Additional constraint equations are utilized to ensure that the resulting command will be the time-optimal command.

Given the previous results in time-optimal control of systems described by (4.1) - (4.4), we know that the time-optimal command is a multi-switch bang-bang function [11, 52, 78, 111, 149]. That is, the command switches between a constant positive value and a constant negative value. Two types of commands will be considered in this section, those that perform rest-to-rest motion and those that accelerate the system up to a constant velocity (spin-up maneuvers). Commands that perform rest-to-rest motion have equal numbers of positive and negative pulses. Commands that accelerate the system up to a constant velocity have more positive pulses than negative pulses [111]. A multi-switch bang-bang function for rest-to-rest motions can be generated by convolving a step function with an input shaper of the form:

$$\begin{bmatrix} A_i \\ t_i \end{bmatrix} = \begin{bmatrix} 1 & -2 & 2 & -2 & \dots & -2 & 1 \\ 0 & t_2 & t_3 & t_4 & \dots & t_{n-1} & t_n \end{bmatrix} \tag{4.5}$$

where A_i is the amplitude of the i^{th} impulse, t_i is the time location of the i^{th} impulse, and n is odd. The amplitude of the step function must cause the maximum acceleration of the system. Figure 4.2 demonstrates that a step function convolved with this type of input shaper results in a MSBB function. Equation 4.5 determines the impulse amplitudes for rest-to-rest input shapers:

$$\begin{aligned} A_i &= 1 && i = 1 \text{ and } n \\ A_i &= 2(-1)^{i-1} && i = 2,\dots,n-1 \end{aligned} \tag{4.6}$$

Note that the amplitudes sum to zero, not to one. This is an important difference between time-optimal input shapers and the real-time input shapers of Chapter 3. In Chapter 3, the command signal being shaped was unknown, and consequently we wanted the shaped command to reach the same final setpoint. Therefore, the shaper was required to have unity gain. In this chapter we require the unshaped command to cause a step function in acceleration. If the shaper amplitudes

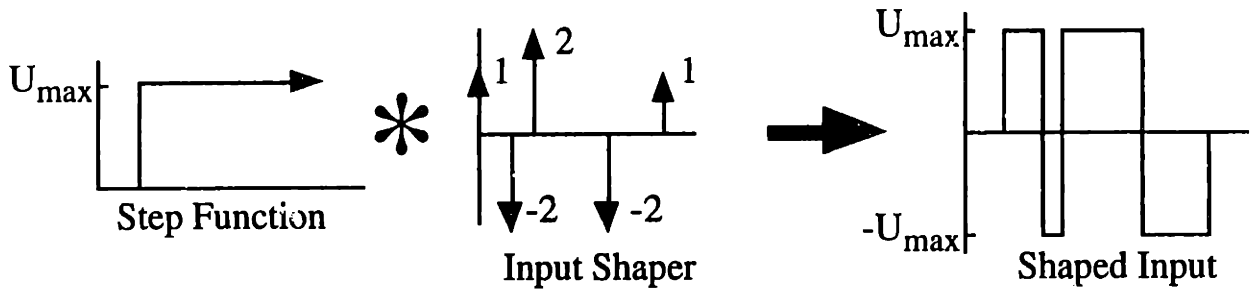

Figure 4.2: Input Shaping to Generate a Multi-Switch Bang-Bang Function.

sum to one, then the final setpoint will cause full acceleration. Under these conditions, the system cannot be brought to rest or to a constant velocity. When the amplitudes sum to zero, the final command state is zero, and consequently the system can be brought to rest.

The time-optimal commands for spin-up maneuvers require one more positive pulse than negative pulses; therefore, the input shaper must take the form:

$$\begin{bmatrix} A_i \\ t_i \end{bmatrix} = \begin{bmatrix} 1 & -2 & 2 & -2 & \dots & 2 & -1 \\ 0 & t_2 & t_3 & t_4 & \dots & t_{n-1} & t_n \end{bmatrix} \tag{4.7}$$

where n is even. This means the impulse amplitudes can be written as:

$$\begin{aligned} A_i &= 1 && i = 1 \\ A_i &= 2(-1)^{i-1} && i = 2,\dots,n-1. \\ A_i &= -1 && i = n \end{aligned} \tag{4.8}$$

Equations 4.6 and 4.8 ensure that the shaped command will be a multi-switch bang-bang function. The following constraint equations ensure that the system's mass center will move the desired amount. The rigid-body motion of the system shown in Figure 4.1 can be described as:

$$\ddot{x} = \frac{u(t)}{(m_1 + m_2)} \tag{4.9}$$

where x is the displacement of the mass center. By integrating (4.9) with respect to time we get an expression for mass center velocity:

$$v_d = \int \frac{u(t)}{(m_1 + m_2)} dt \tag{4.10}$$

where v_d is the desired velocity. Integrating once more gives an expression for move distance:

$$x_d = \iint \frac{u(t)}{(m_1 + m_2)} dt\, dt \tag{4.11}$$

where x_d is the desired move distance. In a flexible rotary system, the transient deflection may cause a time-varying moment of inertia. These cases may require a more general form of rigid-body constraints. However, we use the conditions given in (4.10) and (4.11) because we are considering the benchmark system of Figure 4.1.

The rigid-body motion can be specified by (4.10) and (4.11), however, the main difficulty with generating time-optimal commands for flexible systems is the need to eliminate the residual

vibration. Given that we are solving for an input shaper, we know from Chapter 3 that the equation describing the amplitude of residual vibration is given by (3.1). This expression is restated here for convenience:

$$V(\omega,\zeta) = e^{-\zeta\omega t_n}\sqrt{\left(C(\omega,\zeta)\right)^2 + \left(S(\omega,\zeta)\right)^2} \tag{4.12}$$

where,

$$C(\omega,\zeta) = \sum_{i=1}^{n} A_i e^{\zeta\omega t_i}\cos\left(\omega\sqrt{1-\zeta^2}\,t_i\right) \tag{4.12a}$$

$$S(\omega,\zeta) = \sum_{i=1}^{n} A_i e^{\zeta\omega t_i}\sin\left(\omega\sqrt{1-\zeta^2}\,t_i\right). \tag{4.12b}$$

To produce a command that yields zero residual vibration, we require that (4.12) equal zero at the system frequency and damping ratio. The final constraint for this problem formulation ensures that the solution is time-optimal; that is, it is the shortest command that satisfies the other constraints. The constraint is simply:

$$\textit{minimize}(t_n) \tag{4.13}$$

where t_n is the time of the last shaper impulse.

The constraint equations for determining the time-optimal commands for the system under consideration can now be stated explicitly. For rest-to-rest motions, the commands satisfy (4.6), (4.10) with $v_d = 0$, (4.11) with a nonzero x_d, (4.12) with $V = 0$, and (4.13). For spin-up motions, the commands satisfy (4.8), (4.10) with a nonzero v_d, (4.12) with $V = 0$, and (4.13). Note that the spin-up motions do not satisfy (4.11). This reduction in constraint equations leads to the command having fewer negative pulses. A numerical optimization is used to determine the impulse time locations that satisfy the constraint equations.

At this point it is useful to note the difference in constraint equations used for real-time shaping (Chapter 3) and time-optimal shaping. The time-optimal shapers are subject to three additional types of constraints. First, the amplitudes are constrained to specific values by (4.6) or (4.8).[15] Second, the rigid-body constraints must be satisfied using (4.10) and (4.11). Finally, the resulting shaper must be convolved with a step function that produces the maximum acceleration.

As mentioned previously, Singer's zero derivative constraint has been utilized to produce time-optimal commands with some robustness to modeling errors. To accomplished this, the above set of constraint equations is augmented with:

$$0 = \frac{d}{d\omega}\left[e^{-\zeta\omega t_n}\sqrt{\left(C(\omega,\zeta)\right)^2 + \left(S(\omega,\zeta)\right)^2}\right]. \tag{4.14}$$

[15] The negative shapers described in Section 3.5 were subject to impulse amplitude constraints, but they are different than those given in (4.6) and (4.8). The difference arises because the real-time shaper impulse amplitudes must sum to one, while the time-optimal shaper impulse amplitudes must sum to zero.

4.3 Multi-Switch Bang-Bang Extra-Insensitive Commands

In this section, a new type of robust MSBB command will be designed using the extra-insensitive robustness constraints described fully in Chapter 3. The performance of the new commands are compared to the time-optimal commands obtained using the zero derivative robustness constraints.

The previously proposed time-optimal commands for the benchmark system of Figure 4.1 are referred to by several different names in the literature. To avoid confusion with different types of robust commands, we describe the commands by the constraints they satisfy. The command obtained by setting the residual vibration to zero is labeled the time-optimal zero vibration (TO ZV) command. The robust command derived by setting the residual vibration to zero and by setting the derivative of the vibration to zero is called the time-optimal zero vibration and zero derivative (TO ZVD) command.

The new commands described in this section are generated by first requiring the command to be a multi-switch bang-bang (MSBB) function. The residual vibration is then limited to a small value, V, at the modeling frequency. Additional constraints are obtained by setting (4.12) equal to zero at two frequencies, one higher than the modeling frequency, ω_{hi}, and the other lower, ω_{lo}. The values of the frequencies ω_{hi} and ω_{lo} are variables that depend on the value of V. We also require the derivative constraint, (4.14), to be enforced at the modeling frequency. When the set of constraint equations is solved with an optimization program, the values of the impulse time locations, as well as ω_{hi} and ω_{lo}, are determined and the resulting command profile is the multi-switch bang-bang extra-insensitive (MSBB EI) command.

4.3.1 MSBB Extra-Insensitive Rest-to-Rest Commands

The MSBB EI command for the benchmark model with design parameters of V = 0.05 and x_d = 1, is described by the input shaper:

$$\begin{bmatrix} A_i \\ t_i \end{bmatrix} = \begin{bmatrix} 1 & -2 & 2 & -2 & 2 & -2 & 1 \\ 0 & 0.7286 & 1.6921 & 2.951 & 4.2098 & 5.1733 & 5.9019 \end{bmatrix}. \tag{4.15}$$

When this shaper is convolved with a step function that produces the maximum actuator effort, the resulting function is the MSBB EI command we are seeking.

The TO ZVD command for the same move distance is described by the input shaper [52]:

$$\begin{bmatrix} A_i \\ t_i \end{bmatrix} = \begin{bmatrix} 1 & -2 & 2 & -2 & 2 & -2 & 1 \\ 0 & 0.7124 & 1.6563 & 2.933 & 4.2097 & 5.1536 & 5.866 \end{bmatrix}. \tag{4.16}$$

Note that the MSBB EI command is only slightly longer than the TO ZVD command.

Figure 4.3 compares the sensitivity curve for the MSBB EI command given in (4.15) to the

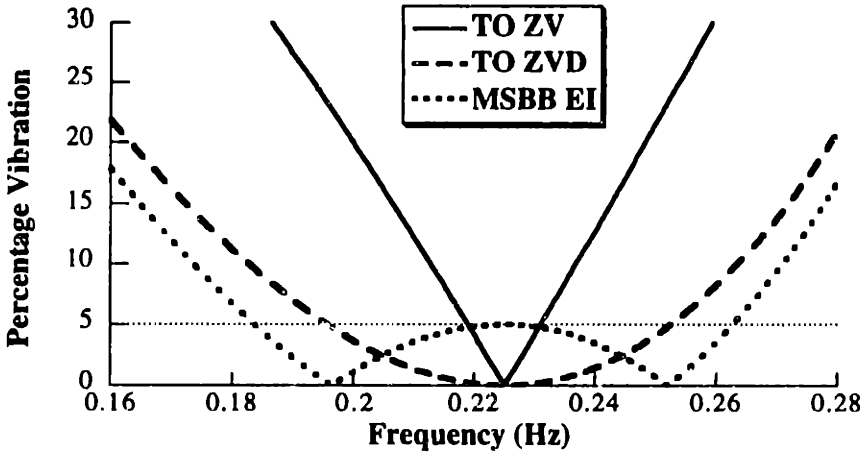

Figure 4.3: Sensitivity Curves for MSBB Commands.

sensitivity curves for the TO ZV command and the TO ZVD command given in (4.16). The 5% insensitivity for the ZV command is 0.0533, the 5% insensitivity for the ZVD command is 0.2523, and the EI command has a 5% insensitivity of 0.3511.[16] The EI insensitivity is 40% more than the ZVD and 660% more than with the ZV. Note that these values are not the same as those of Chapter 3. The commands of this chapter are subject to the additional amplitude constraints of (4.6) and the rigid-body constraints of (4.10) and (4.11). Therefore, it should not be surprising that the insensitivity values are different. Recall that the negative shapers of Section 3.5 had different robustness properties than their all-positive counterparts. As we will see, the robustness of minimum-time commands is highly dependent on the rigid-body constraints.

In general, increasing robustness requires increasing command length. The above ZV command has a duration of 4.218 sec., while the ZVD command has a duration of 5.866 sec. However, the increase in insensitivity obtained by switching from a TO ZVD command to a MSBB EI command comes with a minor time penalty (the EI command is 0.6% longer).

We can obtain an even more robust command by using the multi-hump EI robustness constraints. The two-hump EI command for V = 0.05 and $x_d = 1$ is described by:

$$\begin{bmatrix} A_i \\ T_i \end{bmatrix} = \begin{bmatrix} 1 & -2 & 2 & -2 & 2 & -2 & 2 & -2 & 1 \\ 0 & 0.592 & 1.51 & 2.726 & 3.886 & 5.045 & 6.261 & 7.179 & 7.771 \end{bmatrix} \tag{4.17}$$

The two-hump EI command has a 5% insensitivity of 0.6496. This is 260% more insensitive than the ZVD command. The significant increase in insensitivity is obtained with a 32% increase in command duration (7.771 sec. as compared to 5.866 sec.). Note that these insensitivities only apply when $x_d = 1$. If the move distance is varied, then the robustness will also vary. However, the EI commands will always be more robust than the ZVD commands. The insensitivity measures

[16] Recall that the insensitivity is obtained by measuring the width of the curve to get a frequency range and then dividing by the modeling frequency to get a nondimensional value.

Table 4.1: Rest-to-Rest Command Insensitivity.

Command	Length (sec)	5% Insensitivity
TO ZV	4.2179	0.0533
TO ZVD	5.8660	0.2523
MT MSBB EI	5.9019	0.3511
MT MSBB Two-Hump EI	7.7709	0.6496

for the above commands are summarized in Table 4.1. The specified insensitivity (SI) constraints of Section 3.3 can be used in a MSBB formulation to produce commands that have a known lower bound on their robustness. This straightforward extension will be used in Section 4.3.5 to counteract the dependence of command robustness on slew distance.

4.3.2 Evaluation of Rest-to-Rest Commands

A computer simulation of the system shown in Figure 4.1 was performed using the TO ZVD command, the MSBB EI command, and the MSBB two-hump EI command. Figure 4.4 compares the system response to the command signals when k, the spring constant, is varied from 0.6 to the nominal value of 1.0. The frequency changes from 0.174 Hz to 0.225 Hz during this parameter variation. The envelope on the residual vibration resulting from the one-hump EI command is only 69% of the value obtained with the ZVD command. The envelope resulting from the two-hump EI command is only 36% of the ZVD vibration envelope.

As a further test of the MSBB EI commands, we conducted hardware tests on a rotary table. A 24 in. steel beam was mounted to the table surface and a 2 lb. mass was attached to the end of the beam. The Inland torque motor used to rotate the table was equipped with an HP HEDS-6110 encoder that produced 44,000 counts per table revolution. The motor was powered by an Aerotech DS16020 amplifier and the control signals were generated by a Motion Engineering PC/DSP Motion Controller.

The table was moved with a bang-bang command and an FFT was performed on the residual vibration. The frequency spectrum showed a dominant low mode at approximately 2 Hz, and a second mode close to 8 Hz. Both modes had near zero damping. For the first test, the 8 Hz mode was neglected. A MSBB EI command was designed for 2 Hz, zero damping, V = 5%, and a 1 radian move. The input shaper for this command is:

$$\begin{bmatrix} A_i \\ t_i \end{bmatrix} = \begin{bmatrix} 1 & -2 & 2 & -2 & 2 & -2 & 1 \\ 0 & 0.1795 & 0.2388 & 0.4428 & 0.6467 & 0.706 & 0.8855 \end{bmatrix} \tag{4.18}$$

Figure 4.5 compares the response to the EI command and the response to a bang-bang command. The EI command reduced the vibration to about 16% of the unshaped level. This is certainly better than not using shaping, however, it is about three times the theoretical level of 5%. The deviation

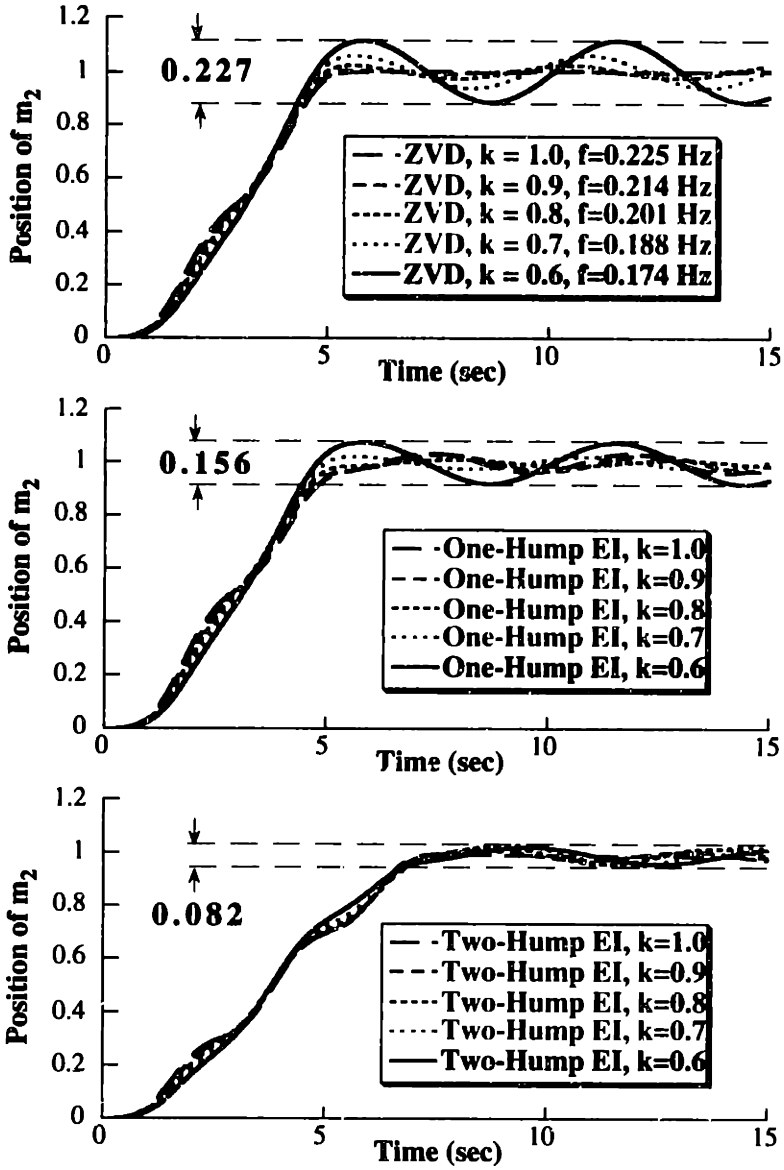

Figure 4.4: Responses to TO ZVD, MSBB EI, and MSBB Two-Hump EI Commands.

from theory can be largely explained by the presence of the unmodeled 8 Hz vibration, which is clearly visible in Figure 4.5. Section 4.4 will discuss MSBB commands for multi-mode systems. Experimental results showing the elimination of the 8 Hz mode will be presented there.

4.3.3 Multi-Switch Bang-Bang Extra-Insensitive Spin-Up Commands

As we know from earlier in this section, the constraint equations used to design spin-up commands are only slight variations on the constraints used for rest-to-rest motion. The impulse amplitude constraint of (4.6) is replaced with (4.8), a nonzero terminal velocity is used in (4.10), and (4.11) is not used.

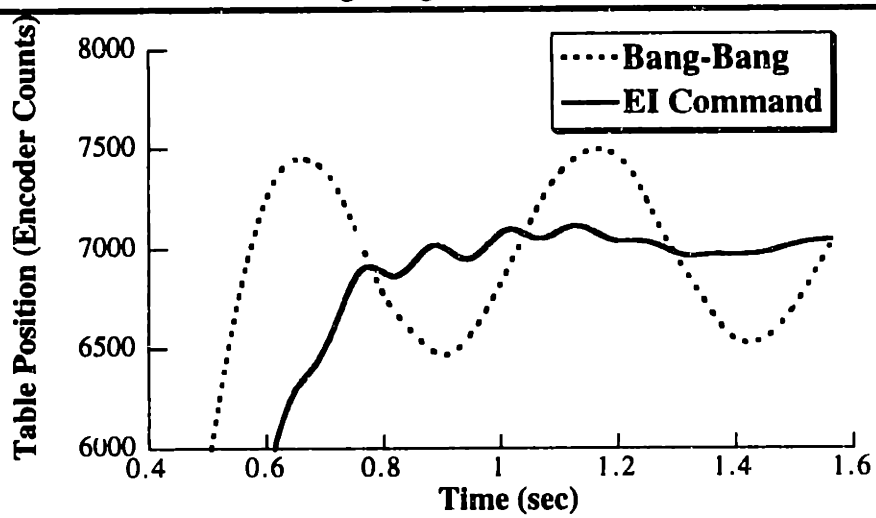

Figure 4.5: Experimental Responses to Bang-Bang and EI Commands.

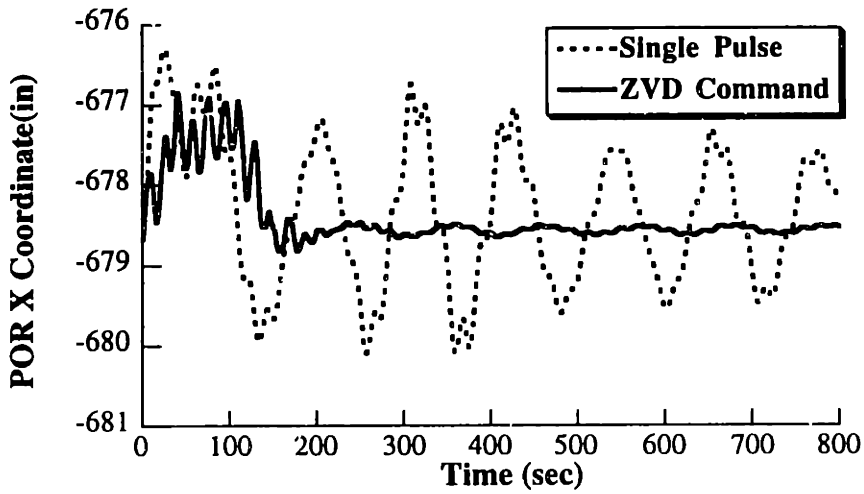

Figure 4.6: Oscillations of the Space Shuttle/Space Station System.

4.3.4 Evaluation of MSBB Spin-Up Commands

To test the minimum-time spin-up commands, tests were performed using Draper Laboratory's simulation (the DRS) of the Space Shuttle and its telerobotic manipulator. The DRS was developed over a period of ten years, and has been verified numerous times with actual shuttle flight data. The two simulations performed for this section included a section of a late 1992 model of the space station attached to the end of the Shuttle's remote manipulator.

The goal of the tests was to accelerate the shuttle/space station system up to a constant velocity. Because the jets used to move the space shuttle are on-off reaction jets, the MSBB commands generated with the above process can be used to accomplish the desired motion. The first simulation used a single jet firing of 38.4 seconds in duration. The second simulation used a TO ZVD command that produced the same terminal velocity as the single pulse. Figure 4.6 compares the responses to the unshaped and shaped commands. The vibration plotted in Figure 4.6 is the

POR (Point of Resolution) X coordinate. The POR is a position vector from the tip of the manipulator to a point fixed in the rigid-body reference frame of the shuttle. The oscillations in the POR are reduced by an order of magnitude with the shaped command. Much of the remaining residual vibration is from modes that were not modeled in the command design process.

4.3.5 Variation in Robustness of Minimum-Time Commands

As mentioned previously, the robustness of minimum-time commands is highly dependent on the desired motion. Figure 4.7 shows two different sensitivity curves of rest-to-rest TO ZVD commands for the benchmark system. One command was designed for a move distance of 6 units and the other for a move distance of 12 units. Although both commands meet the constraint of zero derivative at the modeling frequency, the command designed for a move distance of 12 units provides much better robustness to modeling errors. It keeps the vibration to below 5% over the frequency range from 0.187 Hz to 0.237 Hz. On the other hand, the command designed for a move distance of 6 units keeps the vibration to below 5% only over the range from 0.216 Hz to 0.233 Hz. To explore this effect further, Figure 4.8 shows the 5% insensitivity of the TO ZVD command over a range of move distances. Not only does the insensitivity vary considerably, but it is very small over a wide range of move distances.

The EI robustness constraints will produce a more robust command that is roughly the same length as the TO ZVD command. However, the lower bound on the robustness is unknown. To generate a MSBB command with a known lower bound on insensitivity, the SI robustness constraints can be used. Figure 4.9 shows the 5% insensitivity of the MSBB SI command when the insensitivity is specified to be at least 0.12. Figure 4.10 shows that the duration of this command is roughly the same as the duration of the TO ZVD command. Notice that for some move distances the SI command is slightly shorter than the TO ZVD command. By lowering the minimum level of insensitivity, the duration of the MSBB SI command can be lowered further. On the other hand, increasing the minimum insensitivity causes the command duration to increase.

4.3.6 Summary of Multi-Switch Bang-Bang Commands

The input shaping method can be modified to produce multi-switch bang-bang commands. The modified technique can produce commands for rest-to-rest slews or spin-up motions. The robustness of MSBB commands can vary considerably with the desired motion. However, the MSBB EI commands are significantly more robust to modeling errors than time-optimal commands based on the zero derivative robustness constraints. The specified-insensitivity robustness constraints can be used to produce a MSBB command with a known lower bound on insensitivity. Simulations and experiments have demonstrated the effectiveness of the robust MSBB commands.

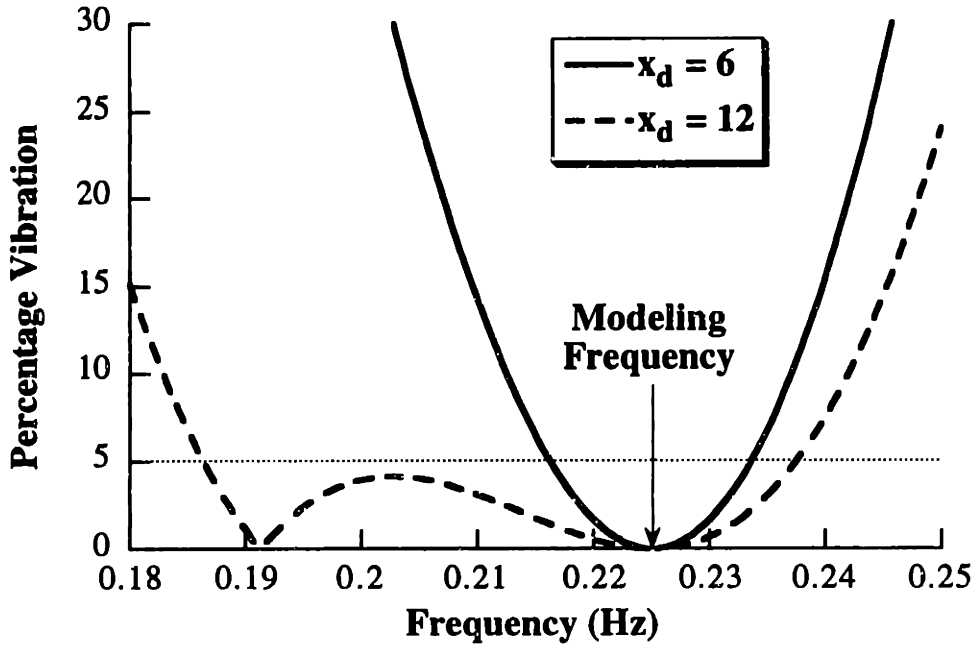

Figure 4.7: Sensitivity Curves of Time-Optimal ZVD Commands.

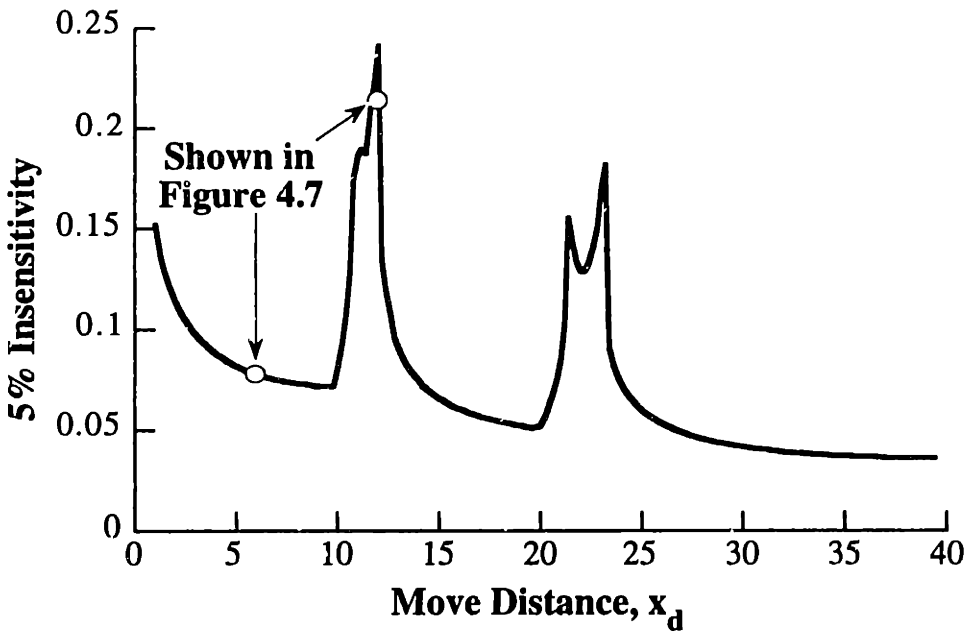

Figure 4.8: Time-Optimal ZVD 5% Insensitivity.

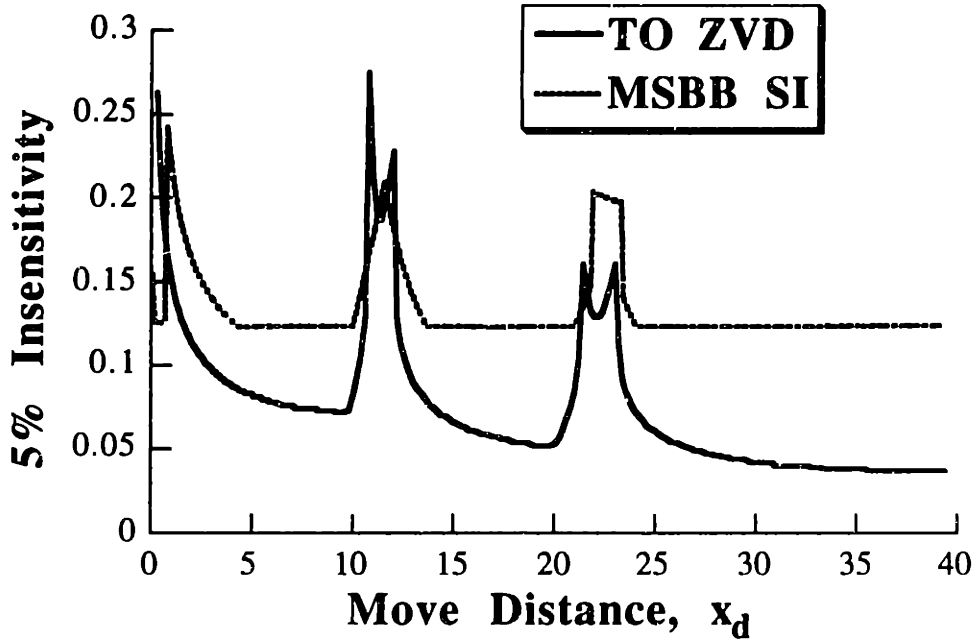

Figure 4.9: 5% Insensitivity of the MSBB SI (I=0.12) Command.

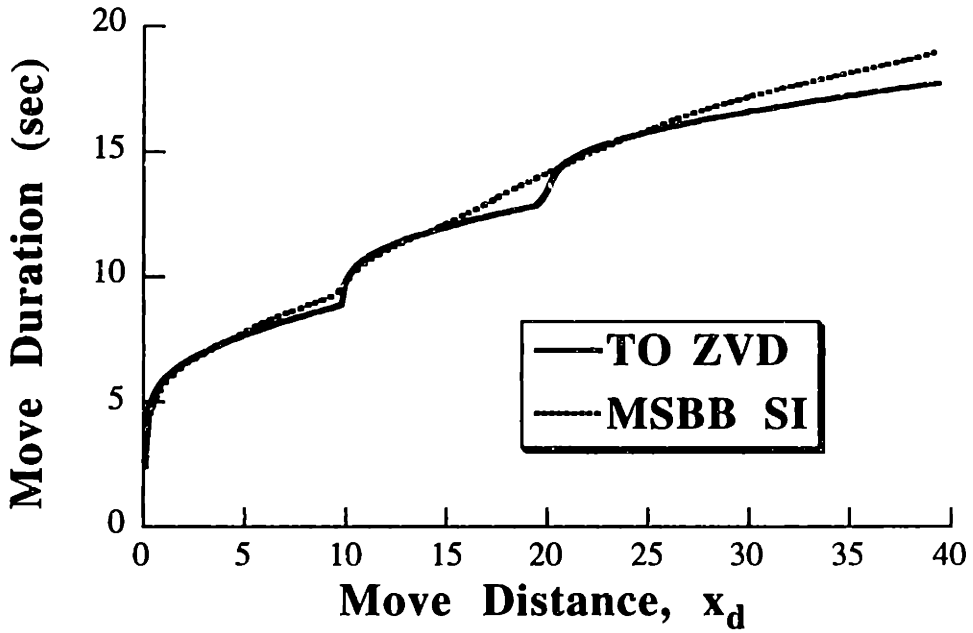

Figure 4.10: Comparison of TO ZVD and MSBB SI Slew Duration.

4.4 Robust MSBB Commands for Multi-Mode Systems

The previous section demonstrated the use of input shaping to generate several types of MSBB commands for a system with a single flexible mode. This section investigates MSBB commands for multi-mode flexible systems. Characteristics of the solution space for two-mode systems will be discussed and then the robustness of TO ZVD commands will be investigated. It will be shown that the robustness to errors in the second mode is highly dependent on the mode ratio. This result, once again, suggests that EI and SI robustness constraints are more useful than zero derivative robustness constraints.

4.4.1 Formulation of Multi-Mode MSBB Input Shaping

For the k^{th} mode of natural frequency, ω_k, and damping ratio, ζ_k, the percentage vibration relative to a step function is given by:

$$V(\omega_k,\zeta_k) = e^{-\zeta_k\omega_k t_n}\sqrt{[C(\omega_k,\zeta_k)]^2+[S(\omega_k,\zeta_k)]^2} \tag{4.19}$$

where,

$$C(\omega_k,\zeta_k) = \sum_{i=1}^{n} A_i e^{\zeta_k\omega_k t_i}\cos(\omega_k\sqrt{1-\zeta_k^2}\,t_i) \tag{4.19a}$$

$$S(\omega_k,\zeta_k) = \sum_{i=1}^{n} A_i e^{\zeta_k\omega_k t_i}\sin(\omega_k\sqrt{1-\zeta_k^2}\,t_i). \tag{4.19b}$$

The zero vibration constraints for j modes are then j versions of (4.19) with V set equal to zero.

In addition to limiting residual vibration amplitude, ZVD commands require the derivative with respect to the frequency of the residual vibration be equal to zero. For the multiple-mode case:

$$0 = \frac{d}{d\omega_k}(V(\omega_k,\zeta_k)), \qquad k=1,\ldots,j. \tag{4.20}$$

Constraints on the rigid-body motion are also needed. For a system modeled as a series of masses, springs, and dampers, the rigid-body constraints are those given in (4.10) and (4.11).

4.4.2 Experimental Verification of Multi-Mode MSBB Commands

Recall that the experiments with the rotary table discussed in Section 4.3 revealed the need to cancel two-modes of vibration. The problem of the 8 Hz vibration is not surprising if we examine the command's sensitivity curve over a region that includes 8 Hz. Figure 4.11 shows that the command will cause an amplification of the 8 Hz mode; the theoretical vibration level at 8 Hz is ten times more than for a step input.

We can eliminate the second mode at 8 Hz by adding a constraint equation limiting the amplitude of its residual vibration. An appropriate constraint is a ZV constraint at the second mode:

$$0 = e^{-\zeta\omega_2 t_n}\sqrt{(C(\omega_2,\zeta))^2+(S(\omega_2,\zeta))^2} \tag{4.21}$$

where $\omega_2 = 2\pi$*(8 Hz). The solution to this augmented set of constraints is:

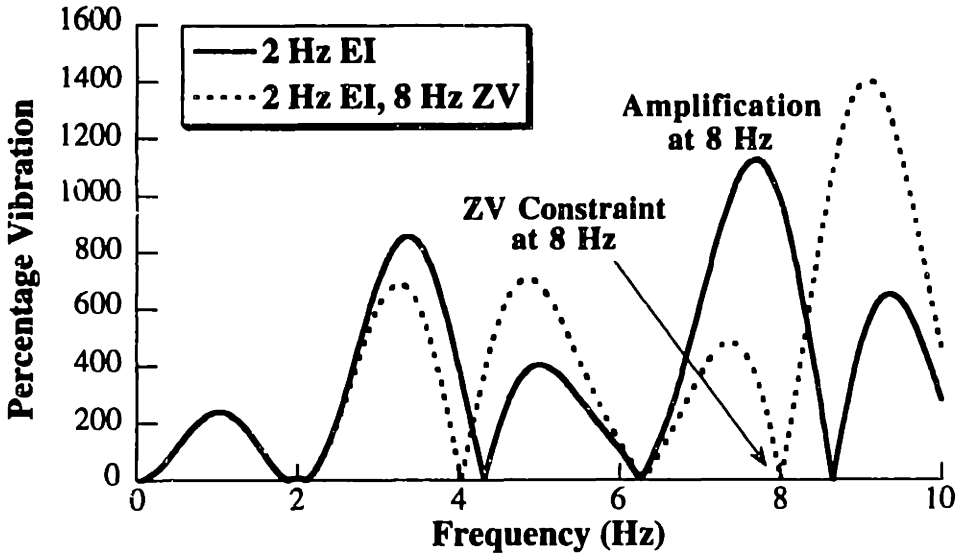

Figure 4.11: Sensitivity Curves for the EI Command and the EI Command with an 8 Hz ZV Constraint.

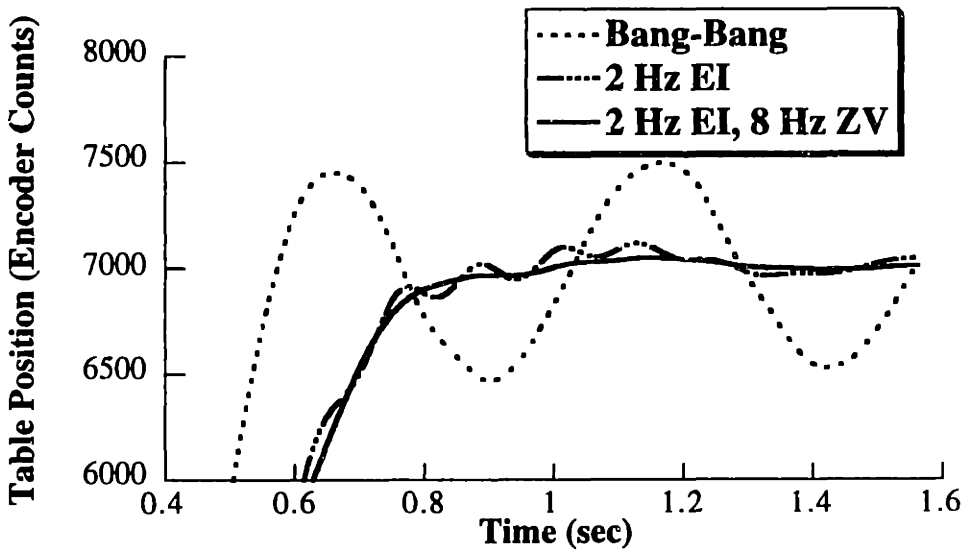

Figure 4.12: Rotary Table Response Using the EI Command with an 8 Hz ZV Constraint.

$$\begin{bmatrix} A_i \\ t_i \end{bmatrix} = \begin{bmatrix} 1 & -2 & 2 & -2 & 2 & -2 & 2 & -2 & 1 \\ 0 & 0.171 & 0.227 & 0.408 & 0.446 & 0.483 & 0.664 & 0.720 & 0.891 \end{bmatrix} \tag{4.22}$$

Comparing (4.22) and (4.18) we find that the command length has increased less than 1% to satisfy this multiple-mode formulation. The sensitivity curve for this command is compared to the original EI command in Figure 4.11.

Figure 4.12 demonstrates that the EI command with the 8 Hz limitation virtually eliminates the high-mode vibration from the response of the rotary table. The residual vibration amplitude is now

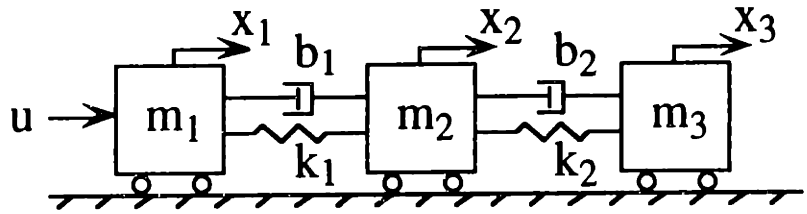

Figure 4.13: Simple Model of a System with Two Flexible Modes.

approximately 5.6% of the unshaped level, very close to the theoretical level of 5%. If it had been necessary, robustness constraints could have been applied to the 8 Hz mode.

4.4.3 Characteristics of Multi-Mode TO ZVD Shaping

The time-optimal multi-mode ZVD shaper for rest-to-rest motion is obtained by satisfying the constraints described above. The amplitudes of the shaper impulses are given by (4.6). The time locations of the impulses are obtained by satisfying (4.19) for each mode with V = 0, (4.20) for each mode, and the rigid-body constraints, while using a numerical optimization to minimize t_n. The solution is a function of the frequencies (ω_k), the damping ratios (ζ_k), the move distance (x_d), and the maximum acceleration (a_m). Characteristics of the solution space will be investigated by varying the move distance and the mode ratio.

Basing the problem formulation on the model shown in Figure 4.13, the force-to-mass ratio is fixed by setting the total mass equal to one and then setting u_{max} equal to the desired value of maximum acceleration, a_m. The values of the masses and spring constants are chosen such that the low mode equals 1 Hz and the second mode equals r Hz. The damping constants are set equal to zero to give undamped behavior.

Figure 4.14 shows the impulse time locations (switch times) of the TO ZVD command as a function of r when $x_d = 0.5$ and $a_m = 1$. As r increases, the slew duration tends to decrease (the time location of the final impulse, t_{11}, is decreasing). The maneuver time decreases rapidly as r increases from 1 to 2, but then levels off.

When the solutions are plotted as a function of move distance, the solution can have various degrees of complexity depending on the mode ratio. To illustrate the most general features, r will be set equal to 4.4. Figure 4.15 shows the impulse time locations when x_d is varied. For certain ranges, both the number of impulses and their time locations change rapidly.

In the regions where the solution changes rapidly, finding the time-optimal solution can be difficult because there are many alternate solutions that are very nearly time-optimal. Fortunately, a procedure for verifying the time-optimality of numerically obtained solutions has been developed and will be discussed in Section 4.5. This procedure was used to verify the solutions shown in Figures 4.14 and 4.15.

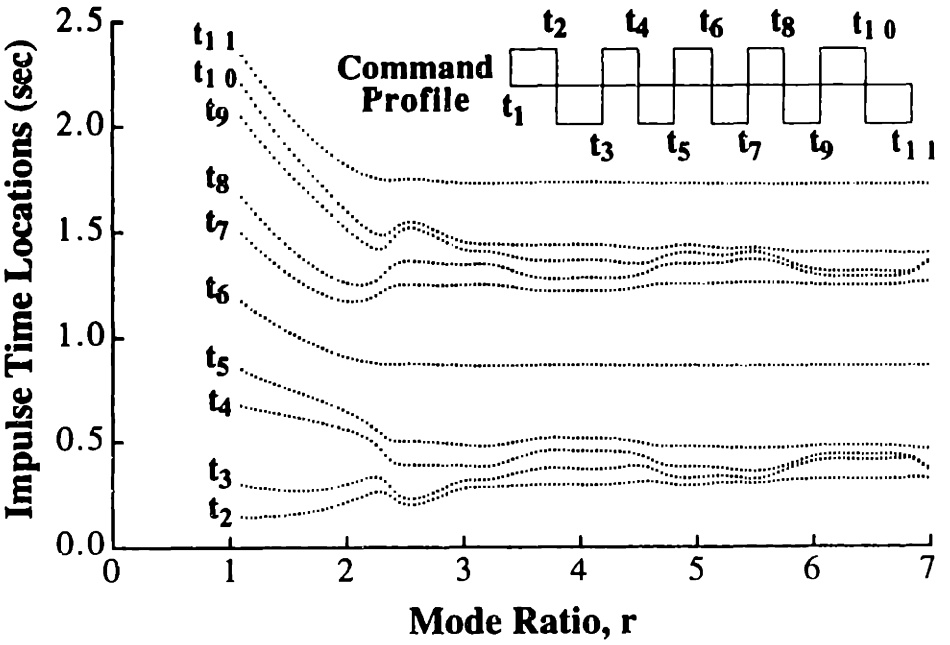

Figure 4.14: Impulse Times as a Function of Mode Ratio (x_d = 0.5 and a_m = 1).

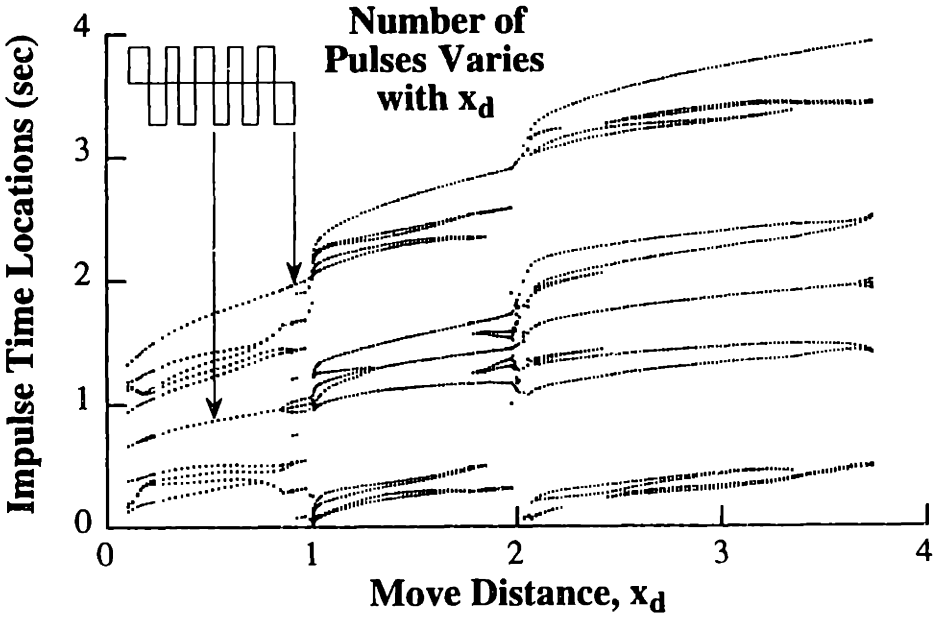

Figure 4.15: Impulse Times as a Function of Move Distance (r = 4.4 and a_m = 1).

4.4.4 Robustness of Multi-Mode MSBB Commands

Although the zero derivative constraint attempts to produce robustness to modeling errors, the degree of robustness is not specified and it can vary considerably. Figure 4.16 shows two normalized sensitivity curves for the system of Figure 4.13; one curve is normalized by the 1 Hz

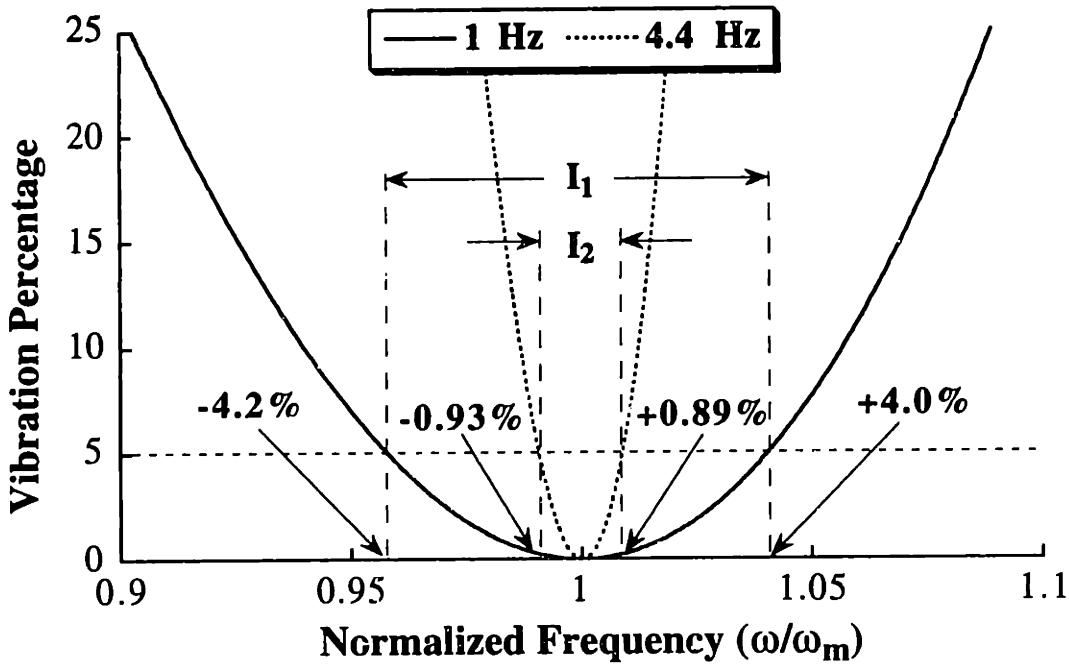

Figure 4.16: Calculation of 5% Insensitivity.

mode and the other by the 4.4 Hz mode. These curves show the residual vibration over a range that is ±10% of each mode. If we assume that 5% residual vibration is acceptable, then the 1 Hz mode can deviate +4.0% and -4.2%. This frequency range is called the 5% insensitivity for the low mode, I_1. In this case, $I_1 = 0.082$. The second mode can vary only +0.89% and -0.93%. That is, $I_2 = 0.0182$. Although ZVD constraints are enforced at both modes, the robustness to modeling errors is over four times better for the low mode.

Figure 4.17 shows both I_1 and I_2 as a function of the mode ratio when $x_d = 0.5$ and $a_m = 1$. This data corresponds to the commands shown in Figure 4.14. While the insensitivity for the low mode is well behaved and remains at a nearly constant level for most mode ratios, the second mode insensitivity varies greatly and is very low for the majority of mode ratios. This problem can be avoided by using the specified-insensitivity robustness constraints.

4.4.5 Discussion of Multi-Mode TO ZVD Commands

The complicated nature of the solution space for time-optimal ZVD commands has been illustrated and the robustness of the commands to modeling errors has been investigated. The robustness to errors in the second mode varies greatly and is poor for large ranges of the system parameters. These results indicate that robustness techniques for multi-mode systems that are based on the zero derivative constraint may not be effective for all parameter values. The methods of Chapter 3 for specifying the robustness should be employed for these types of problems.

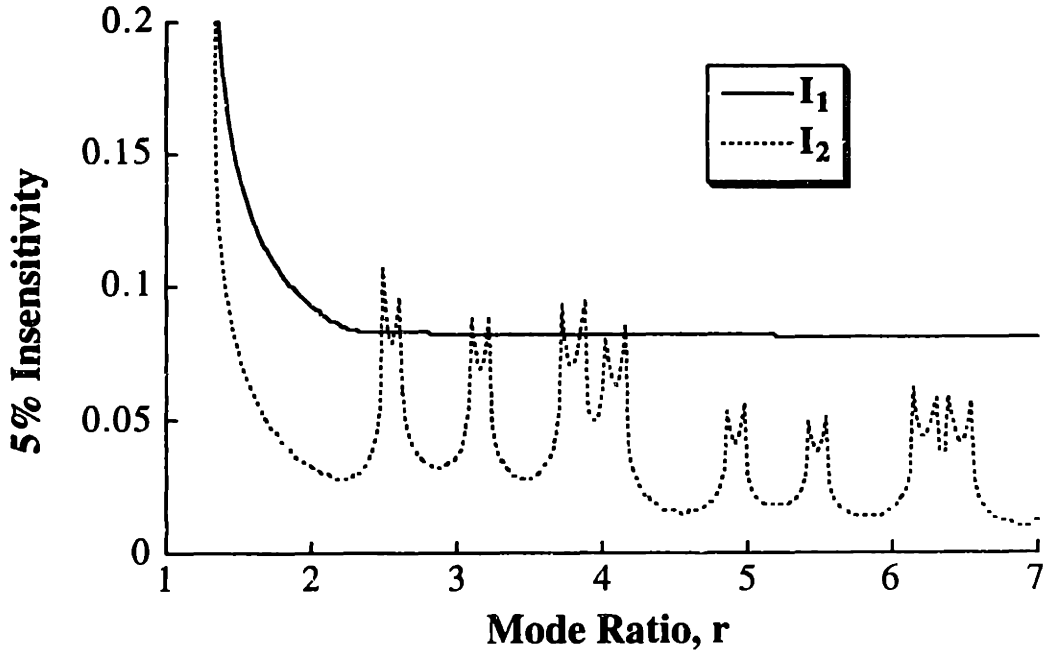

Figure 4.17: Time-Optimal ZVD Insensitivity as a Function of Mode Ratio (x_d = 0.5 and a_m = 1).

4.5 Numerical Verification of Robust Time-Optimal Commands

Consider again the system shown in Figure 4.13 with the parameter values used in the previous section. Figure 4.18 shows the switch times of the time-optimal ZVD command over the small range of $1.96 \le x_d \le 2.06$. (This is a close-up of the information shown in Figure 4.15.) The number of switches and their time locations change in a complicated manner.

The optimal switch times (including the switches at the start and end of the command) for the case of $x_d = 2.02$ are:

$$t_i = \begin{matrix}[0 & 0.042332 & 0.048551 & 1.09422 & 1.27463 & 1.42838 & 1.44837 & 1.51773 \\ & 1.58709 & 1.60709 & 1.76083 & 1.94125 & 2.98692 & 2.99314 & 3.03547]\end{matrix} \tag{4.23}$$

These switch times were obtained by performing a numerical optimization to minimize the command duration while satisfying the constraint equations described in the previous section. If the initial guesses used for the nonlinear optimization are changed slightly, then the optimization finds a local minimum and returns switch times of:

$$t_i = \begin{matrix}[0 & 0.05339 & 0.06250 & 1.04164 & 1.04313 & 1.10669 & 1.29053 & 1.5209 \\ & 1.75127 & 1.93512 & 1.99867 & 2.000162 & 2.97931 & 2.98841 & 3.0418]\end{matrix} \tag{4.24}$$

Note that the command duration (the final t_i) is slightly longer than for the true time-optimal command of (4.23). In general, local minima can yield profiles that are considerably longer and have more or fewer switches than the true time-optimal command.

4.5.1 Algorithm for Verification of Numerical Solutions

We know that the solution space for time-optimal ZVD commands for multi-mode systems is very complicated. Here we present a method for verifying the time-optimality of a prospective solution.[17] Using this method we can discard local minimum solutions such as that of (4.24) and continue searching for the global optimum.

Pontryagin's maximum principle [85] gives the following sufficient and necessary conditions for the time-optimal control, $u^*(t)$:

$$\dot{\mathbf{p}}^*(t) = -\mathbf{F}^T \mathbf{p}^*(t) \qquad t \in [0, t_n^*] \tag{4.25}$$

$$u^*(t) = -u_{max}\, \mathrm{sgn}\left(\mathbf{g}^T \mathbf{p}^*(t)\right) \qquad t \in [0, t_n^*] \tag{4.26}$$

$$H\left(t_n^*\right) = 0 \tag{4.27}$$

where H is the Hamiltonian, $\mathbf{p}(t)$ is the costate vector, t_n is the maneuver time, and the * denotes the optimal solution.

To verify the time optimality of ZV commands, we would consider the system represented by (4.1) - (4.4). However, it has been shown that the time-optimal ZVD command is equivalent to

[17] The procedure in this subsection was first suggested by, and largely developed by Professor Lucy Y. Pao [81].

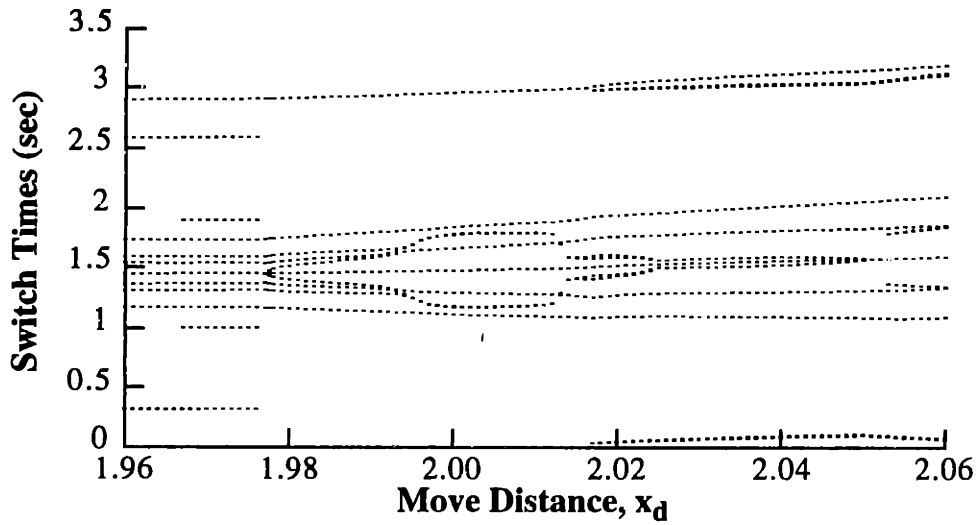

Figure 4.18: Time-Optimal ZVD Switch Times as a Function of Move Distance.

the time-optimal ZV command of a related flexible system that has double poles at each of the flexible poles of the original system [13, 80, 111]. Thus, to verify the optimality of the TO ZVD command, we consider an augmented system where:

$$\mathbf{F}_j = \begin{bmatrix} 0 & 1 & 0 & 1 \\ -\omega_j^2 & -2\zeta_j\omega_j & 0 & 0 \\ 0 & 0 & 0 & 1 \\ 0 & 0 & -\omega_j^2 & -2\zeta_j\omega_j \end{bmatrix} \qquad j = 1,\ 2,\ldots,\ m \tag{4.28}$$

$$\mathbf{g} = \begin{bmatrix} g_0 & 0 & g_{1a} & 0 & g_{1b} & \ldots & 0 & g_{ma} & 0 & g_{mb} \end{bmatrix}^T \tag{4.29}$$

$$\mathbf{h} = \begin{bmatrix} h_0 & h_{1a} & 0 & h_{1b} & 0 & \ldots & h_{ma} & 0 & h_{mb} & 0 \end{bmatrix} \tag{4.30}$$

The sufficient and necessary conditions for the time-optimal ZV command of this augmented system are still those given in (4.25)-(4.27). After the optimization routine obtains a candidate solution, (4.25)-(4.27) can be used to test whether the solution is indeed the time-optimal solution.

The optimality check provided by the necessary and sufficient conditions can be implemented numerically using the following procedure. First, using (4.25) and (4.26), calculate a matrix **P**, where each row is given by:

$$\mathbf{P}(i) = \mathbf{g}^T \exp\left(-\mathbf{F}^T t_i\right) \qquad i = 1,\ldots,n-1 \tag{4.31}$$

The quantity $\mathbf{Pp}(0)$ represents a vector of the switching function ($\mathbf{g}^T\mathbf{p}(t)$) values at the control switch times. Hence, $\mathbf{Pp}(0)$ must be the zero vector and $\mathbf{p}(0)$, the initial costate, must lie in the nullspace of **P**. If the nullspace is empty, then the solution is not optimal. If the nullspace has more than one column and the transversality condition (4.27) does not reduce the subspace to one column, then the solution is again not optimal.

If the nullspace has one column, proceed by calculating the switching function from 0 to t_n:

$$swfn(t) = \mathbf{g}^T\mathbf{p}(t) = \mathbf{g}^T\exp\left(-\mathbf{F}^T t\right)\mathbf{q} \tag{4.32}$$

where $\mathbf{q}$ is the nullspace of $\mathbf{P}$. Finally, determine the time locations at which the switching function changes sign. If these switches correspond to the switch times of the command, then the solution is the unique time-optimal solution. The resolution of the time spacing used to calculate the switching function must be small enough so that every switch is detected. In practice it is useful to use a variable time step that decreases in value as the switching function approaches zero.

Figure 4.19 shows the command profile described by (4.23) and the corresponding switching function. Each time the switching function crosses zero, the sign of the command changes value. The changes of sign in the switching function near the middle of the command are difficult to see, but zooming in on the data reveals a match between zero crossings of the switching function and command switches. In this example, the system matrix is $\mathbf{F} = [\mathbf{F}_0, \mathbf{F}_1, \mathbf{F}_2]$ where $\mathbf{F}_0$ is given by (4.3) and $\mathbf{F}_1$ and $\mathbf{F}_2$ are given by (4.28) with $\omega_1 = 2\pi$, $\omega_2 = 4.4\omega_1$, and $\zeta_1 = \zeta_2 = 0$. The input vector (4.29) is chosen as:

$$\mathbf{g} = \left[0 \quad \frac{1}{3} \quad 0 \quad \frac{1}{3} \quad 0 \quad \frac{1}{3} \quad 0 \quad \frac{1}{3} \quad 0 \quad \frac{1}{3}\right]^T. \tag{4.33}$$

The P matrix, computed according to (4.31) with the switch times in (4.23), is then:

$$\mathbf{P} = \begin{bmatrix}
-0.0141 & 0.3333 & -0.0277 & 0.3100 & -0.0139 & 0.3216 & -0.0194 & -0.0497 & -0.0111 & 0.1300 \\
-0.0162 & 0.3333 & -0.0316 & 0.3027 & -0.0159 & 0.3179 & -0.0194 & -0.1424 & -0.0117 & 0.0755 \\
-0.3647 & 0.3333 & -0.1957 & -0.3628 & -0.0296 & 0.2766 & -0.0554 & 4.7641 & 0.0111 & 0.1316 \\
-0.4249 & 0.3333 & -0.0459 & -1.3702 & -0.0524 & -0.0514 & 0.1764 & 3.4382 & 0.0076 & -0.2590 \\
-0.4761 & 0.3333 & 0.1797 & -0.9508 & -0.0231 & -0.3001 & 0.0341 & -6.4966 & -0.0118 & -0.0725 \\
-0.4828 & 0.3333 & 0.2034 & -0.7994 & -0.0169 & -0.3159 & 0.1554 & -5.0154 & -0.0086 & -0.2325 \\
-0.5059 & 0.3333 & 0.2602 & -0.1546 & 0.0059 & -0.3313 & 0.1268 & 6.1443 & 0.0108 & -0.1457 \\
-0.5290 & 0.3333 & 0.2673 & 0.5801 & 0.0276 & -0.2847 & -0.2611 & 1.1021 & 0.0013 & 0.3315 \\
-0.5357 & 0.3333 & 0.2591 & 0.7882 & 0.0331 & -0.2607 & -0.2493 & -2.9026 & -0.0052 & 0.3005 \\
-0.5869 & 0.3333 & 0.0594 & 1.8623 & 0.0529 & 0.0227 & 0.0224 & 8.1075 & 0.0121 & -0.0049 \\
-0.6471 & 0.3333 & -0.2730 & 1.0444 & 0.0191 & 0.3109 & 0.3173 & 1.9839 & 0.0031 & -0.3221 \\
-0.9956 & 0.3333 & -0.4896 & 0.5890 & 0.0044 & 0.3322 & -0.3255 & -10.5295 & -0.0094 & 0.2085 \\
-0.9977 & 0.3333 & -0.4950 & 0.4681 & 0.0023 & 0.3330 & -0.2567 & -11.9169 & -0.0106 & 0.1609
\end{bmatrix} \tag{4.34}$$

and, $\mathbf{q} = [-0.1402 \ -0.2128 \ 0.2467 \ 0.0044 \ -0.7380 \ 0.1786 \ 0.0118 \ 0.0009 \ -0.5454 \ 0.0069]^T$ (4.35)

lies in the nullspace of $\mathbf{P}$. The switching function is then computed according to (4.32) and the result is that shown in Figure 4.19.

If the switching function has more zero crossings than the command has switches, then the time locations of the crossings can be used as the initial guesses for a subsequent optimization. For the false solution of (4.24), the switching function has extra zero crossings. This discrepancy is shown in Figure 4.20. Using these extra zero crossings and the switch times of the false solution as initial guesses, the true time-optimal solution given by (4.23) was obtained.

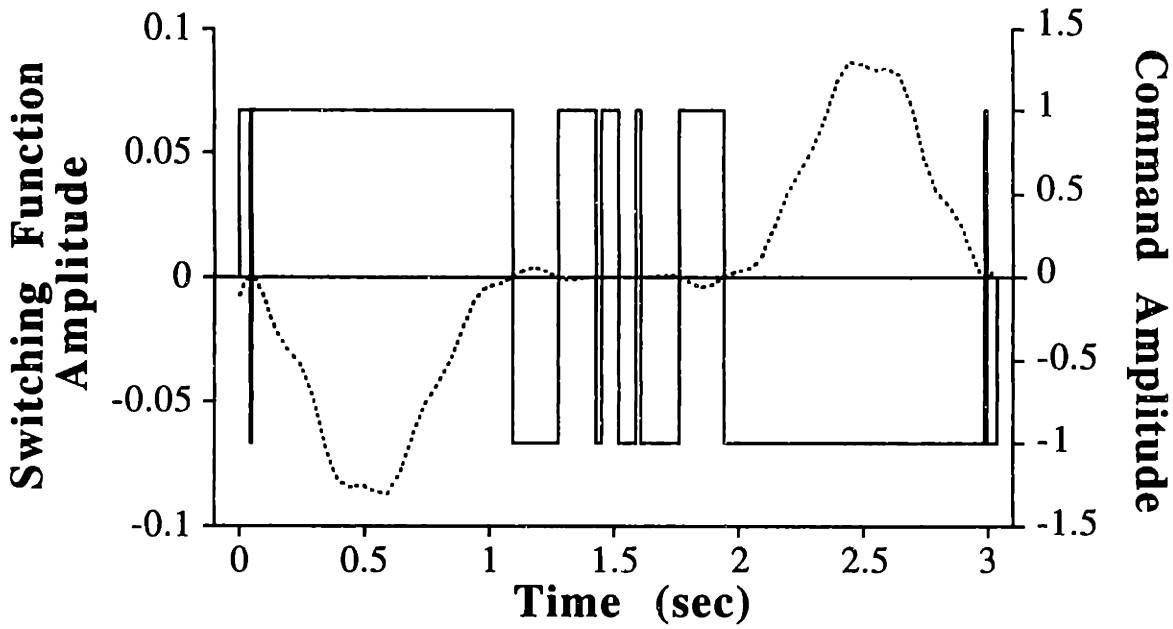

Figure 4.19: Optimal Command and Corresponding Switching Function.

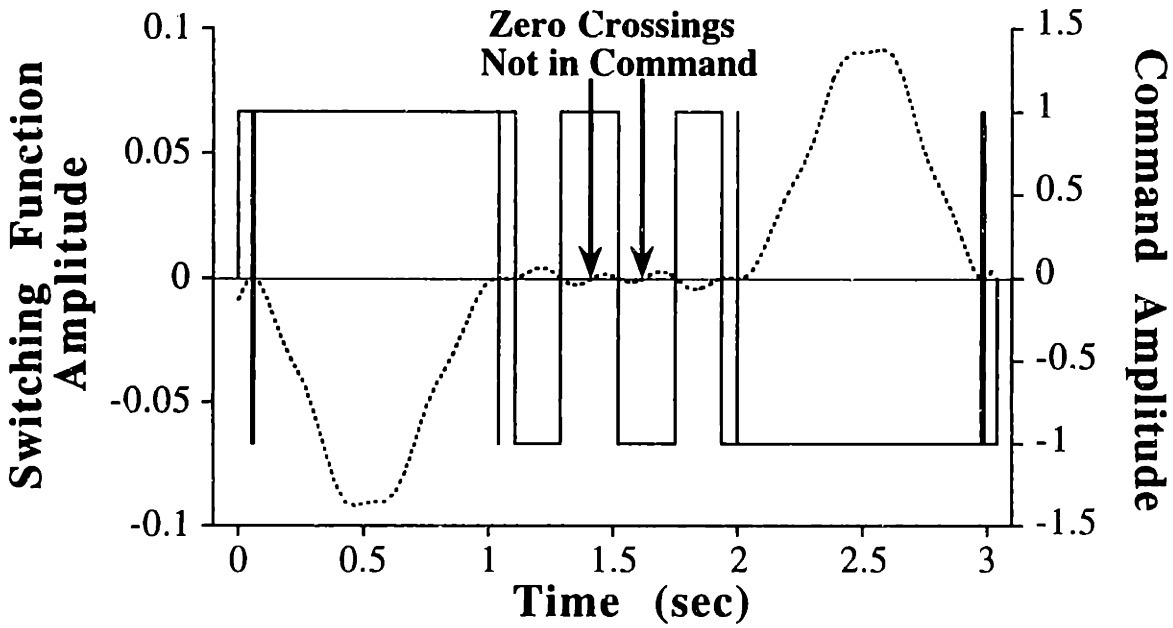

Figure 4.20: Non-Optimal Command and Switching Function.

4.5.2 Discussion of Numerical Verification Method

A procedure for verifying numerically-obtained, time-optimal command profiles for linear multi-mode flexible systems has been presented. The need for such a procedure arises because the nonlinear optimization generally required to obtain time-optimal commands is susceptible to being caught in local minima. Examples have been presented that show the multiplicity of possible solutions and the effectiveness of the proposed method for eliminating sub-optimal solutions.

5 ON-OFF CONTROL OF FLEXIBLE SYSTEMS

5.1 Introduction to On-Off Control

The time-optimal and minimum-time multi-switch bang-bang commands presented in Chapter 4 are a subset of a larger class of commands referred to as on-off control. On-off commands are either a constant positive value, zero, or a constant negative value. The minimum-time commands are a subset that do not contain periods when the actuator effort is zero.

The need for on-off command generators arises in three distinct cases. In some systems, the actuators cannot produce a variable amplitude force (or torque). An example of such actuators are the reaction jets used to move spacecraft. Other types of actuators such as pneumatic and hydraulic cylinders may be treated as on-off actuators in some cases. Another need for on-off control arises when the controller is attempting to perform some type of minimum-time control, as we saw in the previous chapter. Furthermore, optimal commands that weight both fuel usage and move time are on-off functions for many types of linear systems [69, 104, 105, 166]. The final need for on-off control occurs when the transient deflection of the system is being limited to a specific value. By requiring the command to be on-off in nature, the deflection of the system can be limited to a desired value much easier than if the command is allowed to have a variable amplitude.

In certain applications, such as those involving spacecraft, we are concerned not only with accomplishing motion free of residual vibration, but we also care about the amount of fuel used to perform the motion. The minimum-time commands developed in the previous chapter are not acceptable in such applications because they use fuel throughout the motion (the command is always nonzero). Methods for designing shaped commands that limit the fuel usage are discussed in Sections 5.2 and 5.3. In other types of applications the amplitude of transient deflection that the system experiences is of vital importance. All of the command generating methods discussed so far have only controlled the residual vibration. It may happen that the residual vibration is eliminated, but the transient deflection is large enough to damage the system or to cause the endpoint of the system to deviate substantially from a desired path. Techniques for limiting the amplitude of transient deflection are described in Section 5.4.

5.2 Fuel-Efficient On-Off Commands

This section presents a new procedure for designing command profiles that are considerably more fuel efficient than the minimum-time commands previously reported in the literature and in Chapter 4. The command profiles that are generated by the new technique are nearly the same duration as the purely minimum-time commands. If the large fuel savings are considered, the new command profiles are very attractive alternatives to the minimum-time solutions. The simple model representing a flexible system that has been used previously in Chapter 4 and in the references will be used again to evaluate the new profiles and to compare their performance with the techniques previously reported.

5.2.1 Fuel-Efficient Spin-Up Commands

The constraint equations used to develop the commands in this section can be categorized as follows: (1) Constraints on rigid-body motion (2) Residual vibration constraints (3) Robustness constraints (4) Time-optimality constraint and (5) Fuel-efficiency constraints. Note that there is not a separate category for impulse amplitude constraints. As it turns out, the fuel-efficiency constraints act as amplitude constraints. The rigid-body constraints are those given by (4.10) and (4.11). The residual vibration constraints are those given by (4.12) with V = 0. The zero derivative constraint of (4.14) will be used to obtain robustness. The extra-insensitive and specified insensitivity constraints will not be used in this section so that we may concentrate on fuel usage issues.

We know that to generate the minimum-time command for motions that accelerate to a constant velocity (spin-up maneuvers), an input shaper must have the form given by (4.7). Furthermore, the shaper must be convolved with a step input of magnitude u_{max}. The number of impulses, n, in the shaper depends on the type of robustness constraints that are used in the shaper design and the desired terminal velocity, v_d.

The commands developed in this section are motivated by the fact that the minimum-time command profiles use fuel throughout their duration. We postulate that command profiles that contain only positive pulses and allow periods of coasting can accelerate the system to a constant velocity and robustly reduce residual vibration, while being only slightly longer than the minimum-time commands. Therefore, the proposed fuel-efficient shaper for spin-up motions is given as:

$$\begin{bmatrix} A_i \\ t_i \end{bmatrix} = \begin{bmatrix} 1 & -1 & 1 & \dots & 1 & -1 \\ 0 & t_2 & t_3 & \dots & t_{n-1} & t_n \end{bmatrix} \tag{5.1}$$

where n is even.

The constraints for the new command profiles are the same as for the minimum-time commands

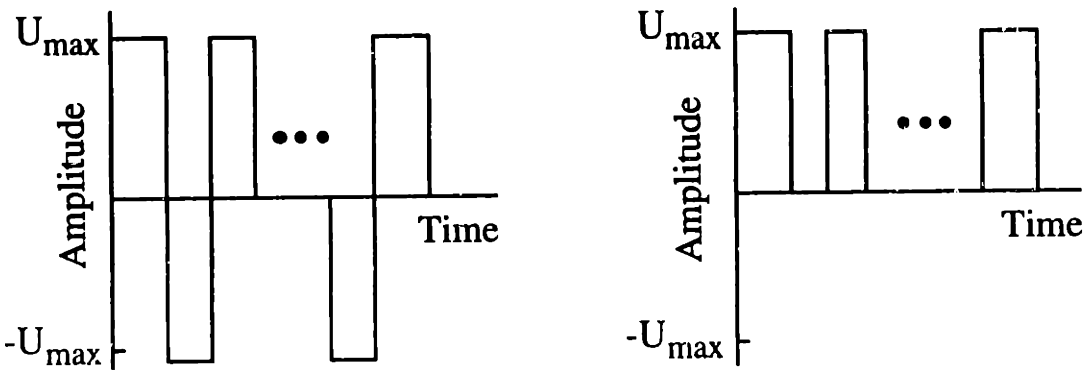

Minimum-Time Command Fuel-Efficient Command

Figure 5.1: On-Off Spin-Up Command Profiles.

except that the amplitude constraints of (4.8) are replaced with the fuel-efficiency (amplitude) constraints of (5.1). The command profiles generated by (5.1) are compared to the minimum-time commands in Figure 5.1. Unlike the fuel-efficient profiles, the minimum-time profiles generate forces in the direction opposite to the desired velocity. While negative pulses are required to slow down a system in rest-to-rest slews, they are not required for spin-up maneuvers. The presence of the negative pulses in spin-up commands leads to large fuel expenditures.

Note that a command profile that contains only positive pulses is not only more fuel-efficient than the minimum-time command, it is the *fuel-optimal* solution. The final velocity is simply the time integral of the command profile divided by the system mass, see (4.10). Therefore, for a given terminal velocity, fuel usage is minimized when the command contains only positive pulses.

Using the fuel-efficiency constraint of (5.1), spin-up commands were designed for the system of Figure 4.1 with parameter values $m_1 = m_2 = k = u_{max} = 1$. Figure 5.2 compares the command durations for the time-optimal and fuel-efficient ZV and ZVD commands for the range of $0.1 \leq v_d \leq 6$. Figure 5.2a reveals that the fuel-efficient ZV profiles are essentially time optimal for all spin-up velocities greater than about 1.2 units/sec. For velocities greater than 1.2, the length of the fuel-efficient profile is at most 1.2% longer than the time-optimal profile. Furthermore, the average duration is only 0.24% longer than the time-optimal over the range $1.2 \leq v_d \leq 6$.

Figure 5.2b shows that the fuel-efficient ZVD profiles are nearly time optimal for all spin-up velocities greater than about 1.7 units/sec. Above $v_d = 1.7$, the length of the fuel-efficient profile is at most 1.8% longer than the time-optimal profile, while the average duration is only 1.0% longer than the time-optimal over the range $1.7 \leq v_d \leq 6$. Whenever possible, dashed lines will be used to represent ZV profiles and solid lines will be used for ZVD profiles. Additionally, open circles will be added to curves representing fuel-efficient profiles.

The fuel usage of the time-optimal and the fuel-efficient commands is compared in Figure 5.3.

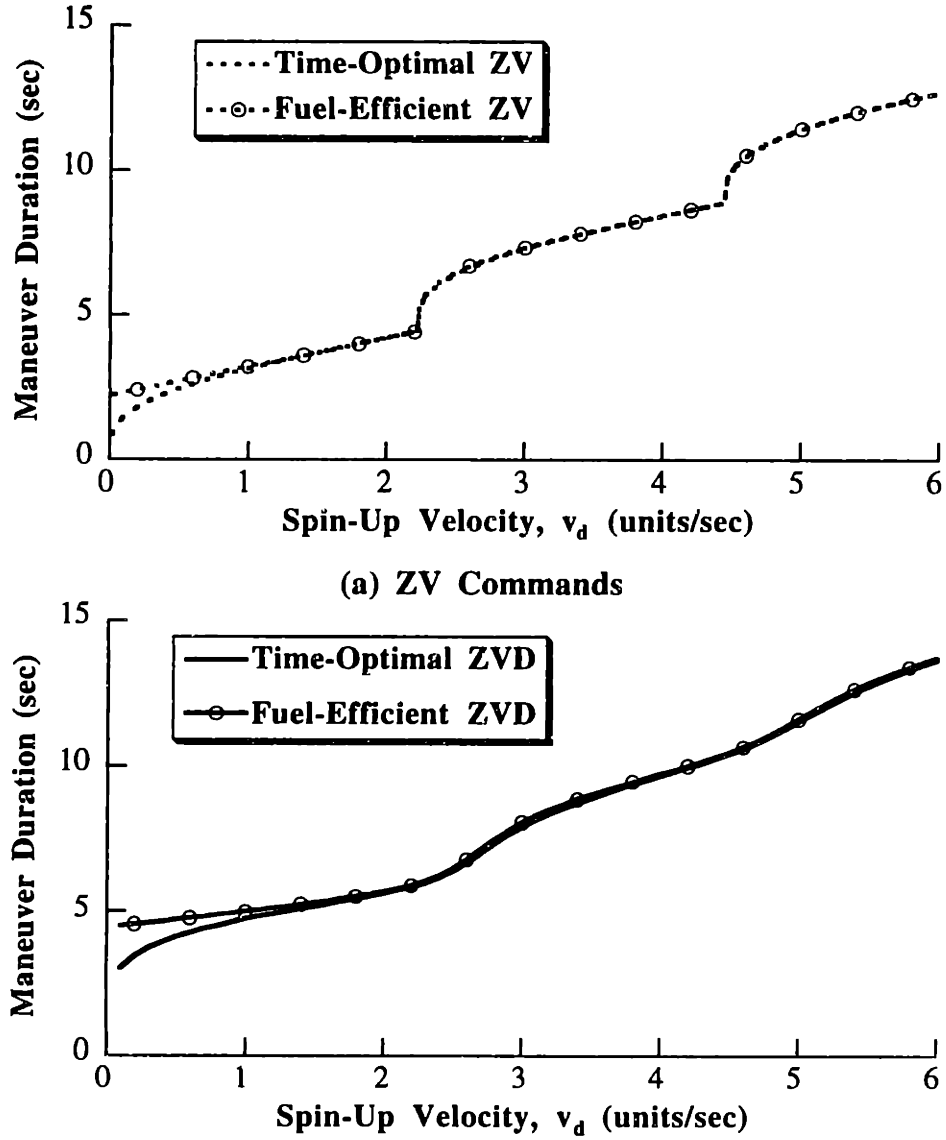

Figure 5.2: Duration of Time-Optimal and Fuel-Efficient Spin-Up Commands.

Fuel usage is measured as the cumulative time that the actuators are turned on. The proposed fuel-efficient profiles use less fuel than their time-optimal counterparts for all terminal velocities. At low spin-up velocities, the fuel usage is reduced by an order of magnitude. At higher velocities the percentage savings decreases, but it is still substantial. Because the fuel-efficient profiles are very nearly time-optimal for most velocities, the difference in fuel usage can be regarded as wasted fuel.

Given the significant fuel savings associated with the fuel-efficient profiles, it is surprising that they are so close in duration to the time-optimal commands. By examining the structure of the commands we can develop a better understanding of this unexpected result. Figure 5.4 shows the impulse times for the fuel-efficient ZV shaper as a function of spin-up velocity. As the velocity is

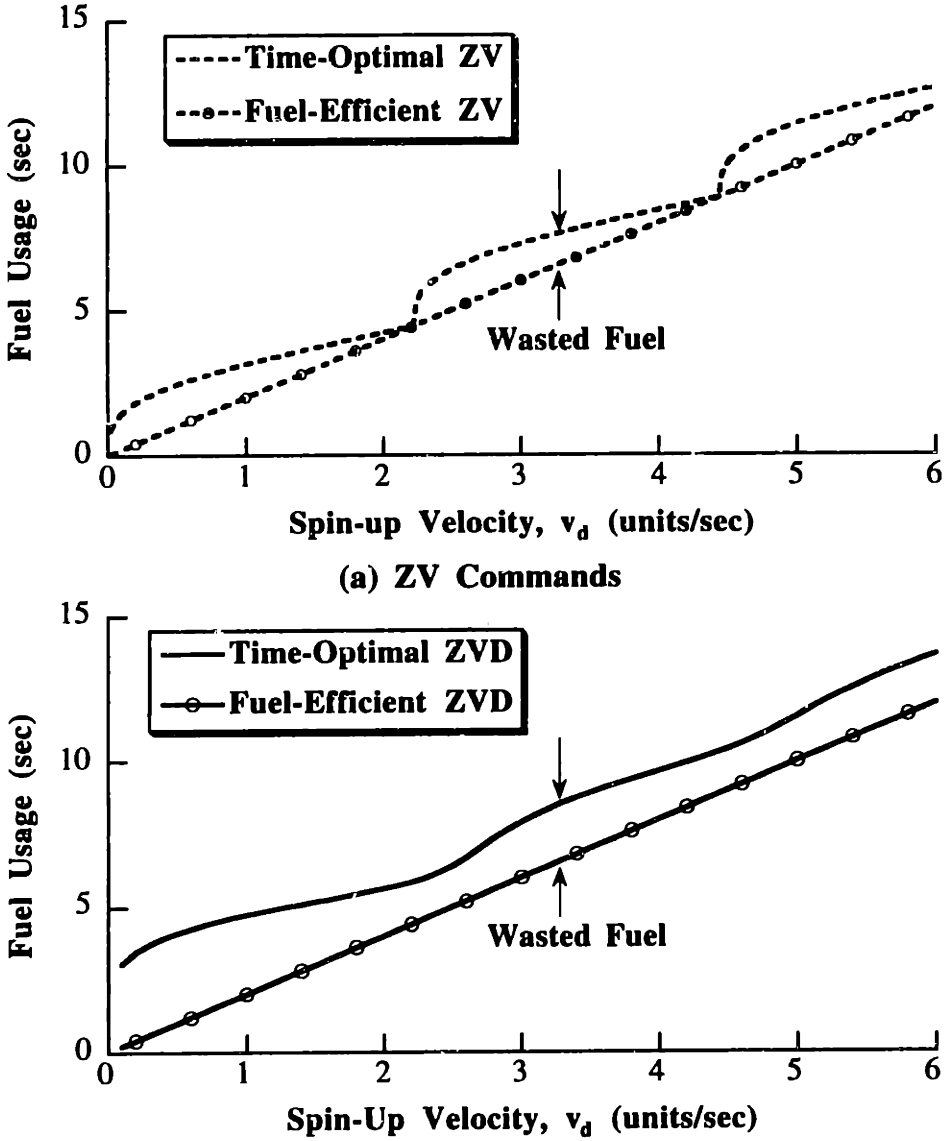

Figure 5.3: Fuel Usage of Time-Optimal and Fuel-Efficient Spin-Up Commands.

increased, the number of pulses in the profile increases. This transition is shown along the top of the figure. The shaded areas indicated periods of coasting.

Figure 5.5 shows the impulse times of both the fuel-efficient and the time-optimal ZV shapers. The impulses of both shapers evolve in a similar fashion. After the first region, the fuel-efficient profiles are very nearly the time-optimal profiles with the negative pulses removed. Put simply, the fuel-efficient profiles tend to coast while the time-optimal profiles decelerate. The same final velocity is obtained because the deceleration pulses are offset by longer acceleration periods in the time-optimal profiles.

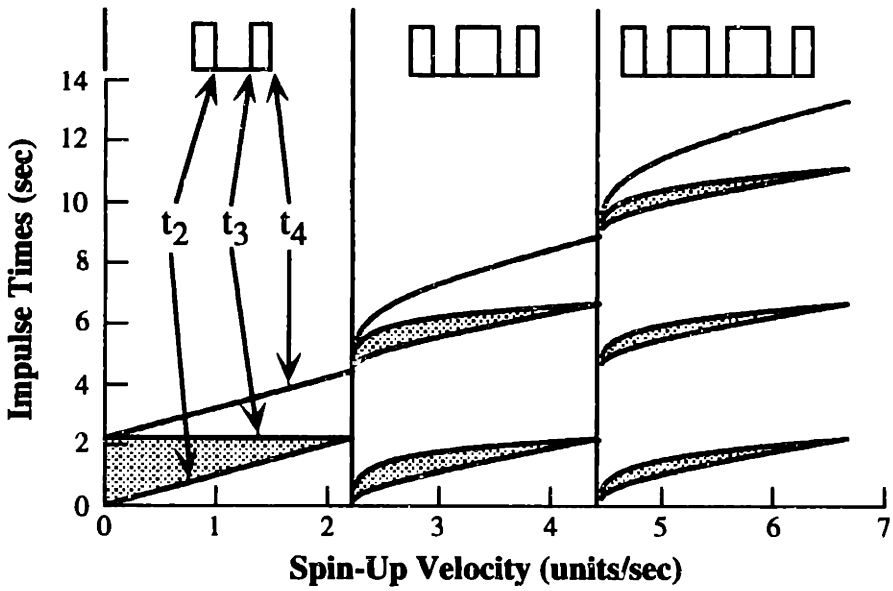

Figure 5.4: Impulse Times for Fuel-Efficient ZV Spin-Up Commands.

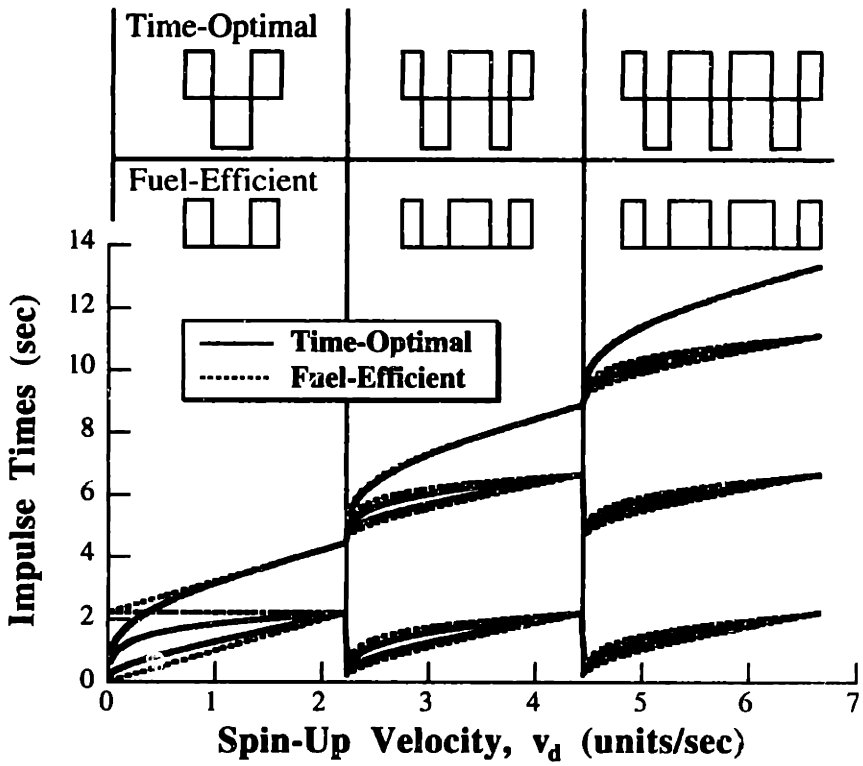

Figure 5.5: Fuel-Efficient and Time-Optimal ZV Spin-Up Impulse Times.

5.2.2 Fuel-Efficient Rest-to-Rest Commands

If the desired motion is a rest-to-rest slew rather than a velocity spin-up, the input shapers used to construct the command must have a different form than those used for the spin-up motions. The

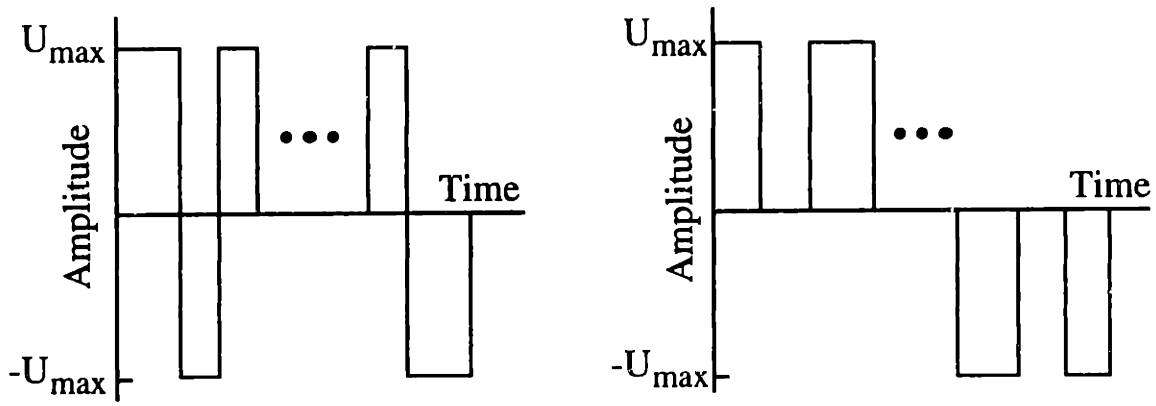

Time-Optimal Command Fuel-Efficient Command

Figure 5.6: On-Off Rest-to-Rest Command Profiles.

command profiles must contain negative pulses. The difference arises out of the constraint equations that govern the two problems. In addition to the constraints used for the velocity, the rigid-body displacement at the end of the command must also be controlled. The time-optimal rest-to-rest command is a multi-switch bang-bang function; therefore, the time-optimal ZV and ZVD shapers for rest-to-rest slews must have the form given by (4.5).

Once again, we postulate that command profiles which allow periods of coasting can robustly reduce residual vibration, while being only slightly longer than the time-optimal commands. The fuel-efficient shapers we propose for rest-to-rest maneuvers have the form:

$$\begin{bmatrix} A_i \\ t_i \end{bmatrix} = \begin{bmatrix} 1 & -1 & 1 & \cdots & -1 & -1 & 1 & \cdots & -1 & 1 \\ 0 & t_2 & t_3 & \cdots & t_{n/2} & t_{(n/2+1)} & t_{(n/2+2)} & \cdots & t_{n-1} & t_n \end{bmatrix} \tag{5.2}$$

Figure 5.6 compares the proposed fuel-efficient rest-to-rest commands to their time-optimal counterparts. The inherent fuel efficiency of the new commands is readily apparent. The pulses that cause acceleration in the desired direction all occur before the deceleration pulses begin.

Note that, unlike the fuel-efficient spin-up profiles, the fuel-efficient rest-to-rest profiles are not the *fuel-optimal* solution. In fact, the fuel-optimal solution for rest-to-rest motion is undefined. As the fuel usage is decreased, the pulses get narrower and the coast periods get longer. In the limit, the pulse widths go to zero and the coast periods go to infinity.

The time-optimal and fuel-efficient rest-to-rest commands were determined for the benchmark system of Figure 4.1. Figure 5.7 compares the maneuver durations for the time-optimal and fuel-efficient ZV and ZVD rest-to-rest commands for the range of $0.1 \leq x_d \leq 40$. The time penalties associated with the fuel-efficient rest-to-rest shapers are almost negligible. For $x_d \geq 3.0$, the fuel-efficient ZV profile is at most 2.3% longer than time-optimal, and the fuel-efficient ZVD is at most 4.2% longer. Over the range $3 \leq x_d \leq 40$, the fuel-efficient ZV profile averages 0.5% longer than the time-optimal, while the fuel-efficient ZVD profile averages 0.6% longer.

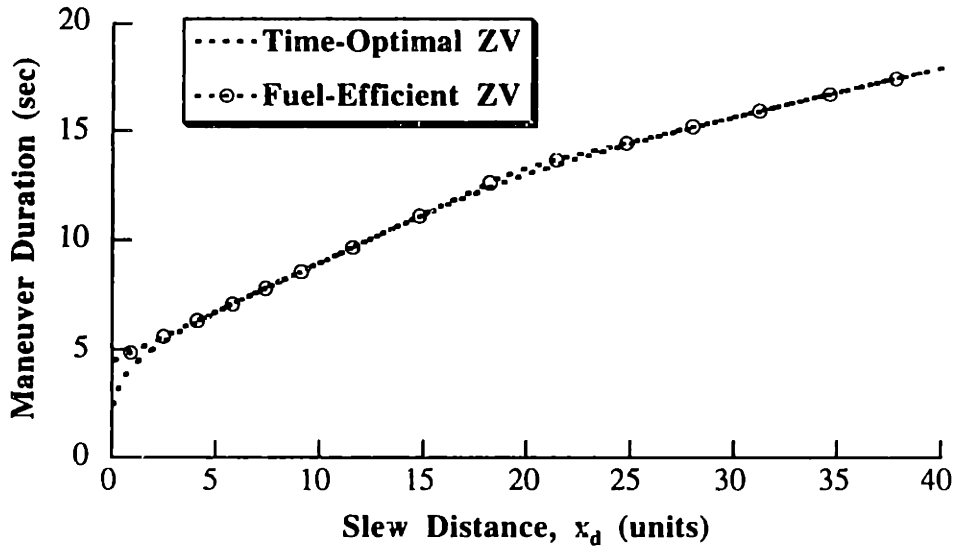

(a) ZV Commands

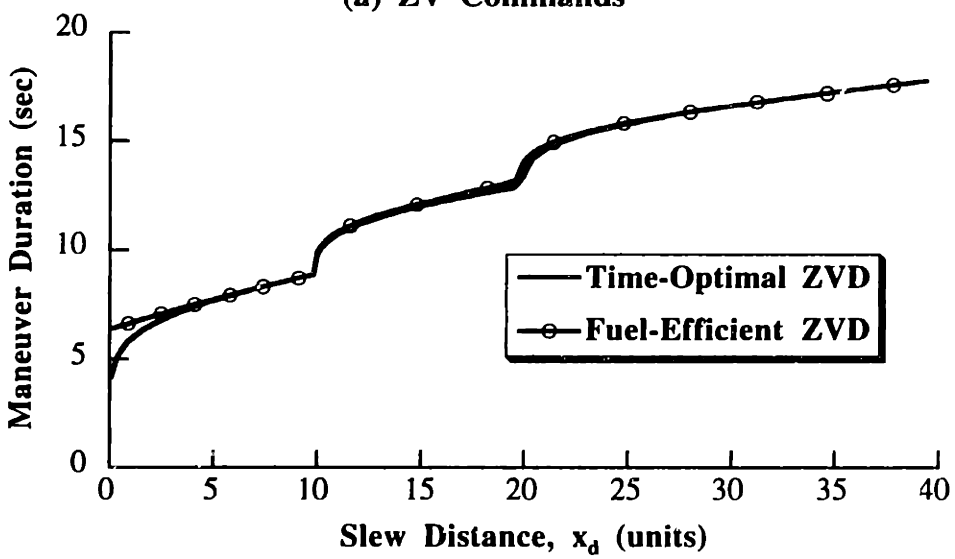

(b) ZVD Commands

Figure 5.7: Duration of Time-Optimal and Fuel-Efficient Rest-to-Rest Commands.

The fuel saved by the new rest-to-rest commands depends on the desired slew distance just as the fuel savings of the spin-up commands depended on terminal velocity. The fuel usage of the time-optimal and the fuel-efficient ZV and ZVD rest-to-rest commands are compared in Figure 5.8. For all values of slew distance the fuel-efficient profiles use less fuel than their time-optimal counterparts. At small distances, the fuel usage is reduced by an order of magnitude. Over the range of move distances shown, the fuel savings averages about 3 seconds.

To gain a better appreciation for the fuel-efficient commands, we can plot the time locations of the shaper impulses as a function of slew distance. Figure 5.9 shows these times for the fuel-efficient ZVD profiles. The structure of the command profile has been plotted along the top of the

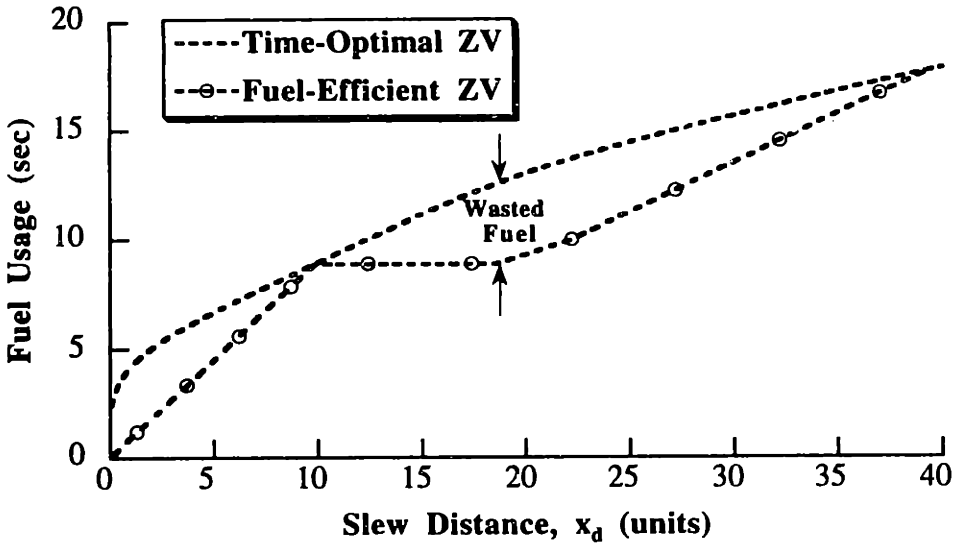

(a) ZV Commands

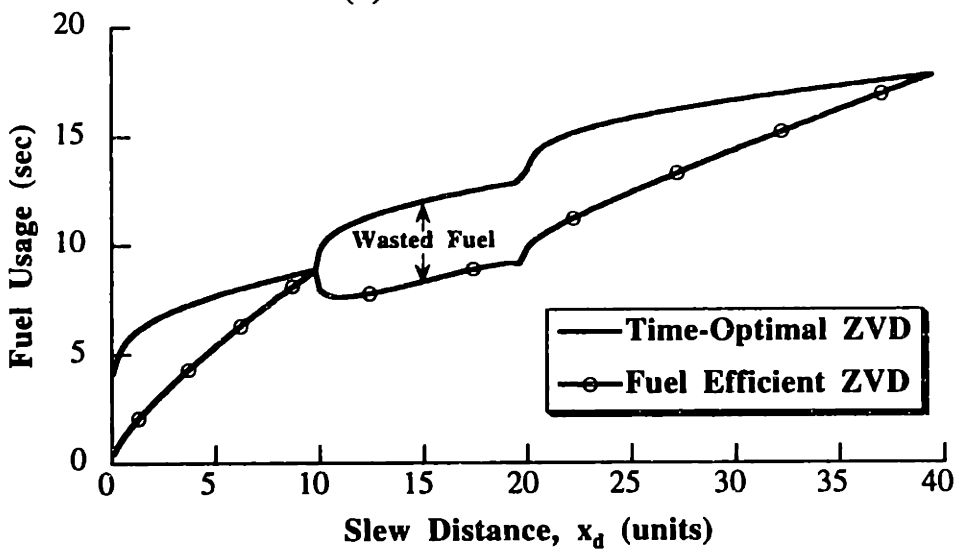

(b) ZVD Commands

Figure 5.8: Fuel Usage of Rest-to-Rest Commands.

figure. For small slew distances, the command profile is composed of two positive pulses followed immediately by two negative pulses. For the intermediate slew distances, there is a period of coasting between positive and negative pulses. Finally, for long slews the profile is three positive pulses followed immediately by three negative pulses. The curves representing the impulse times in Figure 5.9 evolve in a repetitive fashion. As slew distance is increased, impulse times converge and then give rise to additional impulses that translate into additional coast periods or additional pulses. The shaded regions of the figure indicate periods of coasting between pulses.

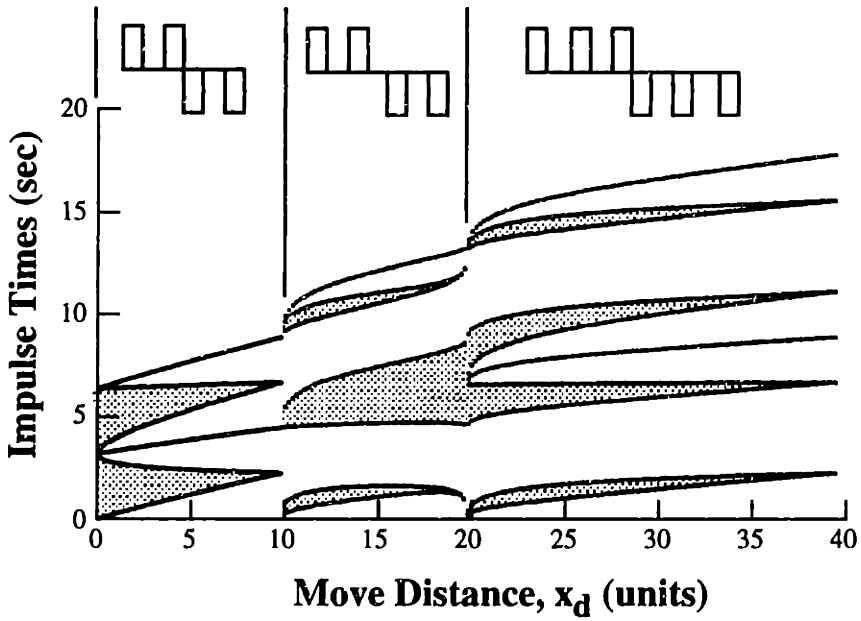

Figure 5.9: Impulse Times for the Fuel-Efficient ZVD Rest-to-Rest Commands.

5.2.3 Variation of Insensitivity

In most previous work generating on-off command profiles it was assumed that using ZVD constraints would guarantee good robustness to modeling errors. This is not the case, as was demonstrated in Section 4.3 and 4.4. For certain move distances, the ZVD shaper will have relatively poor robustness to modeling errors. In this section we will explore the variation of robustness with the fuel-efficient commands. Two important comparisons will be made, the comparison between the insensitivity of ZV and ZVD commands and the comparison between fuel-efficient and time-optimal commands.

Figure 5.10 shows the 5% insensitivity of the fuel-efficient and time-optimal spin-up commands. The figure demonstrates that insensitivity varies considerably with spin-up velocity. For example, the ZVD commands are three times more robust for velocities near 3 units/sec than for velocities close to 4 units/sec. Even though the insensitivity of the ZVD command varies with spin-up velocity, it is almost always significantly larger than that of the ZV command. Figure 5.10 also demonstrates that the fuel-efficient commands have essentially the same robustness as the time-optimal commands.

Figure 5.11 shows the 5% insensitivity of the fuel-efficient and time-optimal rest-to-rest profiles. As expected, the ZVD commands are significantly more robust than the ZV commands. And, once again, the fuel-efficient commands have essentially the same robustness as the time-optimal commands.

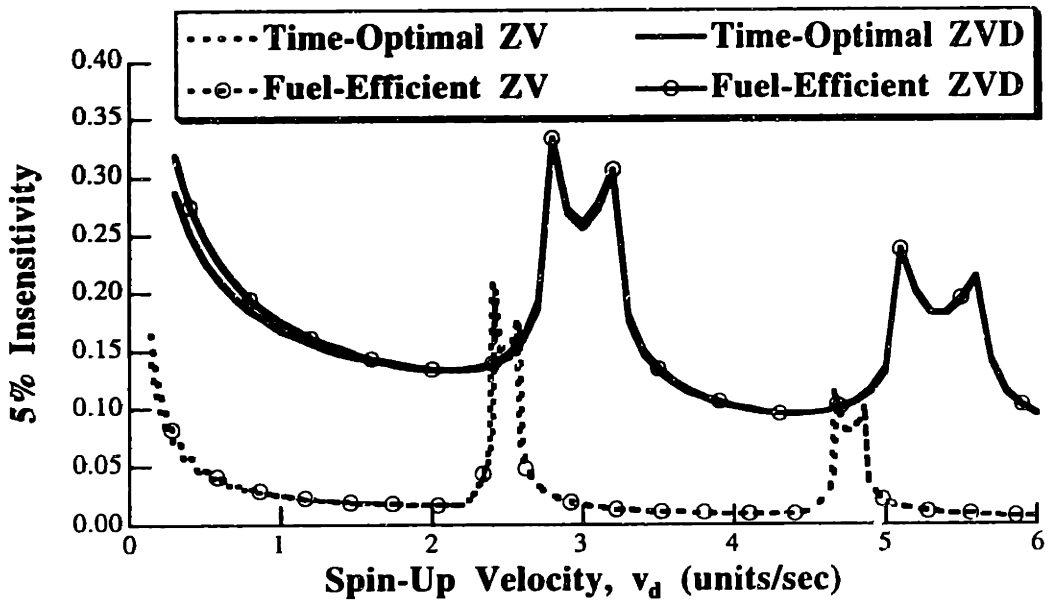

Figure 5.10: Insensitivity of Spin-Up Commands.

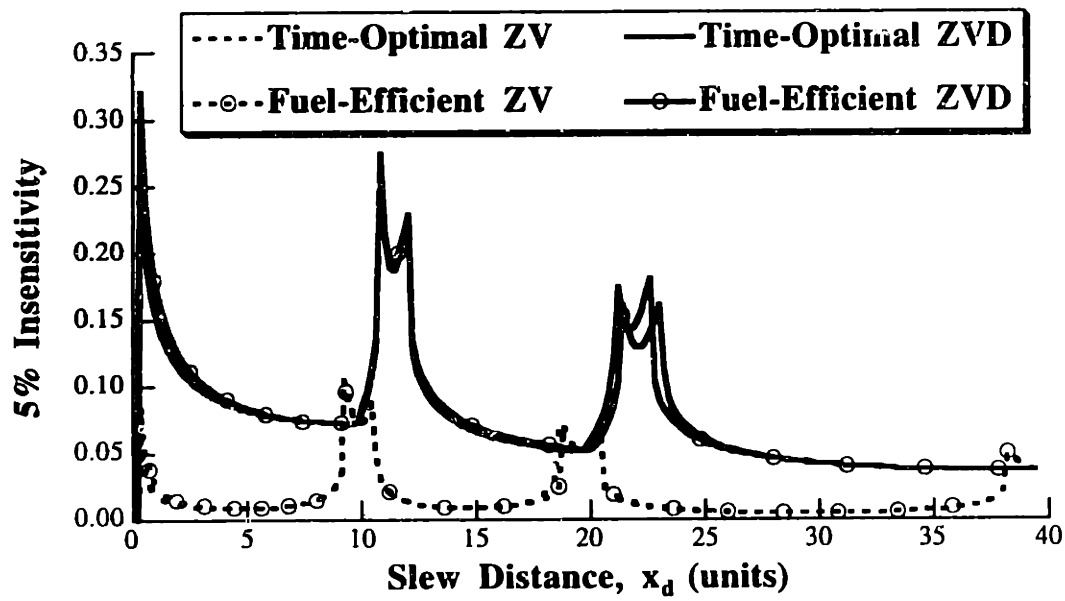

Figure 5.11: Insensitivity of Rest-to-Rest Profiles.

5.2.4 Simulation Evaluations

Experiments using Draper Laboratory's simulation of the space shuttle's remote manipulator and a flexible hardware testbed have verified the benefits of using input shaping to generate on-off commands. See Section 4.3 or the references [117]. Therefore, the simulations used to test the theoretical results of this section will be restricted to simulations of the system shown in Figure 4.1. If the trends in fuel savings and insensitivity are supported by these simulations, then given the previously reported experimental results, there is good reason to believe that the trends will also occur in more complicated hardware.

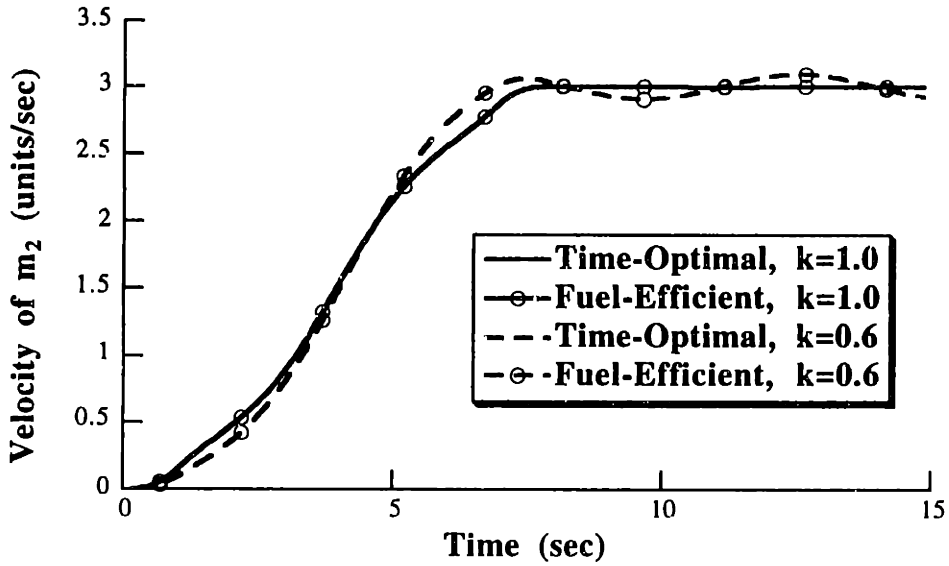

Figure 5.12: Fuel-Efficient and Time-Optimal ZVD Responses.

Two important results of the above theoretical development will be tested. First, we will verify that the fuel-efficient commands yield essentially the same rise time and robustness as the time-optimal commands, even though it uses considerably less fuel. Second, the variation of insensitivity with maneuver distance will be investigated.

Simulations of the system shown in Figure 4.1 were performed using the command profiles generated with the spin-up fuel-efficient and time-optimal ZVD shapers. Figure 5.12 compares the system response to the command profiles when the spin-up velocity is 3 units/sec and the spring constant, k, is set equal to the values of 1.0 and 0.6. The responses with k = 1.0 represent the case when the system model is exact. The data for k = 0.6 represent the responses to a modeling error of 30%; the frequency shifts from 0.225 Hz to 0.174 Hz. Figure 5.12 shows that the fuel-efficient command yields essentially the same response as the time-optimal command (the responses are indistinguishable on the graphs). These results illustrate the similarity of time-optimal and fuel-efficient commands in terms of move duration, as shown in Figures 5.2, and in terms of robustness properties, as shown in Figure 5.10. However, the fuel-efficient command requires 24% less fuel.

Figure 5.13 shows the responses to fuel-efficient ZVD rest-to-rest commands for slew distances ranging from 2 to 20 units in steps of 2. The solid curves represent responses when the model is exact (k = 1.0). The responses achieve the desired setpoint with zero residual vibration. The dashed lines correspond to responses when a modeling error is introduced by changing the spring constant to 0.6. Notice that for the same modeling error, the residual vibration varies significantly with slew distance, reaching a minimum at about 12 units. This result demonstrates that

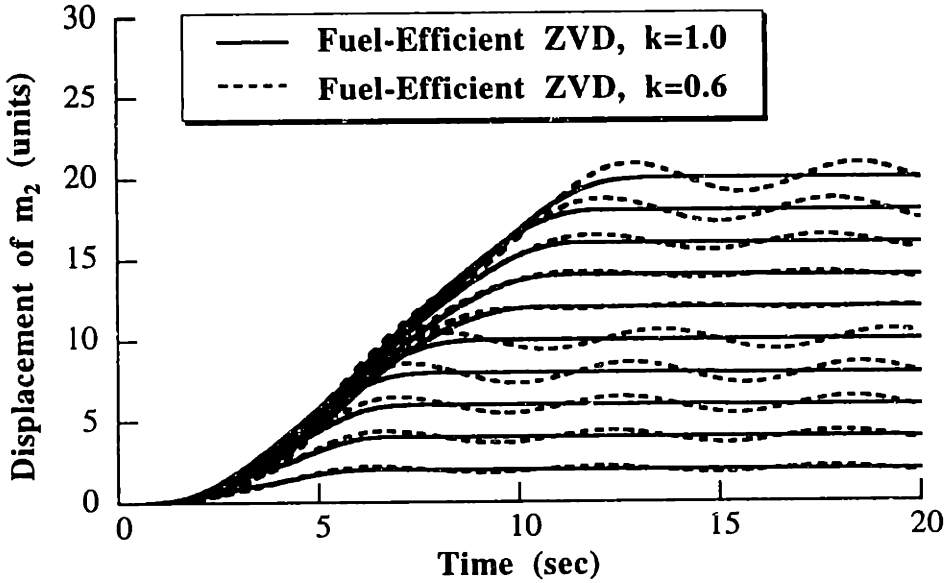

Figure 5.13: Residual Vibration as a Function of Slew Distance. (Constant Modeling Error).

robustness to modeling errors is strongly dependent on slew distance, as was predicted by Figure 5.11. The low level of vibration near 12 units was predicted by the large value of insensitivity shown at that value.

5.2.5 Discussion of Fuel-Efficient On-Off Commands

A new technique for designing on-off command profiles for flexible systems has been presented. The technique can design command profiles for rest-to-rest slews or accelerations to constant velocity. The new profiles are significantly more fuel efficient than time-optimal profiles, even though the commands are effectively the same duration as the time-optimal commands. Additionally, the new profiles have essentially the same robustness to modeling errors as the time-optimal profiles. Other results demonstrate that insensitivity to modeling errors is highly dependent on slew distance and spin-up velocity. Computer simulations demonstrated the effectiveness of the proposed command profiles.

5.3 Specified-Fuel On-Off Commands

Given the significant advantages of the fuel-efficient commands of the previous section, it is reasonable to pursue the topic of fuel-usage in more detail. This section presents a method which generates command profiles that use a specified amount of actuator fuel. Properties of the command profiles, such as, duration, robustness to modeling errors, and profile complexity are examined. Techniques are presented that facilitate implementation and indicate prudent choices for the amount of fuel to be used when no fixed limit exists. The relationship between specified-fuel methods and other techniques that balance fuel usage and slew time is examined.

5.3.1 Statement of Problem

The design of a shaped command profile with specified fuel usage for a flexible linear system can proceed in two ways. The problem can be stated as an optimal control problem in which a cost function is minimized, or it can be formulated as an input shaping problem. The optimal control formulation is useful because it provides a means of checking the validity of numerical solutions, as was shown in Section 4.5. The input shaping formulation provides two advantages. First, it provides a straightforward method for satisfying the state boundary conditions and actuator limits. The command profiles resulting from this straightforward process can then be verified by the check provided by optimal control theory. Second, input shaping can be used to generate command profiles subject to auxiliary constraints such as a fixed number of pulses. These profiles are generated easily with input shaping, but would be more difficult to obtain through an optimal control formulation.

For certain ranges of the parameter values, the command profile for the fuel/time optimal control problem consists of a series of positive pulses followed by a series of negative pulses. In other ranges, the solution is more complicated; it contains intertwined positive and negative pulses. These two types of profiles are illustrated in Figure 5.14. Type 2 profiles arise when the fuel usage is very near the amount of fuel used by a time-optimal command generated without regard to fuel usage. When the fuel usage is not constrained at all, the coast periods between the intertwined pulses go to zero and the profile is a multi-switch bang-bang without coast periods. The profiles that occur when the command transitions from type 2 to type 1 profiles are the fuel-efficient profiles described in the previous section.

The variation in the shape of the optimal profile can make implementation difficult. Furthermore, actuator wear can be reduced by keeping the number of command pulses to a minimum. It is in these situations when the input shaping formulation has its advantage because the shape of the command profile can be forced into a simple form with a constant number of

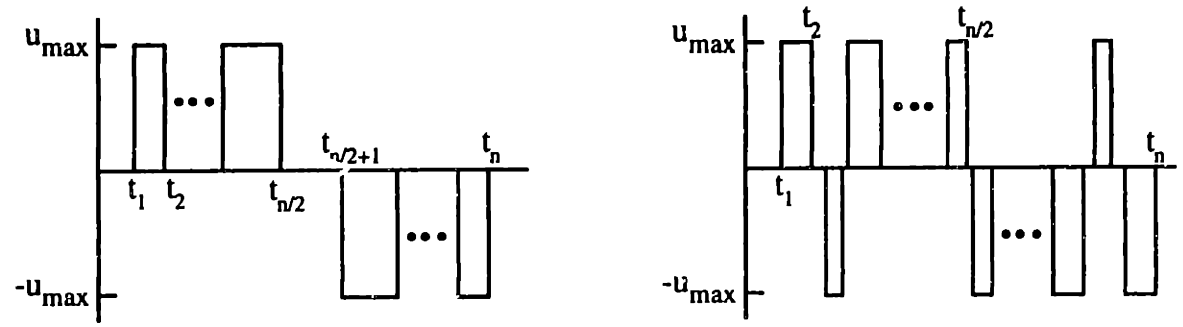

Type 1 Type 2

Figure 5.14: Two Types of Optimal Command Profiles.

pulses. As we will see in a subsequent section, forcing the command profile away from the optimal shape incurs only a minor time penalty.

5.3.1a Time-Optimal Control Formulation[18]

The time-optimal control problem can be stated as a minimization of the cost function:

$$J = \int_0^{t_f} dt = t_f \tag{5.3}$$

where t_f represents the maneuver time. For rest-to-rest slewing of a linear, single-input, time-invariant system described by the equations:

$$\dot{\mathbf{x}}_0 = \mathbf{A}_0\mathbf{x}_0 + \mathbf{B}_0 u \qquad \forall t \in [0,\ t_f] \tag{5.4}$$

the boundary conditions are:

$$\mathbf{x}_0(0) = [-x_d\ \ 0\ \ 0\ \ \ldots\ \ 0]^T \qquad \textit{and} \qquad \mathbf{x}_0(t_f) = \mathbf{0} \tag{5.5}$$

where x_d is the desired slew distance. Actuator constraints can be represented as:

$$-u_{max} \le u \le u_{max}\,. \tag{5.6}$$

The limit on fuel usage can be expressed as:

$$\int_0^{t_f} |u|\,dt \le U \tag{5.7}$$

where U represents the fuel available for the slew. When U is less than or equal to the fuel used for the time-optimal command designed without fuel limitations, then the command will use all the available fuel. In this case, the inequality in (5.7) is replaced with an equality constraint and (5.7) can be rewritten by defining a new variable:

$$\dot{\phi} = |u| \tag{5.8}$$

where ϕ satisfies the boundary conditions:

$$\phi(0) = 0, \qquad \phi(t_f) = U\,. \tag{5.9}$$

[18]This formulation was suggested by Professor Tarun Singh [123].

Augmenting the state equations given in (5.4) with the fuel usage variable given in (5.8), and using the combined boundary conditions given in (5.5) and (5.9), yields a complete description of the problem under consideration.

A time-optimal solution to the above problem can be obtained by performing a nonlinear numerical optimization. Several methods have been proposed for performing optimizations of this type. These methods include performing an integration of the state equations at each step of the optimization [8], using the Switching Time Optimization algorithm [53, 68], and formulating the state boundary conditions as explicit functions of a parameterized command profile [52, 111, 117, 165]. Because the systems considered here are time-invariant linear systems, the necessary optimizations use parameterized boundary conditions. Relying on Pontryagin's Minimum Principle (PMP)[85], the time-optimal command profile can be parameterized by its switch times as shown in Figure 5.14. Stating the boundary conditions in terms of the switch times leads to a set of equations that can be satisfied while minimizing the final switch time (the maneuver duration).

A numerical solution of the above problem may not yield the time-optimal solution because there are multiple solutions and nonlinear optimization is susceptible to selection of local minima. Fortunately, the necessary conditions provided by PMP can be used to verify a candidate solution to this problem, just as was done in Section 4.5 for the purely time-optimal problem. The necessary conditions of PMP utilize the Hamiltonian which in this case is given by:[19]

$$H = 1 + \psi^T(\mathbf{Ax} + \mathbf{Bu}) = 1 + \lambda^T(\mathbf{A_0x_0} + \mathbf{B_0u_0}) + \mu|u| \tag{5.10}$$

where ψ is the vector of costates. The symbols λ and μ represent subsets of the costates which correspond to the costates of the original system and the fuel usage state, respectively. It can be seen from (5.10) that the Hamiltonian for the augmented system is identical to the one defined for a fuel/time optimal controller where μ represents the relative weight of the fuel consumed in the cost function [104, 166]. The necessary conditions for optimality require the following equations to be satisfied [85, 104]:

$$\dot{\lambda} = -\mathbf{A}^T\lambda \qquad \forall t \in [0, t_f] \tag{5.11}$$

$$\dot{\mu} = -\frac{\partial H}{\partial \phi} = 0 \rightarrow \mu(t) = \text{constant} \tag{5.12}$$

$$u = -dez\left(\frac{\mathbf{B}^T\lambda}{\mu}\right) \quad \forall t \in [0,\ t_f] \tag{5.13}$$

dez, the deadzone function is defined as:

$$v = dez(\alpha) \Rightarrow \begin{cases} v = 0 & \text{if } |\alpha| < 1 \\ v = \text{sgn}(\alpha) & \text{if } |\alpha| > 1 \\ 0 \le v \le 1 & \text{if } \alpha = 1 \\ -1 \le v \le 0 & \text{if } \alpha = -1 \end{cases} \tag{5.14}$$

[19] The state space matrices **A** and **B** represent the system augmented with the fuel usage variable; $\mathbf{A_0}$ and $\mathbf{B_0}$ represent the dynamics of the original system.

Using (5.11) and (5.12), the costates can be represented as:

$$\lambda(t) = \exp\left(-\mathbf{A}^T t\right)\lambda(0) \tag{5.15}$$

and,

$$\mu(t) = \text{constant} \tag{5.16}$$

For optimality, the switching function must satisfy the constraint:

$$\mathbf{B}^T \exp\left(-\mathbf{A}^T t_s\right)\lambda(0) = \pm\mu \tag{5.17}$$

where t_s represents a switch time. We can solve for $\lambda(0)$ and μ from the null space of the matrix **P** where:

$$\mathbf{P}\begin{Bmatrix}\lambda(0)\\ \mu\end{Bmatrix} = \begin{bmatrix}\mathbf{B}^T \exp\left(-\mathbf{A}^T t_1\right) & \pm 1\\ \mathbf{B}^T \exp\left(-\mathbf{A}^T t_2\right) & \pm 1\\ \cdots & \pm 1\\ \cdots & \pm 1\end{bmatrix}\begin{Bmatrix}\lambda(0)\\ \mu\end{Bmatrix} = \begin{Bmatrix}0\\ 0\\ \cdots\\ 0\end{Bmatrix} \tag{5.18}$$

If the control profile determined from the equation

$$u(t) = -dez\left(\mathbf{B}^T\lambda(t)/\mu\right) \tag{5.19}$$

matches the profile resulting from the parameter optimization, then the control is optimal. Note that this process for verifying specified-fuel command profiles is analogous to the method for verifying purely time-optimal commands described in Section 4.5.

5.3.1b Input Shaping Formulation

The process of input shaping can be used to generate a command that satisfies the state boundary conditions and actuator limits for the specified fuel problem. The impulse amplitude constraints must be set so that type 1 or type 2 command profiles are obtained. Type 1 profiles are obtained when the input shaper has the form:

$$\begin{bmatrix}A_i\\ t_i\end{bmatrix} = \begin{bmatrix}1 & -1 & 1 & \cdots & -1 & -1 & \cdots & -1 & 1\\ 0 & t_2 & t_3 & \cdots & t_{n/2} & t_{(n/2+1)} & \cdots & t_{n-1} & t_n\end{bmatrix} \tag{5.20}$$

and type 2 profiles are obtained with a shaper of the form:

$$\begin{bmatrix}A_i\\ t_i\end{bmatrix} = \begin{bmatrix}1 & -1 & -1 & 1 & 1 & \cdots & -1 & 1\\ 0 & t_2 & t_3 & t_4 & t_5 & \cdots & t_{n-1} & t_n\end{bmatrix} \tag{5.21}$$

Note that the number of pulses in the command profile can be set by choosing the value of n. Limitations on the number of pulses is an example of a constraint which is straightforward to implement with input shaping, but is much harder to pose in the optimal control formulation.

Because an input shaper described by (5.20) yields only type 1 command profiles regardless of the parameter values, its use facilitates implementation because the command profile will always consist of n/4 positive pulses followed by n/4 negative pulses. For a small range of parameter values, the shaper described by (5.20) will result in command profiles that are slightly longer than the commands designed by the optimal control formulation. Note, however, that the input shaping

profiles are still time-optimal. They are simply subjected to an additional constraint that is not enforced in the optimal control formulation; they are required to produce a type 1 profile with n/2 pulses.

In order to determine the impulse time locations (switch times), the state boundary conditions must be satisfied. These boundary conditions are satisfied in a straightforward manner given the input shaping formulation. If we consider the simple model shown in Figure 4.1, then the rigid-body boundary conditions are given by (4.10) and (4.11). With an input shaper of the form given in (5.20) these boundary conditions can be stated algebraically as:

$$0 = \left(t_2 - t_3 + t_4 - \ldots + t_{n/2} + t_{n/2+1} - t_{n/2+2} + \ldots - t_n\right)/M \tag{5.22}$$

$$x_d = \frac{\begin{pmatrix} -t_2^2 + t_3^2 - \ldots - t_{n/2}^2 - t_{n/2+1}^2 + \ldots - t_n^2 + 2t_2t_n - 2t_3t_n \\ + \ldots + 2t_{n/2}t_n + 2t_{n/2+1}t_n - \ldots - 2t_{n-2}t_n + t_{n-1}t_n \end{pmatrix}}{M}. \tag{5.23}$$

To specify the amount of fuel used (in units of time) the summation of the pulse widths is set less than or equal to the available fuel. For profiles described by (5.20), this constraint is:

$$U \geq \sum_{i=1}^{n} (-1)^i t_i \tag{5.24}$$

Enforcement of the state boundary conditions for rest-to-rest slewing and actuator limits is accomplished by satisfying (4.12) with V = 0, (5.20) or (5.21) and (5.22)-(5.24). To obtain ZVD commands, (4.14) is added to the problem formulation. A numerical optimization can be performed to satisfy the above constraints while minimizing the slew duration.

5.3.2 Evaluation of Specified-Fuel Commands

Command profiles which use a specified amount of fuel can be generated using a variety of system models. If the system has little flexibility, then it can be modeled as a rigid body. Flexibility requires the inclusion of elastic modes in the state equations. Uncertainty in the values of the elastic modes require a robust formulation. The following three types of specified fuel (SF) commands are discussed here:

1) Rigid body (RB)

2) Zero residual Vibration (ZV)

3) Zero Vibration and Derivative (ZVD)

The RB SF profile is obtained by specifying the desired fuel usage and satisfying the rigid-body constraints, such as (4.10) and (4.11). For the system shown in Figure 4.1 this profile is simply a positive pulse, followed by a region of coasting, followed by a negative pulse which is equal in duration to the positive pulse. The coasting period may be absent in some special cases. The ZV SF profile is obtained by adding the zero residual vibration constraint (4.12) with V = 0 to the equations used to generate the RB SF. Finally, the ZVD SF profile is obtained by adding the zero

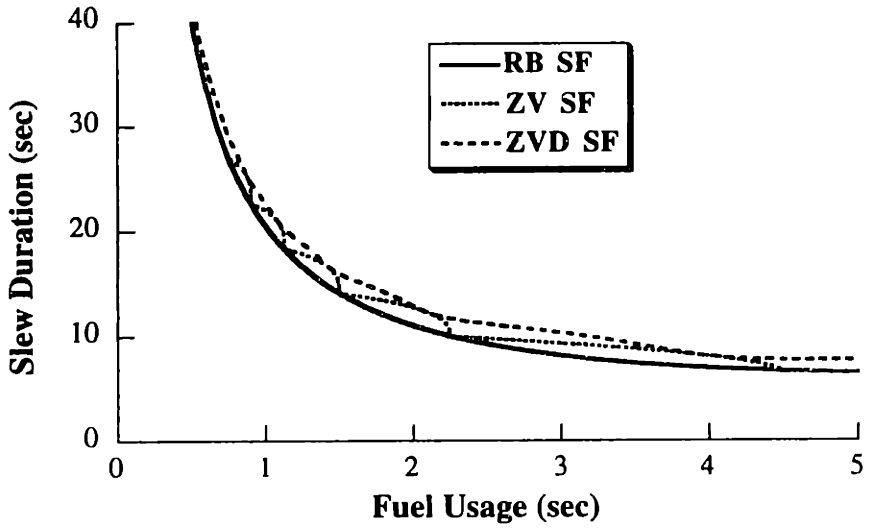

Figure 5.15: Slew Duration as a Function of Fuel Usage (5 Unit Slew).

derivative constraint (4.14) to the equations used to generate the ZV SF command. There are several important qualities of the command profiles which will be investigated: a) slew duration, b) robustness to modeling errors, and c) profile complexity.

To demonstrate the procedure for constructing specified-fuel commands and investigate their properties, profiles will be designed for the single-mode flexible system represented by the benchmark system of Figure 4.1. The force acting on mass m_1 is restricted to $-u_{max} \leq u(t) \leq u_{max}$. If all system parameters (m_1, m_2, k, u_{max}) are set equal to 1, then the system has a natural frequency of $\sqrt{2}$ radians/sec (0.2251 Hz).

5.3.2a Slew Duration

Figure 5.15 shows the move duration as a function of the amount of fuel used when the slew distance is 5 units. The amount of fuel used is measured by the duration of time during which the actuators are turned on. When the fuel usage is high, the fuel consumption can be reduced considerably with very little time penalty. However, attempting to save fuel when the fuel usage is low results in a large time penalty. Considering all three types of commands, the average slew duration increases 1.53 sec. when the fuel is reduced from 4 sec. to 3 sec. On the other hand, the average slew duration is increased 9.55 sec. when the fuel is reduced from 2 sec. to 1 sec.

The RB SF is, of course, the shortest command profile, while the ZVD SF is the longest. The duration of the ZV SF ranges between the other two, equaling one or the other at certain levels of fuel usage. Note that only a small increase in slew duration accompanies the ZVD constraints. The ZVD profile is, at most, 27% longer than the RB profile, while typical increases are on the order of 15-20%. The benefits obtained by sacrificing this time are documented in the following sections.

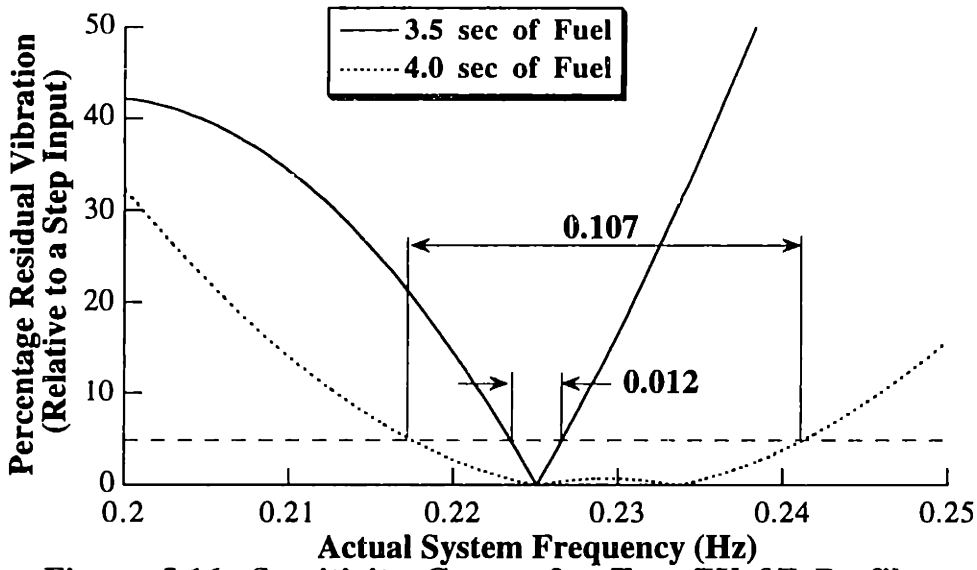

Figure 5.16: Sensitivity Curves for Two ZV SF Profiles.

5.3.2b Robustness to Modeling Errors

Figure 5.16 shows the sensitivity curves for the ZV SF command profile when the fuel usage is 3.5 sec. and 4.0 sec. The data shown in the remainder of this section will be based on a five unit slew. When the system model is exact (0.2251 Hz), both commands yield exactly zero residual vibration. Note that the residual vibration increases rapidly with modeling errors when the command uses 3.5 sec. of fuel. When 4 sec. of fuel is used, the vibration stays at a low level over a much wider frequency range. That is, the ZV SF command that uses 4 sec. of fuel is more robust to modeling errors than the command that uses 3.5 sec. of fuel. The 5% insensitivity, I, for the profile using 3.5 sec. of fuel is only 0.012, while the 5% I for the 4.0 sec. profile is 0.107.

To understand how the robustness (or lack there of) changes, the 5% I can be plotted as a function of the fuel usage. Figure 5.17 shows these curves for both the ZV SF and the ZVD SF commands; the RB SF is not shown because it does not attempt to eliminate vibration and, hence, robustness is poorly defined. The robustness of the ZV profile can vary by an order of magnitude, but it is usually very small. The robustness of the ZVD profile varies by a factor of 3 and it is almost always much greater than for the ZV profile. The advantage of the derivative robustness constraint is clearly visible from Figure 5.17. Furthermore, Figure 5.17 suggests a novel idea: the fuel usage can be used to effect the robustness of the profile. For example, when designing a ZV profile, there is a huge benefit from using 4 sec. of fuel instead of 3.5 sec. as was demonstrated in Figure 5.16. The exact opposite is true for the ZVD profile. Figure 5.17 shows that a 3.5 sec. ZVD command is much more robust than a 4 sec. ZVD command. For either type of profile, small changes in fuel usage can cause large changes in the robustness.

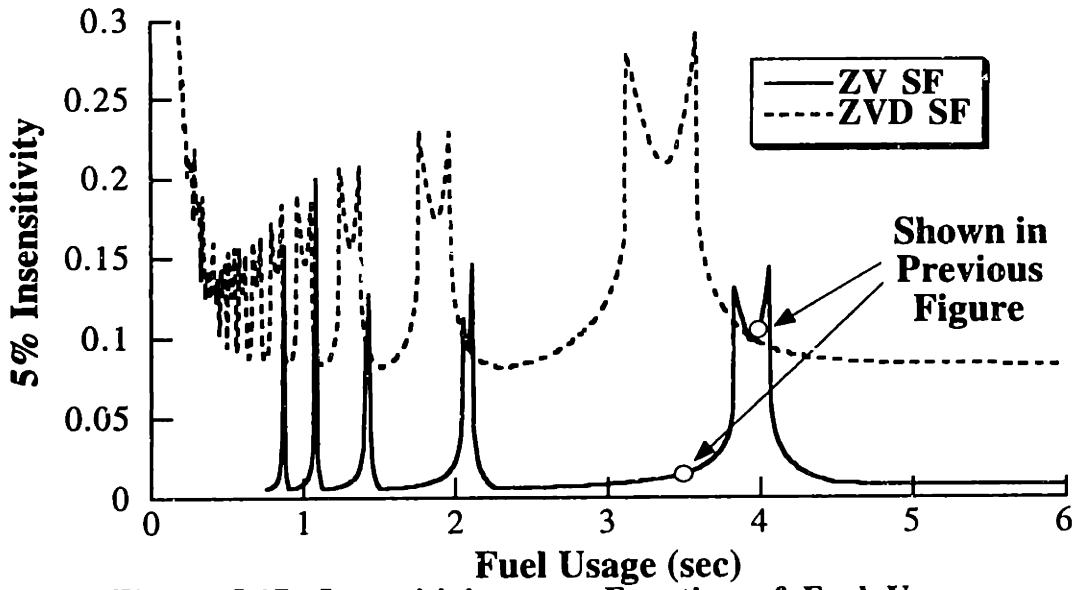

Figure 5.17: Insensitivity as a Function of Fuel Usage.

5.3.2c Profile Complexity

The ease of implementation is not a straightforward quantity to measure. However, the number of pulses in a profile and the ease of which they can be described will certainly effect implementation. Figure 5.18 shows the impulse times for the ZV SF profile as a function of the fuel usage. Two main regions of the solution space are evident. For high levels of fuel usage, the profile consists of alternating positive and negative pulses (a type 2 profile). This region has been labeled Non Fuel-Efficient because increasing the fuel usage in this region yields no meaningful decrease in move duration. (The time of the final impulse is nearly constant.) For example, when the fuel usage is increased from 4.5 sec. to 6.7 sec., the move time is decreased only 0.03 sec. At lower levels of fuel usage the profile consists of positive pulses followed by negative pulses; positive and negative pulses are not intertwined (a type 1 profile). This region is labeled Fuel-Efficient because increases in fuel usage result in noticeable decreases in slew duration.

Note that there are points where small changes in the fuel usage cause large changes in move duration (4.5 sec., 2.2 sec., etc.). These points occur when the profile collapses from 4 pulses down to just 2 pulses, one positive and one negative. The first of these points marks the boundary between the Fuel-Efficient and Non Fuel-Efficient regions. When considering the trade-off between fuel and time, these points represent prudent choices.

Control profiles based on the transition point between type 1 and type 2 profiles are the fuel-efficient commands described in the previous section. Recall that these command profiles are generated by first requiring that the commands be of type 1 and then minimizing the move duration. No explicit limit is placed on the fuel usage. The resulting command corresponds to the

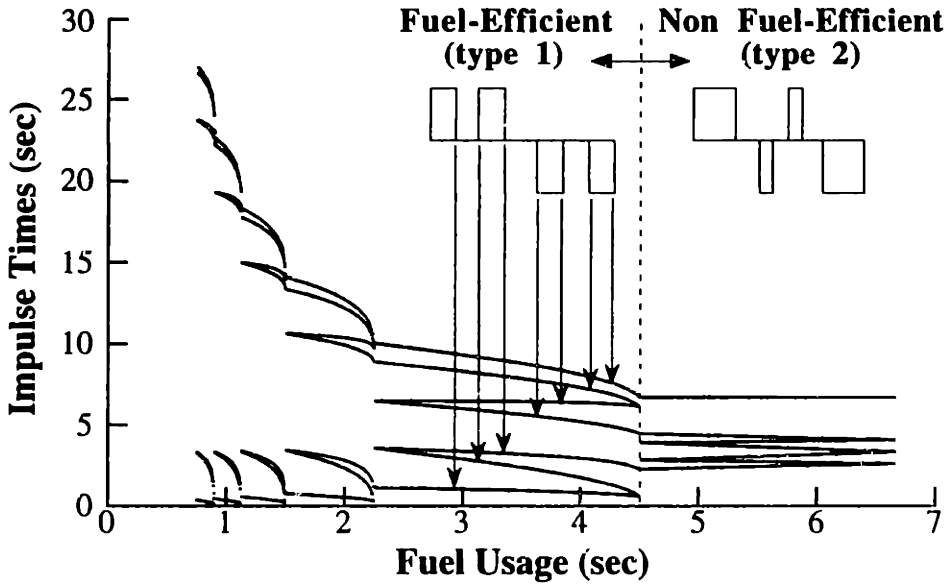

Figure 5.18: Impulse Times (Switch Times) for the ZV SF Profile.

profile at the first node of the fuel/duration curve (the curve formed by the final impulse in Figure 5.18).

Figure 5.19 shows the impulse times for the ZVD SF profile. In this case, the optimal control formulation switches from type 1 to type 2 at a fuel usage of just less than 5 sec. Increasing fuel consumption above 5.0 sec. yields no noticeable decrease in move time. Although the ZVD SF profile does not have distinct points where decreasing fuel leads to rapid increases in slew duration, there are still regions where this effect occurs (at approximately 4 sec. and 2 sec. of fuel). These regions are prudent choices when considering both fuel and time.

By using the input shaping formulation, the profile can be held in the type 1 configuration until a fuel usage of approximately 5.4 sec. The system cannot be made to slew faster by increasing the fuel usage above this amount. Both the optimal control and input shaping solutions are shown in the region between 5.0 and 5.4 sec. of fuel. Differences in the intermediate switch times are evident, but there is no discernible difference in slew time. This indicates that there is essentially no time penalty for using the input shaping formulation to hold the profile in the type 1 configuration. Outside the 5.0 to 5.4 sec. interval the input shaping and time-optimal solutions are identical.

5.3.3 Determination of ZV Command Transitions

It can be seen from Figure 5.18 that the second and third and the sixth and seventh impulse times of the ZV SF profile tend to approach each other as fuel usage increases. To see this, start at the left hand side and move to the right. The impulse time locations approach each other and eventually equal the same value. After this point the impulses separate in a discontinuous jump and

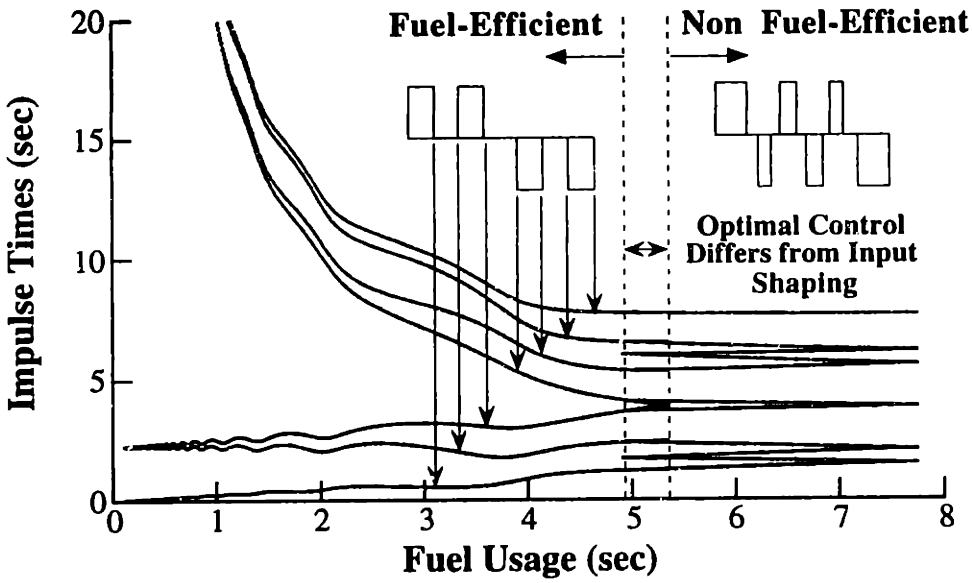

Figure 5.19: Impulse Times (Switch Times) for the ZVD SF Profile.

again start to approach each other with increasing fuel usage. When the impulses come together, the result is a two-pulse profile as shown in Figure 5.20. (Following the discontinuity there is the appearance of two new pulses.) It was noted earlier that these points of discontinuity are prudent choices when there is no specific limit on fuel usage. Furthermore, the first of these points correspond to the fuel-efficient ZV control proposed in the previous section. To fully demonstrate the intersection of fuel-efficient and specified fuel control, we solve for the fuel usage levels that correspond to the transitions in the ZV SF profile.[20]

In order for the profile shown in Figure 5.20 to yield zero residual vibration, the second (negative) pulse must start at an integral multiple of the vibration period. That is,

$$t_3 = n\frac{2\pi}{\omega}. \tag{5.25}$$

The constraint on fuel usage is:

$$t_2 = \frac{U}{2}. \tag{5.26}$$

From the rigid-body boundary conditions we obtain:

$$x_d = \frac{u_{\max}}{M} t_2 t_3 \tag{5.27}$$

Substituting (5.25) and (5.26) into (5.27) yields:

$$x_d = n\frac{U\pi u_{\max}}{M\omega} \tag{5.28}$$

We can now solve for the fuel usage points that correspond to the transitions in the ZV SF profile:

$$U = \frac{M\omega x_d}{nU\pi u_{\max}} \tag{5.29}$$

[20] The following solution was developed by Professor Tarun Singh [123].

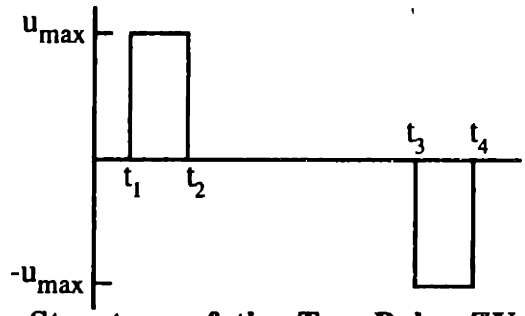

Figure 5.20: Structure of the Two-Pulse ZV SF Profile.

The fuel-efficient ZV commands of the previous section correspond to n = 1. If it is desired to use even less fuel, then n = 2 represents a prudent choice of fuel usage. Higher values of n place greater importance on fuel usage.

The command profiles corresponding to the nodes of the fuel/duration curve can also be obtained using a fuel/time optimal problem formulation, where the cost function is:

$$J = \int_0^{t_f} (1 + \alpha |u|) dt \tag{5.30}$$

The cost function is minimized subject to the boundary conditions and the state equations. The solutions at the nodes are obtained by first calculating an appropriate weight, α_{crit}, and then using α_{crit} in (5.30) [104]. Figure 5.21 shows that in order to obtain fuel-efficient control (commands at the first node of the fuel/duration curve), α_{crit} must be a function of the desired move distance. That is, the fuel-efficient control cannot be obtained using a constant weighting value in the fuel/time optimal control formulation.

If it is desired to use command profiles corresponding to the nodes of the fuel/duration curves, then the easiest procedure is to use the fuel-efficient method proposed in the previous section, as it is valid for any robustness criteria including both ZV and ZVD constraints. Use of (5.29) with the specified-fuel formulation described above is also straightforward when ZV commands are used. The calculation of α_{crit} and then using a fuel/time optimization is a slightly more difficult process.

5.3.4 Discussion of Specified-Fuel Commands

A method was presented for designing on-off command profiles for flexible systems that use a specified amount of actuator fuel. The problem was formulated as both a time-optimal control problem and an input shaping problem. Three types of specified-fuel commands were discussed, those based on rigid-body dynamics, flexible-body dynamics, and robust flexible-body dynamics. Properties of the command profiles were compared as a function of the fuel usage. Plots of the slew duration vs. fuel usage show that the fuel consumption can be significantly reduced (as compared to a purely time-optimal command), with very little increase in slew time. However,

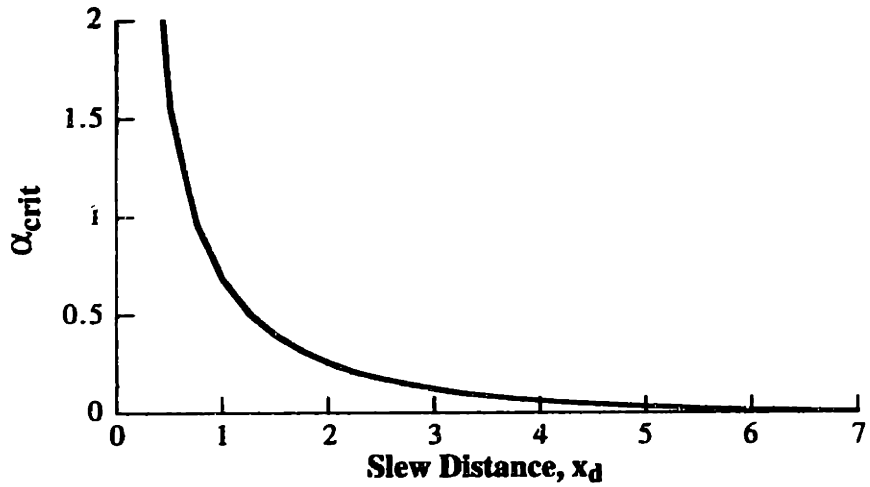

Figure 5.21: α_{crit} as a Function of Move Distance.

very low levels of fuel usage require very long slew durations. The robust formulation of the problem accommodates large modeling uncertainty at the cost of small increases in slew duration. Locations where the command profile based on flexible dynamics transitions from 4 pulses to 2 pulses are prudent choices and the corresponding fuel usage was determined in closed form. Finally, the input shaping formulation was shown to be advantageous because it can be used to force the command profile into a consistent form.

5.4 Deflection-Limiting Commands

Applications such as reorienting the space shuttle with a payload attached to the remote manipulator require large angle slewing with suppression of elastic modes. When the maneuver time is minimized without regard to system flexibility, large amplitude transient and steady state oscillations may occur, especially when the system is equipped with on-off reaction jets. The objective in such applications is often a rest-to-rest slew with limited vibration both during and at the end of the maneuver. For example, it may be necessary to generate a torque profile such that a system like the one shown in Figure 5.22 is rotated through a desired angle, θ_1, while the deflection (θ_2) remains small throughout the slew and goes to zero at the end of the slew. A similar problem would be to move the system shown in Figure 4.1 a finite distance, while limiting the maximum spring compression and eliminating the residual vibration.

Considerable work has been done on the topic of slewing with vibration control, in addition to the work on time-optimal flexible-body control previously cited. Closed loop, near-minimum time control based on Liapunov and sliding mode techniques has been presented [23, 47]. Calculus of variations was used to generate command profiles designed to minimize vibration in a simple flexible spacecraft model [29]. Shaped torque commands constructed from finite trigonometric series were proposed for minimizing modal vibration in a flexible satellite system [142]. Profiles designed using optimal control techniques were applied to a model of a spacecraft with flexible appendages [147].

The previous work with minimum-time commands and the on-off commands of the previous sections has concentrated on eliminating *residual* vibration. No constraints were placed on the amplitude of deflection *during* the slew. Input shaping is very successful at eliminating residual vibration and has the benefit of decreasing transient deflection when compared to bang-bang control [79]. However, the amplitude of the transient deflection is not limited and can still be very large. It is well known that large structural deflections induce large internal loads, and hence, deflection limiting can be very important.

This section presents a robust input shaping method for limiting deflection during the slew. This problem is significantly different than the earlier input shaping problem formulations. The difference arises from the nature of the constraint equations used to design the on-off control profiles. Previously, constraints were placed on the residual vibration amplitude, slew distance, fuel usage, etc. at a specific instant in time – the end of the command profile. However, limiting deflection during the slew requires constraints over the entire period of the slew.

Three procedures for obtaining deflection-limiting input shapers will be presented. The first method places constraints on the extrema points of the system's deflection. This method yields

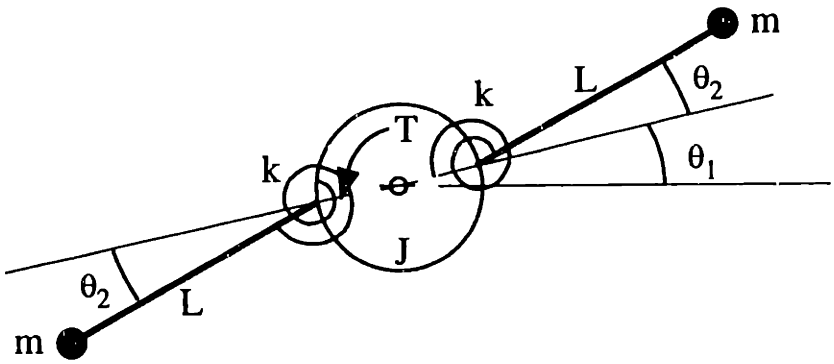

Figure 5.22: Simple Model of Flexible Rotary System.

responses which precisely meet the desired deflection amplitude, but the solutions are difficult to obtain when the deflection is severely limited. The second method yields approximate solutions by limiting the deflection amplitude at specific time intervals, rather than at the extrema points. The final method constrains the global maximum deflection by placing a simulation of the system being controlled inside of an optimization loop. This method is more difficult to use, but has the ability to deal directly with multi-mode and nonlinear systems. Results from computer simulations will be used throughout this section to illustrate key results.

5.4.1 Constraints Used for Deflection-Limiting Input Shaping

As we know, the constraints used thus far for generating on-off commands can be categorized as (1) Residual vibration constraints (2) Robustness constraints (3) Requirement of time optimality (4) Rigid-body constraints (5) Constraints on the impulse amplitudes and (6) Fuel-efficiency constraints. In this section an additional type of constraint is used: (7) Deflection constraints.

5.4.2 Deflection Constraints

In order to control the level of deflection during a motion, an expression for the deflection as a function of the input shaper must be obtained. The desired function can be generated using superposition of deflections from individual step inputs. An expression for the deflection of the system shown in Figure 4.1 is easily derived. The result is applicable to other systems with one flexible mode and a rigid-body mode, such as the system in Figure 5.22. The Laplace transforms of the equations of motion for the system shown in Figure 4.1 are:

$$\mathbf{F}(s) = \left(m_1 s^2 + k\right)\mathbf{x}_1(s) - k\mathbf{x}_2(s) \tag{5.31}$$

$$0 = \left(m_2 s^2 + k\right)\mathbf{x}_2(s) - k\mathbf{x}_1(s). \tag{5.32}$$

Equation (5.32) can be solved for $\mathbf{x}_2(s)$:

$$\mathbf{x}_2(s) = \frac{k}{\left(m_2 s^2 + k\right)}\mathbf{x}_1(s). \tag{5.33}$$

Combining (5.31) and (5.33) and assuming $\mathbf{F}(s) = u_{max}/s$ (assuming F(t) is a step input of magnitude u_{max}) gives:

$$\mathbf{x}_1(s) = u_{max}\left\{\frac{m_2 s^2 + k}{s^2\left[m_1 m_2 s^2 + (m_1 + m_2)k\right]}\right\}. \tag{5.34}$$

The deflection for this system is the change in the natural length of the spring, which is defined as $D(t)=x_2(t)-x_1(t)$. Compression is a negative value; extension is positive. Therefore, from (5.33) we have:

$$\mathbf{D}(s) = \left[\frac{k}{(m_2 s^2 + k)} - 1\right]\mathbf{x}_1(s) \tag{5.35}$$

substituting (5.34) into (5.35) yields:

$$\mathbf{D}(s) = \frac{-u_{max} m_2}{m_1 m_2}\left\{\frac{1}{s(s^2 + \omega^2)}\right\} \tag{5.36}$$

where,

$$\omega^2 = \left(\frac{m_1 + m_2}{m_1 m_2}\right)k. \tag{5.37}$$

Taking the inverse Laplace transform of (5.36) assuming zero initial conditions gives the deflection from a step input as a function of time:

$$D(t) = \frac{D_{max}}{2}[\cos(\omega t) - 1] \tag{5.38}$$

where ω is the natural frequency of oscillation and the maximum deflection magnitude, D_{max}, is given by:

$$D_{max} = \frac{2u_{max} m_2}{k(m_1 + m_2)}. \tag{5.39}$$

The coefficient in (5.38) is written as $D_{max}/2$ because the quantity enclosed in the brackets has a maximum magnitude of two. A deflection equation with a structure identical to (5.38) can be similarly derived for the system shown in Figure 5.22.

Multiple versions of (5.38) can be used to generate a function that describes the deflection throughout a slew containing many step inputs (a pulse in force is composed of two step inputs – one positive and one negative delayed in time). Assuming that the command profile is a fuel-efficient profile obtained by using (5.2), then the deflection throughout the slew is given by:

$$D(t) = D_{(m)-(m+1)}(t) \qquad t_m \le t < t_{m+1}, \quad m = 1, \ldots, n. \tag{5.40}$$

where,

$$D_{(m)-(m+1)}(t) = \sum_{i=1}^{m} A_i \frac{D_{max}}{2}[\cos(\omega(t - t_i)) - 1] \tag{5.41}$$

It is important to note the restriction presented by the qualifier $t_m \le t < t_{m+1}$. The deflection which

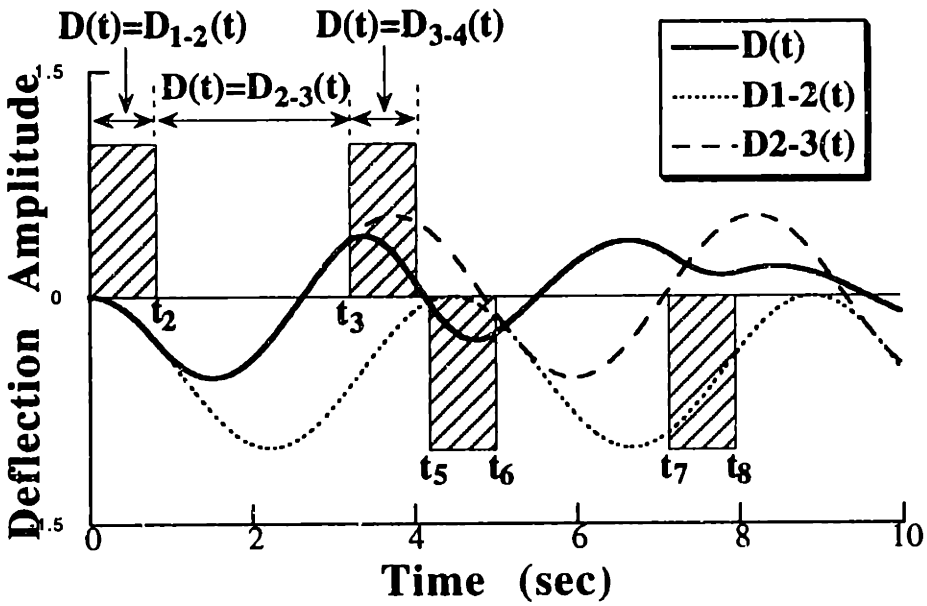

Figure 5.23: Formation of the Deflection Function from Piecewise-Continuous Segments.

occurs between the first and second impulses of the input, $D_{1\text{-}2}(t)$, (the period during the first pulse) is given by (5.40) when m = 1. The deflection, $D_{2\text{-}3}(t)$, between the second and third impulses is given by (5.40) when m = 2. This is the coasting period between the first and second positive pulses (see Figure 3). The deflection, $D_{3\text{-}4}(t)$, that occurs during the second pulse is given by (5.40) with m = 3, etc. This process of generating the deflection function is illustrated in Figure 5.23. Equation 5.40 amounts to a piecewise-continuous function composed of n finite length segments; each of the segments has a limited range of applicability.

Note that the magnitude of deflection caused by a series of pulses can exceed D_{max} if the deflection components from individual pulses interfere constructively. The actual value of the parameter D_{max} is not needed if we generate the constraint equations in terms of a percentage deflection limit. We can form a nondimensional deflection limit, D_L, which is equal to the amplitude of the desired deflection, divided by D_{max}. When the constraints are formed in this manner, the parameter D_{max} does not appear.

5.4.3 Limiting Local Extrema Points

One method to limit the maximum transient deflection is to locate all of the local extrema of the deflection function and place limits on the deflection amplitude at these instances. To obtain the extrema points of the deflection, (5.40) is differentiated with respect to time and the result is set equal to zero. The time values satisfying the resulting equation correspond to the extrema points. To obtain the general expression for the location of the extrema points, we first start with the

extrema point that occurs between the first and second impulses. The deflection between impulses 1 and 2, $D_{1\text{-}2}(t)$, is obtained from (5.40) with m = 1:

$$D_{1-2}(t) = A_1 \frac{D_{\max}}{2}[\cos(\omega t) - 1]. \tag{5.42}$$

Differentiating (22) and setting the result to zero, we obtain

$$\frac{dD_{1-2}}{dt} = A_1 \frac{D_{\max}}{2}[-\omega \sin(\omega t)] = 0. \tag{5.43}$$

Equation 5.43 is satisfied by $\omega t = i\pi$, i = 0, 1, 2,... The even values of i correspond to times when the deflection is at a minimum (zero), while the odd values of i correspond to times when the magnitude of the deflection, $|x_2(t)\text{-}x_1(t)|$, is at a maximum – these are the times we are seeking. If we require that $D_{1\text{-}2}(t)$ given by (5.42) be less than a desired value at $t = \pi/\omega$, then we have obtained a deflection constraint equation which is a function of a specified time. The constraint can be written as:

$$D_{1-2}(\pi/\omega) = \left| A_1 \frac{D_{\max}}{2}[\cos(\pi) - 1] \right| = A_1 D_{1\max} \le D_L \tag{5.44}$$

where D_L is the desired nondimensional deflection limit. Note that (5.44) is only an appropriate constraint if $t = \pi/\omega$ lies between the first and second impulses. If the second impulse occurs before $t = \pi/\omega$, then there will not be an extrema point of the deflection between the first and second impulse and, therefore, (5.44) is not a valid constraint.

The above process for obtaining deflection constraints can be repeated for all n segments of (5.40). The steps required for m = 2 will be shown and then a general purpose formula will be given. When m = 2, the deflection between t_2 and t_3 is:

$$D_{2-3}(t) = A_1 \frac{D_{\max}}{2}[\cos(\omega t) - 1] + A_2 \frac{D_{\max}}{2}[\cos(\omega(t - t_2)) - 1]. \tag{5.45}$$

Differentiating (5.45), we obtain:

$$\frac{dD_{2-3}}{dt} = A_1 \frac{D_{\max}}{2}[-\omega \sin(\omega t)] + A_2 \frac{D_{\max}}{2}[-\omega \sin(\omega(t - t_2))] = 0. \tag{5.46}$$

Assuming that the impulse amplitudes are given by (5.2), then (5.46) is satisfied when:

$$\sin(\omega t) = \sin(\omega(t - t_2)). \tag{5.47}$$

Expanding the term on the right hand side yields:

$$\sin(\omega t) = \sin(\omega t)\cos(\omega t_2) - \cos(\omega t)\sin(\omega t_2). \tag{5.48}$$

Dividing by cos(ωt) and rearranging terms gives:

$$\tan(\omega t) = \frac{-\sin(\omega t_2)}{1 - \cos(\omega t_2)}. \tag{5.49}$$

Finally, taking the inverse tangent gives the extrema point between the second and third impulses:

$$t_{2-3} = \frac{1}{\omega}\tan^{-1}\left[\frac{-\sin(\omega t_2)}{1 - \cos(\omega t_2)}\right]. \tag{5.50}$$

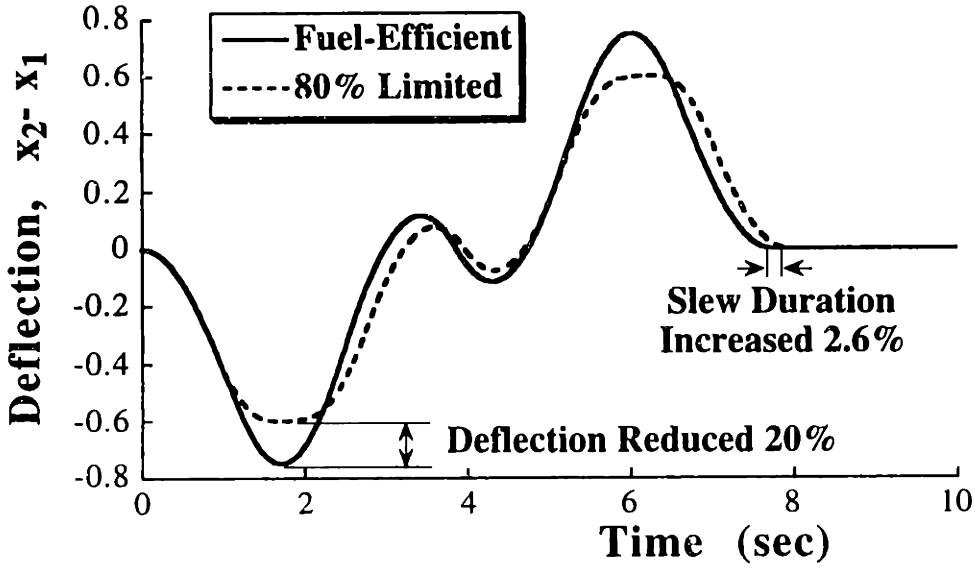

Figure 5.24: Comparison of Unrestricted and Deflection-Limited Responses.

If $t_{2\text{-}3}$ lies between the second and third impulses, then substituting $t_{2\text{-}3}$ as given by (5.50) into (5.45) and limiting the resultant equation to below D_L is an appropriate constraint. Assuming that the impulse amplitudes are either ±1, the location of the extrema point between the impulses i and (i+1) is:

$$t_{i-(i+1)} = \frac{1}{\omega}\tan^{-1}\left[\frac{sgn(A_2)\sin(\omega t_2)+sgn(A_3)\sin(\omega t_3)+...+sgn(A_i)\sin(\omega t_i)}{sgn(A_1)+sgn(A_2)\cos(\omega t_2)+...+sgn(A_i)\cos(\omega t_i)}\right] \tag{5.51}$$

where, the sgn function gives the sign of the impulse amplitude. The extrema points given by (5.51) are substituted back into the appropriate segment of (5.40) and the resulting equations are constrained to be below the desired deflection limit. If the deflection constraint equations are solved simultaneously with the previous on-off input shaping constraint equations, then the resulting switch times will generate the deflection-limiting on-off command profile we are seeking. To assess the above process, command profiles were designed for the system shown in Figure 4.1. A natural frequency of 0.2251 Hz was obtained by setting $m_1 = m_2 = k = u_{max} = 1$. A desired move distance of 5 units was selected as a baseline case. The fuel-efficient command without deflection limiting consists of two positive and two negative pulses and is described by:

$$\begin{bmatrix} A_i \\ t_i \end{bmatrix} = \begin{bmatrix} 1 & -1 & 1 & -1 & -1 & 1 & -1 & 1 \\ 0 & 1.1998 & 2.3854 & 3.8605 & 3.8605 & 5.3356 & 6.5212 & 7.7210 \end{bmatrix}. \tag{5.52}$$

The deflection resulting from this fuel-efficient command is shown in Figure 5.24. The maximum deflection is 0.75 units.

Deflection-limiting constraints were then added to the problem formulation and a new optimization was performed with the deflection limited to 0.6, so that the deflection would be 80%

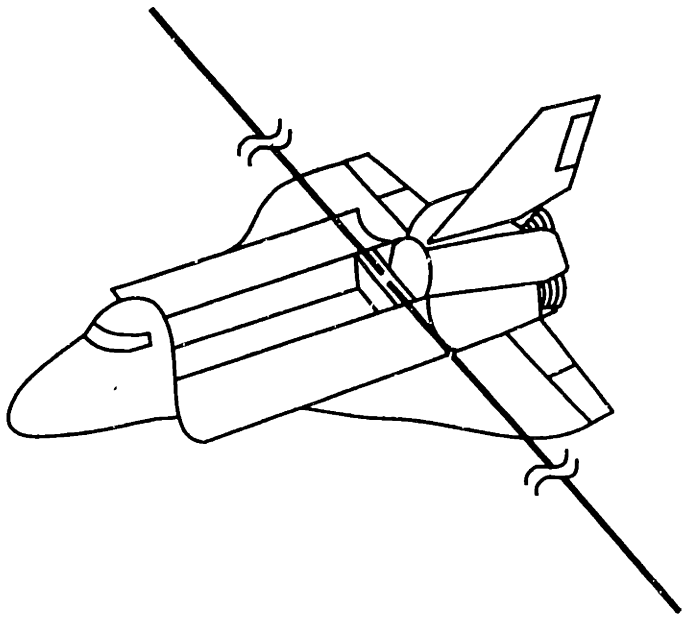

Figure 5.25: WISP System.

of the level with the unconstrained fuel-efficient profile. The 80% limited command profile consists of three positive and three negative pulses given by:

$$\begin{bmatrix} A_i \\ t_i \end{bmatrix} = \begin{bmatrix} 1 & -1 & 1 & -1 & 1 & -1 & -1 & 1 & -1 & 1 & -1 & 1 \\ 0 & 0.9062 & 1.5359 & 2.0527 & 2.7770 & 3.9612 & 3.9612 & 5.1454 & 5.8698 & 6.3865 & 7.0162 & 7.9224 \end{bmatrix}. \quad (5.53)$$

The response to the deflection-limiting profile is also shown in Figure 5.24. Although the deflection is reduced 20%, the slew duration is increased only 2.6%. Note that the residual vibration is completely eliminated by both commands.

For a more rigorous test, deflection-limiting command profiles were designed for the nonlinear Waves In Space Plasma (WISP) system [6]. The WISP system consists of two 150 m long antenna booms attached to the Space Shuttle. A sketch of the system is shown in Figure 5.25. When the system is moved using the thrusters, tens of meters of endpoint deflection can occur.

In order to apply the above method, which is based on the simple models of Figure 4.1, to the nonlinear WISP system, a simulation of the WISP system was performed using the nonlinear model previously described in the literature [6]. An approximate value for the fundamental period of 535 sec. was obtained from time response data and the damping was approximately zero. Using these two parameters and the actuator force-to-mass ratio, the WISP system was modeled as the system shown in Figure 5.22. A deflection-limiting input shaper was designed by limiting the extrema points as described above. The deflection limit was set so that the tip deflection would be 15 m. The resulting command was then used as the input to the nonlinear WISP simulation.[21]

[21] The simulations of the WISP system were performed by Dr. Arun Banerjee.

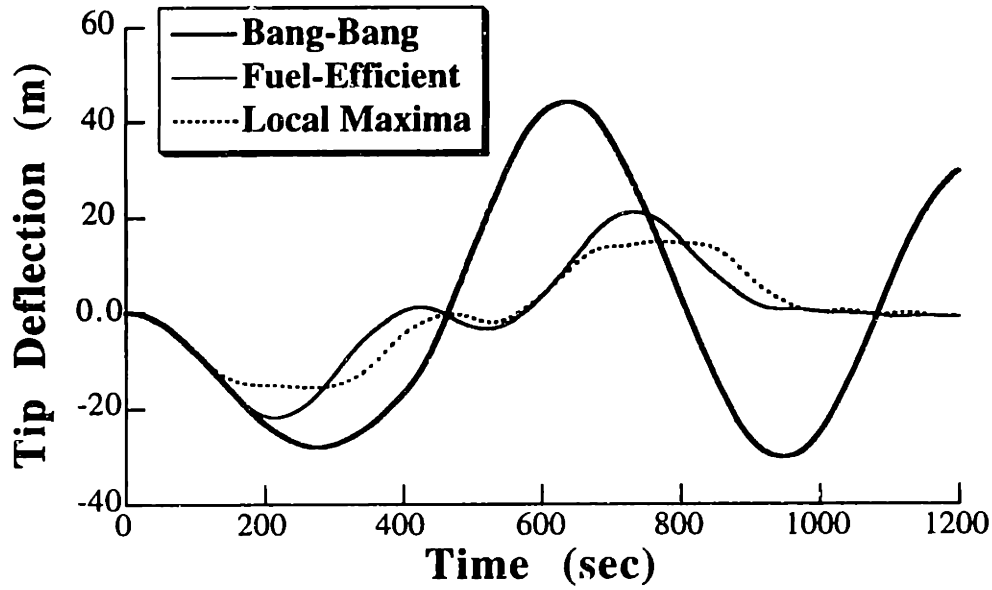

Figure 5.26: Deflection Responses of the WISP System.

Figure 5.26 shows deflection responses to a bang-bang input, a fuel-efficient input, and the deflection-limited input. Not only is the residual oscillation virtually eliminated by the shaped profiles, but the deflection during the slew is very close to the design value. The profile designed for 15 m maximum deflection yields a tip deflection of 15.4 m. Although the profiles were designed using a simple, one-mode linear model, the method provides excellent performance for the nonlinear system. The small level of residual vibration results from system nonlinearities and a second mode whose period is approximately 90 sec.

Using the extrema points to limit the deflection becomes difficult when the deflection is severely limited. A problem arises because severe restrictions on the deflection amplitude require the use of numerous, short duration pulses. Each additional pulse leads to two additional extrema points and consequently two additional versions of (5.51). Because the inverse tangent function is used in (5.51), a time value which falls within one period of the oscillation is returned. The time value must be shifted by an appropriate multiple of the half period to get the true time location of the extrema point. This time shifting becomes difficult to implement with large numbers of pulses and slews that take several periods to complete.

5.4.4 Deflection Sampling

In this section a procedure is presented that does not use (5.51), consequently it can be used when large decreases in the deflection are desired. The method is an approximate method; however, it yields very good solutions. Rather than locate and limit the extrema points, the deflection given by (20) is constrained to be less than some tolerable percentage deflection, D_L at

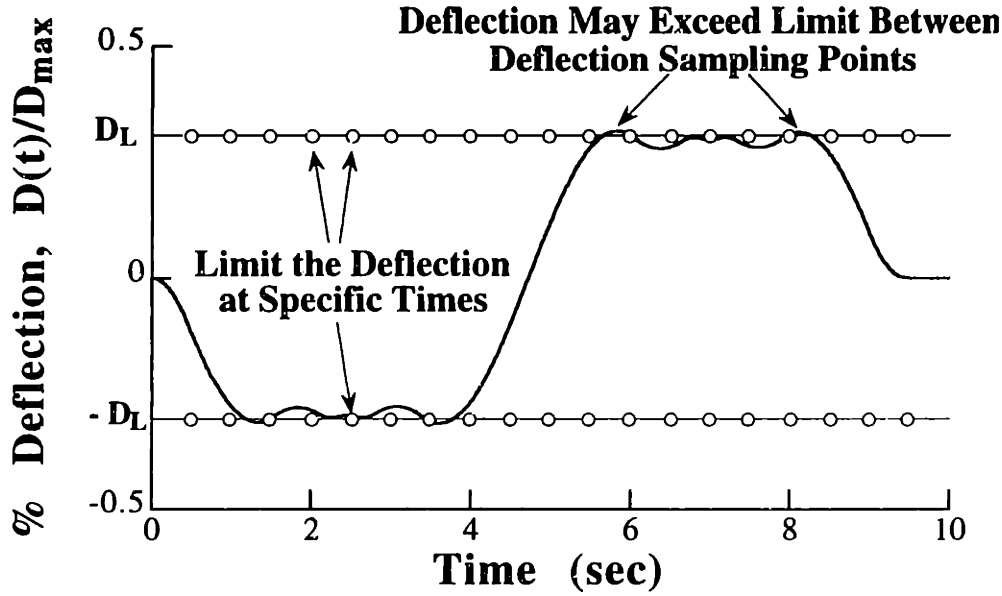

Figure 5.27: Illustration of Deflection Sampling.

periodic instances throughout the slew. That is, the deflection constraints are:

$$D_L \geq \sum_{i=1}^{m} A_i[\cos(\omega(t_s - t_i)) - 1] \qquad t_m \leq t \leq t_{m+1}, \quad m = 1, \ldots, n \tag{5.54}$$

where t_s are specific instances in time at which the deflection function is sampled and required to be bounded by D_L. The process of deflection sampling is illustrated in Figure 5.27. Note that this procedure does not guarantee that the deflection will be bounded by D_L at all times, only at the sampled times. However, by making the sampling points close together, the deflection can be effectively limited. The trade-off is that as the accuracy of the solution is increased, the number of equations which must be satisfied increases.

Rather than using the fixed time interval sampling shown in Figure 5.27, a fixed number of samples per force pulse and coast period is used. The primary reason for this choice is ease of implementation. During each pulse or coast period the deflection constraint is given by one of the n equations listed in (5.54). By using R samples during each pulse or coast period, the constraints can be written easily as R versions of the n equations given in (5.54). That is, the deflection constraints consist of R versions of (5.54) with m = 1, R versions of (5.54) with m = 2, etc. For a given value of m, the R equations differ in that the time location at which they are enforced is different. Within each pulse or coast period, the deflection is sampled at $(t_{m+1}-t_m)/R$.

If a fixed time period sampling is used instead, the deflection constraint that must be used at each sampling point is then a function of the impulse times. Because the impulse times are being changed during the optimization and the change in impulse times triggers a change in the equations being optimized, the optimization becomes very difficult to perform.

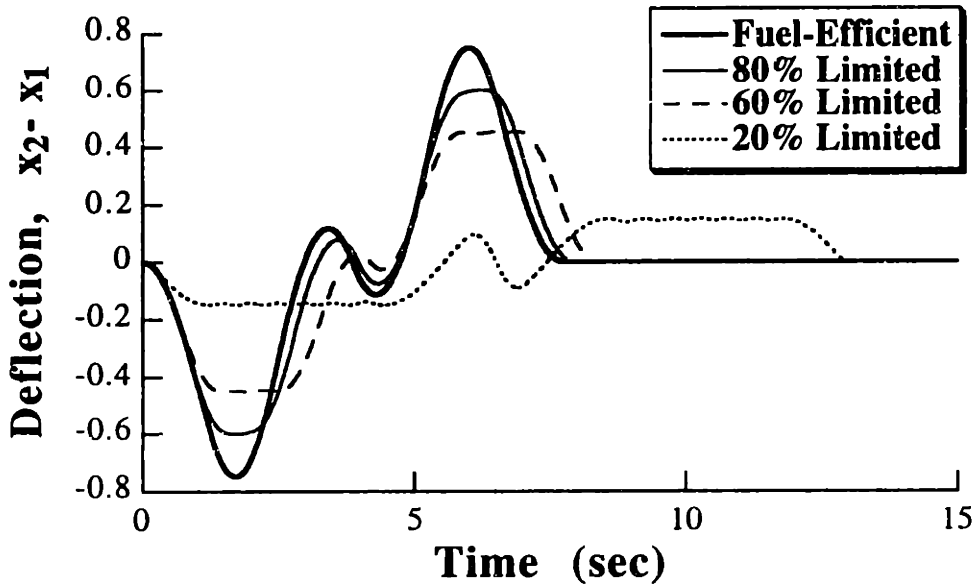

Figure 5.28: Deflection Curves of Linear System for Several Values of the Deflection Limit.

To demonstrate the effectiveness of deflection sampling, new profiles where designed for the system of Figure 4.1 using a sampling resolution of R = 20. The new profiles where designed to meet more severe deflection-limiting constraints. Figure 5.28 shows the responses of Figure 5.24 along with responses when the deflection is limited to 60% and 20% of the baseline level. Note that in all cases the residual vibration is zero. Limiting the deflection causes the slew time to increase. The increase in slew time is small for the 80% and 60% limited profiles. The time penalty increases substantially as the deflection limit approaches zero. Even though deflection sampling is an approximate method, the deflection curves shown in Figure 5.28 are all well within 1% of the desired deflection limit.

The effectiveness of deflection sampling depends on the sampling resolution. The appropriate choice of resolution depends on system parameters such as natural frequency and maneuver duration; however, the most important issue is the acceptable overshoot in maximum deflection amplitude. If the actual deflection is permitted to exceed D_L by a few percent, then the sampling resolution can be very coarse. Two or three samples per command pulse may be all that is needed. If, on the other hand, the deflection limit is a very strict design parameter, then the sampling resolution must be increased or the deflection limit must be decreased slightly to account for the overshoot between sampling points.

5.4.5 Using a Simulation Inside the Optimization Loop

The final method presented here for obtaining deflection-limiting shapers uses a numerical simulation within an optimization loop.[22] To implement this scheme, the nonlinear constraint optimization software, ADS[158] was used, choosing the option of modified method of feasible directions. The deflection amplitude constraint is handled by numerically integrating the equations of motion up to the final time and noting the maximum tip deflection. This global maximum deflection is returned to the optimization and used to drive the search algorithm. All gradients needed in the optimization method are calculated by finite difference. It is found that scaling of the robustness constraint, helps significantly in the convergence of the optimization process.

To proceed, one chooses a particular pulse profile (choose a specific value for n in (5.2)). A solution is sought first neglecting the deflection amplitude information provided by the simulation; this paves the way for "creeping up" on the solution. When the solution without deflection limiting is obtained, it is used as the initial guess for the optimization which includes the simulation feedback. When the deflection limiting is first included in the constraints, D_L, is initially set to a value very close to the deflection that occurs without any deflection constraints. When a solution is obtained, it is used as the initial guess for a more restrictive value of D_L. The process is repeated until the desired value of D_L is reached. The above process is not a requirement; however, it facilitates the optimization.

Although this method usually requires the use of several optimizations, it can directly handle system nonlinearities if a nonlinear simulation is used for feedback to the optimization. Furthermore, it can easily accommodate multi-mode systems. To do this, one integrates the multi-mode system equations and constrains the global maximum deflection below the specified limit. To use the first two deflection-limiting methods on multi-mode systems requires the generation of a multi-mode deflection expression. That is, an expression analogous to (5.40) must be derived which accounts for the multiple modes.

5.4.6 Comparison of Deflection-Limiting Methods

Although the three methods described above are significantly different in their approaches to the problem, they produce very similar command profiles. Limiting local extrema and using a simulation in the loop will produce exactly the same results if the system is perfectly linear. Deflection sampling will not produce exactly the same result due to its approximate nature.

When the system is nonlinear, each technique will produce a slightly different profile. When applied to the WISP system with a 15 m deflection limit, the techniques yield the following profiles:

[22] This procedure was suggested by Dr. Arun Banerjee [8, 114].

Limiting Local Extrema:

$$\begin{bmatrix} A_i \\ t_i \end{bmatrix} = \begin{bmatrix} 1 & -1 & 1 & -1 & 1 & -2 & 1 & -1 & 1 & -1 & 1 \\ 0 & 97.6 & 180.1 & 284.2 & 372.1 & 495.2 & 618.3 & 706.1 & 810.3 & 892.7 & 990.3 \end{bmatrix} \tag{5.55}$$

Deflection Sampling:

$$\begin{bmatrix} A_i \\ t_i \end{bmatrix} = \begin{bmatrix} 1 & -1 & 1 & -1 & 1 & -2 & 1 & -1 & 1 & -1 & 1 \\ 0 & 97.8 & 180.4 & 284.7 & 372.4 & 495.2 & 617.9 & 705.6 & 809.9 & 892.6 & 990.3 \end{bmatrix} \tag{5.56}$$

Simulation in the Loop:

$$\begin{bmatrix} A_i \\ t_i \end{bmatrix} = \begin{bmatrix} 1 & -1 & 1 & -1 & 1 & -1 & -1 & 1 & -1 & 1 & -1 & 1 \\ 0 & 100.9 & 178.5 & 276.3 & 363.8 & 479.1 & 507.6 & 623.5 & 708.9 & 804.9 & 885.7 & 989.2 \end{bmatrix} \tag{5.57}$$

The response to each of these profiles is shown in Figure 5.29. All three methods limit the deflection to near the 15 m limit and produce very small levels of residual vibration.

5.4.7 Deflection-Limiting of Multi-Mode Systems

As mentioned previously, the small level of residual oscillation of the WISP system is composed partly of a secondary mode with a 90 sec. period. A command profile was generated using deflection sampling to eliminate this secondary mode by simply enforcing a second set of ZVD constraints at this higher mode. Figure 5.30 compares the response of this two-mode profile to the three responses shown in Figure 5.29. The secondary mode has been completely eliminated. The downward trend in the response from 1000 to 1200 sec. is caused by the small amplitude residual vibration of the low mode.

Note that the deflection of the second mode was not limited, only its residual amplitude. That is, the deflection constraints where based on the single-mode deflection expression given in (5.54). Multi-mode deflection constraints were not needed in this case because the first mode dominates the transient deflection amplitude. If a secondary mode contributes significantly to the deflection amplitude, then a two-mode deflection expression must be used with deflection sampling. The process of limiting the local extrema gets prohibitively complicated for multi-mode systems. Multi-mode system deflections are handled well by the simulation-in-the-loop method.

5.4.8 Characteristics of Deflection-Limiting Input Shapers

The number of impulses and their time locations in a deflection-limiting input shaper depend on the system frequency, damping, slew distance, force-to-mass ratio, and transient deflection limit. In this section, the characteristics of deflection-limiting shapers will be presented as a function of the deflection limit.

The results shown here are for the benchmark system of Figure 4.1. Figure 5.31 shows the impulse time locations (command switch times) as a function of the percentage deflection. Only the impulse locations for the first half of the profile are shown; the profile is antisymmetrical about the midpoint.

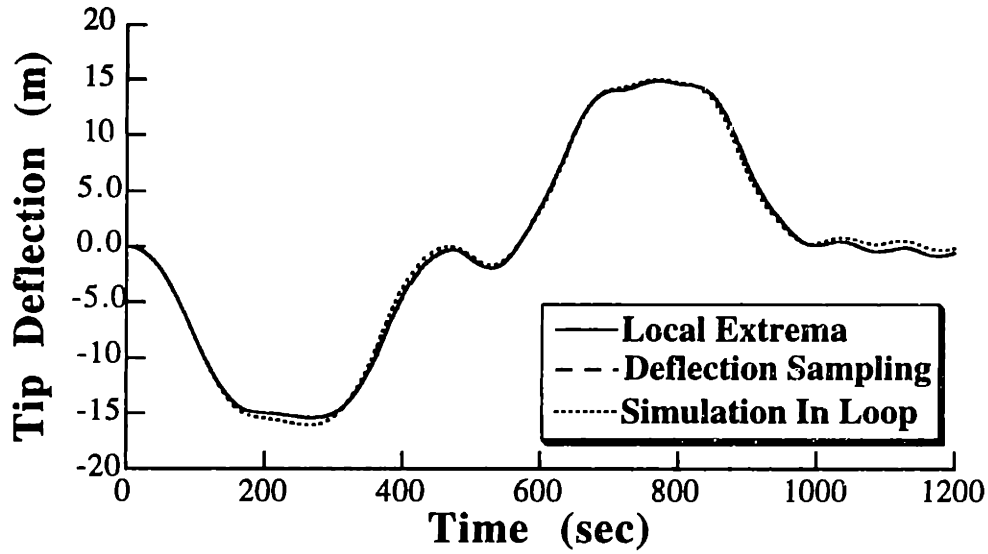

Figure 5.29: Comparison of WISP Response to Three Different Profiles.

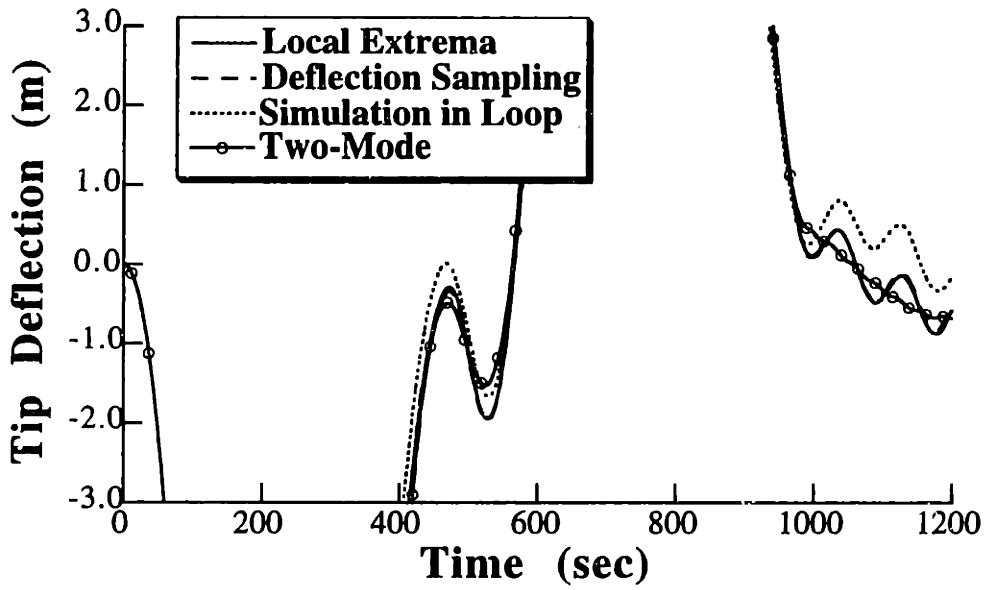

Figure 5.30: WISP Responses to Single and Two-Mode Profiles.

For small reductions in the deflection (large values of the percentage deflection), the command consists of three positive pulses followed immediately by three negative pulses. As the deflection is decreased, additional pulses appear in the profile. This effect makes intuitive sense because the command must accelerate the system for shorter periods of time if the deflection is to be reduced. Mathematically, this means that the optimization problem described above admits a solution only in a manifold of expanding dimension. In seeking a numerical solution, one learns this whenever the constrained optimization fails for an assumed number of pulses (shaper impulses). A solution is then facilitated by increasing the number of pulses. The information shown in Figure 5.31 was

obtained by cycling through the deflection limit and performing an optimization to obtain the impulse times at each value.

We can now make important observations about deflection-limiting command profiles. The first pulse in the command accelerates the system as long as possible without exceeding the maximum allowable deflection. The subsequent positive pulses keep forcing the deflection to the maximum value. Furthermore, the additional pulses that appear when the deflection limit is lowered tend to cluster near the center of the positive pulse train. The width of the middle positive pulses (or, the coast periods between the pulses) is set by a minimum pulse width requirement. If a minimum pulse width requirement is not used, the pulses, or coast periods become very small and would not be realizable because physical systems always take a finite period of time to change the actuator state. If the minimum width is reduced, the number of pulses increases. The negative pulses decelerate the system in a similar manner; they keep the deflection near the maximum allowable.

Implementation of this method would be facilitated if the number of command pulses was independent of the system parameters and deflection limit. The method can be modified slightly to achieve such a result. The number of pulses can be specified by simply fixing the number of impulses, n, in the shaper, see (5.2). However, if the profile is limited to fewer pulses than contained in the optimal solution, then the slew duration will obviously be lengthened.

Figure 5.32 shows the maneuver duration for a 5 unit slew when the command profile is limited to a specified number of pulses. Limiting the command profile to 6 pulses has essentially no effect on the maneuver duration until the deflection is lowered to approximately 50% of the baseline level. Allowing 8 pulses yields essentially time-optimal slews down to a deflection limit of approximately 30%. Only at very low levels of allowable deflection is a significant time penalty incurred by restricting the command profile to a small number of pulses. That is, fixing the number of pulses for ease of implementation is advantageous except in very restricted cases.

5.4.9 Discussion of Deflection-Limiting Commands

Methods for limiting both transient and residual oscillations during the rest-to-rest slewing of flexible systems has been presented. The technique uses a specialized form of input shaping to create appropriate on-off command profiles. Three procedures were presented for designing the necessary input shaper 1) the extrema points of the deflection were located and limited, 2) the deflection was limited at discrete time locations, and 3) a simulation of the system was placed inside an optimization loop. Procedure 1 yields exact solutions, but is difficult to implement when severe limitations are placed on the deflection or when the system has multiple modes. Procedure 2 is the most straightforward and can be used effectively for cases of severe deflection limiting. Procedure 3 is both exact and direct, but requires several optimizations.

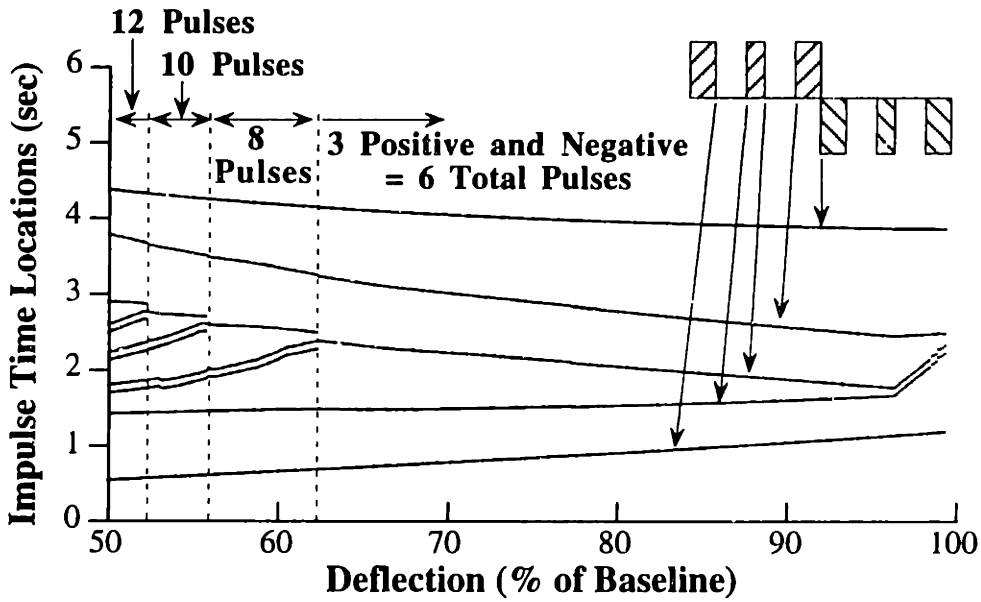

Figure 5.31: Command Structure as a Function of Deflection Limit. Impulse Times are Shown for Positive Pulses Only.

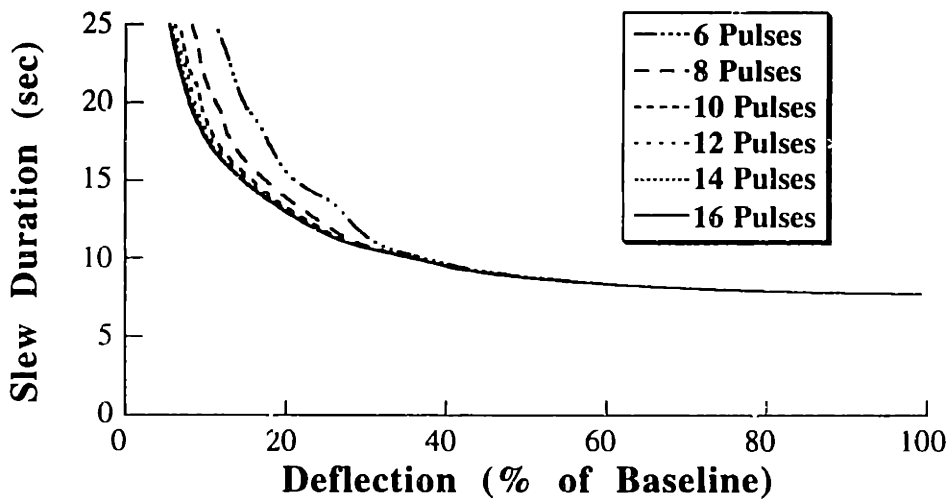

Figure 5.32: Command Duration with Fixed Number of Pulses.

The procedures were combined with previous input shaping techniques to obtain near time-optimal commands that robustly eliminate residual vibration and are fuel-efficient. The deflection and residual oscillation reduction was demonstrated with computer simulations. Furthermore, the robustness of the technique was demonstrated with the use of nonlinear simulations.

It was shown that the deflection can be significantly reduced without a substantial time penalty. As deflection is reduced the complexity of the command profile is increased. However, the command profile can be forced into a simple form for all values of the deflection with only a small penalty in move time.

6 METHODS FOR FACILITATING IMPLEMENTATION OF ON-OFF COMMANDS

6.1 Introduction to Methods for Facilitating Implementation

Generation of the on-off command profiles as presented in the previous two chapters requires the use of a nonlinear optimization to determine the profile for each desired motion (slew distance or spin-up velocity). While optimization methods are very powerful and can produce robust command profiles, they present some difficulties for real-time implementation.

There are two approaches to using the optimized command profiles. First, an optimization could be performed at the start of every slew. This introduces a time delay into the dynamics. Furthermore, nonlinear optimizations are subject to local minima, so for consistent performance some verification or checking algorithm must be performed on the output of the numerical optimization. This introduces an additional delay.

A second approach would be to compute the command profiles off-line and then store them for retrieval on demand. Possible techniques for accomplishing this include storing switch times in a table, generating curve fits to the data, or training a neural network to generate the command profile. For systems that perform a wide range of maneuvers or have limited computer memory, storing tabulated solutions is impractical. As we have seen, the switch times can be very complicated functions of the slew distance. This makes curve fitting a difficult proposition in many cases.

The methods presented in this chapter address the implementation difficulty presented by on-off commands. In Sections 6.2 - 6.4 on-off command profiles will be developed that can be described by simple functions of the system parameters. The necessary parameters are the system frequencies, damping ratios, the desired slew motion, and the maximum acceleration. Because the commands are described by closed-form equations, they can be generated in real-time without performing a numerical optimization. Section 6.2 deals with undamped single-mode systems, while Section 6.3 discusses modifications of the proposed method that allows it to work on

damped systems. Section 6.4 demonstrates the method on multi-mode systems.

Many of the profiles described in the Sections 6.2 - 6.4 are near time optimal. Other important qualities of the proposed command profiles, such as duration, fuel usage, maximum transient deflection, and robustness to modeling errors will be compared to both the time-optimal control of chapter 4, as well as input shaping with the negative input shapers of Section 3.5.

Section 6.5 explores the use of neural networks for implementing on-off control schemes. On-off commands for the benchmark system of Figure 4.1 are generated for a finite number of slew distances. Several types of neural networks are then trained using the data set. The performance of the various networks are compared.

6.2 Transition Shaping for On-Off Control of Undamped Single-Mode Systems

The goal of this section is to develop on-off commands that can be described by closed-form expressions involving the system parameters. A bang-bang function is an example of an on-off command that can be simply described by the system parameters. To demonstrate, a bang-bang command profile will be designed to move the system of Figure 4.1 a desired distance, x_d. If we assume that the bang-bang profile begins at time zero, then the only unknown is the switch time, t_2, because the duration of the negative pulse must equal the duration of the positive pulse to bring the system to rest. The value of t_2 can be obtained from the rigid-body dynamics. If the position of the mass center is given by x, then:

$$\ddot{x}(t) = \frac{F(t)}{m_1 + m_2}. \tag{6.1}$$

The position of the mass center at t_2 must equal one half the desired slew distance, x_d:

$$\frac{x_d}{2} = \iint \frac{F(t)}{m_1 + m_2} dt^2 = \frac{\alpha}{2} t_2^2 \tag{6.2}$$

where $\alpha = u_{max}/(m_1+m_2)$ is the maximum acceleration (force-to-mass ratio). Therefore,

$$t_2 = \sqrt{\frac{x_d}{\alpha}}. \tag{6.3}$$

Figure 6.1 shows the position of mass m_2 when the benchmark system is given a bang-bang input designed for $x_d = 5$. Although the mass center moves to the desired position, significant residual oscillations exist. As we have seen in the previous two chapters, time-optimal and robust time-optimal flexible-body command profiles can be generated by taking into account the system flexibility . Using a numerical optimization, the time-optimal ZV command for the above example was determined. It has switch times of 2.59 s., 3.33 s., and 4.07 s. and a total slew duration of 6.66 s. The response of the benchmark system to the time-optimal ZV command is also shown in Figure 6.1. The rise time is slightly slower than with the bang-bang command, but the residual oscillation has been eliminated.

To avoid the use of numerical optimization, the input shaping schemes of Chapter 3 could be used to modify the bang-bang function, which is known in closed-form. However, the resulting shaped command will not, in general, be an on-off function. The negative unity-magnitude input shapers of Section 3.5 can lead to acceptable on-off command profiles in some cases. The method described here will be compared to input shaping with these negative shapers.

6.2.1 Analytic Profile Generation

The method proposed here for deriving closed-form command profiles is based on two ideas. First, a bang-bang profile is a desirable template function because it produces fast rise times.

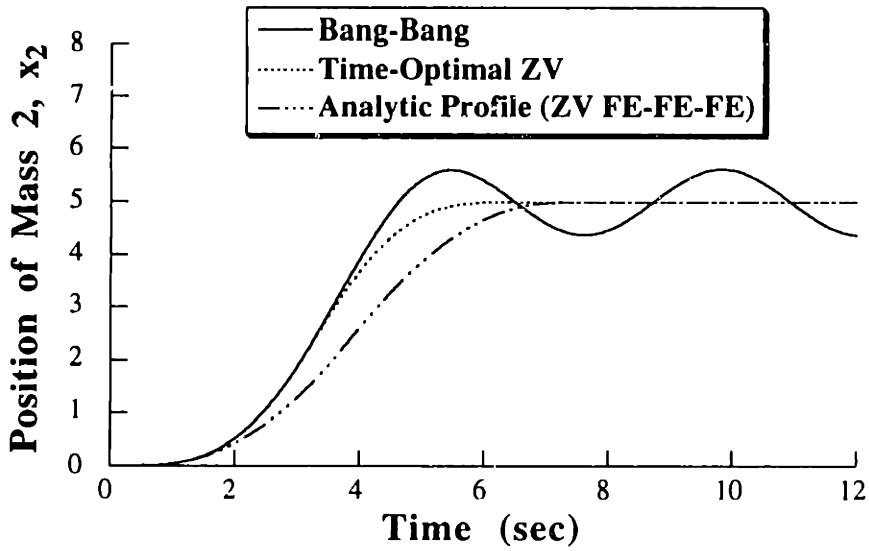

Figure 6.1: Response of the Benchmark System Shown in Figure 4.1.

Second, the three transitions which compose a bang-bang profile (zero to full positive, full positive to full negative, and full negative to zero) can be shaped so that they do not cause residual vibration. If each change in actuator state is performed without residual vibration, then the entire profile will not cause residual vibration. The proposed process is sketched in Figure 6.2. Although the command within the transition regions could have a variable amplitude, here it is restricted to be an on-off function. Once the actuator state transitions are shaped appropriately, the rigid-body motion is determined by the time duration between the transitions. This two-step process will be referred to as transition shaping.

6.2.1a One-Unit Transitions

There are several methods for transitioning the actuator from zero to full positive without causing residual vibration. These methods require turning the actuator on and off at specified times. If the switches are timed correctly, then the vibration caused by each of the switches will cancel out. Perhaps the simplest way to accomplish such a transition for an undamped system is to turn the actuator on for T/6 seconds, where T is the period of system vibration; turn the actuator off for T/6 seconds; and then turn the actuator back on. The vibration caused by the three switches in this process add up to zero. This can be better understood by interpreting the transition as a step input convolved with an input shaper of the form:

$$\begin{bmatrix} A_i \\ t_i \end{bmatrix} = \begin{bmatrix} 1 & -1 & 1 \\ 0 & \frac{T}{6} & \frac{T}{3} \end{bmatrix} \tag{6.4}$$

where A_i and t_i are the impulse amplitudes and time locations. This interpretation is shown in Figure 6.3. If the input shaper yields zero residual vibration, then the command transition formed

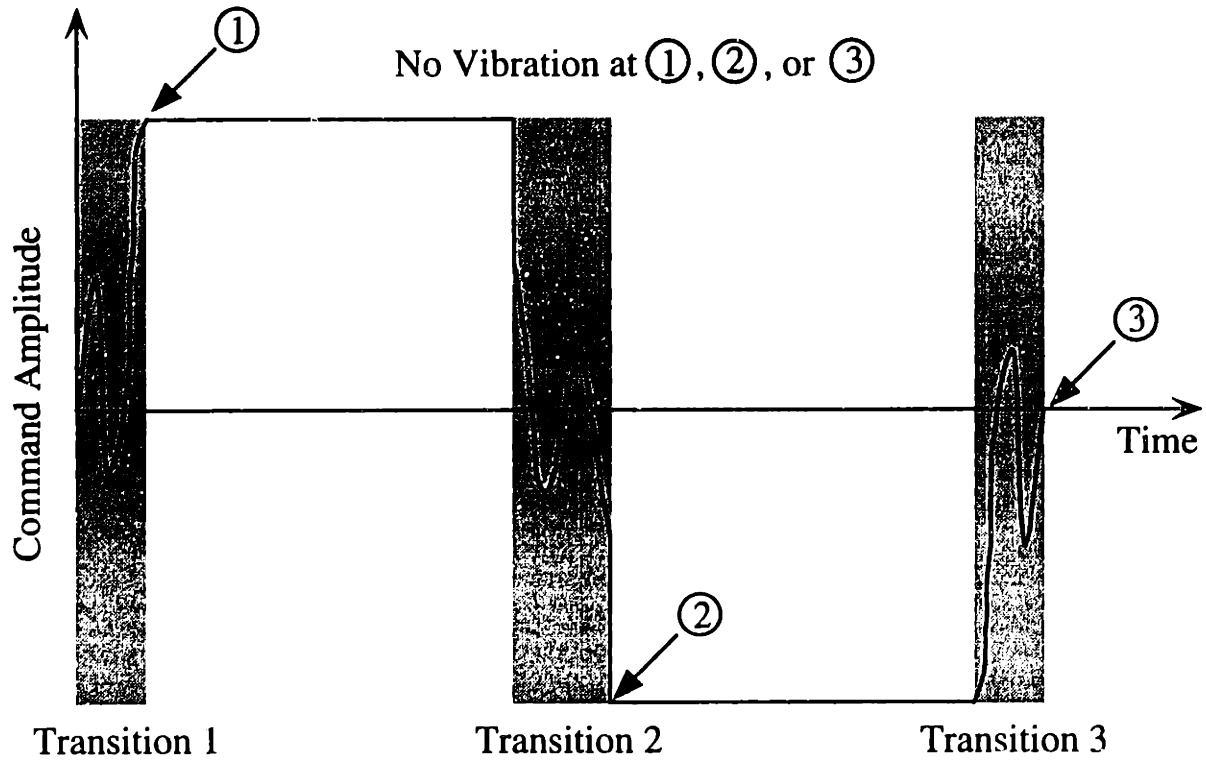

Figure 6.2: Sketch of Transition Shaping.

by convolving the shaper with a step input will also lead to no residual vibration. Note that the input shaper of (6.4) is the negative unity magnitude (UM) ZV shaper described in Section 3.5 and given by (3.48), (3.55), and (3.56). Therefore, we know it will lead to zero residual vibration.

Although the shaper given by (6.4) transitions the command from zero to full positive without residual vibration, it is not the fastest possible transition. It is of interest because it transitions without using negative pulses (the command does not go negative). This leads to a fuel-efficient transition. The time-optimal transition requires a negative pulse and can be obtained by using an input shaper described by [127]:

$$\begin{bmatrix} A_i \\ t_i \end{bmatrix} = \begin{bmatrix} 1 & -2 & 2 \\ 0 & \dfrac{\cos^{-1}(1/4)}{2\pi}T & \dfrac{\cos^{-1}(-1/4)}{2\pi}T \end{bmatrix} = \begin{bmatrix} 1 & -2 & 2 \\ 0 & 0.20978T & 0.29022T \end{bmatrix} \tag{6.5}$$

Note that the input shaper of (6.5) is the negative partial sum (PS) ZV shaper when P = 1.

Four different transitions from zero actuator effort to full positive are shown in Figure 6.4. The transitions are labeled ZV and ZVD because of the vibration and robustness constraints they satisfy. The transitions are further labeled time-optimal (TO) or fuel-efficient (FE). When the switch times given in the figure are combined with the corresponding amplitudes of the transitions, an input shaper is formed. For example, the switches for the ZV TO transition are combined with impulse amplitudes of [1, -2, 2] to form the required input shaper. On the other hand, the ZV FE

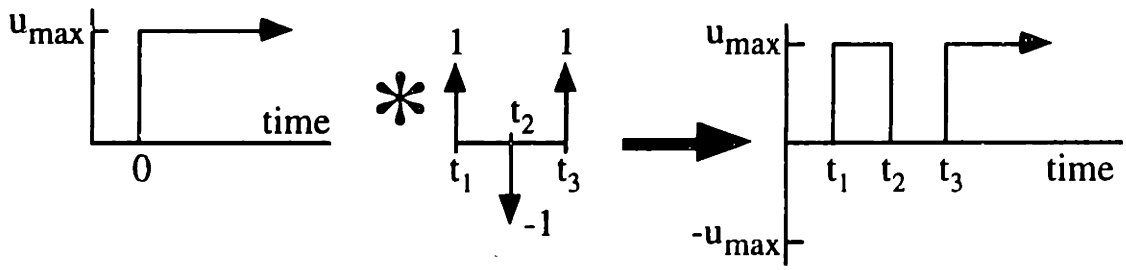

Figure 6.3: Using Input Shaping to Generate a Zero to Full Positive Transition.

switches are used with amplitudes of [1, -1, 1]. Note that the amplitudes always sum to one. The values shown in Figure 6.4 apply only to undamped systems. These transitions can also be used to go from full negative actuator effort to zero by simply reversing the order of the impulse sequence. These input shapers will be referred to as one-unit transitions.

6.2.1b Two-Unit Transitions

The first and third transitions of a bang-bang profile can be generated with the transitions shown in Figure 6.4. However, the second transition of the bang-bang command (full positive to full negative) is shaped differently because a change in the command value of minus two units ($-2u_{max}$) is desired. This requires that the impulse amplitudes sum to -2. The simplest ZV transition from full positive to full negative can be accomplished with only two impulses. That is, the actuator is turned off, the system coasts for a specified time and then the actuator is turned full negative. If the coast period is equal to T/2, then the transition will be accomplished without residual vibration. This transition is the zero-vibration fuel-efficient (ZV FE) transition because command pulses opposite to the desired transition direction are not used. The ZV TO transition uses pulses opposite in direction to the desired transition. Four different two-unit transitions are shown in Figure 6.5.

6.2.1c Complete Profiles

The above transitions (input shapers) can be used in a simple two-step process to generate command profiles that perform rest-to-rest slewing without residual vibration. First, select a desired shaper for each of the three bang-bang transitions. Each of the three transitions will satisfy the requirement of zero residual vibration of the flexible dynamics. Second, determine the necessary time between transitions to satisfy the rigid-body requirements.

To demonstrate this process, a command profile for fuel-efficient zero vibration slewing will be designed. The first and third transitions will use the one-unit ZV FE shaper from Figure 6.4. The center transition will be performed with the two-unit ZV FE shaper from Figure 6.5. To succinctly describe a command profile, it will be labeled with its three types of transitions. The profile under

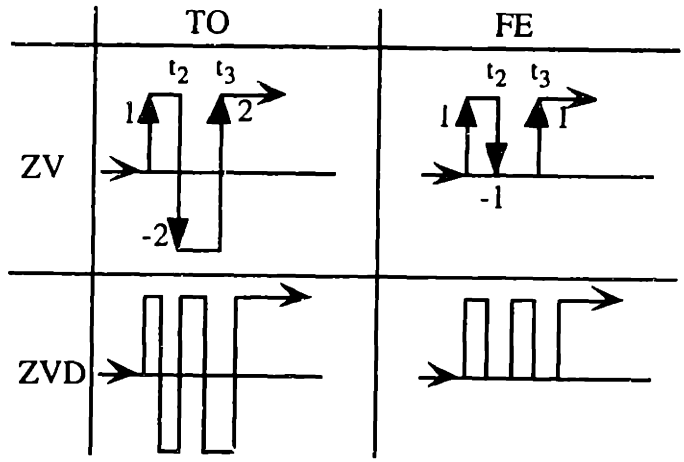

Shaper	t_2	t_3	t_4	t_5
ZV-TO	0.20978T	0.29022T	—	—
ZV-FE	T/6	T/3	—	—
ZVD-TO	0.15241T	0.27740T	0.63131T	0.67895T
ZVD-FE	0.08951T	0.36623T	$2t_3-t_2$	$2t_3$

Figure 6.4: One Unit Transitions (Zero to Full Positive or Full Negative to Zero).

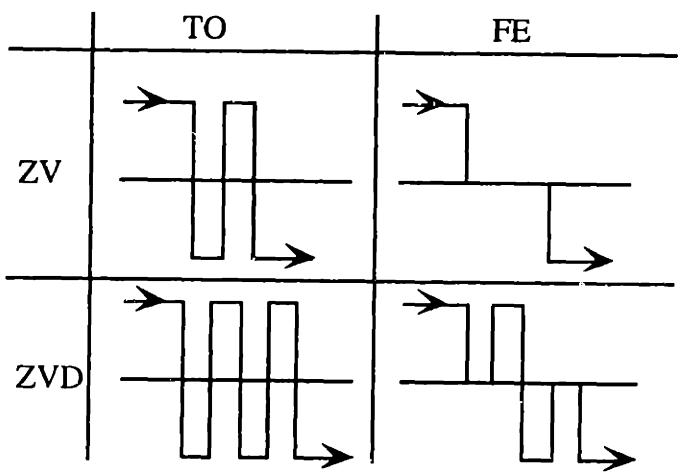

Shaper	t_2	t_3	t_4	t_5
ZV-TO	T/6	T/3	—	—
ZV-FE	T/2	—	—	—
ZVD-TO	0.08951T	0.36623T	$2t_3-t_2$	$2t_3$
ZVD-FE	0.18434T	0.40882T	$2t_3-t_2$	$2t_3$

Figure 6.5: Two-Unit Transitions (Full Positive to Full Negative).

consideration is then a ZV FE-FE-FE profile. Because the first and third transitions are made with the same shaper, the resulting profile is symmetric as shown in Figure 6.6.

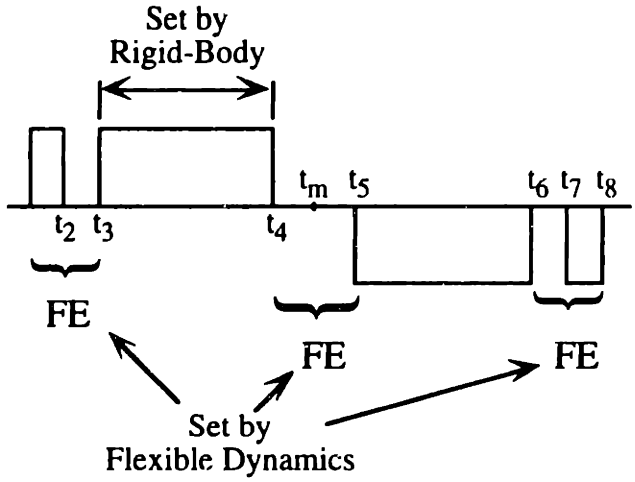

Figure 6.6: ZV FE-FE-FE Profile.

Once the shape of the profile is chosen, the problem reduces to determining the switch times. For symmetric profiles, only the switch times up through mid maneuver, t_m, need to be determined. For the ZV FE-FE-FE profile, t_2, t_3, t_4, and t_m must be determined ($t_1 = 0$). However, from Figure 6.4, t_2 and t_3 are known to be T/6 and T/3, respectively. Furthermore, from Figure 6.5, the spacing between t_4 and t_5 is known to be T/2. Therefore:

$$t_m = t_4 + \frac{T}{4}. \tag{6.6}$$

The value of t_4 is the only remaining unknown and it can be determined from rigid-body mechanics. At mid maneuver the position of the mass center, x_{tm}, must be at one half of the desired slew distance. By simply integrating (6.1) twice, an expression for the mass center position as a function of the switch times is obtained:

$$x_{tm} = \frac{x_d}{2} = \frac{\alpha}{2}\left[-t_2^2 + t_3^2 - t_4^2\right] + \alpha t_m\left[t_2 - t_3 + t_4\right]. \tag{6.7}$$

Using (6.6) and substituting the known values of t_2 and t_3 into (6.7), t_4 can be obtained as a function of the vibration period, the desired slew distance, and the acceleration:

$$t_4 = \frac{-T}{12} + \sqrt{\left(\frac{T}{12}\right)^2 + \frac{x_d}{\alpha}}. \tag{6.8}$$

By symmetry, the entire ZV FE-FE-FE profile is now known. To summarize, the ZV FE-FE-FE profile for an undamped, single-mode system is given by:

$$\begin{aligned} A_i &= [1 \quad -1 \quad 1 \quad -1 \quad -1 \quad 1 \quad -1 \quad 1] \\ t_2 &= \frac{T}{6}, \quad t_3 = \frac{T}{3}, \quad t_4 = \frac{-T}{12} + \sqrt{\left(\frac{T}{12}\right)^2 + \frac{x_d}{\alpha}} \\ t_5 &= t_4 + \frac{T}{2}, \quad t_6 \rightarrow t_8 : \textit{ By Symmetry} \end{aligned} \tag{6.9}$$

A ZV FE-FE-FE profile was designed for the benchmark system by simply plugging the system parameters into (6.9). The response of the system to this analytic profile is shown in

Figure 6.1. The most obvious difference between the time-optimal and analytic shaped profiles is the rise time. As expected, the analytic fuel-efficient profile is slower than the time-optimal flexible-body profile. This drawback is obviously countered somewhat by the ease of designing the analytic profile. What is not obvious thus far are the advantages provided by the analytic profile in terms of fuel savings, robustness to modeling errors, and decreased maximum transient deflection. These advantages will be presented in section 6.2.2.

Before proceeding with the design of profiles with other combinations of transitions, one limitation of the analytic profiles should be pointed out. The analytic profiles cannot be used for very small slew distances. A problem occurs because the time spacings of the three transitions are fixed by the flexible-body dynamics. The minimum slew distance occurs when the three transitions occur sequentially without delay. For the ZV FE-FE-FE profile the minimum slew distance occurs when $t_4 = t_3$. Using this condition, the minimum slew distance for the ZV FE-FE-FE profile can be calculated as:

$$[x_{\min}]_{ZV\ FE-FE-FE} = \frac{\alpha}{6}T^2 \tag{6.10}$$

For the example system, the minimum slew distance using the ZV FE-FE-FE profile is 1.645 units. As an alternate method for expressing this constraint, the minimum slew time can be calculated. In this case, the minimum slew time is 7T/6. That is, slews lasting less than 7/6 of the vibration period cannot be performed using this method.

To improve the rise time, time-optimal transitions can be used. The design of the ZV TO-TO-TO profile proceeds in exactly the same manner as for the ZV FE-FE-FE profile, except that the time-optimal transitions from Figures 6.4 and 6.5 are used. As it turns out, the time-optimal transitions produce only a very small improvement in rise time, while causing a significant increase in fuel usage (the time the actuator effort is nonzero). A similar effect has been noted previously for numerically obtained profiles [115]. The main advantage of time-optimal transitions is that they allow for smaller slew distances. The ZV TO-TO-TO profile shown in Figure 6.7 is described by:

$$\begin{aligned}
&A_i = [1 \quad -2 \quad 2 \quad -2 \quad 2 \quad -2 \quad 2 \quad -2 \quad 2] \\
&t_2 = 0.20978T, \quad t_3 = 0.29022T, \\
&t_4 = -0.0058054T + \sqrt{(0.031643T)^2 + \frac{x_d}{\alpha}}, \\
&t_5 = t_4 + \frac{T}{6}, \quad t_6 \rightarrow t_9 : \ \textit{By Symmetry} \\
&x_{\min} = 0.086627\alpha T^2
\end{aligned} \tag{6.11}$$

Note that the minimum move distance with time-optimal transitions is nearly half as far as with fuel-efficient transitions.

To incorporate robustness to modeling errors, the ZVD transitions shown in Figures 6.4 and 6.5 can be used. The ZVD FE-FE-FE profile is given by:

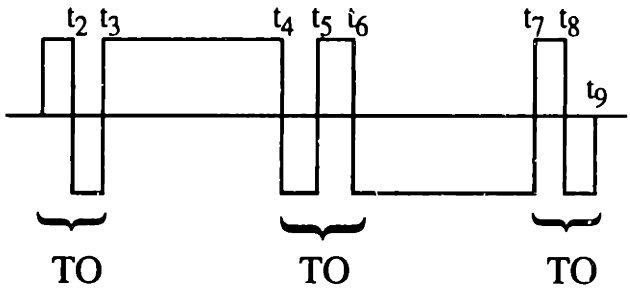

Figure 6.7: ZV TO-TO-TO Profile.

$$
\begin{aligned}
&A_i = [1 \;\; -1 \;\; 1 \;\; \ldots \;\; 1 \;\; -2 \;\; 1 \;\; -1 \;\; \ldots \;\; 1] \\
&t_2 = 0.089513T, \;\; t_3 = 0.366234T, \;\; t_4 = 2t_3 - t_2, \\
&t_5 = 2t_3, \;\; t_6 = -0.042591T + \sqrt{(0.04051T)^2 + \frac{x_d}{\alpha}}, \\
&t_7 = t_6 + 0.099161T, \;\; t_8 = t_6 + 0.323643T, \\
&t_9 \rightarrow t_{15}\text{: By Symmetry} \\
&x_{min} = 0.599075\alpha T^2
\end{aligned}
\tag{6.12}
$$

There are a great variety of profiles that can be designed with the above process. For example, an unsymmetrical profile such as a ZV TO-FE-FE profile can be designed. Or even a profile with both ZV and ZVD constraints could be constructed.

As it turns out, two analytic on-off profiles can be obtained using standard input shaping, rather than the transition shaping described above. To create these profiles, a bang-bang command is convolved with a unity-magnitude (UM) input shaper of the form:

$$
\begin{bmatrix} A_i \\ t_i \end{bmatrix} = \begin{bmatrix} 1 & -1 & 1 & \ldots & -1 & 1 \\ 0 & t_2 & t_3 & \ldots & t_{n-1} & t_n \end{bmatrix} \tag{6.13}
$$

To use these shapers, a bang-bang (BB) command is generated from rigid-body requirements and then convolved with a UM shaper. The resulting ZV UM BB profile is shown in Figure 6.8 and it is given by:

$$
\begin{aligned}
&A_i = [1 \;\; -1 \;\; 1 \;\; -2 \;\; 2 \;\; -2 \;\; 1 \;\; -1 \;\; 1] \\
&t_2 = \frac{T}{6}, \;\; t_3 = \frac{T}{3}, \;\; t_4 = \sqrt{\frac{x_d}{\alpha}} \\
&t_5 = t_4 + \frac{T}{6}, \;\; t_6 \rightarrow t_9 : \; \textit{By Symmetry} \\
&x_{\min} = \frac{\alpha}{9} T^2
\end{aligned}
\tag{6.14}
$$

Although the profile has the same shape as a ZV FE-TO-FE profile, the center transition does not have time-optimal switches. The profile also has a minimum slew distance which occurs when the UM shaper length equals one half of the bang-bang profile duration. Although standard input shaping with UM shapers can produce certain types of analytic profiles, it cannot generate the great variety of profiles that can be constructed by transition shaping.

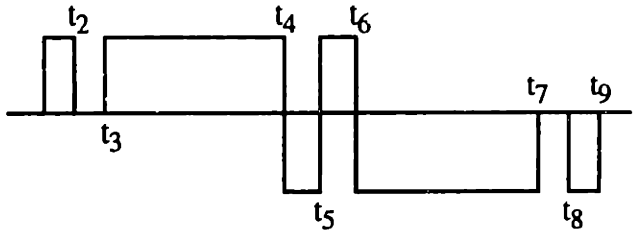

Figure 6.8: ZV UM BB Profile.

6.2.2 Comparison of Profiles

This section will evaluate move duration, fuel usage, maximum transient deflection, and robustness to modeling errors for the analytic profiles as a function of the slew distance. Comparisons will be made to time-optimal and UM BB commands. As mentioned previously, profiles containing three time-optimal transitions are poor alternatives (except for short move distances) to profiles containing fuel-efficient transitions,[23] so they will be excluded from the following evaluation.

6.2.2a Move Duration

Figure 6.9 compares the move duration (the command length) for six types of command profiles as a function of the desired move distance. The profiles are the ZV and ZVD versions of the time-optimal flexible-body command, the UM BB profiles, and the analytic FE-FE-FE profiles given by (6.11) and (6.12). The UM BB profiles are distinguished by circles and the FE-FE-FE profiles are labeled with squares. ZV profiles are shown as dashed lines, while ZVD profiles are represented by solid curves.

Although they have slightly different durations, both the ZV UM BB and the ZV FE-FE-FE profiles average approximately 9.4% longer than the time-optimal ZV profile over the range $10 \leq x_d \leq 40$. The ZVD UM BB and the ZVD FE-FE-FE profiles average 15% longer than the time-optimal ZVD profile. The percentage increase in move time with the analytic profiles decreases with move distance.

6.2.2b Fuel Usage

Figure 6.10 compares the fuel usage (defined as the time the actuators are turned on) for the six types of command profiles. The fuel usage of the time-optimal profiles is equal to the move duration because the actuators are turned on throughout the slew. (The curves for these two commands are identical to those in Figure 6.9.) The analytic profiles with fuel-efficient transitions use less fuel than the other profiles. (The curves labeled with squares are always lower than the

[23] The advantages of the fuel-efficient shaping process was firmly established in Chapter 5.

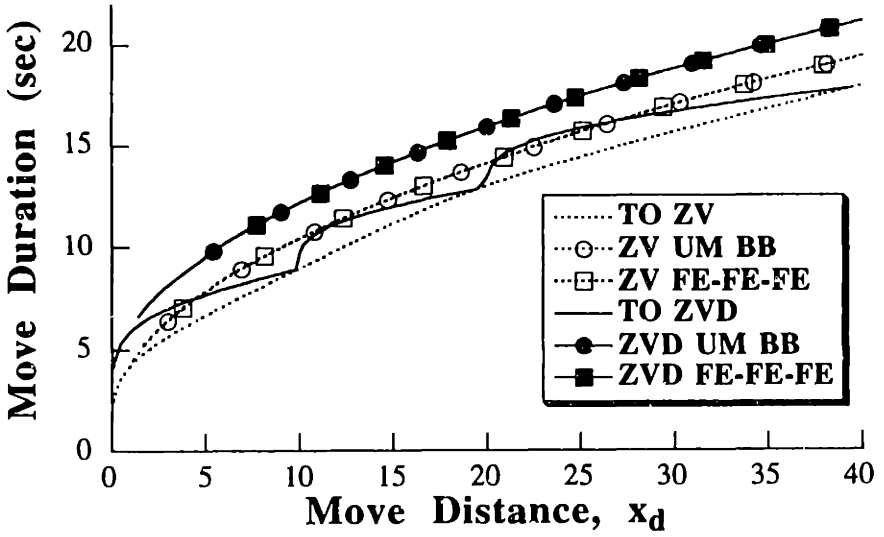

Figure 6.9: Move Duration as a Function of Move Distance.

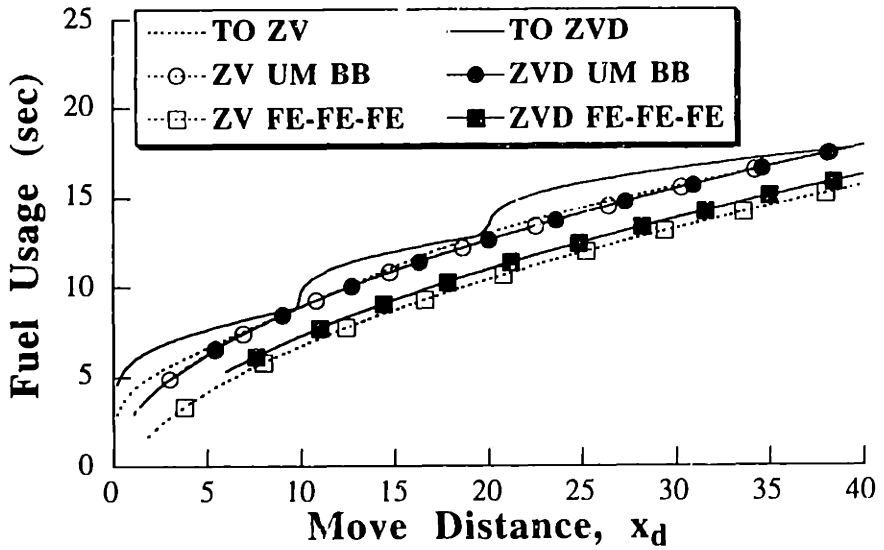

Figure 6.10: Fuel Usage as a Function of Move Distance.

others.) This fuel savings is fairly substantial. The ZV FE-FE-FE profile uses on average 16.8% less fuel than the time-optimal ZV profile, while the ZVD FE-FE-FE uses on average 17.7% less than the time-optimal ZVD profile over the range $10 \leq x_d \leq 40$. The ZV UM BB profile offers essentially no fuel savings when compared to the TO ZV profile. However, the ZVD UM BB profile saves approximately 7% in fuel when compared to the TO ZVD. Note that the ZV and ZVD UM BB profiles overlay each other.

6.2.2c Maximum Transient Deflection

Recall that techniques for limiting maximum transient deflection were presented in Chapter 5.

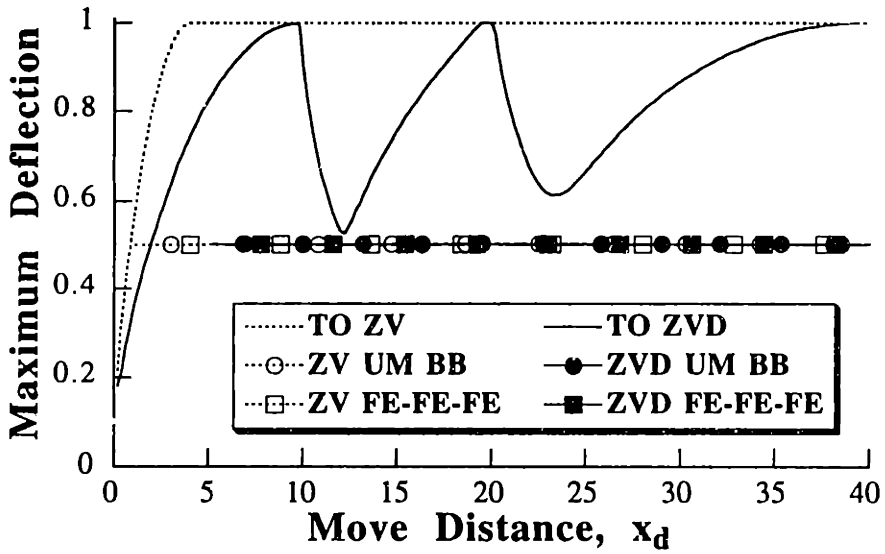

Figure 6.11: Maximum Transient Deflection as a Function of Move Distance.

Employing those methods to develop an analytic profile that limits deflection to a desired amount is difficult. Here we simply evaluate the maximum transient deflection produced by each type of command. Figure 6.11 compares the maximum transient deflection ($|x_2-x_1|$) for the six profiles under consideration. The analytic profiles cause a maximum deflection of 0.5 units, while the time-optimal ZV profiles cause twice as much deflection for most move distances. The time-optimal ZVD profiles cause maximum deflections in the 0.5 to 1.0 range. The analytic and UM BB commands cause the same amount of transient deflection.

6.2.2d Robustness to Modeling Errors

All of the profiles under consideration produce slews with zero residual vibration provided that the system model is exact. The level of robustness to modeling errors is, however, dependent on the move distance and the type of profile. For example, the robustness of the time-optimal ZVD profile differs from both the robustness of the ZVD UM BB and the ZVD FE-FE-FE profiles.

Figure 6.12 compares the 10% insensitivities (widths of the sensitivity curves at the 10% level) of the six profiles. The ZVD profiles are significantly more robust than the ZV profiles as expected. Furthermore, the analytic profiles are considerably more robust than the time-optimal profiles over almost the entire range of slew distances. (The time-optimal ZV profile is more robust than the analytic ZV profiles for move distances in the range of 18-21.) The UM BB and FE-FE-FE profiles have approximately the same robustness. The ZV FE-FE-FE profile averages 800% more insensitivity than the time-optimal ZV profile, while the ZVD FE-FE-FE profile averages 330% more insensitivity than the time-optimal ZVD profile.

The huge increases in robustness provided by the analytic profiles warrant some explanation.

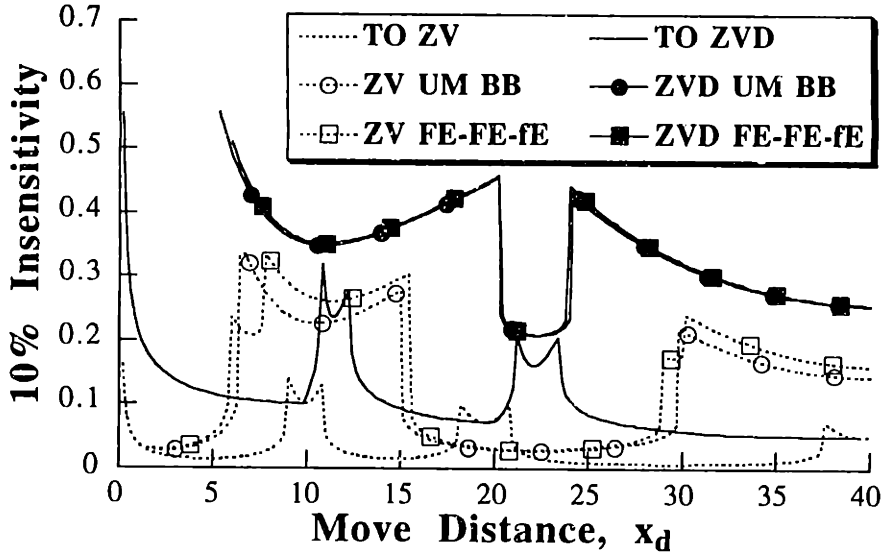

Figure 6.12: Robustness to Modeling Errors as a Function of Move Distance.

Shaped profiles accomplish residual vibration reduction by summing to zero the vibration caused by each switch in the command profile. The time-optimal profiles cancel the vibration only at the end of the maneuver. Viewed another way, the final impulse in the time-optimal profiles cancel the vibration caused by all the previous impulses. The analytic profiles do not wait until the end of the maneuver to cancel vibration; each transition is accomplished without residual vibration.

Now assume the modeling frequency is 10% higher than the actual frequency. The time locations of the impulses in the ZV FE-FE-FE profile will be incorrect by 10%. Consider the impulses in the middle transition (full positive to full negative). The period between t_4 and t_5 is one half of the period of the modeling frequency. That is, t_5 should occur after the vibration from t_4 has completed 180° of its cycle. Given that the actual period is 10% longer than the modeling period, t_5 occurs after the vibration from t_4 has completed 164° of its cycle; t_5 is incorrect by 16°. This type of analysis is applicable to the first and third transitions; each of the impulses in the entire profile is, at most, 16° away from the intended location.

Under the same examination, a very different result is obtained for the time-optimal profiles. Consider the time-optimal ZV command mentioned previously. The final impulse, t_5, is located at 1.5 periods of the modeling frequency; it should occur 540° after the first impulse. Given the same 10% modeling error, t_5 occurs 491° after the first impulse; it is incorrect relative to the first impulse by 49°. It is closer to the correct location relative to the other impulses in the command; however, the errors are still substantially larger portions of a vibration period than the errors with the analytic profiles. Because the time-optimal profiles do not cancel vibration until the final impulse, any modeling error that exists will be multiplied by the number of vibration cycles that occur during the slew. Given that the analytic profiles attempt to cancel the vibration well within

one cycle of vibration, modeling errors do not multiply and the robustness is greatly improved.

Given the results shown in Figures 6.9 through 6.12, we know that the analytic profiles offer considerable advantages over the time-optimal commands. Furthermore, the analytic profiles obtained with transition shaping are more fuel efficient than those obtained with standard input shaping using UM shapers.

6.2.3 Discussion of Closed-Form Methods for Generating On-Off Control

Analytic expressions were presented that describe command profiles for rest-to-rest slewing of undamped single-mode flexible systems. Profiles were designed to achieve vibrationless transitions between actuator states. Although the analytic profiles are not the time-optimal profiles subject to constraints of zero residual vibration and/or robustness to modeling errors, they are close to time-optimal in many cases. The analytic profiles are significantly more robust to modeling errors and they cause less deflection during the slew than the time-optimal profiles. The fuel-efficient versions of the analytic profiles use considerably less fuel with only minor increases in move time. However, the main advantage of the analytic commands is their ease of design. They can be generated using simple formulas rather than a nonlinear optimization, as required with time-optimal profiles.

6.3 Transition Shaping for Damped Systems

Most of the methods described in this thesis have straightforward extensions to damped systems. This is why the undamped version of the benchmark system of Figure 4.1 has been used repeatedly. However, the transition shaping of the previous section assumed a symmetrical command profile. For systems with damping a symmetrical command cannot be used. The modifications necessary to use transition shaping on damped systems will be addressed here.

To utilize transition shaping on damped systems, expressions which describe the transition switches as a function of both the vibration period and the damping ratio must be used. Furthermore, the third transition cannot be obtained by reversing the first transition. Finally, the rigid-body constraints must be enforced at the end of the command rather than at the middle.

The damped first transitions meeting the ZV constraints are:

$$A_i = [1 \quad -1 \quad 1]$$

ZV FE:
$$t_2 = \left(0.16658 + 0.29277\zeta + 0.075438\zeta^2 + 0.21335\zeta^3\right)T \tag{6.15}$$
$$t_3 = \left(0.33323 + 0.0053322\zeta + 0.17914\zeta^2 + 0.20125\zeta^3\right)T$$

$$A_i = [1 \quad -2 \quad 2]$$

ZV TO:
$$t_2 = \left(0.2097 + 0.22441\zeta + 0.08028\zeta^2 + 0.23124\zeta^3\right)T \tag{6.16}$$
$$t_3 = \left(0.29013 + 0.09557\zeta + 0.10346\zeta^2 + 0.24624\zeta^3\right)T$$

Note that (6.15) in the UM ZV shaper given in Table 3.3 and (6.16) is the PS ZV shaper of Figure 3.3 when P=1. Robust first transitions can be obtained from the ZVD or EI versions of the above shapers which are available in Table 3.3.

The damped two-unit transitions meeting the ZV constraints are:

$$A_i = [-2 \quad 1 \quad -1]$$

ZV FE:
$$t_2 = \left(\sqrt{\frac{0.041645(\zeta + 1.1096)^2}{(1.1096)^2} - 0.041645} + 0.10103\zeta + 0.26327\zeta^2\right)T \tag{6.17}$$
$$t_3 = \left(0.50033 - \sqrt{\frac{0.047858(\zeta + 1.0843)^2}{(1.0843)^2} - 0.047858} + 0.14012\zeta + 0.35734\zeta^2\right)T$$

$$A_i = [-2 \quad 2 \quad -2]$$

ZV TO:
$$t_2 = \left(0.16658 + 0.29277\zeta + 0.075438\zeta^2 + 0.21335\zeta^3\right)T \tag{6.18}$$
$$t_3 = \left(0.33323 + 0.0053322\zeta + 0.17914\zeta^2 + 0.20125\zeta^3\right)T$$

Note that the description of the switch times given in (6.17) is of a different form (it is not a polynomial in ζ) than for most other shapers. Also note that the transition of (6.18) is the same as that of (6.15) except that the amplitudes are multiplied by -2.

The damped third transitions meeting the ZV constraints are:

$$A_i = [1 \quad -1 \quad 1]$$

ZV FE:
$$t_2 = \left(0.16658 + 0.29277\zeta + 0.075438\zeta^2 + 0.21335\zeta^3\right)T \tag{6.19}$$
$$t_3 = \left(0.33323 + 0.0053322\zeta + 0.17914\zeta^2 + 0.20125\zeta^3\right)T$$

$$A_i = [2 \quad -2 \quad 1]$$

ZV TO:
$$t_2 = \left(0.080429 + 0.12919\zeta + 0.024804\zeta^2\right)T \tag{6.20}$$
$$t_3 = \left(0.2902 - 0.090225\zeta + 0.136946\zeta^2 - 0.043337\zeta^3\right)T$$

The transition given by (6.19) is the same as that given by (6.15).

6.3.1 Additional Types of Constraints

Given the results shown in Figures 6.9 through 6.12, we know that the analytic profiles offer several advantages over the time-optimal commands and some advantages over standard input shaping using UM shapers. Yet another advantage of transition shaping is its ability to generate a great variety of profiles which can accommodate additional types of constraints or take advantage of a system's distinguishing features.

For example, consider rapid slewing of a system that has damping. If the system is driven by a bang-bang command, then the vibration induced by the first and second transitions will decay somewhat by the end of the command. If the damping is high or the move duration long, then the residual vibration from the first and second transitions may be negligible. In this case, shaping the first and second transitions is unnecessary. A useful command profile might consist of a switch to full positive, followed by a switch to full negative, then a shaped transition to off. Figure 6.13 shows such a profile with a final TO ZV transition. Because the first two transitions are not shaped, the command profile is called 0-0-TOZV. The profile is given by:

$$\begin{aligned}
&A_i = [1 \quad -2 \quad 2 \quad -2 \quad 1] \\
&t_2 = \sqrt{3a^2 - 2ab + \frac{x_d}{\alpha}}, \quad t_3 = 2t_2 + 2a - b, \\
&t_4 = t_3 + a, \quad t_5 = t_3 + b, \\
&a = (0.080429 + 0.12919\zeta + 0.024804\zeta^2)T_d, \\
&b = (0.2902 - 0.090225\zeta + 0.136946\zeta^2 - 0.043337\zeta^3)T_d
\end{aligned} \tag{6.21}$$

where T_d is the damped period of vibration.

To demonstrate the advantage of this profile, a viscous damper with a value of 0.5 is used with

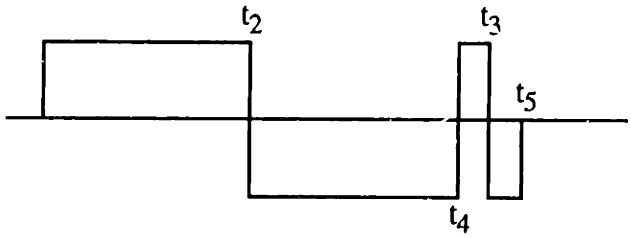

Figure 6.13: 0-0-TOZV Profile.

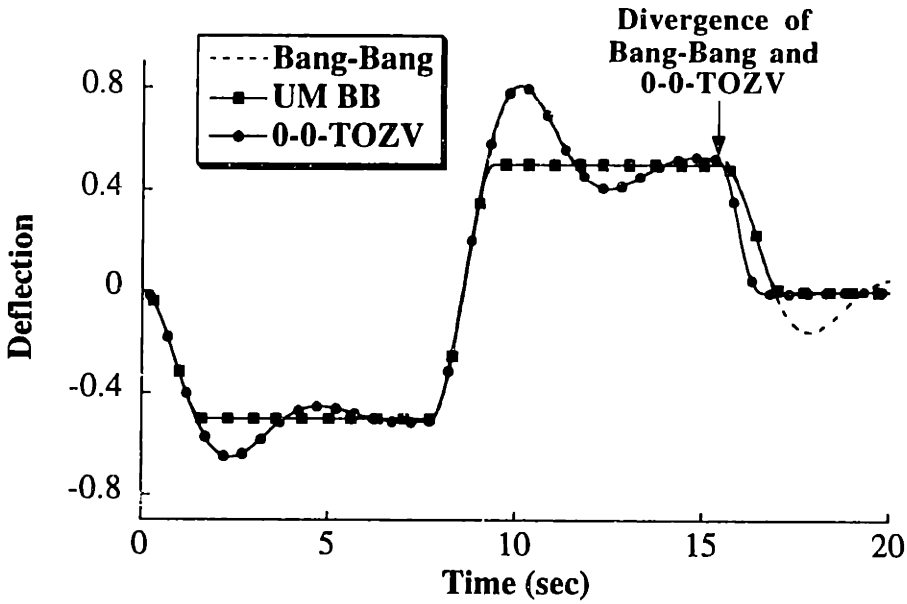

Figure 6.14: Deflection Response of Damped System.

the benchmark system of Figure 4.1. The resulting system has a damping ratio of 0.355. Figure 6.14 shows the deflection of the system when it is slewed 30 units by a bang-bang command, a ZV UM BB command, and a 0-0-TOZV profile. The bang-bang and the 0-0-TOZV responses overlay until the very end of the move. At the end of the move, the 0-0-TOZV profile decelerates the system with essentially zero residual vibration. The bang-bang command causes significant residual oscillation. The ZV UM BB profile also moves the system without residual vibration, but it lags the 0-0-TOZV response by approximately 0.5 seconds. In addition to saving time, the 0-0-TOZV profile also offers the advantage of less actuator wear because it requires fewer switches in the command profile. It uses only 4 pulses, while the ZV UM BB profile consists of 6 pulses.

6.4 Transition Shaping for Multi-Mode Systems

This sections extends the method of the previous two sections to the design of on-off command profiles for multi-mode flexible systems. Because multi-mode transitions are a function of the mode ratios, they cannot be described by simple equations For this reason, the method requires the one-time use of a numerical optimization to obtain the three transitions. Using the optimization results, command profiles are generated that are described by closed-form functions of the move distance.

6.4.1 Multi-Mode Profile Generation

Only fuel-efficient transitions will be considered during this section; however, the proposed method applies to time-optimal transitions. To illustrate the procedure, command profiles will be designed for the benchmark multi-mode system shown in Figure 4.11. The system parameters were selected such that the low mode is at 1 Hz, the second mode is at 4.4 Hz, and the damping is zero, just as was done previously. To obtain the transitions, the standard input shaping vibration and robustness constraints (for example, (3.1) and (3.2)) are combined with an amplitude constraint that produces the desired shape.

6.4.1a One-Unit Transitions

For the benchmark system, the one-unit fuel-efficient ZVD transition is given by:

$$\begin{bmatrix} A_i \\ t_i \end{bmatrix} = \begin{bmatrix} 1 & -1 & 1 & -1 & 1 & -1 & 1 & -1 & 1 \\ 0 & .03491 & .10027 & .15797 & .40351 & .64905 & .70675 & .77212 & .80703 \end{bmatrix} \tag{6.22}$$

6.4.1b Two-Unit Transitions

For the benchmark system, the two-unit fuel-efficient ZVD transition is:

$$\begin{bmatrix} A_i \\ t_i \end{bmatrix} = \begin{bmatrix} -1 & 1 & -1 & 1 & -1 & -1 & 1 & -1 & 1 & -1 \\ 0 & .02983 & .06786 & .22523 & .44018 & .44018 & .65513 & .81290 & .85193 & .88176 \end{bmatrix} \tag{6.23}$$

6.4.1c Complete Profiles

The above transitions can now be used to generate closed-form command profiles which perform rest-to-rest slewing without residual vibration. What remains is to determine the necessary time between transitions to satisfy the rigid-body requirements. A general equation for this unknown time for symmetric profiles about the midpoint is given by:[24]

[24] This equation was derived by Bart Mills [130].

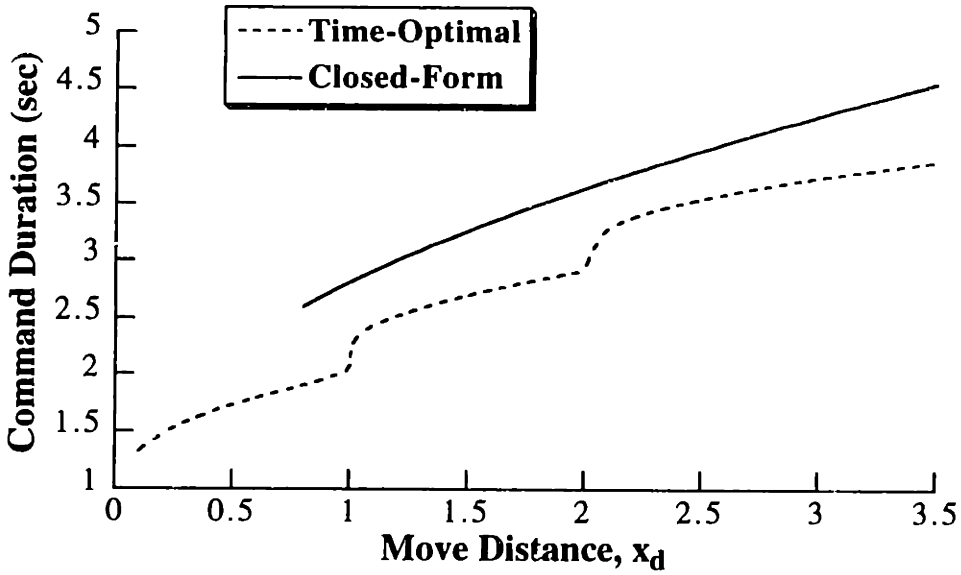

Figure 6.15: Move Duration of ZVD Commands.

$$t_\beta = \left(-t_2 + t_3 - .... + t_{n-1} - 0.5\left(t_y + t_z\right)\right) + \sqrt{\begin{array}{c} 2\left(t_2^2 + t_4^2 + t_6^2 + t_8^2 + ...t_{x-2}^2\right) + \left[-t_a^2 + t_b^2 - t_c^2 ... + 0.25\left(t_y^2 + t_z^2\right)\right] \\ + 2t_2\left(-t_3 + t_4 .... - t_{x-1}\right) + 2t_3\left(-t_4 + t_5 .... + t_{x-1}\right) ... - 2t_{x-2}t_{x-1} \\ -.5t_y t_z + t_y\left(t_a - t_b + t_c ... t_{y-1}\right) + t_z\left(t_a - t_b + t_c ... t_{y-1}\right) + \frac{x_d}{\alpha} \end{array}} \tag{6.24}$$

where t_y and t_z are the two middle times of the second transition.

6.4.2 Evaluation of Closed-Form Profiles

This section will evaluate the move duration, fuel usage, maximum transient deflection, and robustness to modeling errors of the multi-mode closed-form ZVD commands as a function of the slew distance. Comparisons will be made to time-optimal ZVD commands.

6.4.2a Move Duration

Figure 6.15 compares the move duration for the time-optimal and the closed-form ZVD commands. The time-optimal command is, of course, faster than the closed-form command. The time-optimal commands range from 1.4 to 1.7 seconds faster than the closed-form commands, however, the increase in move duration follows a repeating cycle, it does not continually increase. Therefore, the percentage increase in move duration with closed-form commands decreases as the move distance is increased. As we will see, this time difference is the only drawback of the closed-form command when compared to the time-optimal command. Note that the data for the closed-form profile is shown only down to the minimum slew distance of approximately 0.8 units.

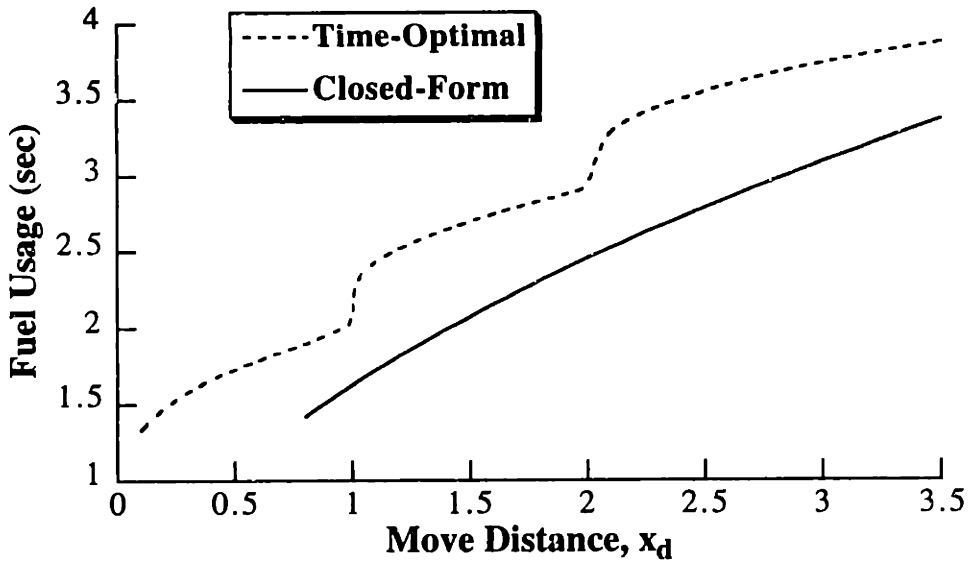

Figure 6.16: Fuel Usage of ZVD Commands.

6.4.2b Fuel Usage

Figure 6.16 compares the fuel usage for the time-optimal and closed-form commands. The closed-form commands always consume less fuel. The fuel savings varies between 1.4 and 1.7 seconds. Again, as with the command duration, the fuel savings follows a repeating cycle. Therefore, the percentage fuel savings decreases as move distance increases.

6.4.2c Maximum Transient Deflection

Figure 6.17a and 6.17b compare the maximum transient deflections for the profiles under consideration. Figure 6.17a compares the maximum deflection, $d_1 = x_2 - x_1$, between m_1 and m_2, while Figure 6.17b compares the maximum deflection, $d_2 = x_3 - x_2$ between m_2 and m_3 for time-optimal and closed-form command profiles. The closed-form profiles cause a maximum deflection of .0077 units for d_1 and .0375 for d_2, while the time-optimal profile causes maximum deflections of .0163 and .078 respectively. So, the time-optimal commands can produce more than twice the maximum deflection than the closed-form profile. Another advantage of the closed-form command, as seen in the figures, is that it has a constant amount of deflection, while the time-optimal command is very erratic. This can facilitate the calculation of the internal loads.

6.4.2d Robustness to Modeling Uncertainty

For multi-mode systems there is an insensitivity associated with each mode. That is, the robustness to modeling errors is different for each mode. Figures 6.18a and 6.18b show the 5% insensitivities for the first and second modes. The closed-form commands are considerably more

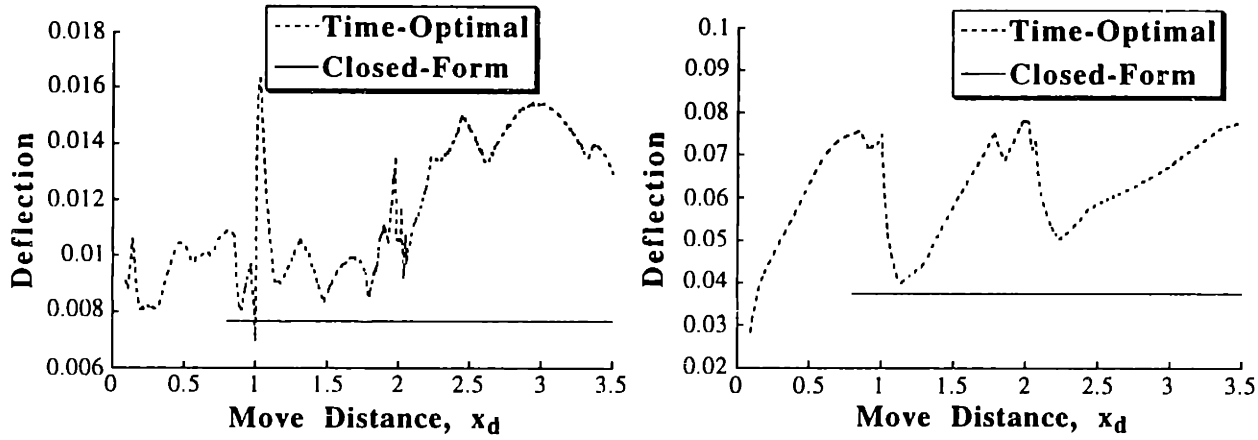

a) x_2-x_1 b) x_3-x_2

Figure 6.17: Transient Deflection Amplitude of ZVD Commands.

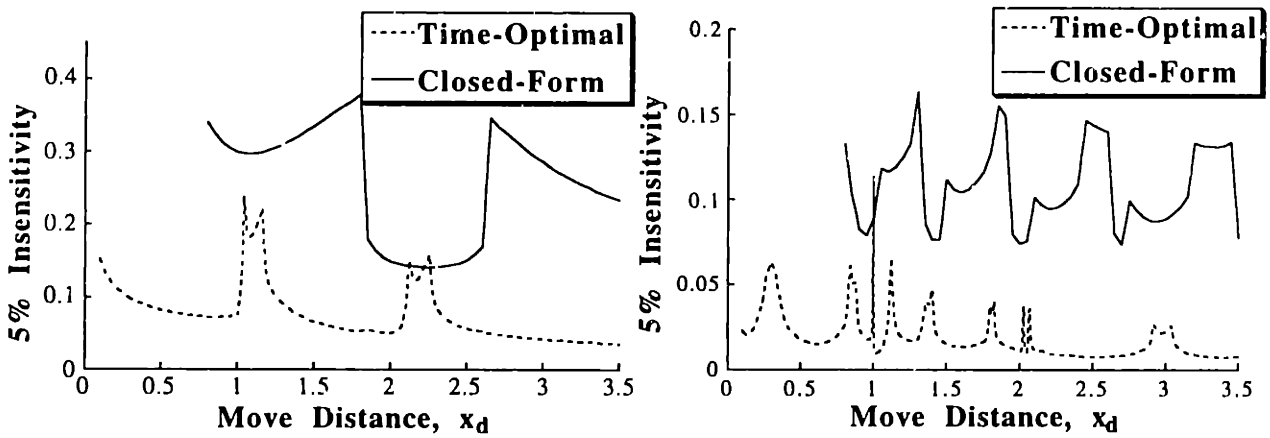

a) Mode 1 b) Mode 2

Figure 6.18: 5% Insensitivity of ZVD Commands.

robust than the time-optimal commands. For certain move distances the closed-form commands are over 6 times as robust and for all but a few move distances they are always greater. This result is very useful because the time-optimal commands are very sensitive to modeling errors, as was thoroughly demonstrated in Chapter 4. Note that the insensitivity for mode 2 is much less than for mode 1.

6.4.3 Simulations of Space Shuttle/Hubble Space Telescope

To test the proposed method for generating command profiles on a complex flexible spacecraft, tests were performed using Draper Laboratory's simulation (the DRS) of the Space Shuttle and its telerobotic manipulator. The simulations performed for this section model the Hubble Space Telescope deployed on the RMS in the extended park position. The simulations reorient the system by firing the shuttle's reaction jets.

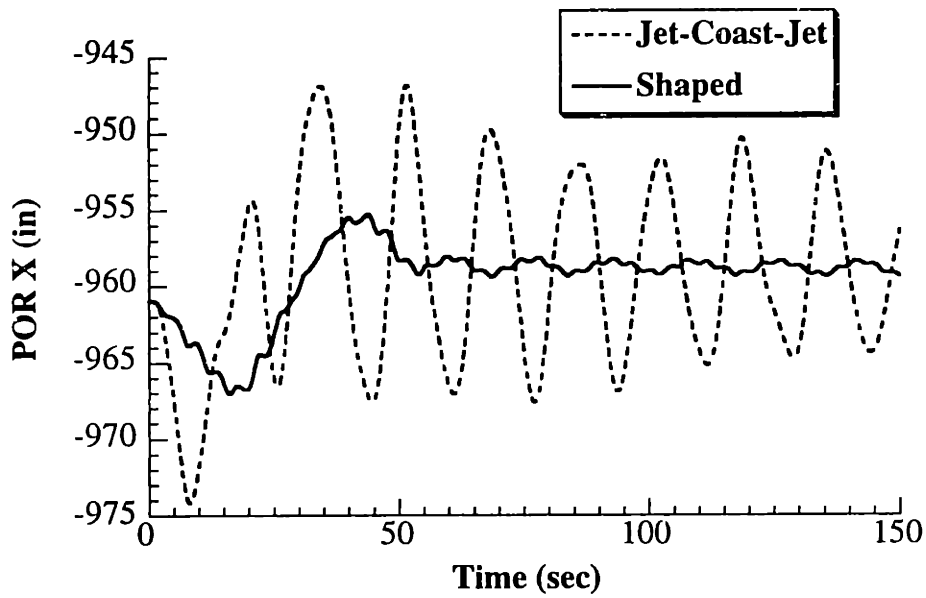

Figure 6.19: Endpoint Response to Jet-Coast-Jet and Shaped Command Profiles.

The first simulation fired a jet for approximately 15 sec, let the system coast for 8 sec., and then fired a roughly opposing jet for 15 sec. to decelerate the system. The second simulation used a closed-form ZVD shaped command profile designed to perform the same rigid-body motion. The shaped transitions were generated for the two most important modes of the system, 0.065 Hz and 0.134 Hz. Figure 6.19 compares the system response to both the jet-coast-jet and shaped command profiles. The data plotted in Figure 6.19 is the POR (Point of Resolution) X coordinate. Using the jet-coast-jet command, the endpoint oscillation is over 20 in. The shaped command produces less than 1.5 in. of residual oscillation; an order of magnitude reduction.

6.4.4 Discussion of Closed-Form Commands for Multi-mode Systems

A process for generating closed-form on-off commands for multi-mode systems has been described. The method requires the one time use of a numerical optimization to generate the transitions in the actuator state. Once these transitions are obtained they can be used to form closed-form expressions that describe the command profile for all desired move distances. The proposed command profiles were compared to time-optimal profiles in terms of maneuver duration, fuel usage, transient deflection, and robustness to modeling errors. The closed-form commands are somewhat slower than time-optimal commands, but they offer large advantages in terms of the other performance measures. Furthermore, they are much easier to derive and implement because only one optimization is required, rather than the repeated optimizations required for time-optimal control. Simulations of the space shuttle/Hubble Space Telescope system verified the vibration reducing abilities of the proposed command profiles.

6.5 Use of Neural Networks for Generating On-Off Commands

This section investigates the use of neural networks for generating on-off command profiles. If a neural network can be used to accurately generate the command switch times for all possible desired motions, then the need for performing a numerical optimization in real time, or storing the results of a vast array of numerical optimizations can be eliminated.

Three types of neural networks will be designed to generate time-optimal and fuel-efficient commands for the benchmark system of Figure 4.1. The first network is a two layer network with nonlinear transfer functions in the hidden layer and linear functions in the output layer. This network is shown in Figure 6.20. The second network is a three layer structure with two hidden layers with nonlinear transfer functions and a linear output layer. The final network to be examined is a radial basis function network. The performance of the three networks is compared.

6.5.1 Two-Layer Networks

Given the two-layer network architecture shown in Figure 6.20, there are a number of choices to be made regarding the hidden layer transfer function, the number of neurons in the hidden layer, and the training procedure. The training procedures used for this section are back propagation with momentum and the Levenberg-Marquardt optimization available in the MATLAB Neural Network Toolbox. The nonlinear transfer functions used here are log-sigmoids. The performance of the network will be examined as a function of the number of neurons in the hidden layer.

6.5.1a Time-Optimal ZV Commands

The training sets for the networks were obtained by performing numerical optimizations to generate the commands for a finite number of possible motions. Figure 6.21 shows the data for the time-optimal ZV commands. These data were then down-sampled by a factor of 2 to obtain the training set. That is, every other data point was used to train the networks. Once a network was trained, its performance was evaluated by comparing its predicted output for every point in the complete data set to the actual values.

Figure 6.22 compares the output of the network with 8 neurons in the hidden layer to the actual switch times for the time-optimal ZV command. The network is able to predict the command switch times (t_2-t_5) very accurately. The summation of the squared error (SSE) was formed by calculating the square of the error in each switch time and then summing these values over the range of move distances from 0 to 40 units. Basically, the SSE for t_2 gives us an average error in the value of t_2 over the range of move distances shown. Figure 6.23 shows the SSE for each switch time as a function of the number of neurons. The SSE for both the training set (Figure 6.23a) and the complete data set (Figure 6.23b) are shown. Note that the scale for the entire data

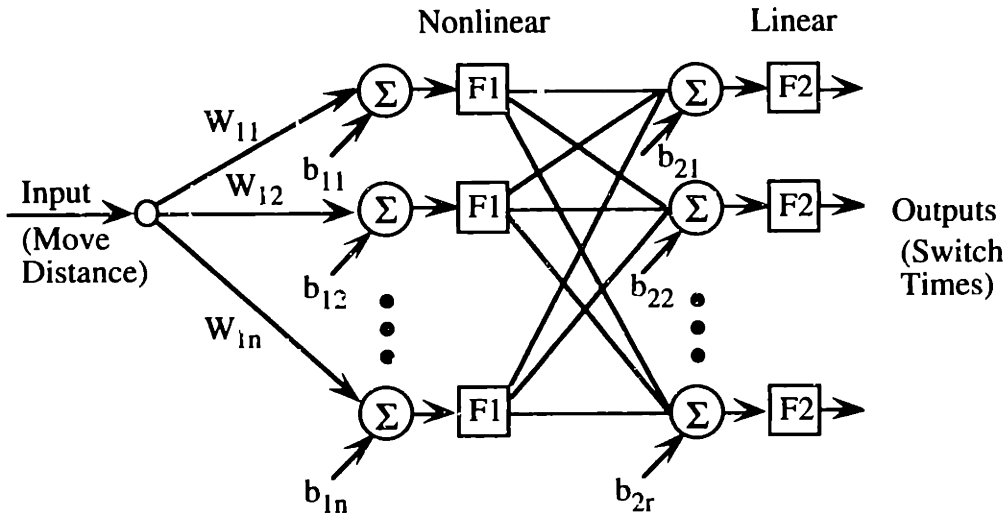

Figure 6.20: Two Layer Neural Network.

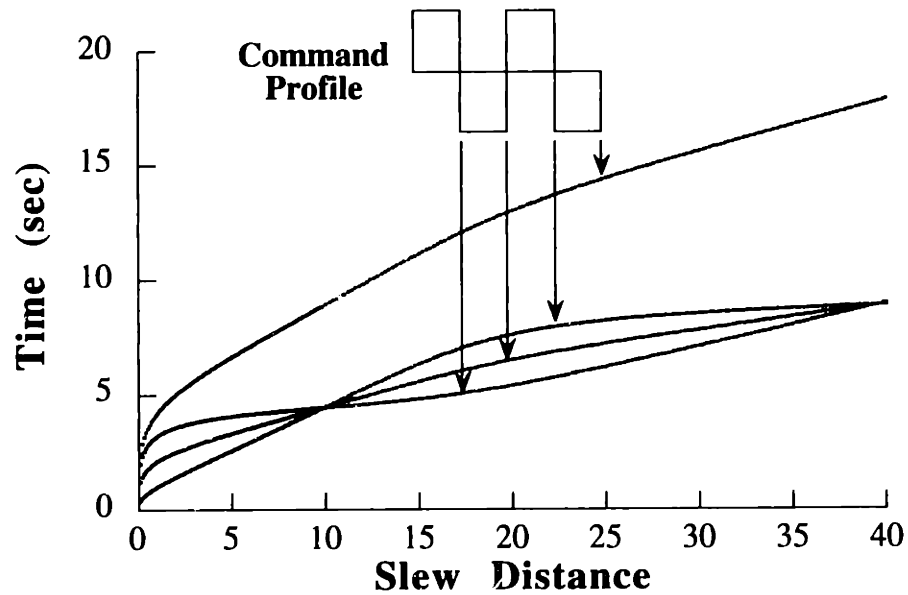

Figure 6.21: Switch Times for the Time-Optimal ZV Command.

set is 20 times larger than for the training set. The data indicates that this network is able to represent the time-optimal ZV commands very well as long as there are 8 or more neurons in the hidden layer. Note that results of this type depend on the training procedure used and the initialization of the network. However, the data shown are representative results.

The SSE for the entire data set is always greater than for the training set because there are more points in the entire set and every point in the training set is contained in the complete set. The SSE for the entire set gives us valuable information if it shows a large disparity from the SSE for the training set. If the network has overfit the training set, that is, the network predicts the training

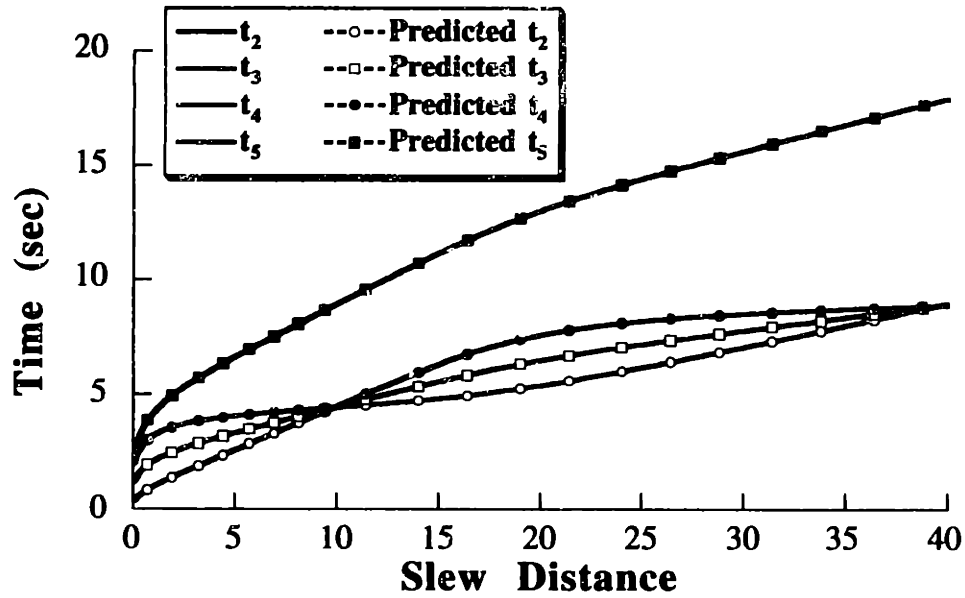

Figure 6.22: Actual and Predicted Switch Times of Time-Optimal ZV Commands.

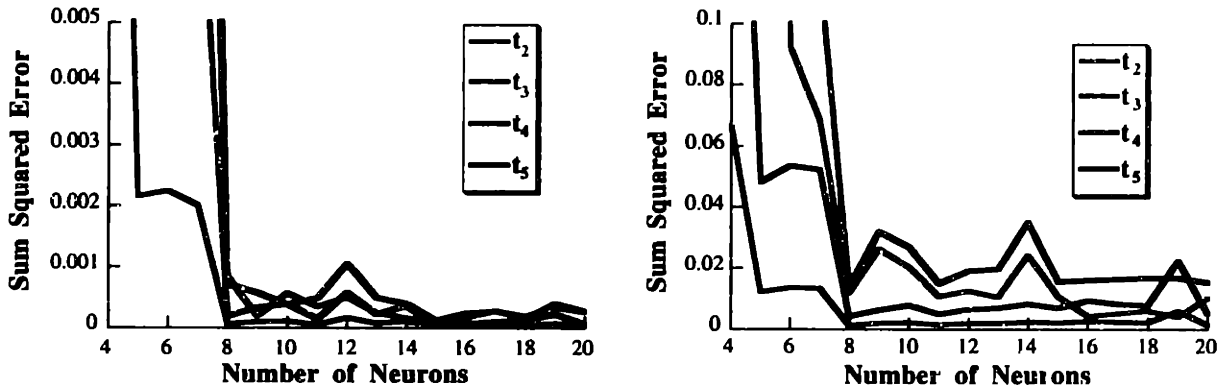

a) Training Set **b) Entire Data Set**

Figure 6.23: Switch Time Error as a Function of the Number of Hidden Neurons. Two-Layer Log-Sigmoid Network Representing the Time-Optimal ZV Switches.

data very well, but it deviates considerably between the training points, then the SSE for the entire set will reflect this problem.

If we want to find out what move distances are the most challenging for the network, we can plot the errors in the switch times as a function of the move distance. In this case the SSE is formed by summing the errors in each of the four switch times, for a given move distance. Recall, the SSE shown in Figure 6.23 was formed by summing the errors in a single switch time over the range of move distances. Figure 6.24 shows the SSE as a function of move distance. The network has the most difficulty predicting the switch times that produce move distances near 10 units. This is not surprising as the switch times converge to a point at a move distance of 9.8 units

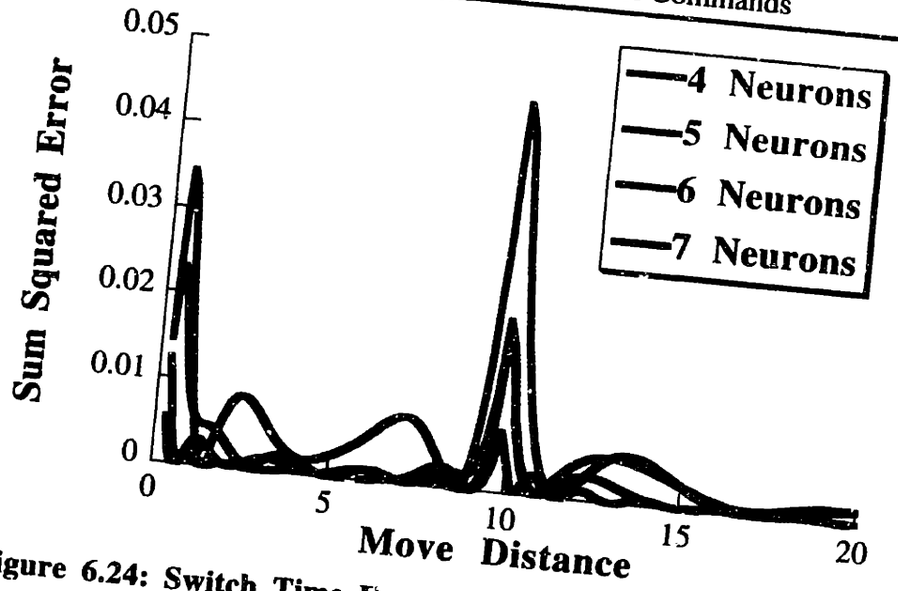

Figure 6.24: Switch Time Error as a Function of Move Distance.

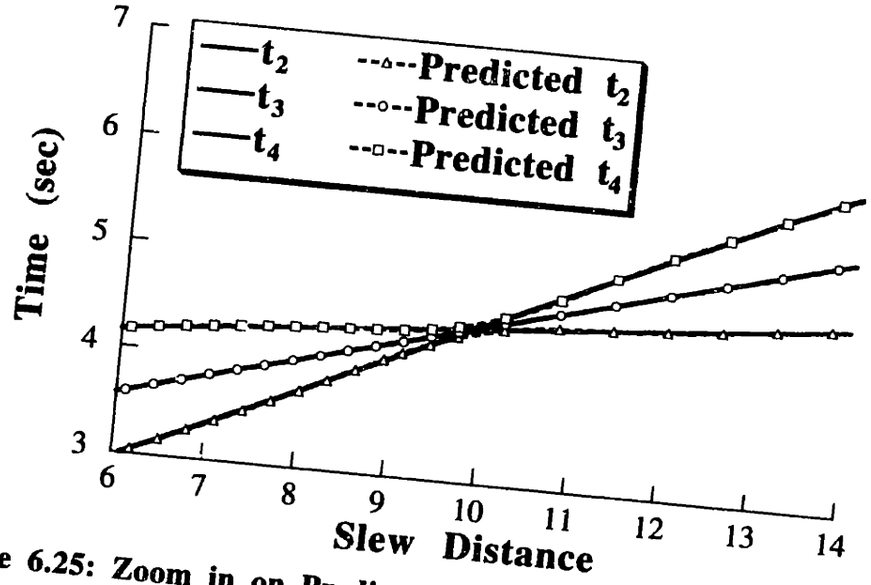

Figure 6.25: Zoom in on Predicted Switch Times (8 Hidden Neurons).

and then diverge for larger move distances.

Figure 6.25 shows that if we zoom in on the switch time data for the network with 8 neurons near $x_d = 10$, there is good agreement between actual and predicted switch times. (This is a close up of the data shown in Figure 6.22.) On the other hand, Figure 6.26 shows the predicted switch times when the network contains only 4 hidden neurons. The predicted switch times deviate considerably from the actual switch times.

The performance of the network can be improved by eliminating the sharp change in slope of

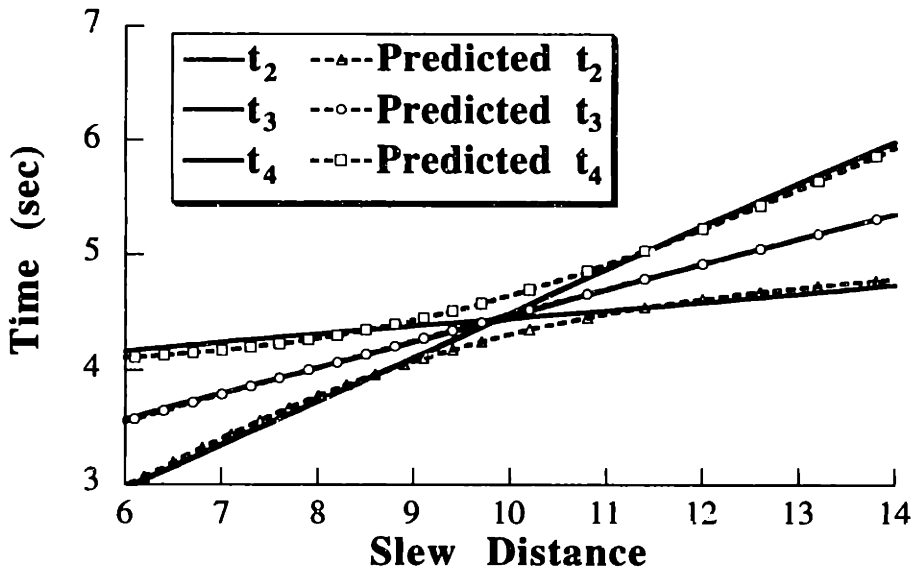

Figure 6.26: Neural Network Predicted Switch Times (4 Hidden Neurons).

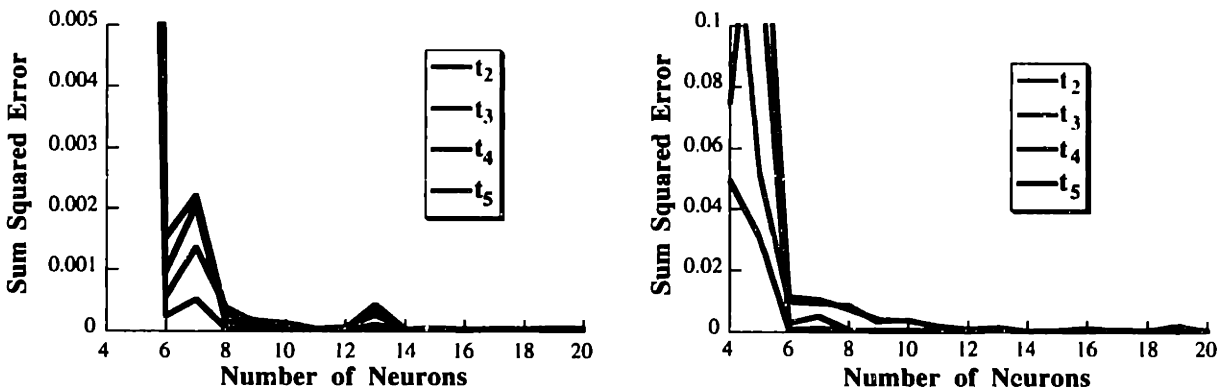

a) Training Set **b) Entire Data Set**

Figure 6.27: Switch Time Error as a Function of the Number of Hidden Neurons When Altered Data Representation is Used.

the switch time curves near 10 units. By referring to Figure 6.22, we see that this can be accomplished by switching t_2 and t_4 after the discontinuity. That is, after the discontinuity the switch times for t_2 become those for t_4 and vice versa. Figure 6.27 shows the SSE as a function of the number of neurons when this altered representation is used. The network now gives good performance with only 6 neurons, rather than the 8 required with the original data representation.

6.5.1b Time-Optimal ZVD Commands

Given the above results we know that time-optimal ZV commands can be effectively represented by a simple two-layer network. However, many real systems will require the robust

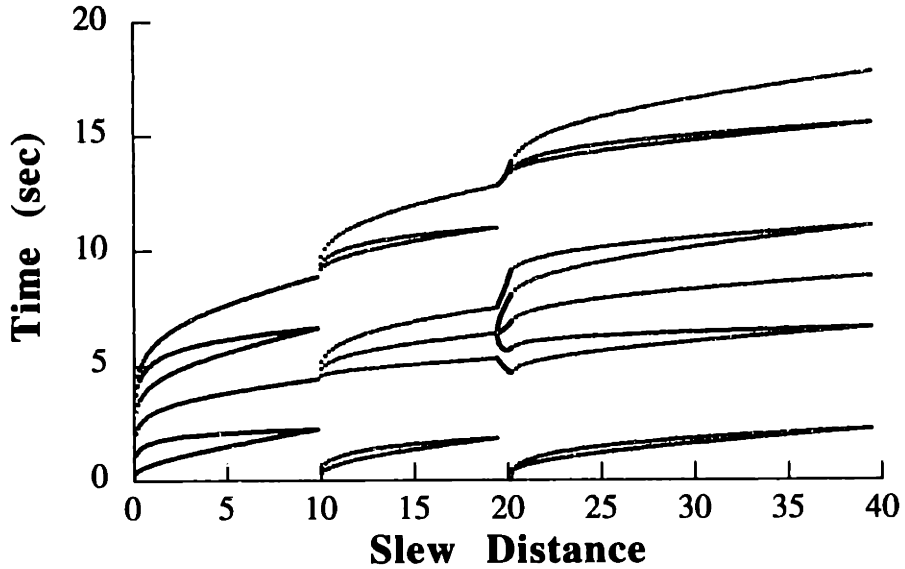

Figure 6.28: Switch Times for the Time-Optimal ZVD Command.

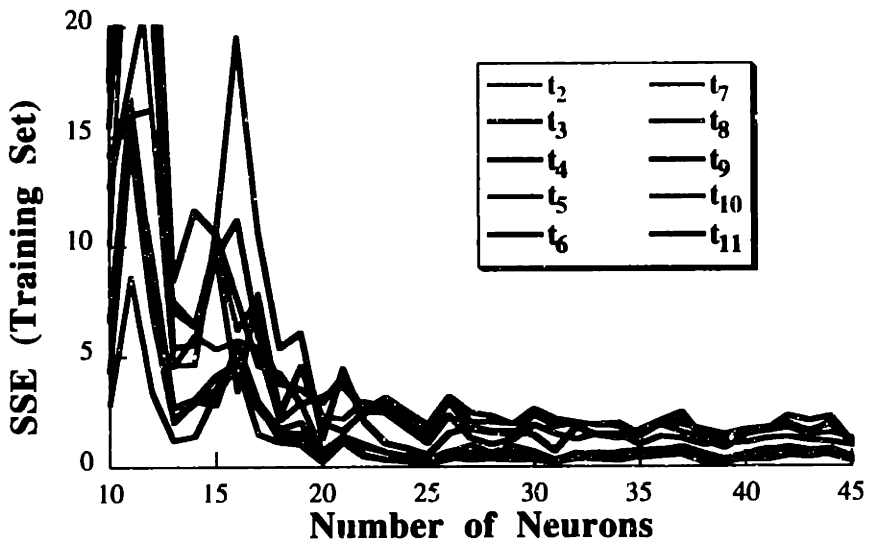

Figure 6.29: Two-Layer Network Representing Time-Optimal ZVD Commands.

ZVD commands for effective vibration reduction. Figure 6.28 shows the switch time data for the time-optimal ZVD commands. Comparing the ZV and ZVD commands shown in Figures 6.21 and 6.28, we can assume that more neurons will be required to represent the more complicated nature of the ZVD commands.

Figure 6.29 shows the SSE for each ZVD switch time as a function of the number of neurons in the log-sigmoid network. Note that the SSE is much larger than for the ZV commands and it takes 20 neurons before the improvement in SSE starts to level off. Figure 6.30 shows the output of a log-sigmoid network with 40 neurons. The network has difficulty predicting the

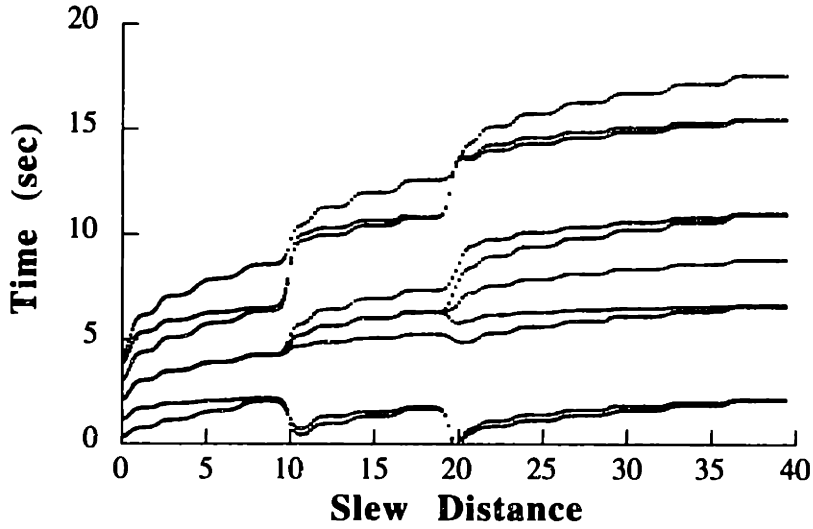

Figure 6.30: Predicted Switch Times of Time-Optimal ZVD Commands.

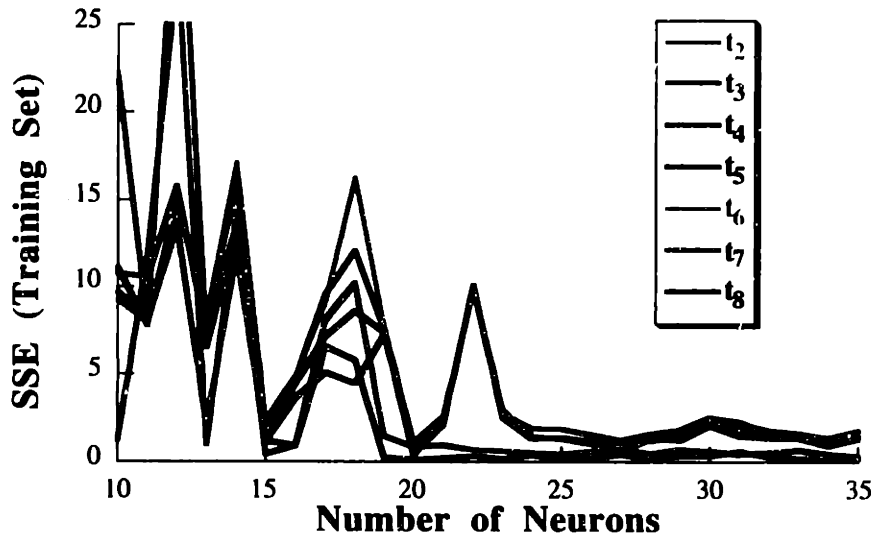

Figure 6.31: Two-Layer Network Representing the Fuel-Efficient ZV Commands.

discontinuous jumps in the switch times. Comparing Figure 6.30 to the actual curves in Figure 6.28, we see that the network has achieved the general pattern of the switch times, but overall it has done a poor job of predicting the switch times.

6.5.1c Fuel-Efficient ZV Commands

If the on-off command signals are being generated for reaction jets, then the fuel-efficient commands should be used. Figure 6.31 shows the SSE for each FE ZV switch time as a function of the number of neurons in the network. Given the large values for the SSE, we can see that this network does a poor job in predicting the FE ZV command switches. It does even worse for the

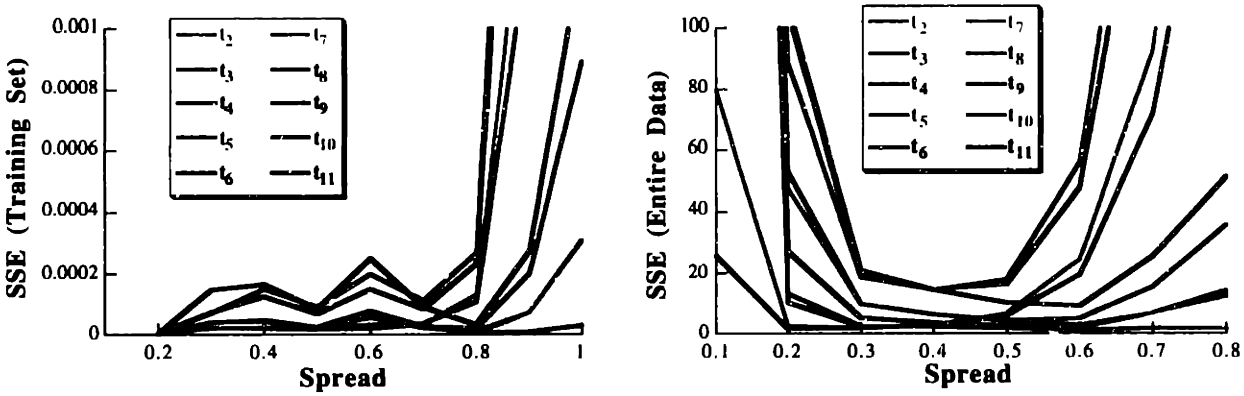

a) Training Set **b) Entire Data Set**

Figure 6.32: SSE of Radial Basis Network for the Time-Optimal ZVD Commands.

FE ZVD commands; even with 40 Neurons the network does a poor job predicting switch times.

6.5.2 Three-Layer Networks

The two-layer architecture had difficulty predicting the time-optimal ZVD, FE ZV, and FE ZVD profiles. The three-layer network performance was found to be marginally better than the performance of the two-layer network with a comparable number of neurons. From these results it appears that three-layer networks offer little advantage over two-layer networks for this particular application.

6.5.3 Radial Basis Networks

The discontinuous jumps in the switch times made it difficult for the above networks to accurately generate the command profiles. In this section results are presented which show that radial basis networks perform better when there are discontinuous jumps. When using a radial basis network one of the important parameters is the spread constant. Figure 6.32 shows the SSE of the time-optimal ZVD switch times as a function of the spread. Low values of the SSE for the training set are obtained up to a spread value of 0.8, while the lowest values of the SSE for the entire data set are obtained over the range from 0.3 to 0.5.

Figure 6.33 shows the predicted switch times of the time-optimal ZVD command when a spread of 0.3 is used. This performance is considerably better than that obtained with the two-layer or the three layer networks. Figure 6.34 shows the predicted switch times of the fuel-efficient ZVD command when a spread of 0.4 is used. If we compare these curves to the ones shown in Figure 5.9, we find a very good match.

6.5.4 Discussion of Neural Network Usage to Generate On-Off Commands

Optimization methods are used to obtain on-off command profiles for a limited number of

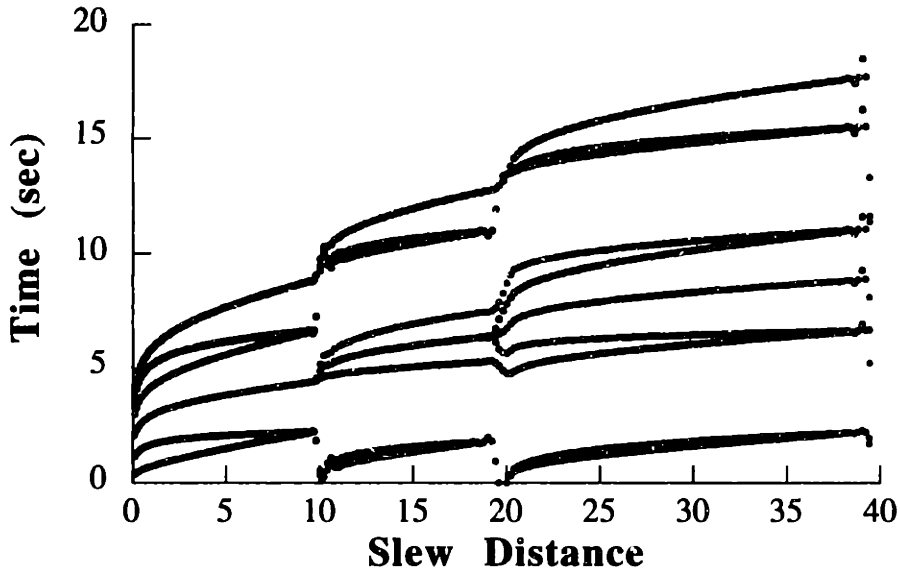

Figure 6.33: Predicted Switches of Time-Optimal ZVD Command (Spread=0.3).

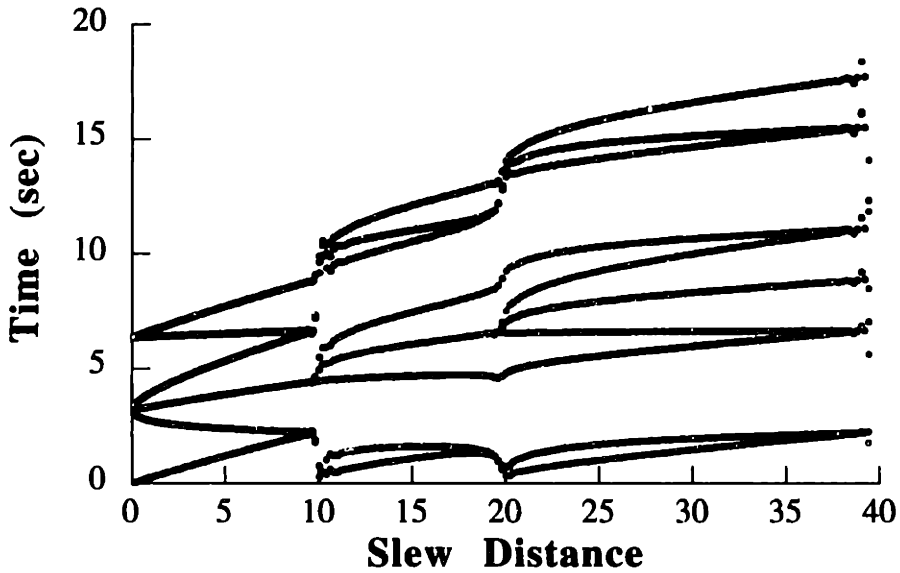

Figure 6.34: Predicted Switches of Fuel-Efficient ZVD Command (Spread=0.4).

possible slew distances. Using this data, neural networks are then trained to generate the command profiles for any desired slew distance. Simple two-layer neural networks can predict time-optimal zero-vibration commands; however, a minimum number of neurons in the hidden layer are required. The minimum number of neurons can be decreased by representing the switch times with smoothly varying curves. It was found that radial basis networks should be used when robust or fuel-efficient commands are being implemented.

7 COMPARISON OF COMMAND GENERATION METHODS

7.1 Introduction to Comparisons

Given the wide variety of command generation techniques presented in Chapters 3 - 6, it is useful to perform comparisons of these various methods to previously proposed methods. To do a thorough comparison, many types of performance criteria need to be examined. The criteria examined in this chapter include: rise time, residual vibration amplitude, robustness to modeling errors, transient deflection, fuel usage, ease of implementation, and excitation of unmodeled high modes. The following section compares input shaping to traditional FIR and IIR filtering for the purpose of generating commands for flexible mechanical systems. Section 7.3 compares input shaping to time-optimal flexible-body control for single-mode systems. Section 7.4 extends this comparison to multi-mode systems. Fuel-efficient commands were already compared to time-optimal commands in Chapter 5, so that comparison will not be repeated here. Also, the closed-form commands developed in Chapter 6 were compared to their time-optimal counterparts, so they will not be reevaluated here.

7.2 Input Shapers Compared to Traditional FIR and IIR Filters

As we know, input shapers can be thought of as finite impulse response (FIR) filters. Input shapers, however, are unlike filters produced by conventional design methods because they do not use a pass band specification and they are not usually designed in the frequency domain. They can be considered notch filters in the decaying sinusoid domain. Traditional notch filters remove a range of frequencies, while input shapers remove a range of decaying sinusoids.

Three criteria will be used to compare input shapers to conventional filters. First, the filter duration is compared because the time required for the system to move depends on the duration of the filter. The time duration of the filter will be reported as the number of system periods required for the output of the filter (which is the input to the system) to settle to within 2% of its steady state value. Second, the residual vibration amplitude will be compared. Finally, the robustness of the shaping techniques to uncertainties in the system model will be examined.

Each of the input shapers and filters described will be used to shape the input to a simple harmonic oscillator with one natural frequency. In order to evaluate the second and third performance criteria, two step responses will be simulated with each filter. One is the response of the system when it has the exact natural frequency that was assumed during the filter design process. The second is the step response when the natural frequency is set 15% lower than expected. Both systems will have no damping so that two quantities can clearly be observed – the time at which the filter finishes, and the residual vibration amplitude.

7.2.1 Zero Derivative Shapers

Figure 7.1 shows the two step responses when the ZVD shaper is used to modify the step input. The solid curve shows the response when the natural frequency is exact and the dashed curve shows the response when the system frequency is lowered by 15%. The envelope of the peak-to-peak vibration amplitude as a percentage of move distance is labeled on the left vertical axis for the exact case and on the right vertical axis for the case with a 15% modeling error. With the 15% error the envelope on residual vibration is approximately 11% of the move distance. This is 5.5% of the unshaped residual vibration level; the unshaped vibration has an amplitude equal to twice the move distance. The rise time is approximately 1 second (1 vibration period) for both responses.

Figure 7.2 shows the responses when the ZVDD shaper is used. Note that the ZVDD shaper yields less vibration for the 15% error than the ZVD shaper; however, the rise time is longer with the ZVDD shaper. It is approximately 1.5 vibration periods for both responses.

7.2.2 Extra-Insensitive Shapers

Figure 7.3 shows the two step responses when the one-hump EI shaper (V = 5%) is used to

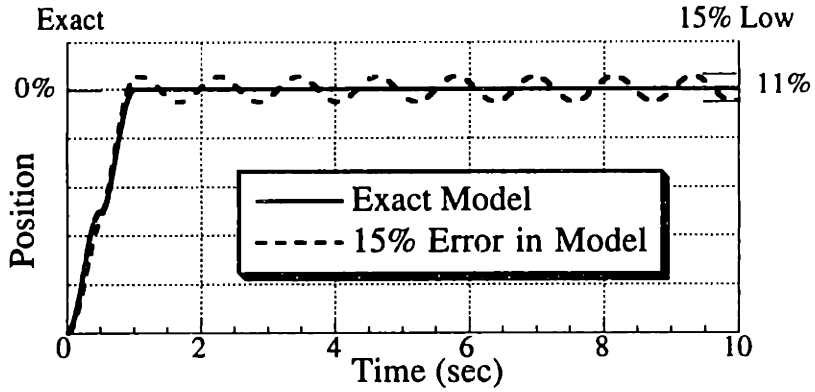

Figure 7.1: ZVD Input Shaper Responses.

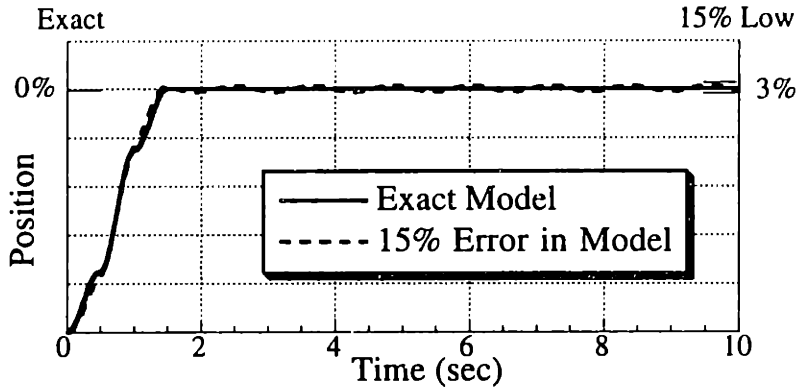

Figure 7.2: ZVDD Input Shaper Responses.

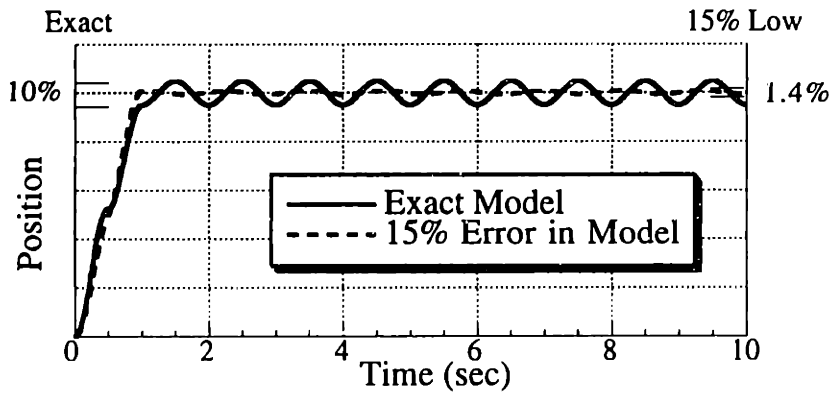

Figure 7.3: One-Hump (V=5%) Input Shaper Responses.

modify the step input. When the system model is exact, the residual vibration amplitude is, of course, 5% of the unshaped vibration level. When the system frequency is lowered by 15%, the amplitude of residual vibration actually decreases to 1.4%. This effect was predicted by the sensitivity curve of Figure 1.13. The rise time is approximately 1 vibration period.

Figure 7.4 shows the responses when the two-hump EI shaper (V = 5%) is used to modify the step input. The test using a 15% modeling error does not do the two-hump EI shaper justice. The

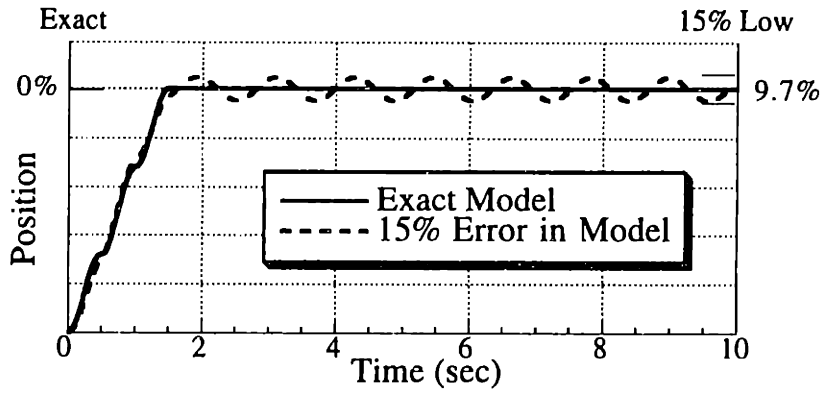

Figure 7.4: Two-Hump (V=5%) Input Shaper Responses.

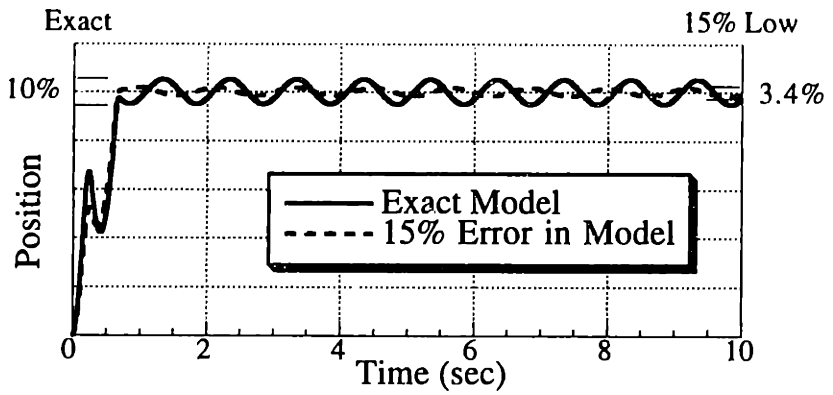

Figure 7.5: Negative EI (V=5%) Input Shaper Responses.

shaper would yield less than 5% of the unshaped vibration even if the system frequency was lowered by 36%. The rise time is approximately 1.5 vibration periods.

7.2.3 Negative Input Shapers

Figure 7.5 shows the responses with a partial sum (P = 1) one-hump EI shaper. The amplitudes of the impulses in the shaper are: [1, -2, 2, -2, 2, -2, 2]. The vibration levels at frequencies near the modeling frequency are similar to those for the all-positive EI shaper, however, the rise time is 30% faster. When there is a modeling error, the negative shapers tend to yield more residual vibration than there all-positive counterparts. Similar results were obtained with the unity-magnitude shapers.

7.2.4 FIR Lowpass Filters

Ideal low pass filters have a rectangular magnitude of response. (See Figure 1.12.) The ideal filter is unrealizable because the impulse response continues indefinitely. In order to shorten the time response of the ideal lowpass, some form of truncation is used. This truncation process is the basis for many FIR filter design techniques. The truncation process (windowing) cannot be made abrupt because the frequency response will be corrupted by the Gibbs Phenomenon.

A common Hamming window with a time duration of three system periods was used to truncate the ideal low pass filter [74]. The response to the step command shaped by the filter exhibited considerable residual vibration. The response using a longer (five period) Hamming window was then determined. The responses indicate that the filter length must be long compared to the period of oscillation in order to achieve a reasonable reduction in residual vibration. These responses are not shown, but their performance is summarized in Table 7.1.

7.2.5 Parks-McClellan Lowpass Filter

FIR lowpass filters were designed using the Parks-McClellan-Rabiner technique [84]. The computation was performed with the original Remez exchange design program written by Parks and McClellan. A 256 point FIR filter was designed using double precision arithmetic. The filter was constrained to have a duration equal to one vibration period – the same time duration as the ZVD and one-hump EI shapers. This filter was designed with a pass band at 80% of the anticipated natural frequency, and a stop band at 95% of the anticipated natural frequency. While the time duration of this filter is comparable to the input shapers, the vibration reduction and ease of implementation is not (due to the larger number of filter coefficients). The performance with this filter is summarized in Table 7.1.

7.2.6 Infinite Impulse Response Lowpass Filters

Oppenheim and Schafer [74] note that FIR filters are different from IIR filters in that they provide greater "flexibility in the attainable filter response". However, infinite impulse response filters are extremely common, so they will be considered. IIR filters are limited because they must have poles and, therefore, contain integration dynamics. Three common IIR Filters were designed – Butterworth, Chebyshev, and elliptic. The Butterworth and Chebyshev filters were designed with a pass band at 70% of the anticipated natural frequency, and a stop band at 95% of the anticipated natural frequency. The Chebyshev filter had a 2 dB ripple and a 50 dB attenuation in the stop band. The elliptic filter was designed with a stop band at the anticipated natural frequency with 10 dB ripple and 30 dB attenuation. Although the vibration reduction associated with these filters is relatively good, the time delays incurred with their use are prohibitive. To demonstrate the sluggish response, Figure 7.6 shows the response when the Chebyshev lowpass is used to filter the step command.

7.2.7 Hamming Window Notch Filter

Ideal notch filters, like ideal lowpass filters are not realizable. Because the magnitude of the response suddenly drops to zero in the notch and becomes unity again in the next pass band, the filter has an infinite duration. However, a Hamming window can be applied to an ideal notch filter

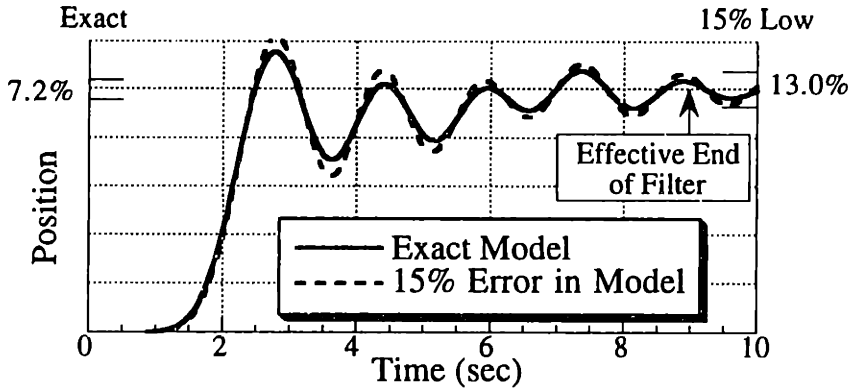

Figure 7.6: Chebyshev Lowpass Filter Responses.

in the same manner as it was applied to the ideal lowpass filter. The windowing process produces realizable filters with frequency responses close to that of the ideal filter. A five period Hamming window was applied to the ideal notch filter frequency response. The center of the notch is at the natural frequency of the system. The notch extends ±30% about the center frequency. The response using this notch filter contains significant residual vibration. See Table 7.1.

7.2.8 Parks-McClellan Notch Filters

A 256 point FIR notch filter was designed using the Parks-McClellan-Rabiner algorithm. The filter was constrained to have the same time duration as the ZVD and one-hump EI shapers. This filter was designed with a pass band of ± 20% about the anticipated natural frequency, and a stop band of ±5% about the anticipated frequency.

The Parks-McClellan notch filter performed the best of any of the tested filters (excluding input shapers). The drawback of this filter is that 256 impulses were required to achieve the high performance. This filter is more difficult to implement in real time than an input shaper because it requires significantly more computation at each time step. The Parks-McClellan filter requires 256 multiplies and accumulates at each time step, whereas, the input shapers typically require only 3 to 10 multiplies and accumulates.

7.2.9 Infinite Impulse Response Notch Filters

The system responses with Butterworth, Chebyshev, and elliptic IIR notch filters were determined. The filters were designed with a pass band of ±30% about the anticipated natural frequency, and a stop band of ±20% about the anticipated frequency. Large time and vibration penalties are incurred by using these filters. See summary in Table 7.1.

7.2.10 Summary of Shaper/Filter Comparison

Table 7.1 lists the duration, exact model vibration, and 15% modeling error vibration for each of

Table 1: Summary of Performance Data.[25]

	Duration	Vibration	
Shaper	(cycles)	Exact	15% Low
ZVD	1.00	0.0%	11.0%
ZVDD	1.50	0.0%	3.0%
ZVDDD	2.00	0.0%	0.5%
One-Hump EI (V=5%)	1.00	10.0%	1.4%
Two-Hump EI (V=5%)	1.50	0.0%	9.7%
Three-Hump EI (V=5%)	2.00	10.0%	1.8%
Negative ZVD	0.67	0.0%	13.0%
Neg. 1-Hump EI (V=5%)	0.68	10.0%	3.4%
Neg. 2-Hump EI (V=5%)	1.12	0.0%	9.6%
Neg. 3-Hump EI (V=5%)	1.58	10.0%	1.0%
Filter			
Hamming Lowpass (short)	2.46	20.0%	54.0%
Hamming Lowpass (long)	3.54	2.0%	30.0%
Parks-McClellan Lowpass	1.00	28.0%	57.0%
Butterworth Lowpass	5.61	6.0%	22.0%
Chebyshev Lowpass	8.90	7.2%	13.0%
Elliptical Lowpass	8.50	6.9%	10.8%
Hamming Notch	3.93	32.0%	73.0%
Parks-McClellan Notch	1.00	7.8%	18.0%
Butterworth Notch	>10.0	16.0%	18.0%
Chebyshev Notch	>10.0	36.0%	44.0%
Elliptical Notch	>10.0	17.0%	23.0%

the shapers and filters discussed, as well as, several shapers not discussed in detail. There are two important trends that can be observed in the results. First, the input shapers are significantly shorter than the filters. The shapers have durations that range from 0.68 to 2.0 times the period of the vibration to be suppressed. The filters have effective durations that range in length from 1.0 to over 10.0 times the vibration period, with most of the filter lengths being over 3.5 times the vibration period. This trend indicates that input shapers would degrade a system's rise time much less than a traditional digital filter.

The input shapers also yield considerably less vibration than the filters. When the system model is exact, the shapers yield either zero vibration, or the small amount of vibration that is specified during the EI design process. When the digital filters are applied to a system with a known frequency, there is often a considerable amount of vibration. When there is a modeling error, the advantage of input shapers is even more pronounced.

In an attempt to evaluate the overall performance of the shapers and filters, we can combine the duration and vibration measures. One possible way of doing this is to multiply the duration (in

[25] Duration is the effective length of the filter as measured in vibration cycles. Exact vibration is the residual vibration divided by the move distance when the system model is exact. 15% Low vibration is the residual vibration when the system frequency is 15% lower than expected.

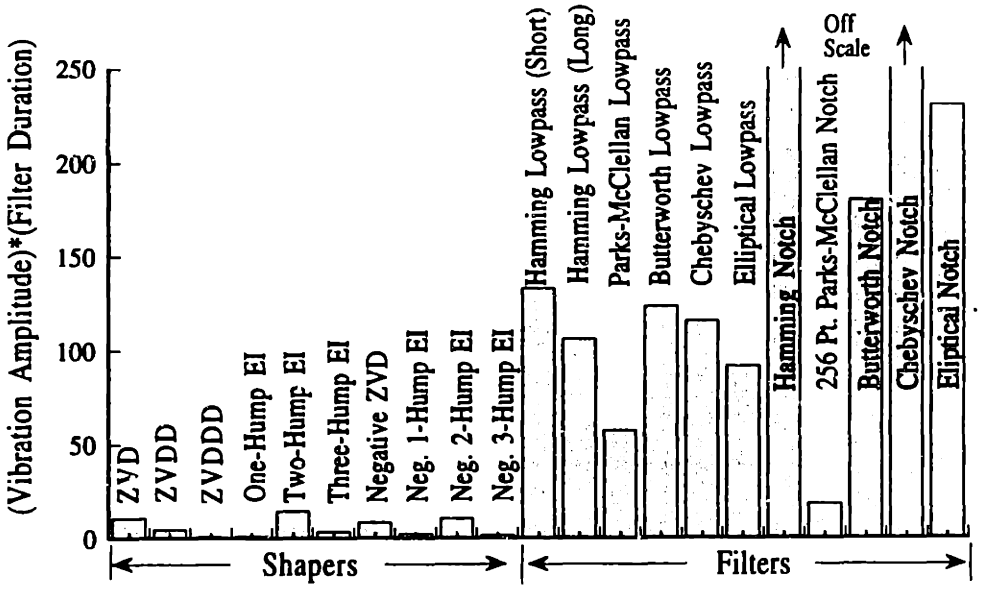

Figure 7.7: Vibration Amplitude (15% Low) Multiplied by the Filter Duration.

cycles) by the 15% modeling error vibration amplitude (in % of move distance). Figure 7.7 shows this measure for each of the shapers and filters. The superiority of shapers over filters given this particular performance measure is readily apparent.

7.3 Single-Mode Input Shaping and Time-Optimal Control

Input shaping is a more general-purpose technique than the time-optimal flexible-body control because once a shaper has been designed, it can be used to shape the reference command for any desired motion. However, the switch times in the time-optimal flexible-body command must be computed for every unique desired motion. Furthermore, the time-optimal commands, unlike commands produced with input shaping, have an inherent open-loop nature that makes them challenging to implement with a closed-loop controller. For example, a neural network might need to be trained to generate closed-loop, near time optimal commands in real-time based on the nature of the time-optimal solutions [62].

To compare input shaping and time-optimal control in terms of their dynamic performance characteristics (ignoring implementation issues), applications of rest-to-rest slewing will be examined [79, 118]. To perform rest-to-rest motion with input shaping, the unshaped command must accomplish rest-to-rest motion of the rigid body. The time-optimal control for rest-to-rest motion of a rigid body is bang-bang, with the switch occurring at mid-maneuver. Therefore, the performance obtained using a shaped bang-bang command will be compared to the response using the time-optimal flexible-body commands. The commands generated by shaping the bang-bang command will be labeled as "Shaper Name" BB. For example, using a UM ZV shaper (a negative shaper subject to the unity magnitude amplitude constraints) on a bang-bang command yields a UM ZV BB command. The five shaped commands that will be examined are the ZV BB, ZVD BB, UM ZV BB, UM ZVD BB, and UM EI BB. The two time-optimal flexible-body commands that will be examined are the TO ZV and the TO ZVD. The two methods are compared in terms of maneuver speed, robustness to modeling errors, transient deflection, high-mode excitation, and ease of implementation.

7.3.1 Maneuver Speed

Figure 7.8 shows the move duration for the seven types of commands as a function of damping ratio, ζ, and move distance, L. Commands satisfying the ZV constraints are shown with a solid line. ZVD commands are shown with a dotted curve and the EI command is represented by a dash-dotted line. Furthermore, positive shapers are distinguished by open circles, and negative shapers are represented by open squares, except for the negative EI shaper which is shown using open triangles.

Although the time-optimal flexible-body commands (TO ZV) always provide the fastest moves, the robust time-optimal (TO ZVD) averages only 8.1% slower, for the range shown in the two figures. The UM ZV BB also provides fast maneuvers; it is approximately 13.5% longer than the

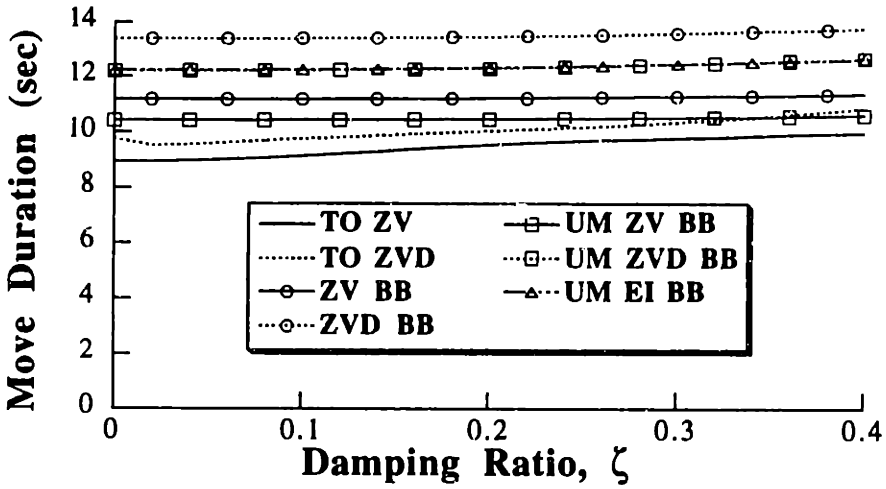

a) As a Function of Damping (L=10)

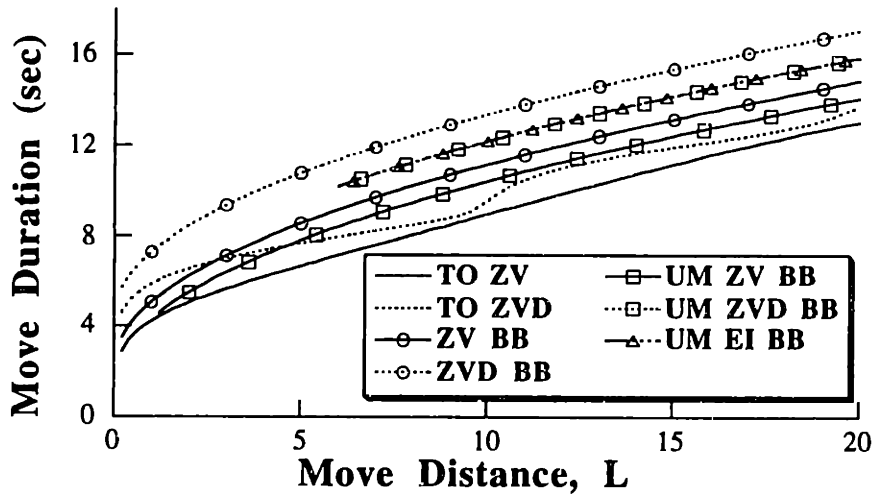

b) As a Function of Move Distance (ζ=0.04)

Figure 7.8: Comparison of Move Duration.

TO ZV command. For a given robustness constraint (ZV or ZVD), the negative shapers lead to faster maneuvers than their corresponding positive shapers. The UM ZVD and UM EI commands yield approximately the same maneuver times. For very short move distances the negative shapers will cause overcurrenting [75, 127]. The results shown for the negative shapers are for move distances with no overcurrenting.

7.3.2 Robustness to Modeling Errors

Figure 7.9 shows the 5% insensitivities of the various commands. The UM ZVD BB and UM EI BB commands offer a significant increase in robustness over the time-optimal commands. Compared with the TO ZV command, the UM ZVD BB and UM EI BB shapers exhibit increases of 300 to 4500 percent in 5% insensitivity for most damping ratios and move distances. Thus,

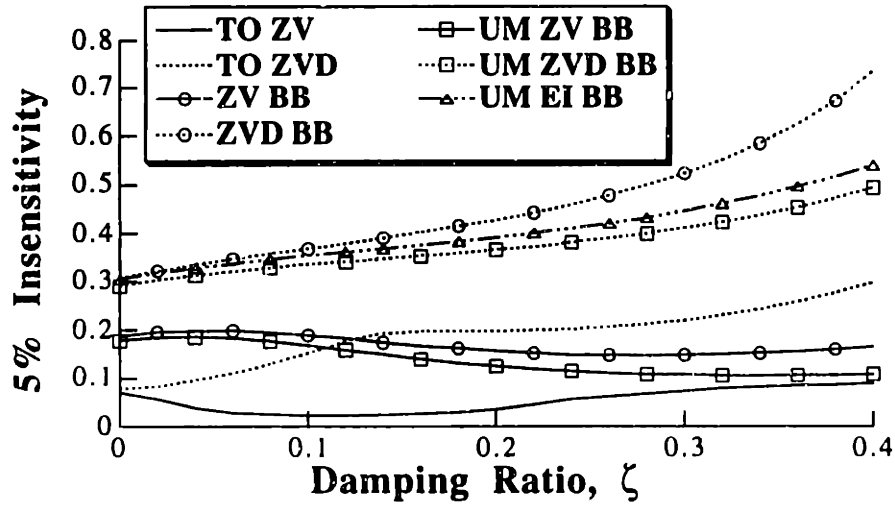

a) As a Function of Damping (L=10)

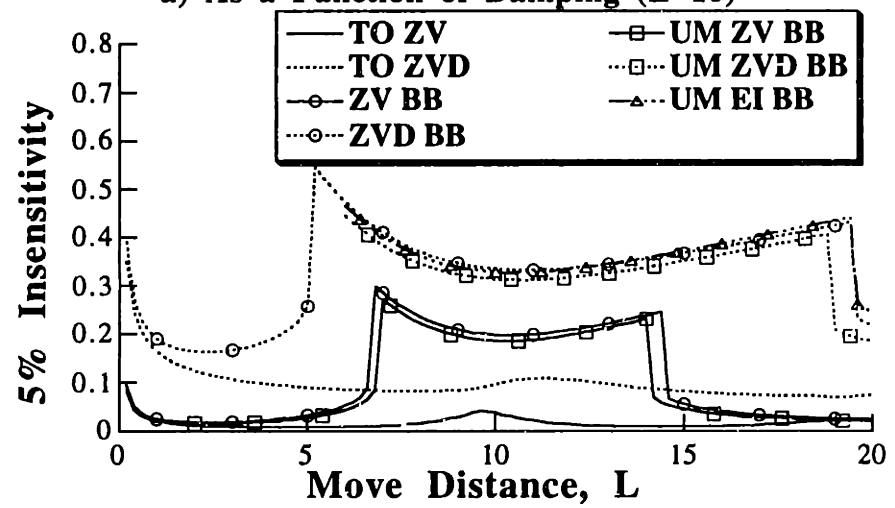

b) As a Function of Move Distance (ζ=0.04)

Figure 7.9: Comparison of 5% insensitivity.

while the TO ZV command leads to the fastest maneuvers, the UM EI BB and UM ZVD BB lead to moderately longer maneuvers that are significantly more robust to modeling errors. The ZVD BB commands offer the most robustness, but incur a larger time penalty than the UM commands.

7.3.3 Transient Deflection

Another important quality to compare is the amount of vibration that is caused *during* the motion. Decreasing vibration during the move can increase the lifetime of many systems and improve the trajectory following of the endpoint. Figure 7.10 shows the maximum transient deflection ($|x_2-x_1|$) for the various commands. The negative shapers yield approximately the same deflection as their positive counterparts over most of the parameter range. However, the time-optimal commands cause approximately twice the deflection as the input shapers.

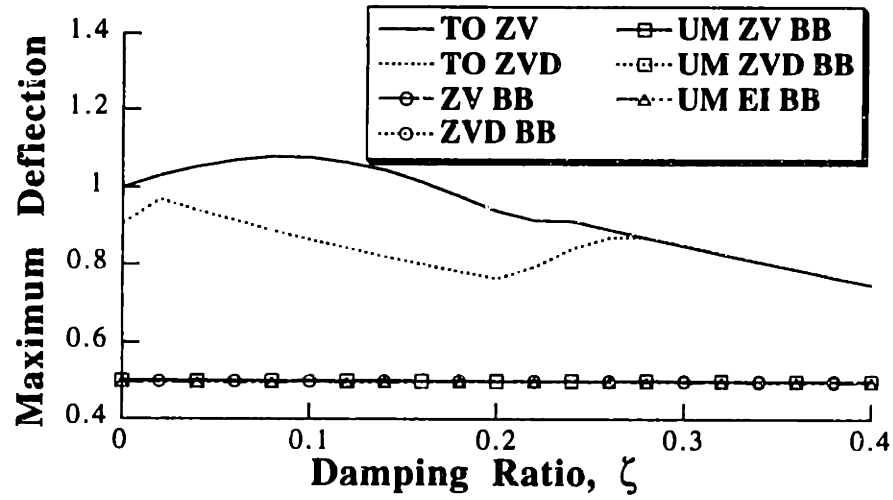

a) As a Function of Damping (L=10)

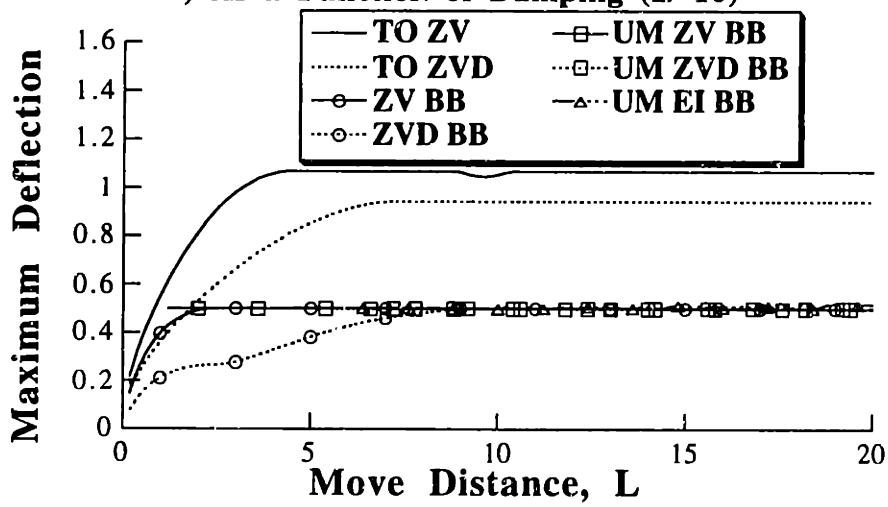

b) As a Function of Move Distance (ζ=0.04)

Figure 7.10: Comparison of Maximum Transient Deflection.

7.3.4 High-Mode Excitation

Both the input shapers and the time-optimal commands are designed to eliminate or reduce vibration at a specific frequency or set of frequencies. Often, only the dominant low-frequency modes are taken into account in the input-shaper design. If the system has modes higher than the frequencies used to generate the shaped or time-optimal commands, then the high modes may be excited. To appreciate this effect, the sensitivity curves can be plotted over a range of high frequencies. Figure 7.11 compares the high-mode sensitivity curves for the ZVD BB and the TO ZVD commands when L = 10 and $\zeta = 0.04$. For frequencies near the modeling frequency, ω, the two curves are similar; however, for frequencies in the range 1.5ω to 10ω, the time-optimal command usually has much higher levels of vibration. Therefore, if the system has unmodeled

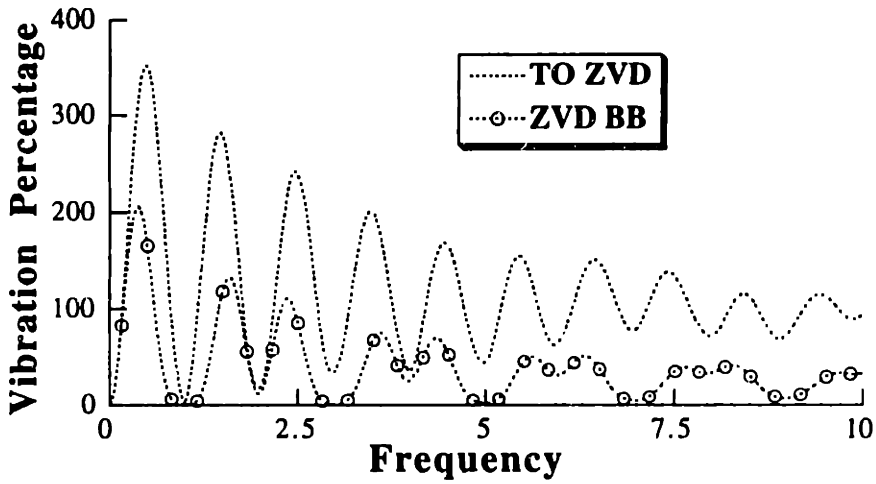

Figure 7.11: High Frequency Sensitivity Curves (L = 10 and ζ = 0.04).

high modes, the time-optimal command will lead to more vibration in those modes than the commands generated with shaping.

To compare the high-mode excitation over a range of system parameters, the mean value of the sensitivity curve over the range 1ω to 10ω was computed. Figure 7.12 compares the mean value of the high-mode sensitivity curve for the seven command profiles over a wide range of damping ratios and move distances. The positive shapers lead to the smallest high-mode excitation levels, but at the greatest cost in move speed (see Figure 7.8).

7.3.5 Ease of Implementation

It is difficult to generate a quantitative measure to compare the ease of implementation of the two control methods. However, based on experience, input shaping is significantly easier to implement than time-optimal control. Analytical or curve fit formulas exist for all the positive input shapers discussed, and hence they can be implemented in real time, with any unshaped command signal. Curve fit formulas exist for the negative shapers used in these comparisons, and they can be used with most unshaped command signals.

In contrast, the time-optimal control must be computed using an optimization for every move distance. While tables of optimal switch times can be stored and interpolated for desired move distances, this process is more cumbersome and interpolation will generally lead to some error in the actual switch times used (i.e., the interpolated switch times will not satisfy the optimal constraint equations exactly). These errors may lead to even lower insensitivities and greater high-mode excitation levels than those displayed in Figures 7.9 and 7.12

7.3.6 Summary of Single-Mode Shaping and Time-Optimal Control

Several types of input shapers have been compared with robust and non-robust time-optimal

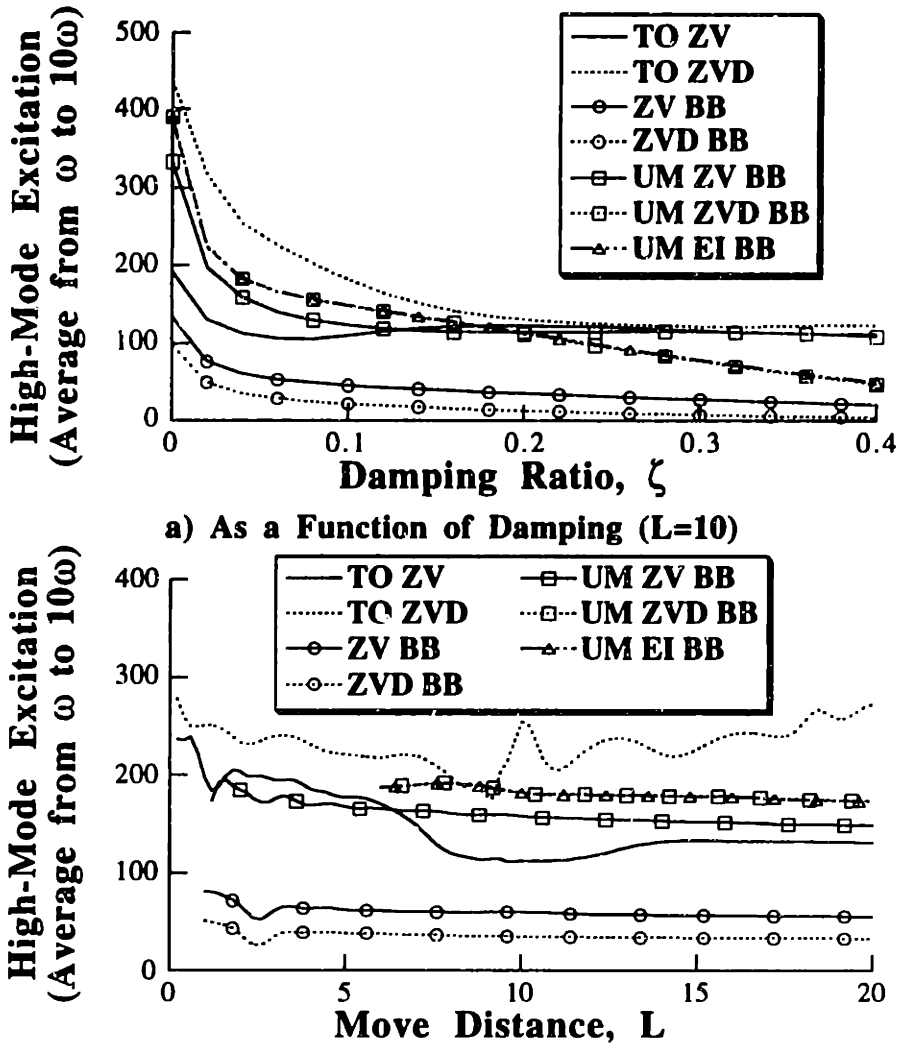

Figure 7.12: Comparison of High-mode excitation.

flexible-body control. The methods were compared in terms of speed, robustness to modeling errors, transient deflection, high-mode excitation, and ease of implementation. While time-optimal commands yield the fastest responses, the negative input shapers provide an attractive alternative for achieving rapid responses. One of the main advantage of input shaping is the robustness to modeling errors. For a given robustness constraint (ZV or ZVD) the input shapers have 2-10 times more insensitivity than the time-optimal commands. The EI shaper provides an additional 5-10% increase in insensitivity over the ZVD shaper. The shapers reduce transient deflections by about a factor of two, although this advantage decreases as the damping increases. Furthermore, the input shapers have less tendency to excite unmodeled high modes and are easier to implement. Given the numerous advantages provided by input shaping, it provides an attractive alternative to time-optimal flexible-body control.

7.4 Comparisons with Multi-Mode Systems

The previous section revealed several key differences between input shaping and time-optimal control for single-mode systems. This section performs the same type of investigation for multi-mode systems [119]. In order to compare the performance of multi-mode input shaping and time-optimal control, rest-to-rest slewing of the benchmark system shown in Figure 4.11 will be examined. As in the previous section, the input shapers will be used in conjunction with a bang-bang command and the commands generated by shaping the bang-bang command will be labeled as "Shaper Name" BB.

Recall from Chapter 3 that multi-mode shapers can be designed in two ways. They can be generated by convolving single-mode shapers together, or they can be obtained by directly solving the constraint equations simultaneously. The three shaped command profiles that will be compared are the convolved ZVD BB, the direct ZVD BB, and the TO ZVD. The non-robust ZV shaping methods are not considered here. The three types of commands are compared in terms of maneuver speed, robustness to modeling errors, transient deflection, and ease of implementation. The system of Figure 4.11 with r = 4.4 will be used.

7.4.1 Maneuver Speed

Figure 7.13 shows the move duration for the three command profiles as a function of move distance. The time-optimal ZVD command is shown with a solid line, the direct ZVD BB is shown with a dotted line and convolved ZVD BB command is shown with a dash-dot line. The TO ZVD command is, of course, the fastest command. The TO ZVD ranges from 0.6 to 1.0 seconds faster than the direct ZVD BB. Note that the increase in move duration follows a repeating cycle; it does not continually increase. Therefore, the percentage increase in move duration decreases as the move distance is increased. The direct ZVD BB is faster than the convolved ZVD BB command by approximately 0.13 sec.

7.4.2 Robustness to Modeling Errors

To quantitatively compare the robustness to modeling errors, the 5% insensitivity for each of the commands was calculated as a function of move distance. (Please see again Figure 3 for the meaning of 5% insensitivity.) Recall from Chapter 3 that for multi-mode systems there is a sensitivity associated with each mode. Figure 7.14 show the 5% insensitivities for the first and second modes. The input shaped commands are considerably more robust than the time-optimal commands. Input shaping (convolved or direct) gives an average of nearly 4 times more robustness than the time-optimal commands to errors in the first mode (Figure 7.14a). The direct shapers give an average of 3.7 times the robustness to second-mode errors, while the convolved

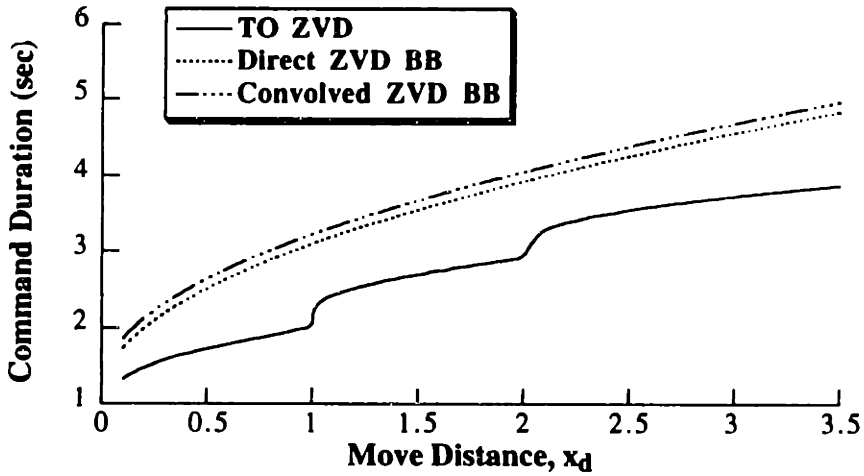

Figure 7.13: Duration of Command Profiles as a Function of Move Distance.

shapers offer more than an order of magnitude improvement in second-mode robustness as compared to the TO ZVD commands (Figure 7.14b). Note that the direct and convolved shapers give approximately the same robustness to errors in the first mode, but differ largely in second-mode robustness, with the convolved shapers being much more robust. This effect has been previously noted [26, 43]. By comparing Figures 7.14a and 7.14b it can be seen that the first mode robustness is usually better than second mode robustness, except for the convolved shapers.

7.4.3 Transient Deflection

Although the shaping methods under consideration yield zero residual vibration when the model is perfect, there is deflection during the motion. Decreasing vibration during the move can increase life span and improve trajectory following. Figure 7.15 shows the deflection of the benchmark system when a time-optimal ZVD command is used to slew the center of mass 3.0 units. The deflection between m_1 and m_2, D_1, is defined as x_2-x_1; the deflection D_2 is x_3- x_2.

Figure 7.16 shows the maximum transient deflection as a function of the move distance. The time-optimal commands result in significantly more deflection than the shaped bang-bang commands. The direct and convolved shapers yield approximately the same transient deflection. Note that maximum deflection results are highly dependent on the system parameters. A system with a low mode of 1 Hz and a second mode of r Hz can be obtained using a variety of values for the masses and springs constants. In each case, the deflection would differ. However, the same general trends shown in Figure 7.16 would occur. Namely, the convolved ZVD shaper tends to cause the least transient deflection, while the TO ZVD command causes the most deflection. Furthermore, the maximum deflection with shaping reaches a constant value after some minimum move distance, while the deflection with time-optimal control varies in a complicated manner.

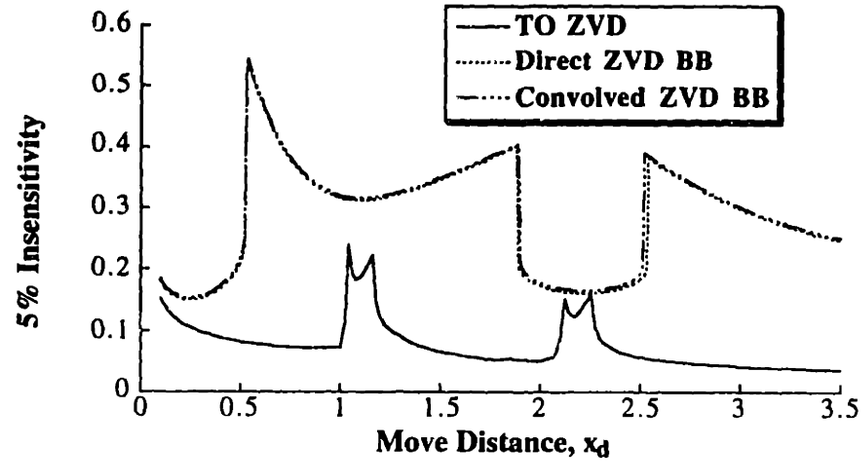

a) First Mode

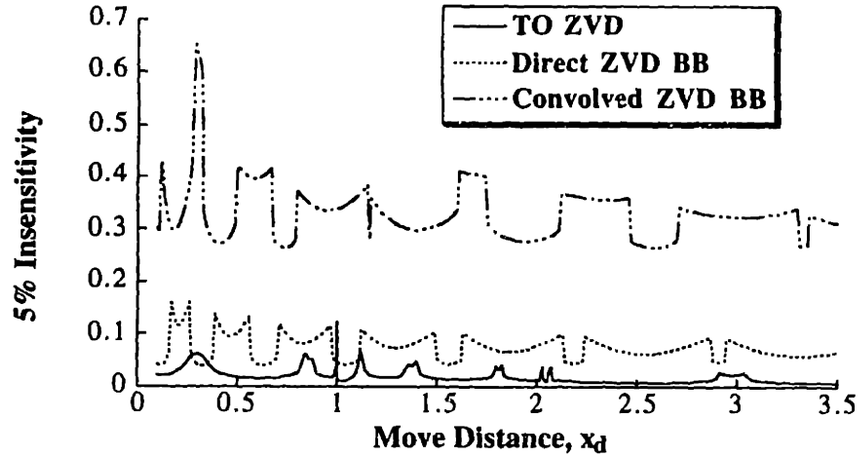

b) Second Mode

Figure 7.14: Insensitivity (5%) as a Function of Move Distance.

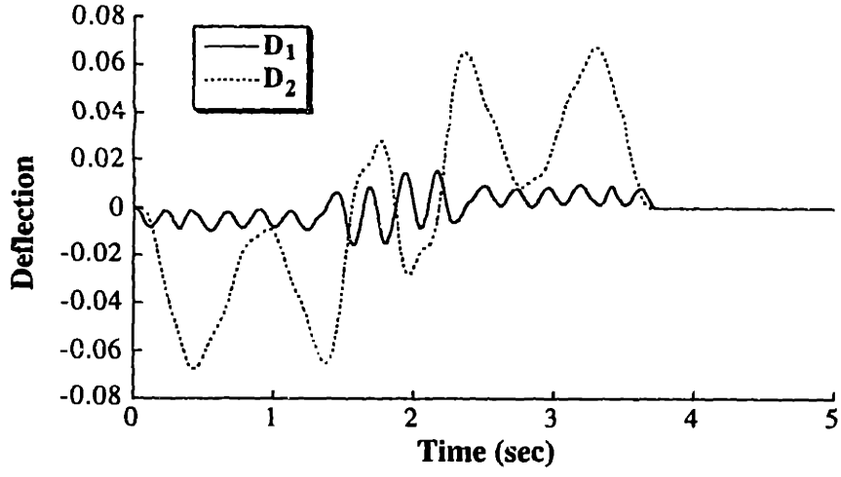

Figure 7.15: Transient Deflection (x_d = 3.0).

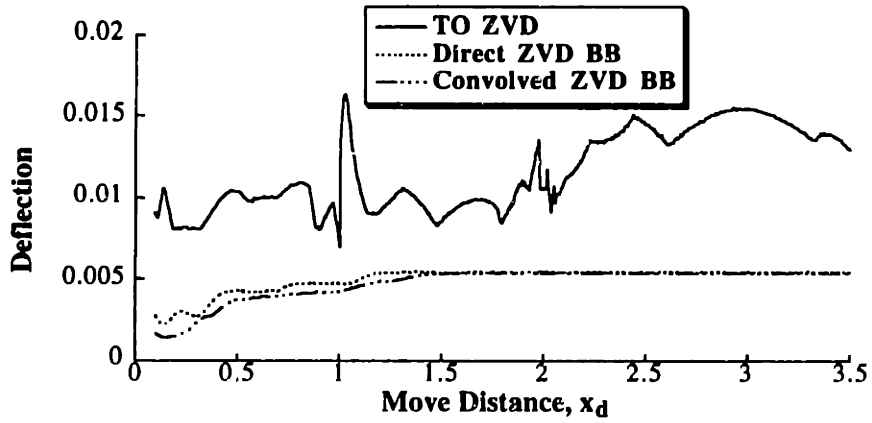

a) D_1

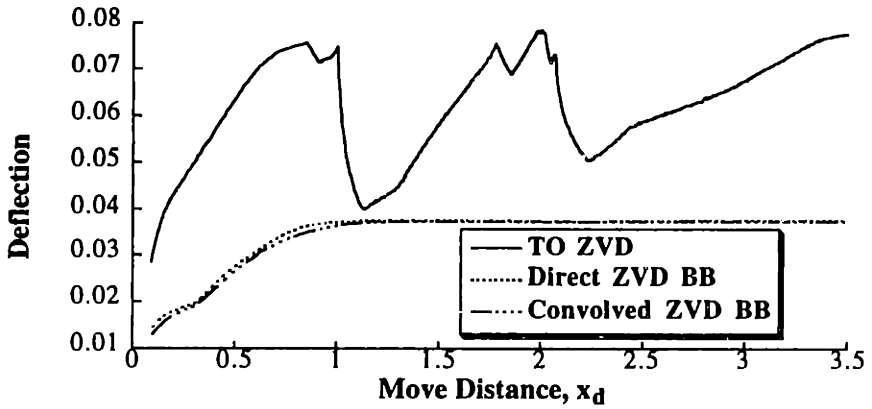

b) D_2

Figure 7.16: Maximum Transient Deflection as a Function of Move Distance.

7.4.4 Ease of Implementation

As mentioned in the previous section, input shaping is much easier to implement than time-optimal commands. For multi-mode systems, ease of implementation is even more pronounced. From Chapter 4 we know that multi-mode time-optimal command switch times are complicated functions of the desired motion and mode ratios. Although the input shapers are functions of the mode ratio, they are relatively easy to obtain and are useful for every desired motion.

7.4.5 Summary of Multi-Mode Shaping and Time-Optimal Control

Multi-mode input shaping has been compared with robust time-optimal flexible-body control. The methods were compared in terms of speed, robustness to modeling errors, transient deflection, and ease of implementation. While time-optimal commands yield the fastest responses, the percentage increase in move duration with input shaping decreases as move distance increases. Input shaping provides vastly increased robustness to modeling errors, while being much easier to implement. Furthermore, input shaping generates significantly less transient deflection than does time-optimal control.

8 EFFECTS OF INPUT SHAPING ON COMPLEX PERFORMANCE SPECIFICATIONS

8.1 Introduction

Although command generators can be designed to meet a wide variety of performance specifications, certain specifications cannot be formulated (or would be extremely difficult to formulate) as constraint equations and used in the design of a command generator. These complex specifications are usually functions of several low-level performance specifications such as rise time and settling time. For example, the throughput of a manufacturing machine may depend on the settling time for each phase of its motion, the number of motions, the quality of the stock given to the system, the skill of the operator (if any), the quality of the closed-loop controller, and the environment noise. Designing a command generator that gives a throughput of X units per hour is a poorly defined problem because the command generator does not have control over many of the factors influencing throughput.

This chapter does not propose a method for getting around this problem; rather, it simply investigates the effect of command generation on complex performance specifications. Section 8.2 investigates the effect of input shaping on the repeatability of coordinate measuring machines. Measurement repeatability is a function of many variables including structural deflection, sensor probe accuracy, operating speed, and temperature. Input shaping only seeks to limit residual vibration, so its impact on measurement repeatability is not immediately obvious. Section 8.3 investigates the effect of input shaping on trajectory following. When a flexible system attempts to follow a specified trajectory, the deviation from the intended path depends on many parameters including the path itself, the speed of travel, and the mode shapes, just to name a few. Section 8.4 investigates a related problem of obstacle avoidance with flexible systems. The flexibility of a system makes obstacle avoidance more difficult because the system will deviate from the intended path. Therefore, obstacle avoidance depends on many of the same variables as trajectory following, but it also depends on the number, size, and locations of the obstacles.

8.2 Coordinate Measuring Machine Repeatability

Coordinate Measuring Machines (CMMs) measure manufactured parts to determine if tolerance specifications have been achieved. A CMM consists of a workspace in which parts are fixtured, a sensor for detecting the part surfaces, a mechanical assembly for moving the part sensor around the workspace, and a computer for calculating the part dimensions based on the sensor measurements. CMMs are available in numerous sizes and styles. Some are "desktop" mechanisms moved manually, while others are computer driven and are large enough to measure car bodies. This section concentrates on the behavior of a moving bridge CMM like the one sketched in Figure 8.1.

The CMM of Figure 8.1 is shown with a touch-trigger probe part sensor. This sensor uses a ruby-tipped stylus to sense the part. When the stylus is brought into contact with a part surface, the deflection of the stylus triggers the computer to record the position indicated by the x, y, and z encoders. By probing the part on appropriate surfaces and recording their locations, the dimensions of the part can be calculated.

For the CMM under consideration, the measurement cycle consists of four phases. First, the CMM performs a gross motion to move the part sensor to the vicinity of the part feature that is to be measured. Second, the probe is allowed to come to rest. Third, the probe is reaccelerated to a small constant velocity in the direction of the part. This portion of the measurement is called the probe approach. Finally, the stylus contacts the part and the computer records the location of the contact. The position of a touch-trigger probe during a measurement with a 2 mm probe approach distance is shown in Figure 8.2. This four phase measurement cycle is not used on all CMMs; some do not come to a complete stop before the probe approach begins.

If a CMM is to provide valuable quality control, then its accuracy and repeatability must be greater than the tolerance specifications for the part. Repeatability is "a measure of the ability of the instrument to produce the same indication when sequentially sensing the same quantity under similar measurement conditions" [2]. Many CMM designs strive for accuracies of 8-12 μm and repeatabilities of 3-5 μm. The measurement quality of a CMM is limited by background vibration levels, environmental conditions (temperature changes, cleanliness of the environment, etc.), accuracy in the measurement equipment (encoders and part sensor), and structural deflections between the encoders and the part sensor.

The most important limitation on CMM performance depends on the design of the CMM and the operating conditions; however, structural deflection between the encoders and touch-trigger probe is almost always an important limitation. As we know from the previous chapters, input shaping tends to reduce structural deflections; therefore, input shaping should have some effect on measurement repeatability.

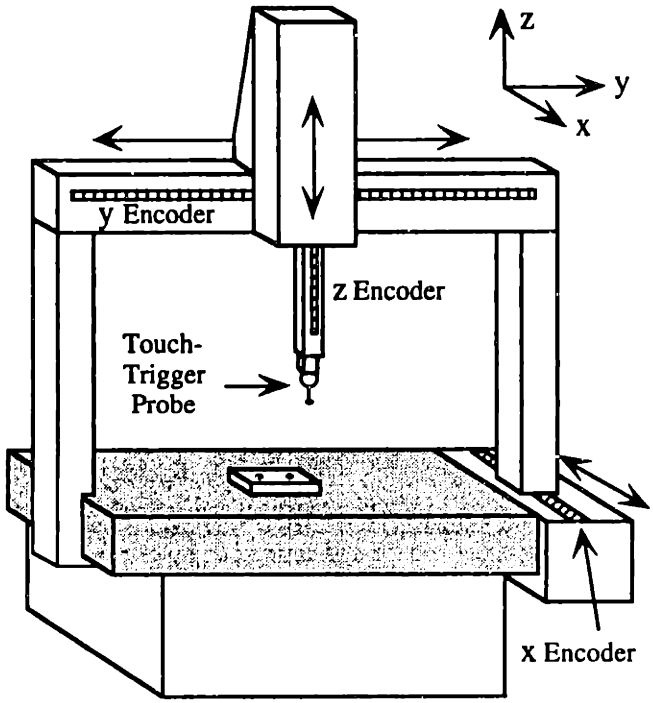

Figure 8.1: Sketch of a Moving Bridge CMM.

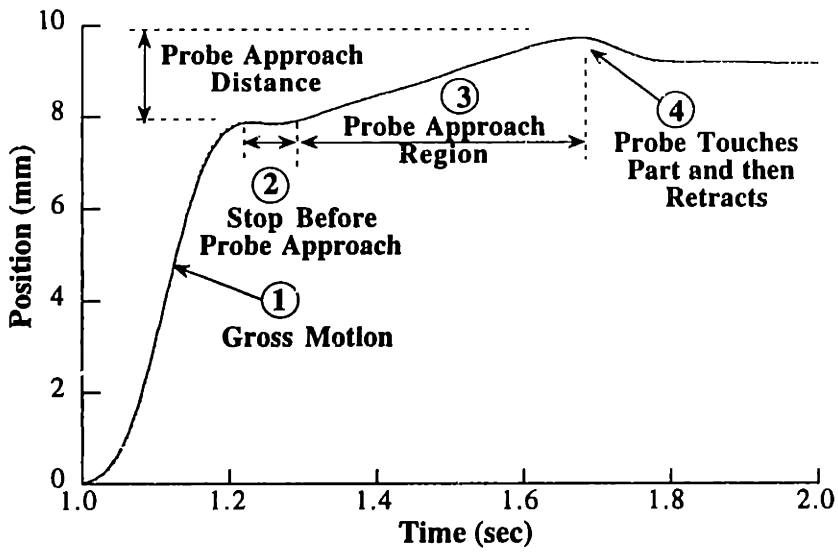

Figure 8.2: Probe Position During a Measurement of the Moving Bridge CMM.

Figure 8.3 graphically demonstrates how deflection in a CMM structure can adversely effect measurement quality. In Figure 8.3a the part width is determined from two measurements. First, the probe is moved into contact with the left side of the part. At the moment the contact is made, the position indicated by the encoders is recorded. Next, the probe is moved to the opposite side of the part and brought into contact with the right face. The two encoder positions are then

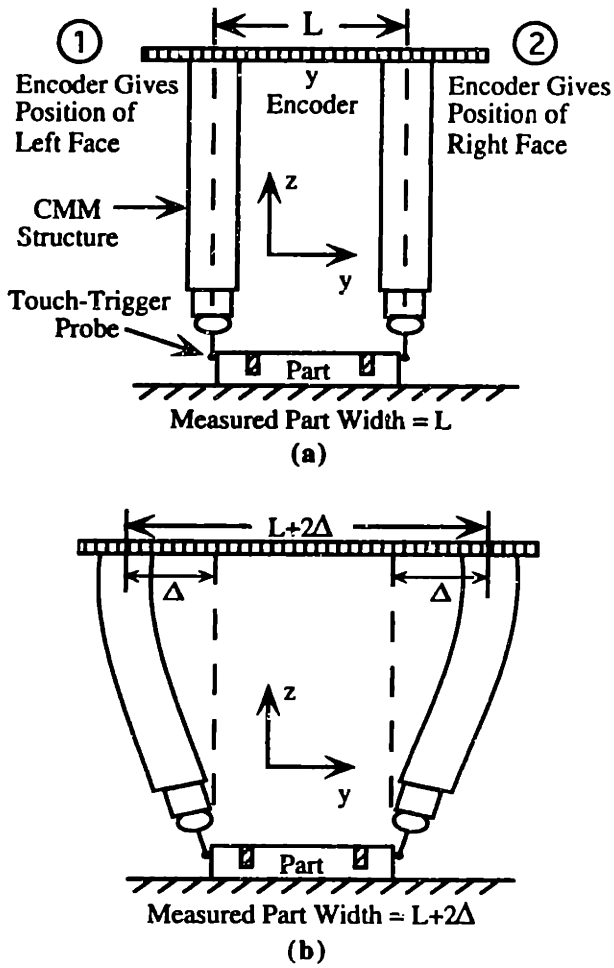

Figure 8.3: Deflections Cause Measurement Errors.

subtracted to obtain the part dimension. In Figure 8.3a the part is measured accurately because the encoders indicate the true position of the probe. In Figure 8.3b the measurement is inaccurate because the structural deflections make the encoder readings differ from the true location of the contact points. If the structure is vibrating with an amplitude of Δ during the probe approach region, then the calculated dimension can have an error as large as $\pm 2\Delta$.

Several methods exist for limiting the structural deflection of a CMM. First, the maximum acceleration and velocity can be limited. This solution is effective at reducing deflections, but it has the drawback of decreasing the throughput. Second, the mechanical structure can be modified with additional stiffening members, damping materials, or configuration changes. This solution involves many of the classic design tradeoffs such as cost versus performance and solutions may not apply across a product line containing CMMs of many sizes and accuracy levels. Alternatively, the hardware can be left unaltered and the command signals sent to the motors can be shaped so that deflections during the measurement phase are decreased.

This section will investigate the effect of input shaping on the repeatability of CMM measurements. The operation of a CMM is not the typical point-to-point application for which input shaping was designed. Rather, the important phase (the part detection) occurs while the machine is in motion and its timing occurs with some uncertainty because there is no way to know *a priori* where the part is located or how much the structure will be deflected at the time of contact.

The remainder of this section is organized as follows. First, important parameters of the moving bridge CMM measurement cycle are discussed. These parameters are used throughout the remainder of the section to describe experimental conditions. Experimental results showing the effect of input shaping on the structural deflections during the measurement will then be presented. The effect of input shaping on the measurement quality will be demonstrated with the use of repeatability studies. Finally, conclusions will be drawn from the experimental results.

8.2.1 Important Parameters of the Measurement Cycle

There are several important parameters that determine structural deflection. During the gross motion which precedes the probe approach, the acceleration and distance traveled are significant parameters. As the maximum machine acceleration is increased, the vibrations during the gross motion increase and lead to larger deflections during the probe approach.

The period of time that is spent waiting between the gross motion and the probe approach phase is also an important parameter because it allows the vibrations induced by the gross motion to settle out. As the waiting period increases, the residual structural vibration decreases, however, the throughput also decreases.

The two important parameters characterizing the probe approach phase are the probe approach velocity and probe approach distance. The probe approach velocity is usually a small percentage of the maximum velocity used during the gross motion phase. (The probe approach velocities used in our experiments were 1% of the maximum velocity.) Increasing the probe approach velocity would be desirable for throughput, but would lead to larger deflections because the acceleration to probe approach velocity would last longer. On the other hand, a longer probe approach yields better repeatability because vibrations from both the gross motion phase and the acceleration to probe approach velocity have a longer period of time to damp out before contact is made with the part. While increasing probe approach distance improves repeatability, it also degrades throughput considerably because the CMM is moving at a very low velocity during the probe approach.

8.2.2 Reducing Structural Deflections

In order to detect the micron level probe vibration that is important in CMM measurements, a laser interferometer with a resolution of three nanometers was used to measure x-direction motions

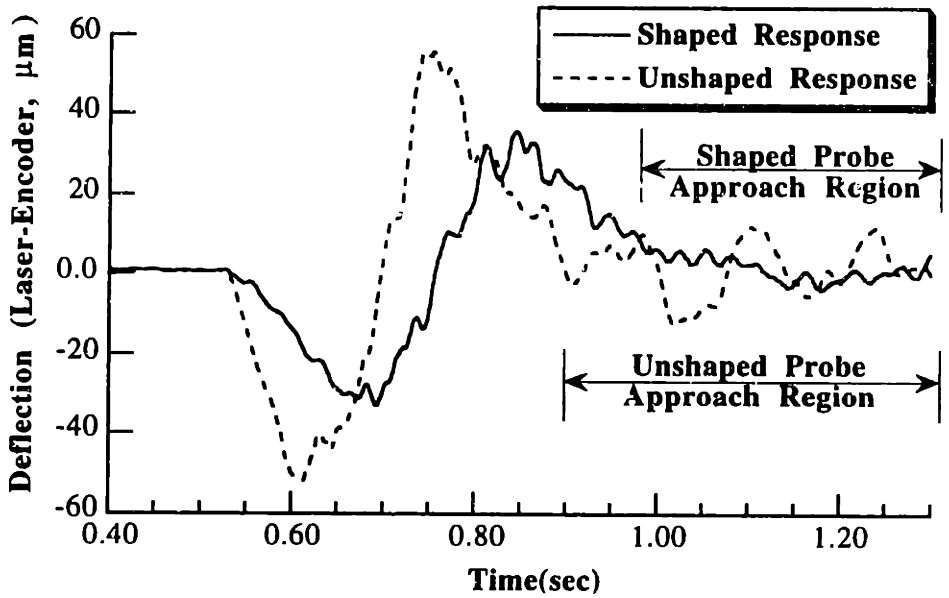

Figure 8.4: Comparison of Deflections During Shaped and Unshaped Measurement Cycles.

of the probe. The interferometer retro-reflector was mounted on the z-axis structural member in close proximity with the probe, while the laser itself was positioned on the CMM's granite base. The position measured by the encoders was subtracted from the laser measurements to obtain the deflection between the encoders and the touch-trigger probe.

Figure 8.4 compares the structural deflection using the standard CMM controller to the deflection when input shaping is added to the controller. The two curves are both from a measurement cycle with a 25 mm gross motion. Note that input shaping significantly reduces the deflections after the gross motion has been performed. However, the decrease in deflection is not without a cost; the CMM takes longer to perform the measurement. This can be seen as the increased time required to reach the probe approach region. If the CMM has available overhead in its controller, then the controller gains or maximum acceleration can be increased to offset this effect.

The large deflections during the first part of the move are caused by the accelerations during the gross motion. The amplitudes of these deflections during the gross motion are relatively unimportant, however, the amplitudes become important during the probe approach phase, when the probe contacts the part. If the deflection is not zero when the part is encountered, then the deflection leads to an inaccuracy in the measurement, as was demonstrated in Figure 8.3. The deflection amplitude during the probe approach is decreased by a factor of about three when input shaping is used.

8.2.3 Repeatability Tests

The performance of a CMM is generally measured with an array of tests described in an ANSI/ASME standard [2]. The standard includes tests for repeatability, linear displacement accuracy, streamlined artifact testing with a ball bar, rotary axis testing, and bi-directional length measurements. The data presented here will consist of several types of repeatability tests. The tests used are not exactly the same as described in the standard, however, they are representative tests that exemplify the effect of input shaping on structural deflections.

8.2.3a Constant-Parameter Repeatability Tests

For the purposes of this section, a repeatability test is the repeated measurement of a fixtured part a large number of times. After each measurement, the probe returns to its starting position. The minimum measured value is subtracted from the maximum measurement to obtain the repeatability of the CMM. Most CMMs have a repeatability of just a few microns. In addition to the repeatability, the mean value and the standard deviation of the measurements will be reported.

Figure 8.5 shows 50 individual measurements of a repeatability test using a 1 mm probe approach distance and a 20 mm gross motion. The repeatability range for the unshaped measurements is: 625.2735 mm - 625.2687 mm, which equals 4.8 μm. The mean value and standard deviation of the unshaped measurements are 625.2711 mm and 1.23×10^{-3}, respectively. Figure 8.5 also shows 50 measurements obtained with input shaping enabled. For the shaped measurements the repeatability is only 3.3 μm, the mean is 625.2670 mm, and the standard deviation is 6.7×10^{-4}. For this set of measurement parameters input shaping improves the repeatability by 1.5 μm and the standard deviation by 45%.

The improved repeatability with input shaping is a straightforward result given the deflection curves of Figure 8.4. The curves show the unshaped measurements have considerably more variation in the deflection during the probe approach region. During the course of the repeatability test, the part is contacted at slightly different locations on the deflection curve. The decrease in deflection variability with input shaping translates directly into a decrease in measurement variability (an improvement in repeatability).

The difference in mean value between the unshaped and shaped measurements warrants some additional explanation. Figure 8.4 shows that the mean value of the shaped and unshaped deflection curves are different over any small segment. For example, the mean value of the unshaped deflection shown in Figure 8.4 between 1.00 and 1.05 seconds is -9.00 μm, while the mean value of the shaped deflection is 4.47 μm during the same time period. Therefore, we can reason that the difference in the mean values of the measurements results from the difference in the mean values of the structural deflection.

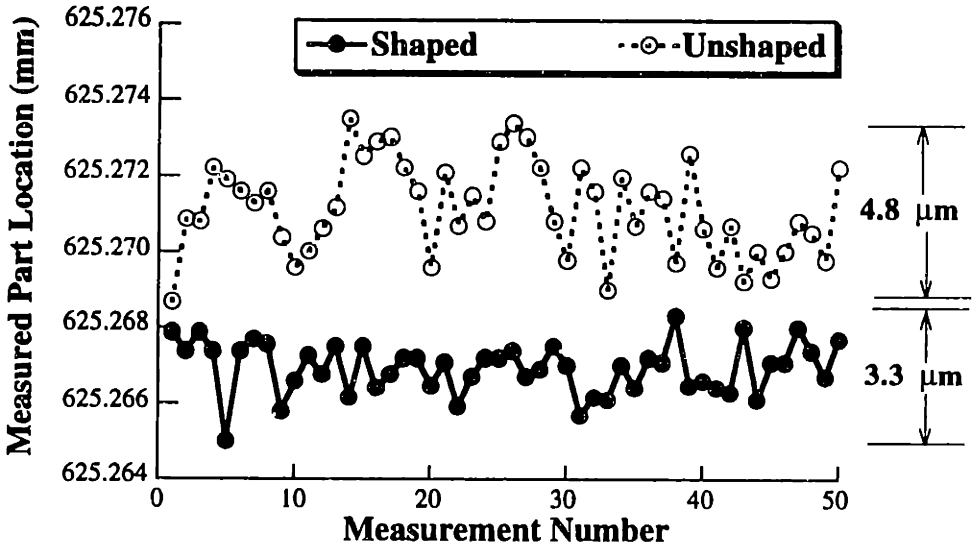

Figure 8.5: Measurements During a 50 Point Repeatability Test (1 mm Probe Approach Distance, 20 mm Gross Motion).

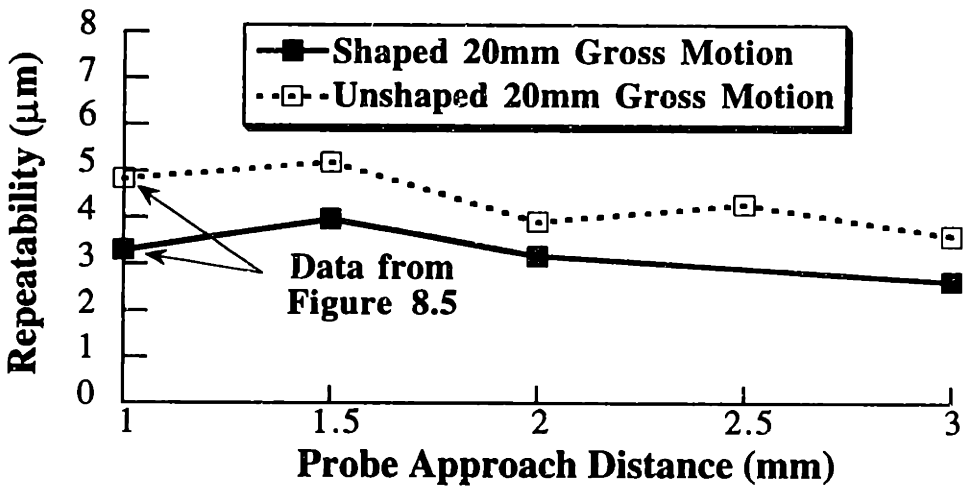

Figure 8.6: Repeatability for Several Probe Approach Distances.

To ensure that the benefit of input shaping is not limited to this particular set of parameters, repeatability tests were conducted with several probe approach and gross motion distances. Figure 8.6 shows the repeatability as a function of probe approach distance for measurements with a 20 mm gross motion. Each data point in Figure 8.6 represents the range of measurements obtained from a 50 point repeatability test with the given probe approach distance and a 20 mm gross motion. In general, repeatability improves with increasing probe approach distance. Figure 8.6 also demonstrates that input shaping improves repeatability over a wide range of probe approach distances. Figure 8.7 shows that input shaping also improves repeatability when a 10 or 15 mm gross motion is used. Note that as the probe approach distance increases, the benefit of input shaping over the standard controller decreases.

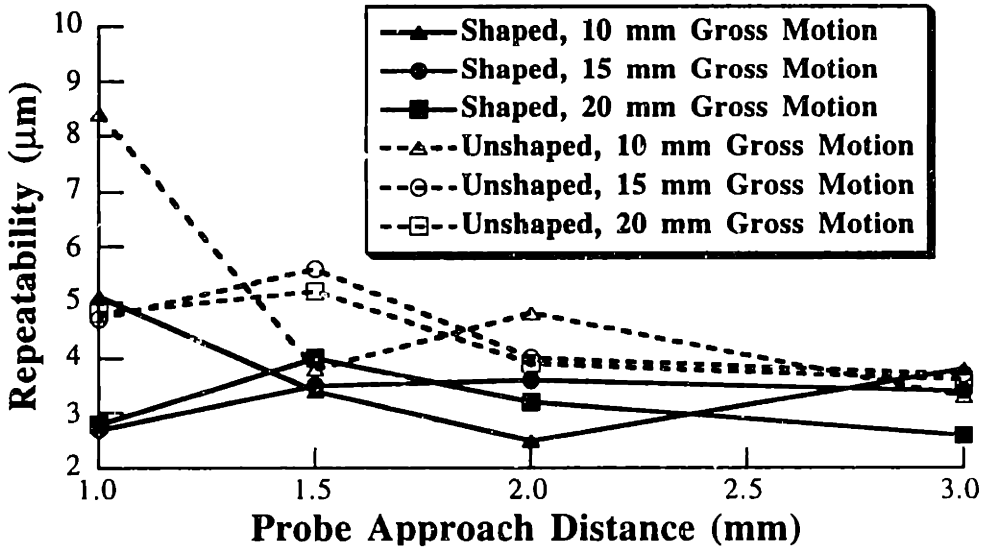

Figure 8.7: Repeatability with 10, 15, and 20 mm Gross Motion.

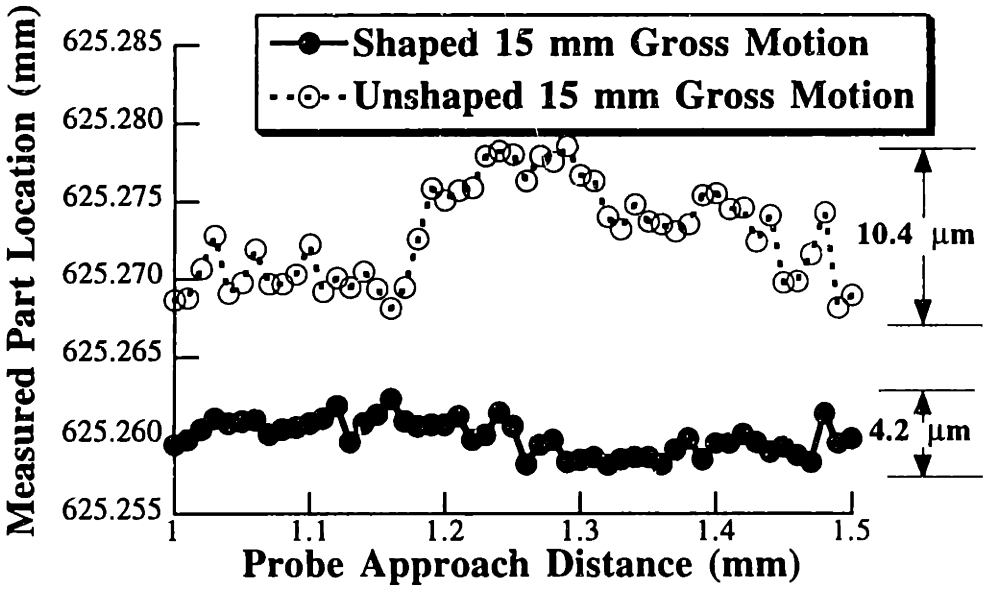

Figure 8.8: Measurements During a Variable Probe Approach Distance Repeatability Test.

8.2.3b Variable-Probe-Approach-Distance Repeatability Tests

For the repeatability tests summarized in Figure 8.7, the probe approach distance and gross motion were held constant throughout the 50 measurements. These types of repeatability tests are very valuable for evaluating CMM performance when parts are fixtured in the workspace consistently and when part geometries do not very greatly. However, if consistent part fixturing is not used, then probe approach distances could vary from part to part. Also, "Many machines/probe systems exhibit vastly different characteristics depending on the probe approach distance and the probe approach rate" [2].

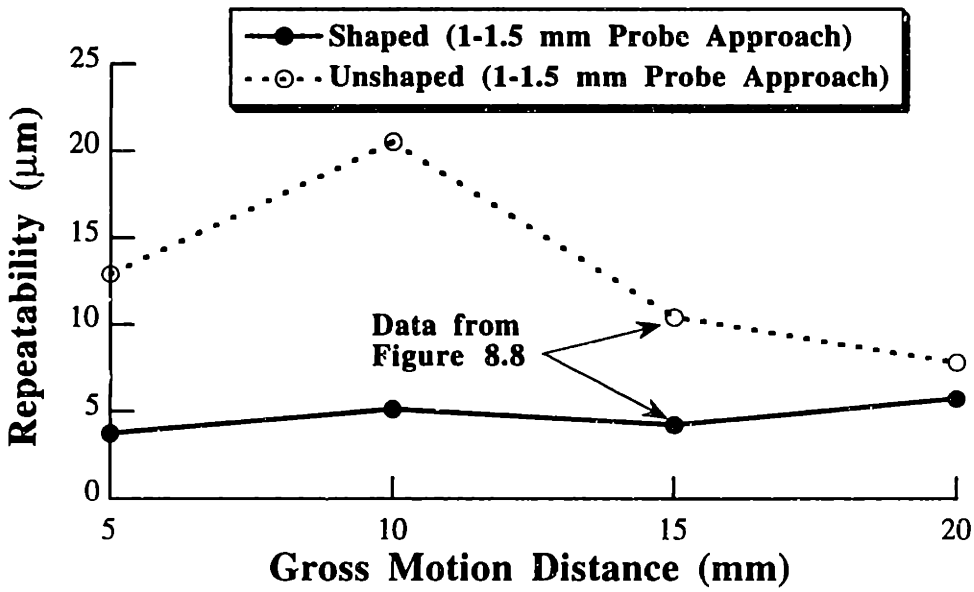

Figure 8.9: Variable Probe Approach Distance Repeatability.

To evaluate the CMM performance under conditions of varying probe approach distances, tests were performed with a probe approach distance that changed for each measurement in the repeatability test. For the first measurement of the repeatability test the probe approach distance was set at 1 mm. During each subsequent measure, the probe approach distance was increased by 0.01 mm until the probe approach distance reached 1.5 mm. Each of the measurements composing this 51 point repeatability test are shown in Figure 8.8 for a gross motion of 15 mm. The variable-probe-approach-distance repeatability is 10.4 µm without shaping and 4.2 µm with shaping. Furthermore, the standard deviation of the measurements is decreased from 3.13×10^{-3} to 1.1×10^{-3} when input shaping is used. This improvement with input shaping is much larger than the improvement revealed by the fixed probe approach repeatability tests shown in Figure 8.7.

The large improvement with shaping is not restricted to a gross motion of 15 mm; Figure 8.9 shows significant improvement for gross motions ranging from 5 to 20 mm. Furthermore, Figure 8.10 shows that shaping improves repeatability when the test covers the range of probe approach distances of 1.5-2.0 mm and 2.0-2.5 mm. Figure 8.10 also shows a clear trend in repeatability with input shaping; as gross motion increases, repeatability slowly degrades. The repeatability without shaping is not only larger, it is more widely varying.

8.2.3c Variable-Gross-Motion Repeatability Tests

In another variation on the repeatability test, the gross motion distance can be varied instead of the probe approach distance. Figure 8.11 shows the 51 measurements of a repeatability test when the gross motion was varied from 10-12 mm at a step of 0.04 mm and the probe approach distance

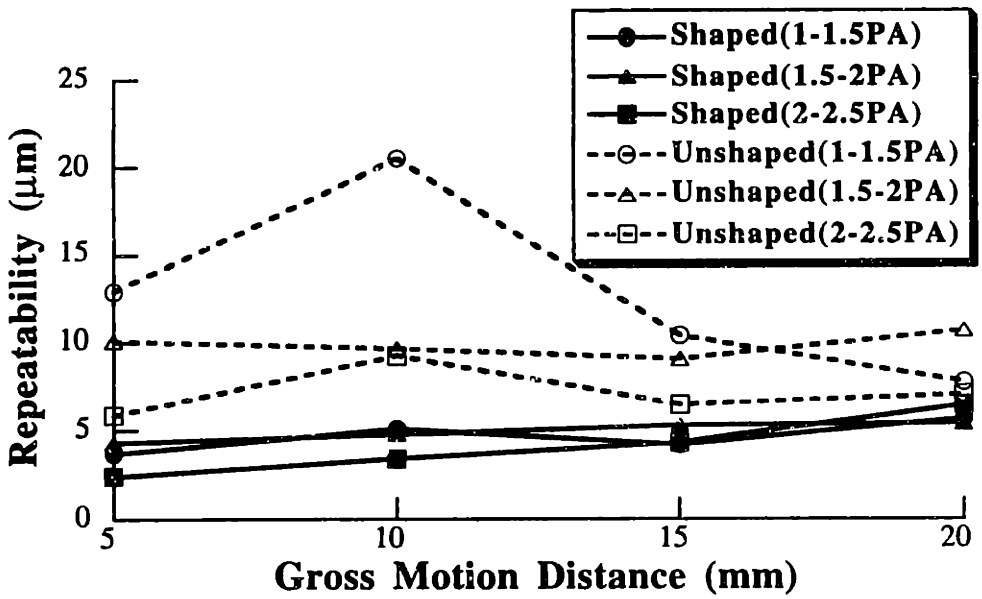

Figure 8.10: Variable Probe Approach Distance Repeatability for Several Ranges of Probe Approach Distances.

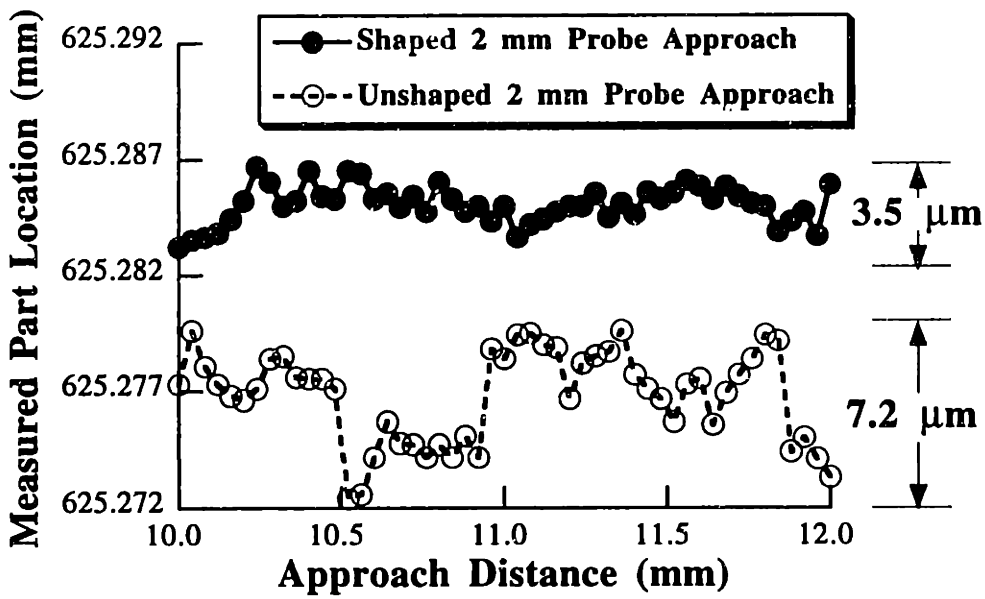

Figure 8.11: Measurements During a Variable Gross Motion Repeatability Test.

was held constant at 2 mm. For this variable-gross-motion repeatability test the input shaping improved the repeatability from 7.2 μm to 3.5 μm and the standard deviation from 0.00197 to 0.00082.

Figure 8.12 shows that shaping improves the 10-12 mm variable gross motion repeatability over a range of probe approach distances. Figure 8.13 demonstrates that improvement in repeatability also occurs for gross motions varying from 5-7 mm and from 15-17 mm. Once again, the

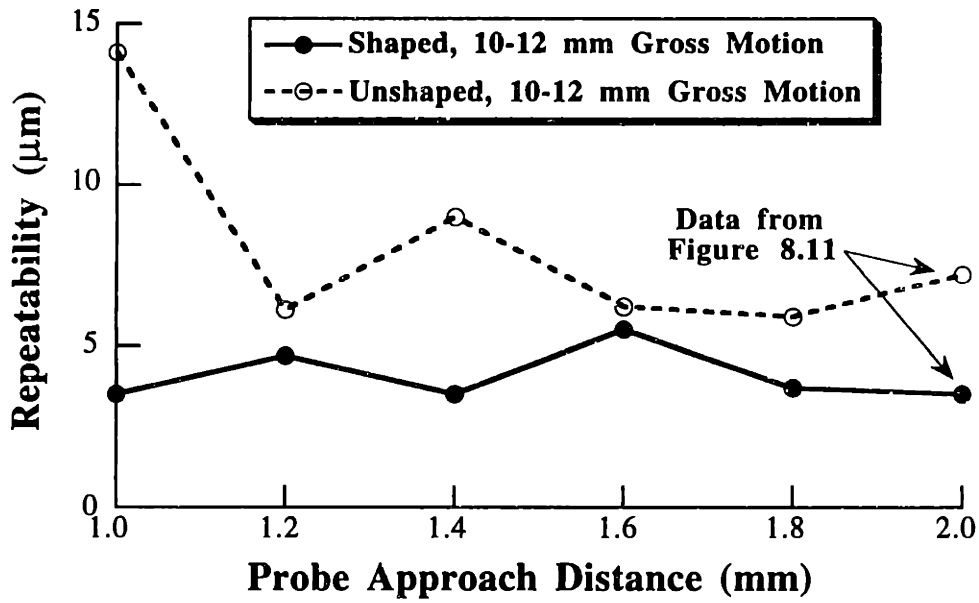

Figure 8.12: Shaped and Unshaped Variable Gross Motion Repeatability.

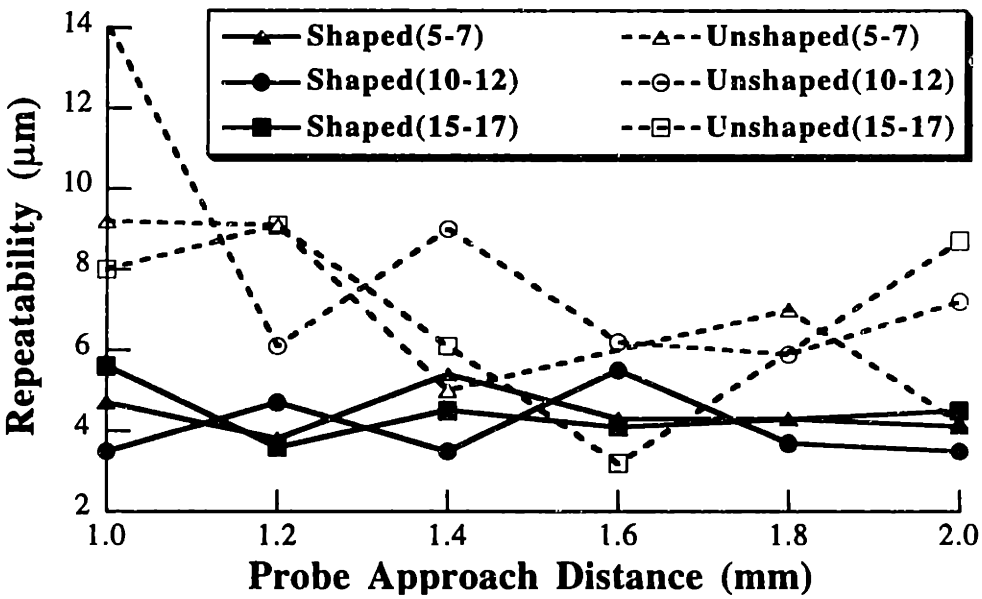

Figure 8.13: Variable Gross Motion Repeatability for Several Ranges of Gross Motion Distances.

repeatability with input shaping is consistent over a wide range of parameters, while the unshaped measurement repeatability is considerably larger and more unpredictable.

The statistical data for the three tests discussed in detail (Figures 8.5, 8.8, and 8.11) are summarized in Table 8.1.

Table 8.1: Summary of Repeatability Tests.

Repeatability Test	Unshaped		Shaped	
	Repeat	Std	Repeat	Std
Fixed Probe Approach (1mm) and Gross Motion (20 mm)	4.8	0.00123	3.3	0.00067
Variable Probe Approach (1-1.5mm) and Fixed Gross Motion (15 mm)	10.4	0.00313	4.2	0.00110
Variable Gross Motion (10-12 mm) and Fixed Probe Approach (2 mm)	7.2	0.00197	3.5	0.0082

8.2.4 Summary of CMM Measurement Repeatability

Deflections in the structural components of a coordinate measuring machine introduce error into the measurements because the CMM encoders do not indicate the true position of the part sensor. Experiments on a moving bridge CMM revealed that input shaping decreases the structural deflections during the critical phase when the sensor is brought into contact with the part. The decrease in deflection translates directly into improved measurement repeatability.

8.3 Trajectory Following

The effectiveness of input shaping for reducing residual vibration in point-to-point motions has been well established. However, very little work has been done to determine how input shaping affects trajectory following. Experiments have shown a five-bar-linkage manipulator follows a clover pattern better with shaping than without shaping [99]. Shaping has also shown promise for tracking control of flexible two-link manipulators [7]. The shaping process alters the desired trajectory, so it seems possible that input shaping could degrade trajectory following. While this may be true for temporal trajectories, trajectories where the location as a function of time is important, this section will show that it is untrue for spatial trajectories, where only the shape of the trajectory is important.

For this investigation we studied a linear two-mode system and gave it simple, yet representative trajectories to follow. The model, shown in Figure 8.14, represents a system with two orthogonal flexible modes. The flexibility and damping of the controller and structure have been lumped together into a single spring and damper for each mode. The inputs to the system are x and y position commands. This model is representative of gantry robots, coordinate measuring machines, and XY stages. Experiments with an XY stage are used to verify the simulation results.

The next two subsections describe how input shaping affects the response to circular and square trajectory commands. Sections 8.3.3 and 8.3.4 then present two simple methods for altering the unshaped command to better utilize input shaping. In Section 8.3.5, experimental results are presented and compared to simulation results.

8.3.1 Circular Trajectories

The response of the model to unshaped and shaped constant-velocity unit-circle inputs was simulated for a large range of modeling parameters. The response without input shaping is a function of the commanded speed around the circle, the ratio of the two vibration modes, the damping, and the initial departure angle relative to the lower mode (for this section the low mode will always be in the x direction). The response to shaped circular inputs depends on the above variables and on the type of input shaper selected.

Figure 8.15 compares the unshaped and ZVD shaped responses for the case where the frequencies are $f_x = f_y = 1$ Hz, the damping ratios are $\zeta_x = \zeta_y = 0.05$, and the unit-circle trajectory command has a duration of 10 seconds. The circle is initiated in the negative x direction at location (0, 0). By examining Figure 8.15 we can say, qualitatively, that the shaped response is closer to the desired trajectory than the unshaped response. Note, however, that the shaped response is not a perfect circle.

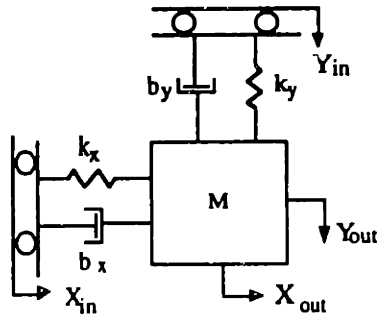

Figure 8.14: Two-Mode Model of a Flexible System Under PD Control.

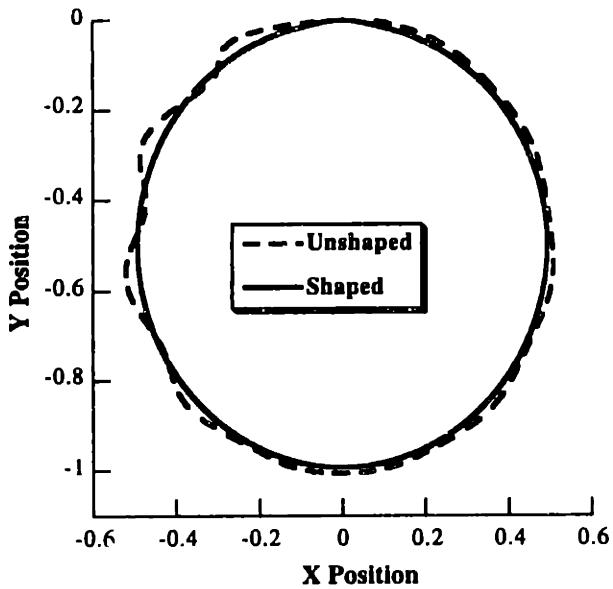

Figure 8.15: Comparison of ZVD Shaped and Unshaped Responses to a Unit-Circle Input.

We can compare the responses quantitatively by examining the maximum and minimum values of the response radius, the envelope enclosing the radius, and the mean and standard deviation of the error. This comparison is shown in Table 8.2 along with the performance measures for the desired unit-circle response. The shaped response is substantially closer to the desired performance measures in every category except mean value. The mean value results are understandable because the unshaped response oscillates about the desired radius, while the shaped response tracks almost the entire circle with a nearly constant, but slightly smaller than desired radius. Input shaping leads to a smaller than commanded radius because the shaped inputs lag the unshaped inputs. We will address this issue in a subsequent section.

Input shaping improves circular trajectory following over a large range of ζ, r (frequency ratio), and command speeds. To display this data, we combine f_x and the command speed into one unit called vibration cycles/circle. This measure tells us how fast the system is commanded relative to

Table 8.2: Performance Measures for an Unshaped, ZVD Shaped, and Desired Unit Circle Response.

Radius of Response	Unshaped	ZVD Shaped	Desired
Maximum	0.5313	0.5000	0.5000
Minimum	0.4804	0.4927	0.5000
Envelope	0.0509	0.0073	0
Mean	0.5052	0.4935	0.5000
Std	0.0091	0.0020	0

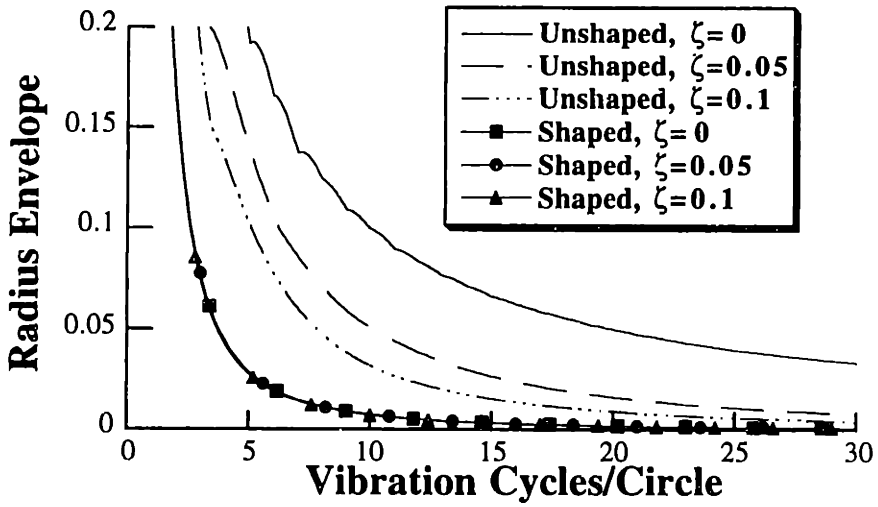

Figure 8.16: Unshaped and ZVD Shaped Radius Envelopes (r = 1). Note: Values with Shaping are Nearly Independent of ζ.

its lowest natural frequency. For the responses shown in Figure 8.15, the command speed was 10 cycles/circle because the frequency was 1 Hz and the desired input lasted for 10 seconds. As this measure is decreased, the system is required to move more rapidly, so trajectory following worsens as the value of cycles/circle is lowered. By displaying results as a function of cycles/circle, the dependence on the actual numerical values of the system frequencies is eliminated.

Figure 8.16 compares the ZVD shaped and unshaped radius envelope as a function of cycles/circle and ζ for the case of r = 1. For every command speed and damping ratio, the envelope on the shaped response is smaller than that for the unshaped response. Furthermore, the performance is no longer a function of ζ when input shaping is used. Although Figure 8.16 only displays data for r = 1, the benefit from shaping is greatest in cases with low damping for all values of the frequency ratio.

For all of the results presented so far, the unit circle command has been initiated in the negative x direction, which is parallel to the low mode of our model. If the angle of departure is varied relative to the x direction, the trajectory following performance will also vary. Figure 8.17 shows

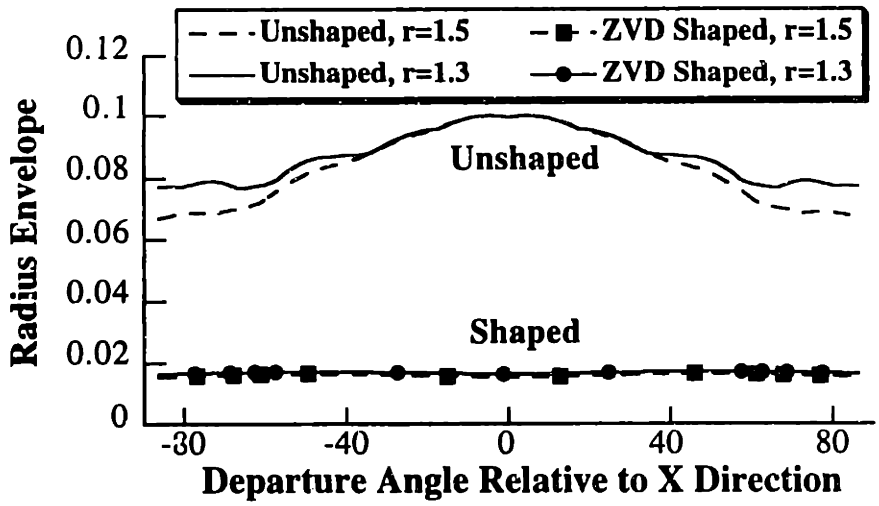

Figure 8.17: Radius Envelope vs. Departure Angle (Cycles/Circle = 10).

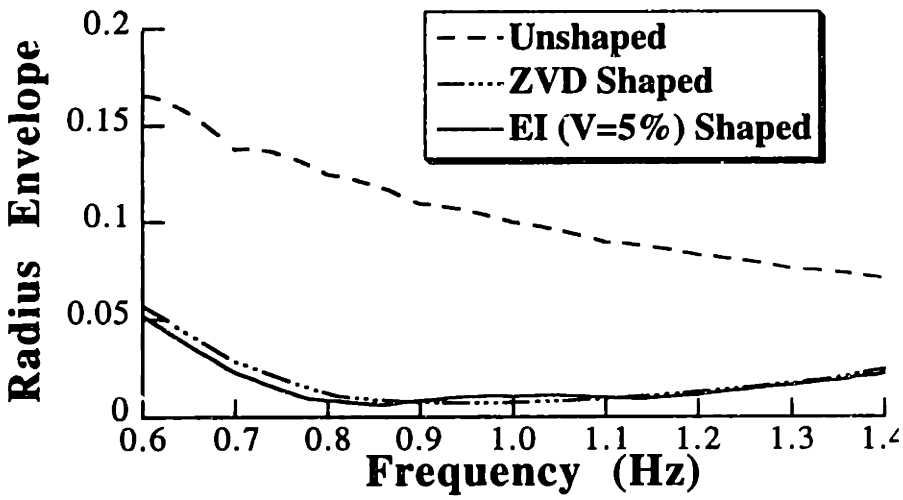

Figure 8.18: Response Radius Envelope as System Frequency Varies.

the radius envelope for the cases of r = 1.5 and 1.3 when cycles/circle = 10, and $\zeta_x = \zeta_y = 0$. For every value of the departure angle, the envelope with shaping is at least four times smaller than without shaping. Figure 8.17 also reveals that it is a poor idea to start the circle in the direction of the low mode when shaping is not used. This makes sense, as the start-up transient excites the low mode instead of the high mode which has a smaller vibration amplitude. With input shaping it makes little difference what departure angle is used to commence the circular trajectory.

To evaluate shaping circular trajectories in the presence of modeling errors, we plot the trajectory performance measures over a range of possible system frequencies that differ from the modeling frequency. Unshaped and shaped inputs were designed for the case of $f_x = 1$ Hz, r = 1, $\zeta_x = \zeta_y = 0$, and cycles/circle = 10. Figure 8.18 shows the response radius envelope for these inputs when the simulation frequency is varied over the range of $0.6 \leq f_x \leq 1.4$ Hz. Figure 8.18

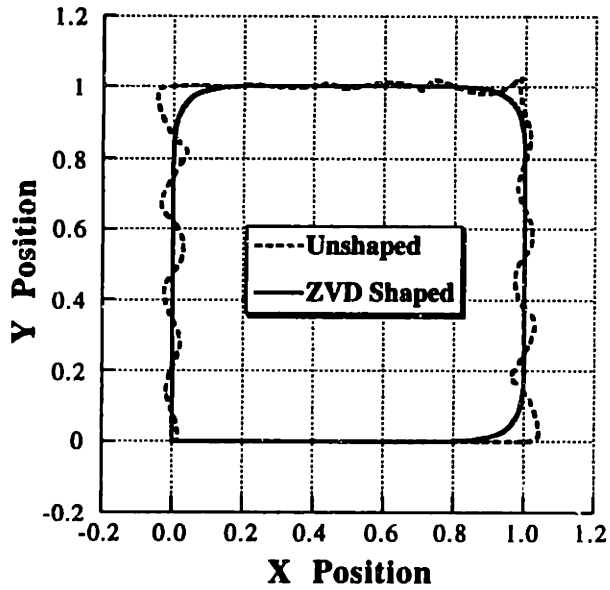

Figure 8.19: Comparison of ZVD Shaped and Unshaped Responses to a Unit-Square Input.

shows that even when the actual frequency deviates significantly from the modeling frequency, the performance with shaping is still much better than without shaping. When the frequency is 40% less than expected, the performance measure is 3.2 times better with input shaping than without. With a frequency 40% higher than expected, the performance improves by a factor of 2.9. (When the model is exact, shaping gives nearly a 10 fold improvement.) If we compare the circular trajectory sensitivity curve of Figure 8.18 with the sensitivity curves of Figure 1.13, we see a similarity; the ZVD shaper performs better than the EI shaper at frequencies very close to the modeling frequency, but the EI shaper is better at all other frequencies.

8.3.2 Square Trajectories

The results from our simulations with circular trajectories indicate input shaping is often beneficial for following smooth spatial trajectories. The question of how shaping works with trajectories containing rapid directional changes remains unanswered. For this reason, we simulated the response of the model to constant-velocity square trajectory commands.

Figure 8.19 compares the unshaped and ZVD shaped responses for the case of r = 1.5, $\zeta_x = \zeta_y$ = 0.05, and cycles/square = 15. The square is initiated in the +x direction at location (0,0). Figure 8.19 reveals that the response with shaping is much closer to a square than the unshaped response. To compare the results quantitatively, we calculated the distance from the position to the desired square at each time step of the simulation. Table 8.3 compares the maximum, mean, and standard deviation of the square tracking error for the shaped and unshaped cases. The shaped response

Table 8.3: Performance Measures for an Unshaped, ZVD Shaped, and Desired Unit-Square Response.

Tracking Error	Unshaped	ZVD Shaped	Desired
Maximum	0.0461	0.0413	0
Mean	0.0106	0.0034	0
Std	0.0113	0.0083	0

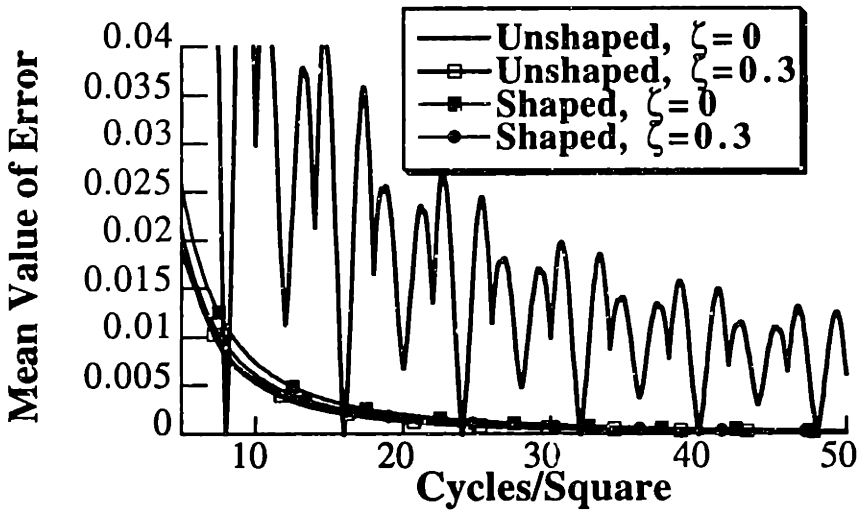

Figure 8.20: ZVD Shaped and Unshaped Mean Error as a Function of Cycles/Square and ζ.

error has a much lower mean and standard deviation; however, the maximum deviation is 90% of the unshaped deviation. The maximum shaped tracking errors occur at the corners of the square, which are rounded by the input shaping process.

Figure 8.20 compares the ZVD shaped and unshaped mean tracking error as a function of cycles/square and ζ for the case of r = 1.5. The performance increase from input shaping is most significant at low damping values. If the system has a high damping ratio, the unshaped tracking error can be smaller than the shaped tracking error; note the curves for $\zeta = 0.3$.

The square trajectory following performance will vary with modeling errors just as the circular tracking performance varied. Unshaped and shaped inputs were designed for the case of $f_x = 1$ Hz, r = 1, $\zeta_x = \zeta_y = 0$, and cycles/square = 15. Figure 8.21 shows the mean value of the square tracking error with these inputs over the range of $0.6 \leq f_x \leq 1.4$ Hz. The square tracking performance with shaping is very insensitive to modeling errors.

8.3.3 Improving Shaped Circular Responses

Our simulation results indicate that input shaping improves trajectory following in many cases; however, the shaped responses are never exactly the desired trajectories. The primary problem

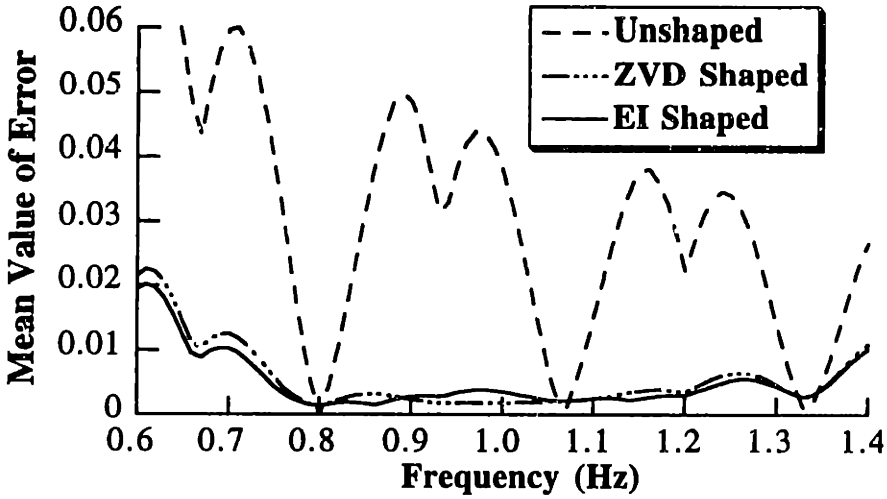

Figure 8.21: Mean of Square Tracking Error as System Frequency Varies.

with shaped circular trajectories is the smaller-than-desired radius around most of the circle. We can reduce this problem by using an unshaped circle command that has a radius larger than desired.

If the radius is chosen correctly, the shaped response will track very closely the correct radius at all times except the initial and final L seconds, where L is the length of the shaper. If the application for trajectory following contains a process that can be turned on and off, such as painting or cutting, then the transient deviation from the desired radius can also be eliminated by using an unshaped circular command that has a duration of:

$$CC*T + L, \tag{8.1}$$

where CC is the desired cycles/circle for the low mode (CC has units of cycles), $T = 1/f_x$ is the period of the low mode (sec/cycle), and L is the shaper length (sec). The shaped command is initiated, and then after L seconds the process is started. At L seconds from the end of the shaped command, the process is stopped. For $r = 1$, this procedure yields a circular response during the process. For $r \neq 1$ there will exist a small oscillation in the radius during the process-on portion of the trajectory. Even with this small oscillation, the shaped trajectory following performance is far better than the unshaped performance.

8.3.4 Improving Shaped Square Responses

The primary problem with the shaped response to square inputs is the rounding of the corners. The rounding occurs because there are periods near the corners when the shaped x and y commands are changing at the same time. To eliminate the rounding, we can use a system command signal that has no overlap in its shaped x and y components. The requisite unshaped command signal has a delay equal to one shaper length at each of the three corners during the trajectory (the fourth corner of the square does not have to be navigated to complete the square).

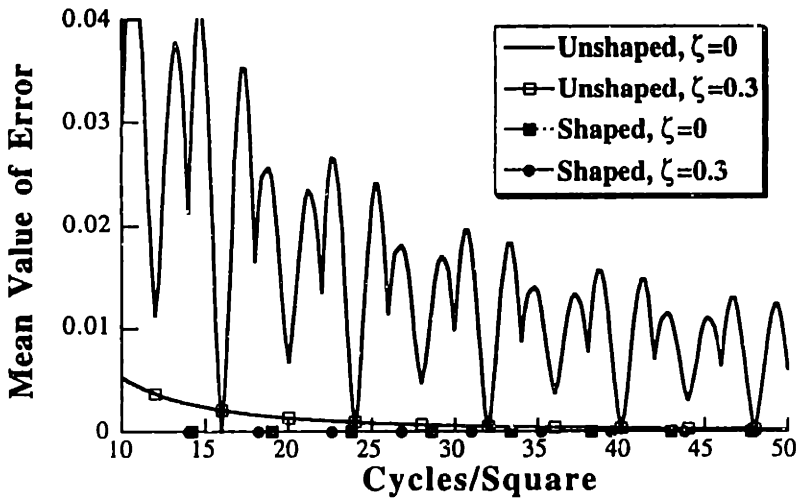

Figure 8.22: ZVD Corner-Delayed Shaped and Unshaped Mean Error as a Function of Cycles/Square and ζ (r = 1.5, Square Initiated in the +x Direction).

For a departure angle of 0°, this procedure results in an exact square response. When the departure angle is not zero and $r \neq 1$, a small amount of deviation from a square will result. The deviation does not occur at the corners; rather, it occurs during the transient acceleration and deceleration portions of each side of the square. The response deviates from a square because the flexibility of the system that is excited during the transients is not parallel to the side of the square being traversed when the departure angle is non-zero.

The above procedure for improving square trajectories results in a command signal that is four shaper lengths longer than the original command (three shaper lengths at the corners + one shaper length from the convolution). While we are not concerned here with temporal trajectories, we want to make a fair comparison between unshaped trajectories and the modified trajectories described above. Obviously, when a flexible system is given a much longer period of time to traverse a trajectory, it can follow the trajectory better. The improvement in trajectory following comes with the cost of decreased throughput.

To make a fair comparison in this study (at the same level of throughput), the command is shortened by four shaper lengths before the delays are inserted at the corners and the shaping is performed. When this is done, the unshaped and shaped commands will have the same time duration. Figure 8.22 compares the square tracking errors of the unshaped and corner-delayed shaped commands. The total command length is still measured in terms of cycles/square. Figure 8.22 confirms that corner-delayed shaped commands perform better than unshaped commands for all parameter values. Note that the curves indicating the deviation with shaping are zero for all cases.

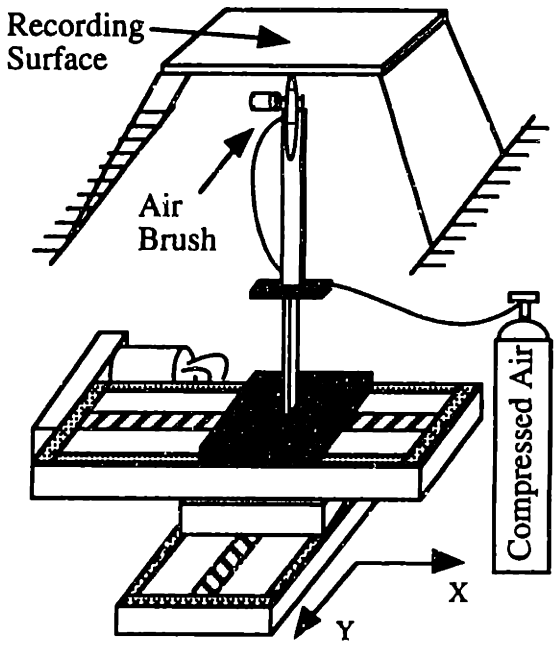

Figure 8.23: Experimental Setup.

8.3.5 Experimental Results

To test our simulation results, a flexible structure with orthogonal decoupled modes was constructed by mounting a two-stage beam vertically to an Aerotech XY stage moving in a horizontal plane. (See Figure 8.23). The first section of the beam consisted of a 9x1x1/8in. steel beam mounted with its flexibility parallel to the x direction. The second section was a 12x3/4x1/16in. steel beam attached to the end of the first section, but mounted with its flexibility in the y direction. The XY stage was driven by Aerotech DS16020 amplifiers. The command signal was sent to the amplifiers by a Macintosh Quadra 700 running a PD controller at 500 Hz.

To record endpoint position, a Paasche compressed-air paint brush was mounted vertically to the end of the flexible structure. A flat plane with recording paper attached was suspended above the airbrush. The air flow valve on the paint brush was fixed open so that the flow of paint could be controlled by a remote valve. The resulting system had uncoupled modes at 4.5 Hz and 6.2 Hz, for a frequency ratio of approximately 1.4.

Experiments were conducted by manually turning on the flow of air to the paint brush, commencing the desired trajectory, and then shutting off the flow of air at the end of the move. Figure 8.24 shows the trajectory when a 1.5 inch radius circular trajectory was commanded. (The circle may not may appear exactly 3 inches in diameter due to scaling of the figure after digitization of the painting.) The trajectory was initiated to the left, starting at the top of the circle. The inexact nature of the air flow control is revealed as excess paint at the start of the trajectory (top center).

A plot of the response predicted by our simulation is shown inside the experimental data. The

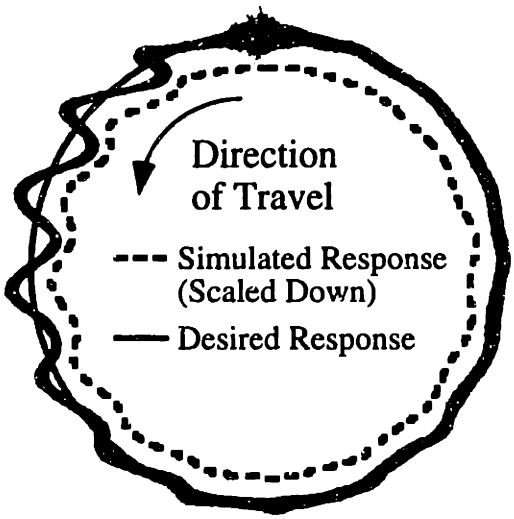

Figure 8.24: Unshaped Response to Circular Trajectory.

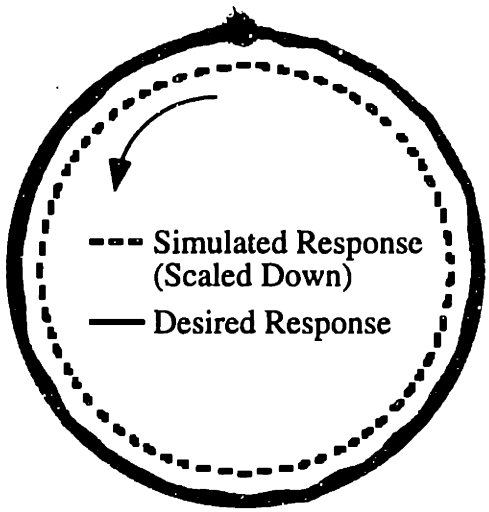

Figure 8.25: EI Shaped Response to Circular Trajectory.

simulation results have been scaled down only for the purposes of comparison; plotting the simulation results directly on top of the experimental results and desired trajectory makes the figure indecipherable.

Figure 8.25 shows the painted circle when an EI shaper is used to modify the command signal. The shaping process greatly improves the trajectory following. Once again the simulated response is plotted inside the experimental response for comparison. Comparing Figures 8.24 and 8.25, we see that input shaping performs as well on real hardware as predicted by our model. Even though our simple simulation does not predict the exact amplitude values of our hardware data, the relative improvement with input shaping is verified by the experimental results.

To test the effect of modeling errors, additional mass was added to the endpoint of the flexible

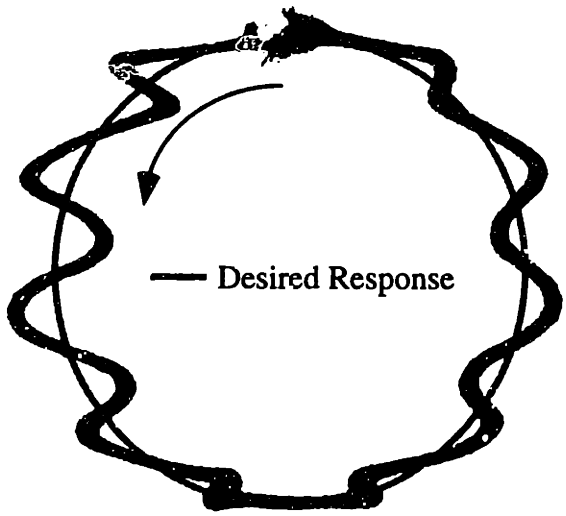

Figure 8.26: Unshaped Circular Response with Additional Endpoint Mass.

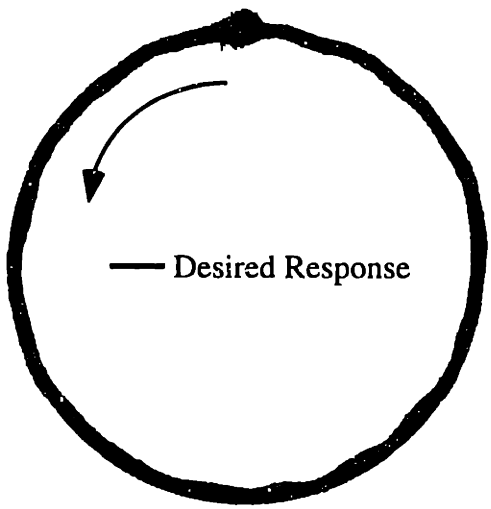

Figure 8.27: EI Shaped Circular Response with Additional Endpoint Mass. (Modeling Errors of 30% for the Low Mode and 16% for the High Mode.)

beam. The frequencies were lowered to 3.1 Hz and 5.2 Hz, changes of 30% and 16%, respectively. The unshaped response is shown in Figure 8.26. The vibration amplitude is noticeably larger with the additional mass. The response with the EI shaper designed for the original system is shown in Figure 8.27. Even with very large modeling errors, the shaped response is much closer to a circle than the original unshaped response of Figure 8.24.

Tests similar to those described above were conducted with 3in x 3in square trajectories. Figure 8.28 shows the recorded trajectory when an unshaped square with delays at each corner is commanded. Delays were added at each corner so that the total move length would be equal to the corresponding shaped move. Figure 8.29 shows the response for a 3in x 3in EI shaped square.

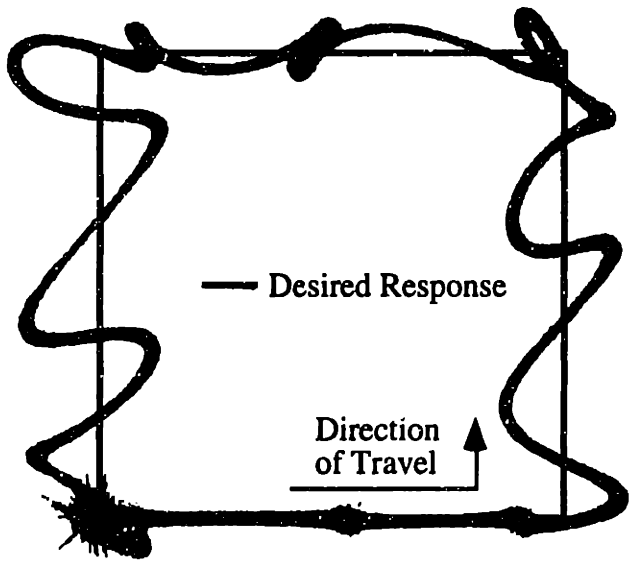

Figure 8.28: Unshaped Response to Square Trajectory.

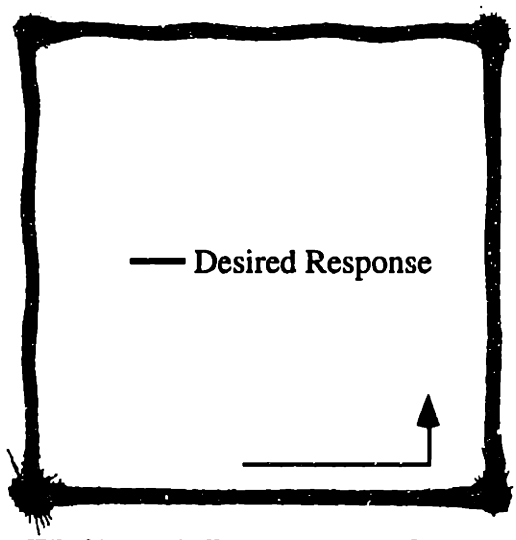

Figure 8.29: EI Shaped Response to Square Trajectory.

8.3.6 Effects of Shaping on Complicated Trajectories

The previous subsections have demonstrated the usefulness of using input shaping on square and circular trajectories. Most applications will involve a trajectory that is more complicated than a square or a circle. It is difficult to predict exactly how input shaping will affect the following of a complicated trajectory. However, the qualitative effects produced by input shaping do apply to complicated trajectories. As an example, Figure 8.30 shows the response of a lightly damped system when it attempts to track a trajectory in the shape of an "M".[26] Figure 8.31 shows the

[26] The MATLAB code used to perform these simulations was provided by Thomas Chuang [116].

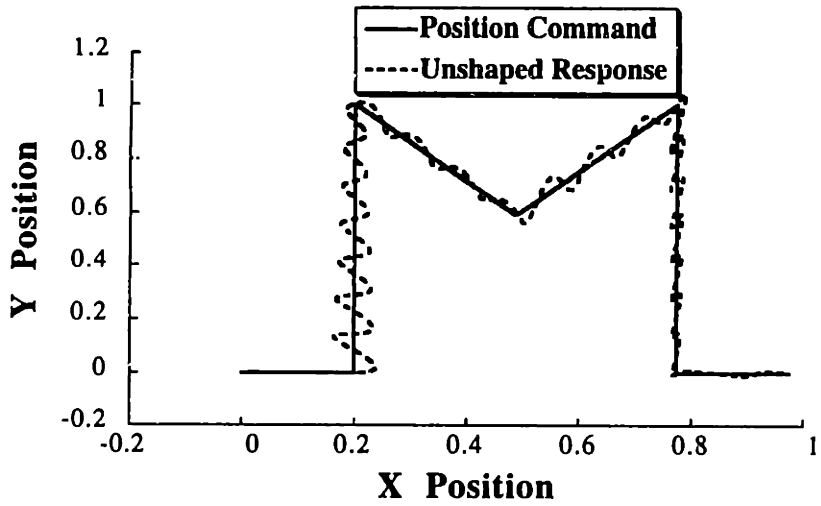

Figure 8.30: Example Response to an "M" Trajectory Command.

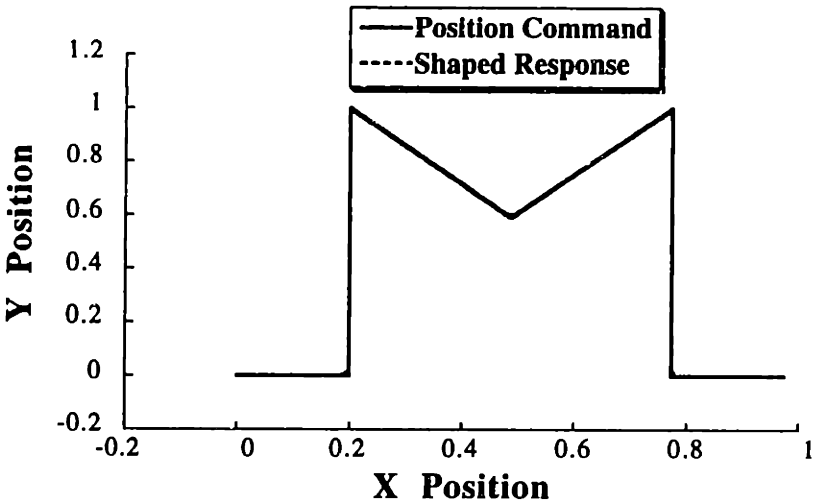

Figure 8.31: Input Shaped Response to an "M" Trajectory Command.

response of the same system when the commands are shaped with a ZV shaper. The shaping allows for better trajectory tracking, but once again the sharp corners in the trajectory have been rounded. Delays could be introduced at the corners to further improve trajectory following.

8.3.7 Summary of Trajectory Following Investigation

Input shaping was shown to improve the tracking of two-dimensional circular and square trajectories for nearly all values of command speed, trajectory departure angle, damping, and frequency ratio. By making simple adjustments to the unshaped command signal, the performance with shaping is superior to that without shaping for all parameter values. Experiments with an XY positioning stage demonstrated that input shaping improves the tracking of circular and square trajectories, even in the present of large modeling errors.

8.4 Obstacle Avoidance

The robotic manipulation of suspended payloads can be a very challenging task, especially in a cluttered work environment. The flexibility of the suspended payload introduces two main problems for the control system, the residual oscillations and the transient sway. Suspended payloads make the task of obstacle avoidance more difficult because the payload sway may cause considerable deviation from the intended path.

Gantry cranes, like the one sketched in Figure 8.32, are an illustrative case for such problems. Experienced crane operators attempt to eliminate the residual sway by causing a deceleration oscillation that cancels the oscillation induced during acceleration. In hardened industrial settings, such as shipping docks, the operator may even brush the payload against obstacles to damp out oscillations.

Transient sway is a more challenging problem for a human operator. The difficulty of this problem is not surprising because a crane cannot be moved at all without causing some amount of transient sway. As an example, Figure 8.33 shows the path of an xy gantry crane trolley and payload through a cluttered environment. When no attempt is made to control the payload sway, the payload may collide with obstacles even when the xy position of the overhead trolley is far from the obstacles.

The majority of work done on controlling suspended payloads has concentrated on eliminating residual oscillations. If a computer controller is utilized and cable swing is considered in the control design, the time-optimal commands which results in zero residual vibration can be generated [5, 36]. Load hoisting during the slew increases the difficulty of generating the optimal commands because the system frequency is time-varying. Optimal controls based on nonlinear models are considerably more difficult to generate [70]. One method for developing optimal controls divides the motion into five fundamental sections. The optimal control for each section is then derived and pieced together by satisfying boundary conditions [91]. Even when optimal commands can be generated, implementation is often impractical because the boundary conditions (the move length) must be known at the beginning of the move. When feedback is available, adaptive controllers and combinations of open and closed-loop controllers are possible [22, 92].

Recently, the process of input shaping [101] has proven effective at eliminating the residual oscillations of suspended payloads [49, 73, 97, 133]. Input shaping is easier to derive and implement than time-optimal control schemes and does not require the feedback mechanisms of closed-loop and adaptive controllers.

In this section we examine the problem of collision avoidance with suspended payloads. Rather than propose a completely computer controlled scheme, we assume that a human operator

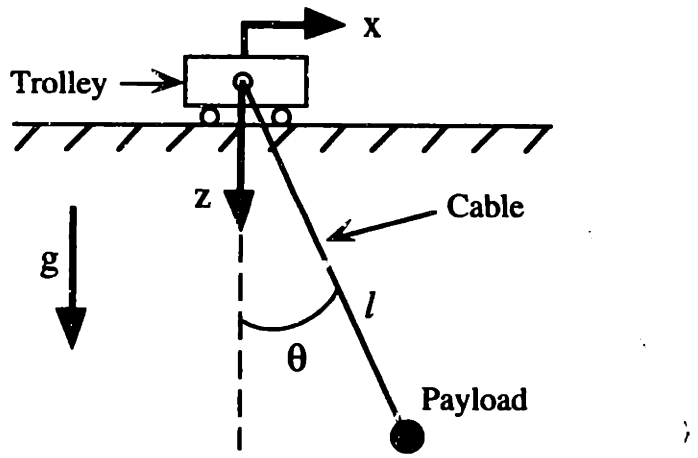

Figure 8.32: Sketch on an X Direction Gantry Crane.

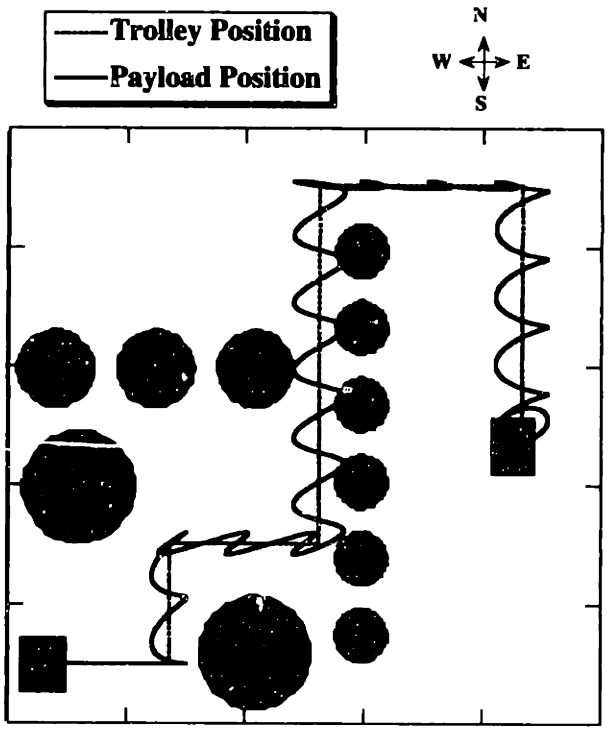

Figure 8.33: Motion of a Gantry Crane Through a Cluttered Environment.

generates the desired path through the obstacle field. We then augment the efforts of the human operator by shaping the command signals generated by the operator. If the transient sway can be decreased, then the human operator should be more successful at avoiding obstacles and could potentially plan higher performance paths. That is, they can generate paths that come closer to the obstacles so that the desired goal can be reached in less time.

Systems that manipulate suspended payloads can have a variety of dynamic properties.

However, most are characterized by a dominating low frequency mode that is lightly damped. In this paper, we restrict our attention to large gantry cranes. During operation of a typical gantry crane (cable lengths between 20 and 100 ft.), the payload position can deviate a foot or more from the planar position of the overhead trolley. The deviation is not caused by a large angle deflection; rather, it is due to the long cable length. For example, the payload of a crane with a 30 ft. cable sways 1 ft. with an angular deflection of less than 2 degrees.

Sections 8.4.1 through 8.4.3 describe the model of a gantry crane on which we base our work and also describe a simple model of the human operator behavior. A brief review of input shaping is then given at the end of the section. Sections 8.4.4 through 8.4.6 present theoretical results that predict the transient sway and residual oscillation of the system when the operator commands are subject to input shaping. The ramifications for collision avoidance are then discussed in Section 8.4.7.

8.4.1 Gantry Crane Model

Assuming relatively small angle deflection of the suspended payload, an xy gantry crane can be modeled as a simple linear pendulum.[27] The equation of motion along one direction is given by:

$$\ddot{\theta}(t)+\frac{g}{l}\theta(t)=\frac{a(t)}{l}. \tag{8.2}$$

Here $\theta(t)$ is the time varying angle deflection from the vertical down position of the payload, g is the acceleration due to gravity, l is the length of the suspension, and $a(t)$ is the acceleration input to the system. (See Figure 8.32). A model of an xy gantry crane is obtained by using two versions of (8.2), one for the x direction and one for the y direction. The oscillations in the two directions are assumed to be uncoupled.

Here we have assumed that the length of the cable is constant. This restricts our investigation to cases where the operator is generating two-dimensional commands. When the payload is hoisted during operation, the linearized frequency changes and the dynamics become more complicated. However, our main concern here is with path following, so the two-dimensional case will be illustrative. Furthermore, input shaping has been shown to be effective at reducing residual oscillations when hoisting occurs [133]. Therefore, the results we obtain here have some direct relevance to the more general case of three dimensional path following.

8.4.2 Model of Operator Behavior

Human operators usually generate commands for gantry cranes by moving levers or pressing buttons. Figure 8.34 shows a typical operator pendant when on-off buttons are used. Pressing

[27] For an angular deflection of $\pm 10^{\circ}$ (well above the normal deflection of a gantry crane), the error in using the linearized model is about $\pm 0.5\%$.

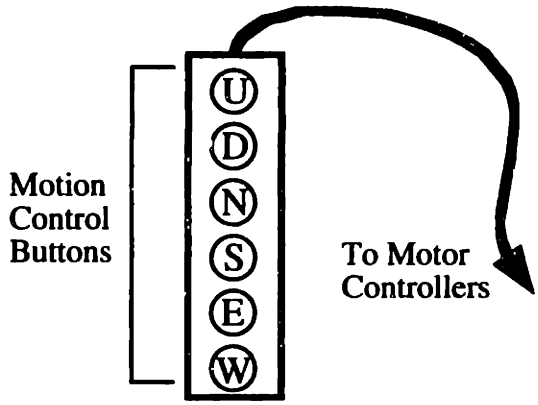

Figure 8.34: Typical Operator Pendant.

the buttons causes the trolley of the crane to move in the North, South, East, or West directions. (Recall that we are assuming that the Up and Down buttons are not used.)

In order to limit the set of possible commands, we make the following assumptions about the behavior of the human operator:

1) The operator presses only one button at a time. Holding the pendant and pressing more than one button at a time is awkward for the casual operator. Although experienced operators routinely press multiple buttons, they are less likely to do so in the cluttered environments we are considering.

2) Directional changes occur instantly. That is, an operator releases the button for one direction and immediately presses the button for a new direction. We could insert an arbitrary time delay to model the operator reflexes, but it makes little difference in the results, so we assume a time delay of zero.

3) The operator makes no attempt to eliminate residual vibration. For example, if the operator wants to perform an "L" shaped motion, then he presses the South button for some amount of time. When the crane arrives at the knee of the "L", the South button is released and the East button is pressed, which produces perpendicular motion. That is, there is no multiple button pressing along the vertical portion of the "L" that attempts to eliminate residual vibration at the knee of the desired motion. This is a poor assumption for a skilled operator, but a realistic model of a casual operator. Our main intention here is to investigate the effect of input shaping operators' commands, not to develop a very accurate model of operator behavior.

8.4.3 Model of Actuator Dynamics

In order to simulate the dynamic response of the crane using (8.2), we must know a(t), which is a function of the human operator actions and the motor dynamics. If input shaping is not used, we assume that when an operator presses a button, the system experiences a constant acceleration

until a velocity limit is reached, at which point the acceleration goes to zero and the trolley moves at the constant velocity. When the operator releases the button, the trolley undergoes a constant deceleration until the velocity reaches zero. Simply put, the system is subjected to trapezoidal velocity profiles. If the button is released before maximum velocity is achieved, then the command is a triangular velocity (bang-bang acceleration). When input shaping is used, we assume that pressing a button produces the same desired command as without shaping; however, this command is intercepted and convolved with the input shaper. The result of the convolution is then the acceleration function, a(t), that is used to drive the system.

8.4.4 Theoretical Results

Given the crane dynamics described by (8.2) and our model of human behavior, we can solve for the endpoint position analytically. Our assumption that the input signals are on/off implies that a(t) will consist only of positive and negative steps. Solving (8.2) for a step input $a_S(t)$ at time t = 0 yields the angular deflection:

$$\theta_S(t) = \frac{a_S}{g}(\cos\omega t - 1), \tag{8.3}$$

where ω is the angular frequency of the system and is given by $\omega = \sqrt{g/l}$. Due to the linearity of (8.3), any motion of the crane can be described by a superposition of (8.3).

Given the actuator limits (accelerations), the maximum velocity of the trolley, and the desired trajectory of the payload, the starting times and magnitudes of the step inputs that compose the command can be found analytically. These times and magnitudes can be found for a crane operating with or without input shaping.

Starting the operation at t = 0, the sway caused by a step input of magnitude a_1 starting at t_1 is given by equation (8.3) with a time delay of t_1, that is:

$$\theta_1(t) = \frac{a_1}{g}(\cos\omega(t - t_1) - 1). \tag{8.4}$$

For consistency, define $t_{o1} = t_1$ and $c_1 = a_1 / g$. Equation (8.4) can be rewritten using a single cosine with amplitude $A_1 = \frac{a_1}{g}\cos\omega(t_{o1} - t_1)$ and offset c_1, that is:

$$\theta_1(t) = A_1 \cos\omega(t - t_{o1}) + c_1, \qquad t > t_1. \tag{8.5}$$

Using this notation, the angular deflection after the k^{th} (positive or negative) step input is given by the generalization of equation (8.5). That is:[28]

$$\theta_k(t) = A_k \cos\omega(t - t_{ok}) + c_k, \qquad t > t_k, \tag{8.6}$$

where the time delay t_{ok} is given by:

---

[28] This solution and notation was provided by Hans Jacob Feder. Note that this expression is entirely analogous to the expression developed in Chapter 5 for the deflection of the benchmark mass-spring system.

$$t_{ok} = \frac{1}{\omega}\tan^{-1}\left[\frac{A_{k-1}\sin\omega t_{ok-1} + \frac{a_k}{g}\sin\omega t_k}{A_{k-1}\cos\omega t_{ok-1} + \frac{a_k}{g}\cos\omega t_k}\right], \tag{8.7}$$

and the offset $c_k = c_{k-1} - a_k/g$. The amplitude A_k is defined by:

$$A_k = A_{k-1}\cos\omega(t_{ok} - t_{ok-1}) + \frac{a_k}{g}\cos\omega(t_{ok} - t_{ok-1}). \tag{8.8}$$

Thus, using equation (8.6), the angular deflection of the endpoint can be computed analytically for all times given any combination of step inputs to the system.

8.4.5 Residual Vibrations

It is desirable to find the residual vibration of the payload after a rest-to-rest motion. In the context of industrial cranes, the trolley has a maximum velocity given by v_{max}. The time to reach this velocity is $t_p = a_s/v_{max}$. Thus, the acceleration a_s is only applied in this time period, and can be approximated by a square pulse of duration t_p and magnitude a_s. This is valid because the time constant of acceleration is usually much faster than the duration of the acceleration t_p for industrial cranes.

The resulting angular deflection $\theta(t)$ for an on-off signal by the crane operator is given by first applying a positive step of amplitude a_s at $t_1 = 0$ and then a negative step at $t = t_p$ of the same magnitude. The angular deflection for this pulse for $t > t_p$ is:[29]

$$\theta_p(t) = \frac{a_s}{g}(\cos\omega t - \cos\omega(t - t_p)), \qquad t > t_p. \tag{8.9}$$

This can be rewritten in the form of a single cosine with delay t_{op} given by:

$$t_{op} = \frac{1}{\omega}\tan^{-1}\left[\frac{\sin\omega t_p}{\cos\omega t_p - 1}\right], \tag{8.10}$$

and amplitude

$$A_p = \theta_p(t = t_{op}) = \frac{a_s}{g}(\cos\omega t_{op} - \cos\omega(t_{op} - t_p)), \qquad t > t_p. \tag{8.11}$$

That is, the angular deflection resulting from a pulse input of duration t_p is given by:

$$\theta_p(t) = A_p\cos\omega(t - t_{op}), \qquad t > t_p. \tag{8.12}$$

Note that there is no offset, since the acceleration after t_p is zero.

To bring the trolley to a complete stop at $t_p + t_2$ seconds, an equal but negative acceleration pulse is initiated at time t_2 with duration t_p. The resulting endpoint oscillation of this rest-to-rest motion of the trolley is given by the superposition of a positive pulse at $t = 0$, (8.12), and a negative pulse at t_2:

$$\theta_{rr}(t) = A_p(\cos\omega(t - t_{op}) - \cos\omega(t - t_2 - t_{op})), \qquad t > t_2 + t_p \tag{8.13}$$

---

[29] The analytic results of this subsection were provided by Hans Jacob Feder.

The residual vibration can be expressed using a single cosine function with a time shift given by:

$$t_{rr} = \frac{1}{\omega}\tan^{-1}\left[\frac{\sin\omega t_{op} - \sin\omega(t_2 + t_{op})}{\cos\omega t_{op} - \cos\omega(t_2 + t_{op})}\right], \tag{8.14}$$

and amplitude $A_{rr} = \theta_{rr}(t = t_{rr})$. That is:

$$\theta_{rr}(t) = A_{rr}\cos\omega(t - t_{rr}), \qquad t > t_p + t_2. \tag{8.15}$$

Equation (8.15) gives the residual vibration due to a rest-to-rest movement. Figure 8.35 shows a plot of the normalized rest-to-rest amplitude, $\langle A_{rr}\rangle$, versus t_2/T both with input shaping (line at zero) and without input shaping (the sine-like shape). The period of the system, $T = 2\pi/\omega$, is assumed to be exactly known. Notice that t_2 is directly related to the distance moved. Through some trigonometry and algebraic manipulation, it can be shown that the normalized rest-to-rest amplitude $\langle A_{rr}\rangle$ is given by:

$$\langle A_{rr}\rangle = \left|\sin\left(\frac{t_2\pi}{T}\right)\right|. \tag{8.16}$$

As can be seen from Figure 8.35, the only thing that matters for the residual vibrations of the endpoint when no input shaper is used is the relative magnitude of t_2 to the system period T. Using the input shaper, the residual vibrations are independent of t_2 and are always zero as long as t_2 is greater than the shaper length. For times shorter than the shaper length, actuator saturation may occur, thus changing the dynamics of the system.

8.4.6 Worst Case Residual Amplitude

So far we have only discussed oscillations given that the exact times of the on and off signals are known, or equivalently, we have assumed perfect knowledge of the distances the crane operator moves. However, when the crane operator *plans* how to move in a cluttered environment, he will not be able to predict exactly the distances the crane will move and the oscillations that will result from the movement. Thus, it is important to find a worst case scenario that can occur after *n* moves.

According to (8.16) the largest oscillations occurs when the negative pulse starts at $t_2 = nT + T/2$ where *n* is an integer and $T = 2\pi\sqrt{l/g}$ is the period of the system. In this case, the positive and the negative pulse are phase shifted by exactly 180°, making them reinforce each other completely. Again, assuming that the time to reach maximum velocity is t_p, the maximum amplitude of oscillation (for $t > t_2 + t_p$) is:

$$A = 2A_p. \tag{8.17}$$

Thus, given *k* rest-to-rest motions in one direction, the maximum possible endpoint sway amplitude is:

$$A_k = 2kA_p, \qquad t > \text{end of last pulse}. \tag{8.18}$$

Using this result, the maximum residual amplitudes can be found given any planned movement of

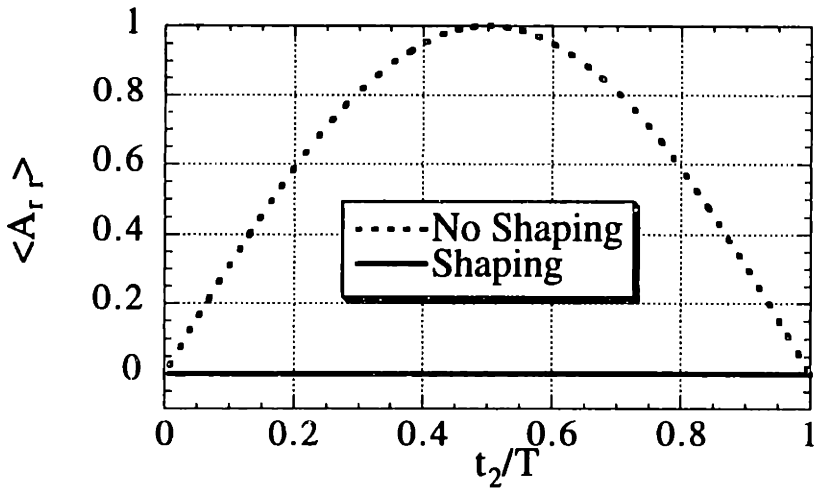

Figure 8.35: Rest-to-Rest Residual Amplitude vs. Move Distance.

the payload. For instance, if the operator wishes to perform three moves in the x-direction of the plane, and two in the y-direction of the plane, the maximum residual sway oscillations of the payload after the completion of the moves would be $6A_p$ in the x-direction and $4A_p$ in the y-direction.

8.4.7 Effect of Input Shaping on Path Following

Recall the example of crane behavior shown in Figure 8.33. When the commands used to generate the response are shaped with a UM ZV shaper, the response to these new commands are shown in Figure 8.36. The input shaping eliminates sway perpendicular to the desired path. (There is still sway along the path direction.) This greatly reduces the possibility of collision. If the operator generates a collision-free path for the trolley (projected down to the plane of the obstacles), then the payload will also follow a collision-free path.

When input shaping is used, the only deflection of the payload from the trolley path occurs at the corners of the path. This is due to our assumption that directional changes occurs instantly. This deflection depends on the shaper length. The payload will deviate from the trolley path one shaper length before the corner. One shaper length after the corner, the payload will again coincide with the path of the trolley. (See Figure 8.36).

We also point out the possibility that, given input shaping, the operator can generate higher performance paths. That is, paths that achieve the final position in less time. For the same cluttered environment as shown in Figures 8.33 and 8.36, several alternate paths can be safely navigated when the perpendicular sway is eliminated with input shaping. One such path is shown in Figure 8.37. Furthermore, if no input shaping is applied, the maximum deviation from the path can be considerable, as shown in Figure 8.37.

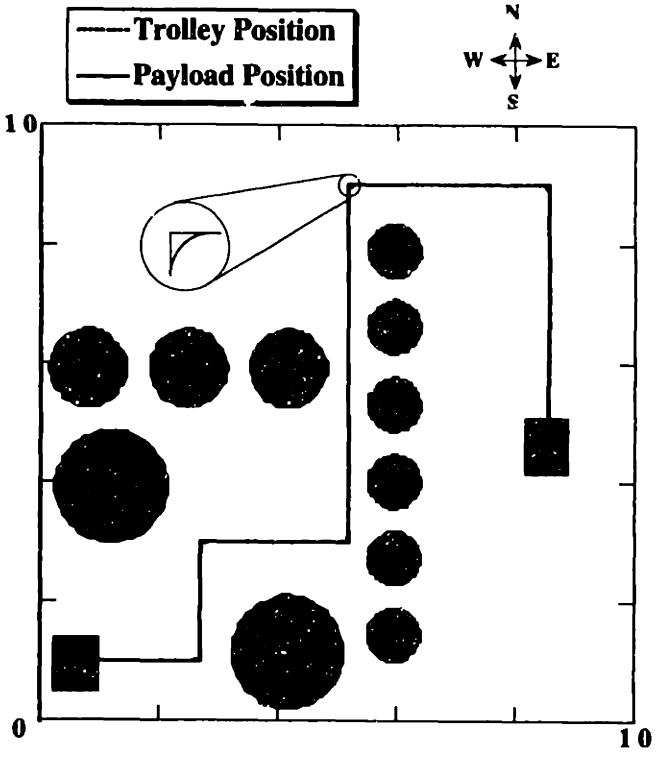

Figure 8.36: Motion of Gantry Crane with Input Shaped Commands. Same Desired Trolley Path as in Figure 8.31.

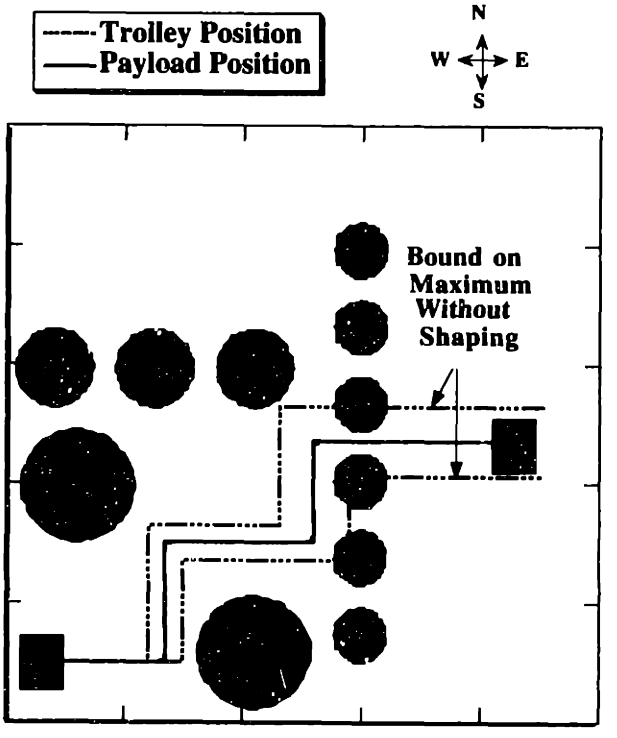

Figure 8.37: Motion Along a Shorter Path Allowed by Input Shaping.

8.4.8 Summary of Obstacle Avoidance

This section has shown the effectiveness of input shaping on the practical problem of moving suspended payloads in a cluttered environment. Input shaping of gantry cranes is most beneficial for inexperienced operators, as skilled operators perform some manual forms of command shaping. However, input shaping reduces the stress on experienced operators, while improving the performance in terms of transient sway. Input shaping can greatly improve the performance of less-skilled operators because the residual oscillation is always eliminated. Finally, input shaping can allow any operator to plan higher performance paths through cluttered environments because there is the assurance that sway perpendicular to the desired path will be eliminated.

Simple analytical models have been developed and used to predict the transient and residual oscillation of the payload, with or without input shaping. Further, a simple rule has been given to find the maximum oscillation that can occur without input shaping. This maximum value is a function of the natural period of the suspended payload and the number of straight line movements that compose a desired path. Given the analytic expressions for transient and residual oscillations derived in this paper, one could develop path-planning algorithms that take into account the beneficial nature of input shaping.

9 SUMMARY

This thesis has examined the issue of command generation for flexible systems. The importance of the command signal has been demonstrated for a variety of systems and applications. Numerous tools for designing and evaluating command signals have been developed and demonstrated throughout the text.

Robust methods of filtering command signals in real time were developed. These filtering methods allow specification of the robustness to modeling errors. Techniques for applying these methods to multi-mode systems were developed. Furthermore, time lag introduced by the filtering process was reduced by using negative filter coefficients. Many of the proposed filtering schemes were implemented on industrial machines and shown to work very effectively.

Techniques for generating multi-switch bang-bang commands were developed. These commands provide very rapid motion. Because these commands tend to be very sensitive to modeling errors, methods for specifying the robustness were developed. This work was extended by examining the problem of generating on-off commands. Commands of this type can have periods of coasting as well as periods of full positive and full negative actuator effort. Fuel-efficient on-off commands were developed and shown to be nearly time-optimal. Methods for precisely specifying the fuel usage were also presented. On-off commands that limit the transient deflection to a desired level were developed and shown to be effective with nonlinear simulations of flexible spacecraft.

Because multi-switch bang-bang commands and on-off commands can be difficult to implement, methods for facilitating their use were examined. One method attempted to describe the command profiles by simply closed-form equations. Another method used neural networks to generate the command in real time.

Given the great variety of command generation techniques described in this thesis and in the literature, the need for head-to-head comparisons arises. Several comparisons were presented. Real-time filtering methods were compared to time-optimal commands for single and multi-mode systems. The new filtering methods developed in this thesis were also compared to more traditional FIR and IIR filtering methods.

Although commands were generated to meet a large variety of performance specifications, there are some specifications that proved too difficult to incorporate into the design process. The effect of command generation schemes on these complex performance specifications was examined. In particular, it was shown that the real-time filtering methods presented in this thesis improve the repeatability of coordinate measuring machines. Furthermore, they improve trajectory tracking and aid in obstacle avoidance.

REFERENCES

[1] *MATLAB User's Guide*. Natick, MA: The MathWorks, Inc., 1991.

[2] "Methods for Performance Evaluation of Coordinate Measuring Machines," *ASME B89.1.12M-1990*, 1990.

[3] D.M. Aspinwall, "Acceleration Profiles for Minimizing Residual Response," *ASME Journal of Dynamic Systems, Measurement, and Control*, March, 1980, pp. 3-6.

[4] M. Athens and P.L. Falb, *Optimal Control*. New York: McGraw-Hill, 1966.

[5] J.W. Auernig and H. Troger, "Time Optimal Control of Overhead Cranes with Hoisting of the Load," *Automatica*, July, 1987, pp. 437-446.

[6] A.K. Banerjee, "Dynamics and Control of the WISP Shuttle-Antennae System," *J. of Astronautical Sciences*, 1, 1993, pp. 73-90.

[7] A.K. Banerjee and W.E. Singhose, "Command Shaping in Tracking Control of a Two-Link Flexible Manipulator," *AIAA Astrodynamics Conf.* Sun Valley, ID, 1997.

[8] A.K. Banerjee and W.E. Singhose, "Minimum Time Fuel Efficient Maneuver of Flexible Spacecraft with Vibration Amplitude Constraint," *AAS Astrodynamics Specialist Conf.* Halifax, Nova Scotia, 1995.

[9] A.K. Banerjee and W.E. Singhose, "Slewing and Vibration Control of a Nonlinearly Elastic Shuttle Antenna," *AIAA/AAS Astrodynamics Specialists Conf.* Scottsdale, AZ, 1994.

[10] B.B. Bederson, R.S. Wallace, and E.L. Schwartz, "Control and Design of the Spherical Pointing Motor," *IEEE Int. Conf. on Robotics and Automation*. Atlanta, GA, 1993, pp. 630-636.

[11] J. Ben-Asher, J.A. Burns, and E.M. Cliff, "Time-Optimal Slewing of Flexible Spacecraft," *J. of Guidance, Control, and Dynamics*, 2, 1992, pp. 360-367.

[12] S.P. Bhat and D.K. Miu, "Precise Point-to-Point Positioning Control of Flexible Structures," *ASME Winter Annual Meeting*. San Francisco, CA, 1989.

[13] S.P. Bhat and D.K. Miu, "Precise Point-to-Point Positioning Control of Flexible Structures," *J. of Dynamic Sys., Meas., and Control*, 4, 1990, pp. 667-674.

[14] S.P. Bhat and D.K. Miu, "Solutions to Point-to-Point Control Problems using Laplace Transform Technique," *American Control Conf.* San Diego, CA, 1990.

[15] S.P. Bhat and D.K. Miu, "Solutions to Point-to-Point Control Problems Using Laplace Transform Technique," *J. of Dynamic Sys., Meas., and Control*, 1991.

[16] S.P. Bhat, M. Tanaka, and D.K. Miu, "Experiments on Point-to-Point Position Control of a flexible Beam Using Laplace Transform Technique-Part 1: Open-Loop," *Journal of Dynamic Systems, Measurement, and Control*, 1991, pp. 432-437.

[17] S.P. Bhat, M. Tanaka, and D.K. Miu, "Experiments on Point-to-Point Position Control of a flexible Beam Using Laplace Transform Technique-Part II: Closed-Loop," *J. of Dynamic Sys., Meas., and Control*, 1991, pp. 438-443.

[18] M. Bodson, "Experimental Comparison of Two Input Shaping Methods for the Control of Resonant Systems," *IFAC World Congress*. San Francisco, CA, 1996.

[19] W.J. Book, "Controlled Motion in an Elastic World," *J. of Dynamic Sys., Meas., and Control*, June, 1993, pp. 252-261.

[20] A. Brooke, D. Kendrick, and A. Meeraus, *GAMS: A User's Guide*. Redwood City, CA: The Scientific Press, 1988.

[21] A. Bryson and Y.-C. Ho, *Applied Optimal Control*. Hemisphere Publishing, 1975.

[22] H. Butler, G. Honderd, and J.V. Amerongen, "Model Reference Adaptive Control of a Gantry Crane Scale Model," *IEEE Control Systems*, January, 1991, pp. 57-62.

[23] R.M. Byers, S.R. Vadali, and J.L. Junkins, "Near-Minimum Time, Closed-Loop Slewing of Flexible Spacecraft," *J. of Guidance, Control, and Dynamics*, 1, 1990, pp. 57-65.

[24] G. Cook, "An Application of Half-Cycle Posicast," *IEEE Trans. on Automatic Control*, 3, 1966, pp. 556-559.

[25] G. Cook, "Control of Flexible Structures Via Posicast," *Eighteenth Southeastern Symp. on System Theory*. Knoxville, TN, 1986, pp. 31-35.

[26] E.A. Crain, W.E. Singhose, and W.P. Seering, "Derivation and Properties of Convolved and Simultaneous Two-Mode Input Shapers," *IFAC World Congress*. San Francisco, CA, 1996.

[27] V. Drapeau, "Design, Modelling and Control of a Five-bar-linkage Manipulator with One Flexible Link," Masters, University of Waterloo, 1994.

[28] V. Drapeau and D. Wang, "Verification of a Closed-loop Shaped-input Controller for a Five-bar-linkage Manipulator," *IEEE Int. Conf. on Robotics and Automation*. Atlanta, GA, 1993, pp. 216-221.

[29] R.L. Farrenkopf, "Optimal Open-Loop maneuver Profiles for Flexible Spacecraft," *J. of Guidance and Control*, 6, 1979, pp. 491-498.

[30] J. Feddema, C. Dohrmann, G. Parker, R. Robinett, V. Romero, and D. Schmitt, "A Comparison of Maneuver Optimization and Input Shaping Filters for Robotically Controlled Slosh-Free Motion of an Open Container of Liquid," *American Control Conf.* Albuquerque, NM, 1997.

[31] J. Feddema, C. Dohrmann, G. Parker, R. Robinett, V. Romero, and D. Schmitt, "Control for Slosh-Free Motion of an Open Container," *IEEE Control Systems*, 1, 1997, pp. 29-36.

[32] J. Feddema, C. Dohrmann, G. Parker, R. Robinett, V. Romero, and D. Schmitt, "Controlled Slosh-Free Motion of an Open Container of Liquid," *AIAA Aerosciences Meeting, Symposium on Nonlinear Dynamics*. 1997.

[33] J. Feddema, C. Dohrmann, G. Parker, R. Robinett, V. Romero, and D. Schmitt, "Robotically Controlled Slosh-Free Motion of an Open Container of Liquid," *IEEE Int. Conf. on Robotics and Automation*. 1996.

[34] J.T. Feddema, "Digital Filter Control of Remotely Operated Flexible Robotic Structures," *American Control Conf.* San Francisco, CA, 1993, pp. 2710-2715.

[35] H.J.S. Feder, W.E. Singhose, and W.P. Seering, "Input Shaping for Collision Avoidance with Robotic Manipulation of Suspended Payloads," *11th Symposium on Structural Dynamics and Control*. Blacksburg, VA, 1997.

[36] A.R. Golafshani and J.D. Aplevich, "Computation of Time-Optimal Trajectories for Tower Cranes," *IEEE Conf. on Control Apps*. 1995, pp. 1134-1139.

[37] K.L. Hillsley and S. Yurkovich, "Vibration Control of a Two-Link Flexible Robot Arm," *J. of Dynamics and Control*, 1993, pp. 261-280.

[38] K.L. Hillsley and S. Yurkovich, "Vibration Control of a Two-Link Flexible Robot Arm," *IEEE Int. Conf. on Robotics and Automation*. Sacramento, CA, 1991, pp. 2121-26.

[39] J.M. Hyde, "Contact Transition Control: An Experimental Study," *IEEE Int. Conf. on Robotics and Automation*. Atlanta, GA, 1993.

[40] J.M. Hyde, "Multiple Mode Vibration Suppression in Controlled Flexible Systems," *AITR 1295*, Massachusetts Institute of Technology, 1991.

[41] J.M. Hyde and M.R. Cutkosky, "Controlling Contact Transition," *IEEE Control Systems Magazine*, Feb., 1994, pp. 25-30.

[42] J.M. Hyde and W.P. Seering, "Inhibiting Multiple Mode Vibration in Controlled Flexible Systems," *American Control Conf.* Boston, MA, 1991.

[43] J.M. Hyde and W.P. Seering, "Using Input Command Pre-Shaping to Suppress Multiple Mode Vibration," *IEEE Int. Conf. on Robotics and Automation*. Sacramento, CA, 1991, pp. 2604-2609.

[44] J.F. Jansen, "Control and Analysis of a Single-Link Flexible Beam with Experimental Verification," *ORNL/TM-12198*, Oak Ridge National Laboratory, 1992.

[45] S.D. Jones, "Quantification and Reduction of Dynamically Induced Errors in Coordinate Measuring Machines," Ph.D., University of Michigan, 1993.

[46] S.D. Jones and A.G. Ulsoy, "Control Input Shaping for Coordinate Measuring Machines," *American Control Conf.* Baltimore, MD, 1994, pp. 2899-2903.

[47] J.L. Junkins, Z.H. Rahman, and H. Bang, "Near-Minimum Time Control of Distributed Parameter Systems: Analytical and Experimental Results," *J. of Guidance, Control, and Dynamics*, 2, 1991, pp. 406-415.

[48] F. Khorrami, S. Jain, and A. Tzes, "Adaptive Nonlinear Control and Input Preshaping for

Flexible-Link Manipulators," *American Control Conf.* San Francisco, CA, 1993, pp. 2705-2709.

[49] R.L. Kress, J.F. Jansen, and M.W. Noakes, "Experimental Implementation of a Robust Damped-Oscillation Control Algorithm on a Full Sized, Two-DOF, AC Induction Motor-Driven Crane," *5th ISRAM.* Maui, HA, 1994, pp. 585-92.

[50] D.-S. Kwon, D.-H. Hwang, S.M. Babcock, and B.L. Burks, "Input Shaping Filter Methods for the Control of Structurally Flexible, Long-Reach Manipulators," *IEEE Conf. on Robotics and Automation.* San Diego, CA, 1994, pp. 3259-64.

[51] T.-C. Lin, "Design an Input Shaper to Reduce Operation-Induced Vibration," *American Control Conf.* San Francisco, CA, 1993, pp. 2502-6.

[52] Q. Liu and B. Wie, "Robust Time-Optimal Control of Uncertain Flexible Spacecraft," *J. of Guidance, Control, and Dynamics*, 3, 1992, pp. 597-604.

[53] S.-W. Liu and T. Singh, "Robust Time-Optimal Control of Nonlinear Structures with Parameter Uncertainties," *AIAA Guidance, Nav., and Cont. Conf.* San Diego, CA, 1996.

[54] L.J. Love, D.P. Magee, and W.J. Book, "A Comparison of Joint Control Algorithms for Teleoperated Pick and Place Tasks Using a Flexible Manipulator," *IEEE Int. Conf. on Systems, Man, and Cybernetics.* 1994, pp. 1257-62.

[55] D. Magee and W. Book, "The Application of Input Shaping to a System with Varying Parameters," *Japan/USA Symposium on Flexible Automation.* 1992, pp. pp. 519-25.

[56] D.P. Magee and W.J. Book, "Eliminating Multiple Modes of Vibration in a Flexible Manipulator," *Proceedings of the IEEE International Conference on Robotics and Automation.* Atlanta, GA, 1993, pp. 474-479.

[57] D.P. Magee and W.J. Book, "Experimental Verification of Modified Command Shaping Using a Flexible Manipulator," *Proceedings of the 1st International Conference on Motion and Vibration Control.* Yokohama, Japan, 1992.

[58] D.P. Magee and W.J. Book, "Filtering Micro-Manipulator Wrist Commands to Prevent Flexible Base Motion," *American Control Conference.* Seattle, WA, 1995.

[59] D.P. Magee and W.J. Book, "Filtering Schilling Manipulator Commands to Prevent Flexible Structure Vibration," *American Control Conf.* Baltimore, MD, 1994, pp. 2538-42.

[60] D.P. Magee and W.J. Book, "Implementing Modified Command Filtering to Eliminate Multiple Modes of Vibration," *Proceedings of the American Controls Conference.* San Francisco, CA, 1993, pp. 2700-2704.

[61] J.E. Marshall and S.V. Salehi, "Improvements of System Performance by the use of Time-Delay Elements," *IEE Proc.*, 5, 1982, pp. 177-181.

[62] W.E. McDermott, "On the use of Neural Networks in Approximating Optimal Control Solutions," Master's, Massachusetts INstitute of Technology, 1994.

[63] P.H. Meckl, "Controlling Velocity-Limited System to Reduce Residual Vibration," *Proceedings of the 1988 IEEE International Conference on Robotics and Automation.* Philadelphia, PA, 1988.

[64] P.H. Meckl and W.P. Seering, "Experimental Evaluation of Shaped Inputs to Reduce Vibration for a Cartesian Robot," *ASME Journal of Dynamic Systems, Measurement, and Control*, June, 1990, pp. 159-165.

[65] P.H. Meckl and W.P. Seering, "Minimizing Residual Vibration for Point-to-Point Motion," *Journal of Vibration, Acoustics, Stress and Reliability in Design*, October, 1985, pp. 378-382.

[66] P.H. Meckl and W.P. Seering, "Reducing Residual Vibration in Systems with Time Varying Resonances," *IEEE Int. Conf. on Robotics and Automation.* Raleigh, NC, 1987, pp. 1690-1695.

[67] D.H. Mee, "A Feedback Implementation of Posicast Control Using Sampling Circuits," *Proceedings of the Institute of Radio and Electronics Engineering*, Jan-Feb, 1974, pp. 11-15.

[68] E.-B. Meier and A.E. Bryson, "Efficient Algorithm for Time-Optimal Control of a Two-Link Manipulator," *J. of Guidance, Control, and Dynamics*, 5, 1990, pp. 859-866.

[69] J.L. Meyer and L. Silverberg, "Fuel Optimal Propulsive Maneuver of an Experimental Structure Exhibiting Spacelike Dynamics," *J. of Guidance, Control, and Dynamics*, 1, 1996, pp. 141-9.

[70] K.A.F. Moustafa and A.M. Ebeid, "Nonlinear Modeling and Control of Overhead Crane Load Sway," *Transactions of the ASME*, September, 1988, pp. 266-271.

[71] B.R. Murphy and I. Watanabe, "Digital Shaping Filters for Reducing Machine Vibration," *IEEE Transactions on Robotics and Automation*, April, 1992, pp. 285-289.

[72] M.W. Noakes, G.K. Corbett, and C.T. Kring, "An Application of Oscillation Damped Motion for Suspended Payloads to the Advanced Integrated Maintenance System," *Annual Meeting of the American Nuclear Society.* Nashville, TN, 1990.

[73] M.W. Noakes and J.F. Jansen, "Generalized Inputs for Damped-Vibration Control of Suspended Payloads," *Robotics and Autonomous Systems*, 2, 1992, pp. 199-205.

[74] A.V. Oppenheim and R.W. Schafer, *Digital Signal Processing*. Englewood Cliffs, NJ: Prentice Hall, Inc., 1975.

[75] L. Pao and W. Singhose, "Unity Magnitude Input Shapers and Their Relation to Time-Optimal Control," *IFAC World Congress.* San Francisco, CA, 1996.

[76] L.Y. Pao, "Characteristics of the Time-Optimal Control of Flexible Structures with Damping," *IEEE Conference on Control Applications.* Glasgow, Scotland, 1994, pp. 1299-1304.

[77] L.Y. Pao, "Input Shaping Design for Flexible Systems with Multiple Actuators," *IFAC*

World Congress. San Francisco, CA, 1996.

[78] L.Y. Pao, "Minimum-Time Control Characteristics of Flexible Structures," *J. of Guidance, Control, and Dynamics*, 1, 1996, pp. 123-9.

[79] L.Y. Pao and W.E. Singhose, "A Comparison of Constant and Variable Amplitude Command Shaping Techniques for Vibration Reduction," *IEEE Conference on Control Applications*. Albany, NY, 1995, pp. 875-81.

[80] L.Y. Pao and W.E. Singhose, "On the Equivalence of Minimum Time Input Shaping with Traditional Time-Optimal Control," *IEEE Conference on Control Applications*. Albany, NY, 1995, pp. 1120-5.

[81] L.Y. Pao and W.E. Singhose, "Verifying Robust Time-Optimal Commands for Multi-Mode Flexible Spacecraft," *J. of Guidance, Control, and Dynamics*, 4, 1997, pp. 831-833.

[82] G.G. Parker, G.R. Eisler, J. Phelan, and R.D. Robinett, "Input Shaping for Vibration-Damped Slewing of a Flexible Beam Using a Heavy-Lift Hydraulic Robot," *American Control Conf.* 1994.

[83] T.W. Parks and C.S. Burrus, *Digital Filter Design*. New York: John Wiley & Sons, Inc., 1987.

[84] T.W. Parks and J.H. McClellan, "Chebyshev Approximation for Nonrecursive Digital Filters with Linear Phase," *IEEE Transactions on Circuit Theory*, March, 1972.

[85] L.S. Pontryagin, V.G. Boltyanskii, R.V. Gamkrelidze, and E.F. Mishchenko, *The Mathematical Theory of Optimal Processes*. New York: John Wiley & Sons, 1962, pp. 360.

[86] B.W. Rappole, N.C. Singer, and W.P. Seering, "Input Shaping With Negative Sequences for Reducing Vibrations in Flexible Structures," *Proc. of the American Control Conference*. San Francisco, CA, 1993, pp. 2695-2699.

[87] B.W. Rappole, N.C. Singer, and W.P. Seering, "Multiple-Mode Impulse Shaping Sequences for Reducing Residual Vibrations," *23rd Biennial Mechanisms Conference*. Minneapolis, MN, 1994, pp. 11-16.

[88] K.S. Rattan and V. Feliu, "Feedforward Control of Flexible Manipulators," *Proceedings of the IEEE International Conference on Robotics and Automation*. Nice, France, 1992, pp. 788-793.

[89] R.D. Robinett, J.T. Feddema, G.R. Eisler, D.G. Wilson, and G.G. Parker, "Flexible Robotic Manipulator Research at Sandia National Laboratories," *11th Symposium on Structure Dynamics and Control*. Blacksburg, VA, 1997.

[90] K. Rogers and W.P. Seering, "Input Shaping for Limiting Loads and Vibration in Systems with On-Off Actuators," *AIAA Guidance, Navigation, and Control Conference*. San Diego, CA, 1996.

[91] Y. Sakawa and Y. Shindo, "Optimal Control of Container Cranes," *Automatica*, 3, 1982, pp. 257-66.

[92] K. Sato and Y. Sakawa, "Modeling and Control of a Flexible Rotary Crane," *Int. Journal of Control*, 5, 1988, pp. 2085-2105.

[93] S. Scrivener and R. Thompson, "Survey of Time-Optimal Attitude Maneuvers," *J. of Guidance, Control, and Dynamics*, 2, 1994, pp. 225-233.

[94] N. Seth, K.S. Rattan, and R.W. Brandstetter, "Vibration Control of a Coordinate Measuring Machine," *IEEE Conf. on Control Apps.* Dayton, OH, 1993, pp. 368-73.

[95] V.C. Shields and G. Cook, "Application of an Approximate Time Delay to a Posicast Control System," *International Journal of Control*, 4, 1971, pp. 649-657.

[96] N. Singer and W.P. Seering, "Experimental Verification of Command Shaping Methods for Controlling Residual Vibration in Flexible Robots," *Proceedings of the American Control Conference*. 1989.

[97] N. Singer, W. Singhose, and E. Kriikku, "An Input Shaping Controller Enabling Cranes to Move Without Sway," *ANS 7th Topical Meeting on Robotics and Remote Systems*. Augusta, GA, 1997.

[98] N.C. Singer, "Residual Vibration Reduction in Computer Controlled Machines," *MIT Artificial Intelligence Laboratory Technical Report Number AITR-1030*, MIT Artificial Intelligence Lab, 1989.

[99] N.C. Singer and W.P. Seering, "Design and Comparison of Command Shaping Methods for Controlling Residual Vibration," *Proceedings of the IEEE International Conference on Robotics and Automation*. Scottsdale, AZ, 1989, pp. 888-893.

[100] N.C. Singer and W.P. Seering, "An Extension of Command Shaping Methods for Controlling Residual Vibration Using Frequency Sampling," *IEEE International Conference on Robotics and Automation*. Nice, France, 1992, pp. 800-805.

[101] N.C. Singer and W.P. Seering, "Preshaping Command Inputs to Reduce System Vibration," *J. of Dynamic Systems, Measurement, and Control*, March, 1990, pp. 76-82.

[102] N.C. Singer, W.P. Seering, and K.A. Pasch, *Shaping Command Inputs to Minimize Unwanted Dynamics*, MIT, Editor^Editors. 1990, U.S. Patent 4,916,635: .

[103] G. Singh, P.T. Kabamba, and N.H. McClamroch, "Planar, Time-Optimal, Rest-to-Rest Slewing Maneuvers of Flexible Spacecraft," *Journal of Guidance, Control, and Dynamics*, 1, 1989, pp. 71-81.

[104] T. Singh, "Fuel/Time Optimal Control of the Benchmark Problem," *Journal of Guidance, Control, and Dynamics*, 6, 1995, pp. 1225-31.

[105] T. Singh, "Fuel/Time Optimal Control of the Benchmark Two-Mass/Spring System,"

Proceedings of the American Control Conference. Seattle, WA, 1995, pp. 3825-3829.

[106] T. Singh and G.R. Heppler, "Shaped Input Control of a System With Multiple Modes," *ASME Journal of Dynamic Systems, Measurement, and Control*, September, 1993, pp. 341-437.

[107] T. Singh and G.R. Heppler, "Shaped Inputs for a Multimode System," *Proceedings of the IEEE International Conference on Robotics and Automation*. Atlanta, GA, 1993, pp. 484-489.

[108] T. Singh and S.R. Vadali, "Input-Shaped Control of Three-Dimensional Maneuvers of Flexible Spacecraft," *J. of Guidance, Control, and Dynamics*, 6, 1993, pp. 1061-8.

[109] T. Singh and S.R. Vadali, "Robust Time-Delay Control," *ASME Journal of Dynamic Systems, Measurement, and Control*, June, 1993, pp. 303-306.

[110] T. Singh and S.R. Vadali, "Robust Time-Delay Control of Multimode Systems," *Int. Journal of Control*, 6, 1995, pp. 1319-1339.

[111] T. Singh and S.R. Vadali, "Robust Time-Optimal Control: A Frequency Domain Approach," *J. of Guidance, Control and Dynamics*, 2, 1994, pp. 346-353.

[112] T. Singh, S.R. Vadali, and N. Abhyankar, "Robust Time-Delay Control of Multimode Systems," *American Control Conference*. Baltimore, MD, 1994.

[113] W. Singhose, "A Vector Diagram Approach to Shaping Inputs for Vibration Reduction," *MIT Artificial Intelligence Lab Memo No. 1223*, 1990.

[114] W. Singhose, A. Banerjee, and W. Seering, "Slewing Flexible Spacecraft with Deflection-Limiting Input Shaping," *J. of Guidance, Control, and Dynamics*, 2, 1997, pp. 291-298.

[115] W. Singhose, K. Bohlke, and W. Seering, "Fuel-Efficient Pulse Command Profiles for Flexible Spacecraft," *J. of Guidance, Control, and Dyn.*, 4, 1996, pp. 954-960.

[116] W. Singhose and T. Chuang, "Reducing Deviations From Trajectory Components With Input Shaping," *American Control Conference*. Seattle, WA, 1995, pp. 929-33.

[117] W. Singhose, S. Derezinski, and N. Singer, "Extra-Insensitive Input Shapers for Controlling Flexible Spacecraft," *J. of Guidance, Control, and Dynamics*, 2, 1996, pp. 385-91.

[118] W. Singhose and L. Pao, "A Comparison of Input Shaping and Time-Optimal Flexible-Body Control," *Control Eng. Practice*, 4, 1997, pp. 459-467.

[119] W. Singhose and L. Pao, "Comparison of Input Shaping Techniques for Speed-Critical Multi-Mode Flexible Systems," *IEEE Conf. on Control Applications*. Dearborn, MI, 1996.

[120] W. Singhose, L. Porter, and N. Singer, "Vibration Reduction Using Multi-Hump Extra-Insensitive Input Shapers," *American Control Conference*. Seattle, WA, 1995, pp. 3830-34.

[121] W. Singhose and W. Seering, "Generating Vibration-Reducing Inputs with Vector Diagrams," *IFToMM Eighth World Congress on the Theory of Machines and Mechanisms*. Prague, Czechoslovakia, 1991, pp. 315-318.

[122] W. Singhose, W. Seering, and N. Singer, "Residual Vibration Reduction Using Vector

Diagrams to Generate Shaped Inputs," *J. of Mechanical Design*, June, 1994, pp. 654-659.

[123] W. Singhose, W. Seering, and T. Singh, "On-Off Control of Flexible Spacecraft with Specified Fuel Usage," *American Control Conf.* Albuquerque, NM, 1997.

[124] W. Singhose and N. Singer, "Effects of Input Shaping on Two-Dimensional Trajectory Following," *IEEE Trans. on Robotics and Automation*, 6, 1996, pp. 881-887.

[125] W. Singhose and N. Singer, "Initial Investigations into the Effects of Input Shaping on Trajectory Following," *American Control Conference*. Baltimore, MD, 1994, pp. 2526-32.

[126] W. Singhose, N. Singer, and W. Seering, "Comparison of Command Shaping Methods For Reducing Residual Vibration," *Third European Control Conf.* Rome, Italy, 1995, pp. 1126-1131.

[127] W. Singhose, N. Singer, and W. Seering, "Design and Implementation of Time-Optimal Negative Input Shapers," *International Mechanical Engineering Congress and Exposition, DSC 55-1*. Chicago, IL, 1994, pp. 151-7.

[128] W. Singhose, N. Singer, and W. Seering, "Improving Repeatability of Coordinate Measuring Machines with Shaped Command Signals," *Precision Engineering*, April, 1996, pp. 138-146.

[129] W. Singhose, N. Singer, and W. Seering, "Time-Optimal Negative Input Shapers," *J. of Dynamic Systems, Measurement, and Control*, June, 1997, pp. 198-205.

[130] W.E. Singhose, B.W. Mills, and W.P. Seering, "Closed-Form Methods for On-Off Control of Multi-Mode Flexible Structures," *IEEE Conf. of Decision and Control*. San Diego, CA, 1997.

[131] W.E. Singhose, L.Y. Pao, and W.P. Seering, "Slewing Multi-Mode Flexible Spacecraft Using Zero Derivative Robustness Constraints," *J. Guidance, Control, and Dynamics*, 1, 1997, pp. 204-206.

[132] W.E. Singhose, L.Y. Pao, and W.P. Seering, "Time-Optimal Rest-to-Rest Slewing of Multi-Mode Flexible Spacecraft Using ZVD Robustness Constraints," *AIAA Guidance, Navigation, and Control Conf.* San Diego, CA, 1996.

[133] W.E. Singhose, L.J. Porter, and W.P. Seering, "Input Shaped Control of a Planar Gantry Crane with Hoisting," *American Control Conf.* Albuquerque, NM, 1997.

[134] W.E. Singhose, L.J. Porter, T.D. Tuttle, and N.C. Singer, "Vibration Reduction Using Multi-Hump Input Shapers," *J. of Dynamic Systems, Measurement, and Control*, June, 1997, pp. 320-326.

[135] W.E. Singhose, W.P. Seering, and A. Banerjee, "An Evaluation of Fuel-Efficient On-Off Input Shaping with Deflection Limiting," *AIAA/AAS Astrodynamics Specialist Conf.* San Diego, CA, 1996.

[136] W.E. Singhose, W.P. Seering, and A.K. Banerjee, "Limiting Deflection During the Slewing of Flexible Spacecraft Using Deflection Sampling," *AIAA Guidance, Navigation, and Control Conf.* San Diego, CA, 1996.

[137] W.E. Singhose, W.P. Seering, and N.C. Singer, "Input Shaping for Vibration Reduction with Specified Insensitivity to Modeling Errors," *Japan-USA Sym. on Flexible Automation.* Boston, MA, 1996.

[138] W.E. Singhose, W.P. Seering, and N.C. Singer, "Shaping Inputs to Reduce Vibration: A Vector Diagram Approach," *IEEE Int. Conf. on Robotics and Automation.* Cincinnati, OH, 1990, pp. 922-927.

[139] W.E. Singhose and N.C. Singer, "Improving Coordinate Measuring Machine Repeatability with Input Shaping," *NSF Design and Manufacturing Grantees Conf.* Cambridge, MA, 1994, pp. 467-8.

[140] O.J.M. Smith, *Feedback Control Systems.* New York: McGraw-Hill Book Company, Inc., 1958, pp. 331-345.

[141] O.J.M. Smith, "Posicast Control of Damped Oscillatory Systems," *Proceedings of the IRE*, September, 1957, pp. 1249-1255.

[142] C.J. Swigert, "Shaped Torque Techniques," *J. of Guidance and Control*, 5, 1980, pp. 460-467.

[143] G. Swisher and A. Huang, "Posicast Control of Third- and Fourth-Order Feedback Control Systems," Tennessee Technological University,

[144] G.H. Tallman and O.J.M. Smith, "Analog Study of Dead-Beat Posicast Control," *IRE Transactions on Automatic Control*, March, 1958, pp. 14-21.

[145] F. Taylor, *Digital Filter Design Handbook.* New York: Marcel Dekker, Inc., 1983.

[146] R.C. Thompson, J.L. Junkins, and S.R. Vadali, "Near-Minimum Time Open-Loop Slewing of Flexible Vehicles," *J. of Guidance, Control, and Dynamics*, 1, 1989, pp. 82-88.

[147] J.D. Turner and J.L. Junkins, "Optimal Large-Angle Single-Axis Rotational Maneuvers of Flexible Spacecraft," *Journal of Guidance and Control*, 6, 1980, pp. 578-585.

[148] T. Tuttle, "Creating Time-Optimal Commands for Linear Systems," Ph.D., M.I.T., 1997.

[149] T. Tuttle and W. Seering, "Creating Time-Optimal Commands for Systems with Denominator Dynamics," *IEEE Int. Conf. on Control Applications.* Dearborn, MI, 1996.

[150] T. Tuttle and W. Seering, "Deriving and Verifying Time-Optimal Commands for Linear Systems," *American Control Conf.* Albuquerque, NM, 1997.

[151] T.D. Tuttle and W.P. Seering, "Vibration Reduction in 0-g Using Input Shaping on the MIT Middeck Active Control Experiment," *American Control Conf.* Seattle, WA, 1995, pp. 919-923.

[152] T.D. Tuttle and W.P. Seering, "Vibration Reduction in Flexible Space Structures Using Input Shaping on MACE: Mission Results," *IFAC World Congress*. San Francisco, CA, 1996.

[153] T.D. Tuttle and W.P. Seering, "A Zero-placement Technique for Designing Shaped Inputs to Suppress Multiple-mode Vibration," *American Control Conf.* Baltimore, MD, 1994, pp. 2533-2537.

[154] A. Tzes and S. Yurkovich, "An Adaptive Input Shaping Control Scheme for Vibration Suppression in Slewing Flexible Structures," *IEEE Transactions on Control Systems Technology*, June, 1993, pp. 114-121.

[155] A.P. Tzes, M.J. Englehart, and S. Yurkovich, "Input Preshaping With Frequency Domain Information For Flexible-Link Manipulator Control," *Proceedings of the AIAA Guidance, Navigation and Control Conference*. Boston, MA, 1989, pp. 1167-1175.

[156] A.P. Tzes and S. Yurkovich, "Adaptive Precompensators for Flexible-Link Manipulator Control," *28th Conference on Decision and Control*. Tampa, FL, 1989, pp. 2083-88.

[157] M. Valasek, "Input Shaping Control of Mechatronical Systems," *Ninth World Congress on the Theory of Machines and Mechanisms*. Milan, Italy, 1995, pp. pp. 3049-3052.

[158] G.N. Vanderplaats, *ADS - A Fortran Program for Automated Design Synthesis, Version 2.01, User's Manual*. Santa Barbara, CA: Engineering Design Optimization, Inc., 1987.

[159] W. VanderVelde and J. He, "Design of Space Structure Control Systems Using On-Off Thrusters," *J. Guidance, Control and Dynamics*, 1, 1983, pp. 53-60.

[160] D. Wang, "Comparison of Optimal and Nonoptimal Control Strategies for the Single Flexible Link," *Int. Journal of Robotics and Automation*, 3, 1993, pp. 130-6.

[161] J. Watkins and S. Yurkovich, "Input Shaping Controllers for Slewing Flexible Structures," *Proceedings of the IEEE International Conference on Control Applications*. 1992, pp. 188-93.

[162] J. Watkins and S. Yurkovich, "Vibration Control for Slewing Flexible Structures," *American Control Conference*. 1992, pp. 2525-9.

[163] B. Wie and D.S. Bernstein, "Benchmark Problems for Robust Control Design," *J. of Guidance, Control, and Dynamics*, 5, 1992, pp. 1057-9.

[164] B. Wie and Q. Liu, "Comparison Between Robustified Feedforward and Feedback for Achieving Parameter Robustness," *Journal of Guidance, Control, and Dynamics*, 4, 1992, pp. 935-943.

[165] B. Wie, R. Sinha, and Q. Liu, "Robust Time-Optimal Control of Uncertain Structural Dynamic Systems," *J. of Guidance, Control, and Dynamics*, 5, 1993, pp. 980-983.

[166] B. Wie, R. Sinha, J. Sunkel, and K. Cox, "Robust Fuel- and Time-Optimal Control of Uncertain Flexible Space Structures," *AIAA Guidance, Navigation, and Control Conf.* Monterey,

CA, 1993, pp. 939-948.

[167] J.L. Wiederrich, "Residual Vibration Criteria Applied to Multiple Degree of Freedom Cam Followers," *ASME Journal of Mechanical Design*, October, 1981, pp. 702-705.

[168] J.L. Wiederrich and B. Roth, "Design of Low Vibration Cam Profiles," *Conference on Cams and Cam Mechanisms*. Liverpool, England, 1974.

[169] J.L. Wiederrich and B. Roth, "Dynamic Synthesis of Cams Using Finite Trigonometric Series," *ASME Journal of Engineering for Industry*, February, 1975, pp. 287-293.

[170] W.W. Wierwille, *Trans. AIEE Comm. Electronics*, 63, 1962.

[171] K. Zou, V. Drapeau, and D. Wang, "Closed Loop Shaped-Input Strategies for Flexible Robots," *Int. J. of Robotics Research*, 5, 1995, pp. 510-529.

[172] K. Zuo and D. Wang, "Closed Loop Shaped-Input Control of a Class of Manipulators with a Single Flexible Link," *Proceedings of the IEEE International Conference on Robotics and Automation*. Nice, France, 1992, pp. 782-787.

[173] A. Zverev, *Handbook of Filter Synthesis*. John Wiley & Sons, 1967.

INDEX